

ÉCOLE NORMALE SUPÉRIEURE

Paris

Thèse présentée par

Günther KAMPFER

pour l'obtention du

Diplome de Docteur

de l'École Normale Supérieure, Paris

Modélisation et Instrumentation en

Physique, Energies, Géosciences et Environnement

Laboratoire d'accueil : Laboratoire de Géologie de l'ENS, Paris

SUJET: PLIS ET FRACTURES D'EXTENSION DANS LES ROCHES STRATIFIÉES

(FOLDS AND TENSION FRACTURES IN STRATIFIED ROCKS)

Soutenue le 13 Octobre 2010

devant un jury composé de:

M. BAZALGETTE Loic	Examineur (Géologue, SIEP)
M. FRIZON de LAMOTTE Dominique	Président (Prof., Univ. Cergy-Pontoise)
M. GUITON Martin	Examineur (Ingénieur de recherche, IFPEN)
M. LEROY Yves	Directeur de Thèse (Dr. CNRS, ENS)
M. MAERTEN Frantz	Examineur (Direct. R&D, IGEOS)
M. MAILLOT Bertrand	Rapporteur (M. de Conf., Univ. Cergy-Pontoise)
M. RAPHANEL Jean	Rapporteur (Dr. CNRS, Ecole Polytechnique)

Résumé

Le premier but de cette thèse est de développer une méthode objective pour l'interprétation de profils sismiques et des structures qui sont susceptibles d'être des réservoirs pétroliers. Le deuxième but est l'amélioration de la prévision des fractures dans les roches laminées, qui déterminent la perméabilité.

Les expériences et les résultats analytiques montrent l'initiation, l'évolution et l'arrêt d'un kink et d'un pli de propagation de rampe (PPR). Les expériences avec paraffine multicouches établissent la relation entre la distribution des fractures, la formation des charnières endommagées et l'évolution d'un pli de kink. Les résultats analytiques se fondent sur des règles géométriques combinées à l'approche externe de l'analyse limite. Les bandes de compaction, les failles et les plis sont en concurrence à l'initiation du kink. Le mode dominant dépend de l'inclinaison des couches et de la profondeur d'enfouissement de la structure. Les résultats sont présentés dans une carte de mécanismes dominant dans l'espace des enfouissements et l'inclinaison des couches. La même approche est utilisée pour étudier le PPR dont l'évolution se termine à cause de l'initiation d'une faille. Parmi tous les paramètres, c'est l'angle de friction dans les charnières qui contrôle cette transition.

La deuxième partie de cette thèse présente les résultats expérimentaux, numériques et analytiques sur les fractures. Une couche composée de gypse compacté, est en extension par sa base et se fracture en mode I. La relation entre la distance entre les fractures et l'épaisseur d'une couche est linéaire, quand la structure est saturée en fractures. Cette saturation est liée à un décollement de la base de la couche. La méthode des éléments finis et la théorie de la plasticité permettent de valider ces résultats. L'approche analytique (analyse limite) a donné un critère simple pour prédire si un décollement ou une fracture va se former. Un nouveau critère pour la distance entre deux fractures est proposé.

Dans la dernière partie de cette thèse, un nouveau dispositif expérimental est présenté afin d'étudier les fractures en flexion. L'épaisseur d'une couche n'influence pas la distance entre les fractures si il y a seulement une flexure. Cette influence est par contre grande si la couche est cintrée et en extension.

Mots-clés: analyse limite, décollement, éléments finis, expériences, fractures, plis.

Abstract

The first objective of this thesis is to contribute to the development of quantitative tools for an objective interpretation, based on mechanical equilibrium and material strength, of kink-folds and fault-related folds which are potential oil reservoirs. The second objective is to improve the prediction of fracture distributions in layered sequences which control the permeability.

Experiments and analytical results are presented on the onset, the development and the arrest of kink-folds and fault-propagation folds. The experiments, with a sequence of paraffin layers under compression, show the relation between the fracture distribution, the formation of damaged hinges and the development of kink-folds. The analytical results are obtained by combining simple geometrical rules with the application of the maximum strength theorem (limit analysis). It is shown how compaction bands, reverse faults and kinks are competing at the onset of a kink fold, depending on the initial dip of the layered structure and the burial depth. The same methodology is applied to the development of the fault-propagation fold which is shown to be potentially interrupted by thrusting, depending on the frictional properties of the various hinges.

The second part presents experimental, numerical and analytical results on the extension of a block, composed of an analogue material (compacted gypsum), resulting from the stretching of its foundation. A linear relation between the bed thickness and the fracture spacing is observed at saturation. Saturation is linked to the delamination of the interface between the block and its foundation. The finite-elements calculations, based on plasticity theory, to produce strain localisation, confirms the competition between the delamination and the fracture process. The analytical approach, based again on the maximum strength theorem, provides a simple criterion to decide on the dominant mode of failure as well as a new relation for the fracture spacing.

The last part of this thesis presents a new experimental device to create bending fractures. It is shown that layer thickness does not influence the fracture spacing under bending. To the contrary, this influence is remarkable if a combination of bending and stretching is applied.

Keywords: delamination, experiments, folds, finite elements, fractures, limit analysis

Zusammenfassung

Das erste Ziel der vorliegenden Arbeit ist die Anwendung einfacher quantitativer Werkzeuge (mechanisches Gleichgewicht und Materialfestigkeit), die auch zur objektiven Interpretation seismischer Profilschnitte benutzt werden können. Die angewandte analytische Methode stellt sich als überaus effektives Instrument heraus, um die Entwicklung von Faltenstrukturen zu studieren, die potentielle Erdöl-Lagerstätten darstellen. Das zweite Ziel ist es, die Vorhersage von Rissystemen in Mehrlagensystemen zu verbessern, welche die Permeabilität von vielen Reservoirs bestimmen.

Experimente und analytische Ergebnisse werden präsentiert, welche die Initiierung und das Ende der Entwicklung von Knickfalten und frontaler Knickungen (*Fault-propagation folds, FPF*) beschreiben. Experimente mit Mehrschichtplatten aus Wachs zeigen die Beziehungen zwischen Risseverteilung, Scharnieren und der Genese von Knickfalten. Die Grundlage der analytischen Ergebnisse sind geometrische Beziehungen und die Berücksichtigung der maximalen Materialfestigkeit eines Körpers (*Maximum Strength Theorem*). Die Initiierung von Kompaktionsbändern, von Überschiebungen und von Knicken wird für verschiedene Überlagerungshöhen und Neigungen der Lagen gegenübergestellt und die Domänen der vorherrschenden Strukturen in einer *Deformations-Karte* präsentiert. Die selbe analytische Methode wird für die Beschreibung von FPFs angewandt, deren Wachstum durch das Ansetzen einer Überschiebung beendet wird. Die Reibungseigenschaften in den Scharnieren der Struktur bestimmen massgeblich den Übergang zwischen Faltung zur Überschiebung.

Im zweiten Teil der Arbeit werden experimentelle, numerische und analytische Resultate präsentiert, bei denen Lagen aus verdichtetem Gipspulver an der Unterseite gedehnt werden. Eine lineare Beziehung zwischen Lagendicke und Rissabstand ist festzustellen, wenn der Probekörper mit Rissen gesättigt ist. Diese Sättigung steht im Zusammenhang mit auftretendem Schlupf zwischen Probekörper und seiner Basis. Mit Hilfe von Finiten-Elementen und Plastizitätstheorie wird der Wettbewerb zwischen Schlupf und Rissentwicklung bestätigt. Die selbe analytische Methode, die auch für den strukturellen Teil angewandt wurde, liefert ein einfaches Kriterium, um zwischen die Dominanz der beiden Versagensmechanismen voraussagen zu können. Eine neue Beziehung zwischen Rissabstand und Lagendicke wird ebenfalls vorgestellt.

Im letzten Teil dieser Dissertation wird ein neuer experimenteller Apparat vorgestellt, mit dem Biegerisse hergestellt werden können. Erste Experimente zeigen, dass die Lagendicke keinen Einfluss auf den Abstand von Biegerissen hat. Im Gegensatz dazu, wird ein bemerkenswerter Einfluss der Lagendicke beobachtet, wenn einer Lage zusätzlich zur Biegung, Dehnung aufgezwungen wird.

Schlagerwörter: Experimente, Falten, Finite-Elemente, Limit Analysis, Risse, Schlupf

Remerciements

There are many people who deserve to be mentioned on these first pages because without them, this thesis would not have been realized as it is.

I would like to begin with the acknowledgements to my parents. Without them I would not exist and they supported me throughout my life as good as they could. It is a pity that my father cannot experience this event but he would probably have not expected something different from his son.

I also have to thank my dear wife Kathrin. She agreed to give up our well situated life in Salzburg /Austria and to return to a modest students life in a tiny apartment in Paris. I would not have been capable taking care of all the bureaucratic obstacles in the french system. She managed everything courageously and was my best friend throughout the last years. In the meanwhile we became three Austrians, far away from home. Kathrin and I are enjoying our little son Paul Halldor Nikolaus, who was born on the 9th December 2009 in the Clinique Jeanne D'Arc in the 13th Arrondissement in Paris. Thanks Paul, for not crying too much during the night, so I could sleep and recover for the challenges which were waiting for me at the ENS.

Thank you, Yves M. Leroy for the great time and all your support during the last three years. Under your supervision I have spent probably the most delightful and best time I could ever have on a Grande École. It has been a privilege to work with you!

I would like to thank the grandfather of this thesis Florian K. Lehner, who always had some good advices based on his experience, working for Shell and in Academia. He was the one, who introduced me in April 2007 to the father of this thesis Yves M. Leroy. Together with Florian, I worked on Part III of this thesis which was financed by Prof. Franz Neubauer from the Geology department of the University of Salzburg, which I appreciate very much.

I am grateful for several discussions and constructive input from Bertrand Maillot and Dominique Frizon de Lamotte from the University of Cergy-Pontoise during the work on the structural part.

Thanks to Françoise Larincq, the good spirit of the Laboratoire de Geology for her administrative help. A big "merci beaucoup" also to Pierpaolo Dubernet and Baptiste Mulot for their support concerning computer issues. I also have to thank Françoise Vivent from the library for her help organizing all the literature and Angélique Manchon for her efficient support getting reimbursed for the expenses from journeys. Further thanks to Marline Francis and Gilles Druilhe for taking care of the inscription issues and the working contracts, respectively. I would also like to thank my colleagues from the department who welcomed and accompanied me through a great time at the ENS: Abdeltif Lahfid, Adeline Pons, Alexandra Robert, Audrey Ougier-Simonin, Corentin Le Guillou, Chang Liu, Christian Chopin, Dominique Janots, Eva Hoise, Jean-Noel Rouzaud, Jerome Fortin, Julien Gasc, Manuel Pubellier, Myriam Kars, Nadege Fremont, Nathaniel Findling, Pauline Souloumiac, Ramzi Ammar, Yves Gueguen and all the others which I have forgotten, in the final rush.

Special thanks to Manuel Willemse for re-connecting Loic Bazalgette and Yves Leroy. Without him, the collaboration between the Carbonate Research Team of Shell in Rijswijk/The Netherlands and the

Laboratoire de Geologie of the ENS would probably have never been born. I also need to thank Najwa Yassir, the former team leader of the Carbonate Research Team, and Loic Bazalgette for arranging the funding of the thesis and the challenging time with interesting discussions I had during two internships in their team. I appreciate very much the support during the experimental work from the staff in the laboratory environment of SIEP-Rijswijk: Fons Marcelis, Rien Groenewegen, Xander Boersma and many others. Last but not least I thank Anita Csoma, Xiomara Marquez, Brigitte Vlaswinkel, Erwin Adams, Rob Forkner, Iulian Huela, Sadok Lamine, Pal Mayur, Paul Milroy, Chris Nicholls, Danny Long and all the others from the Carbonate Team for the warm welcome during the previous internships and the great time we also had at the Hora Feliz on Friday evening in the Halve Maan.

I appreciate very much the suggestions from the reviewers Bertrand Maillot and Jean Raphanel, which improved the quality of this manuscript. Thanks also to the other members of the jury Dominique Frizon de Lamotte, Frantz Maerten, Martin Guiton and Loic Bazalgette for their careful reading and suggestions which have been considered in this final version of my thesis.

Contents

Résumé	i
Abstract	iii
Zusammenfassung	v
1 Introduction	7
1.1 Introduction en Français	7
1.2 Introduction in English	9
I Structural Analysis	11
2 Review on folding and faulting	13
2.1 Folds and faults in the lab	15
2.2 Geometrical construction of folding and faulting	17
2.3 Folding and faulting with analytical and numerical approaches	18
2.3.1 Folding, no faulting	20
2.3.2 Methods for capturing folding and faulting	23
2.4 The maximum strength theorem	26
2.4.1 The support function for the discontinuity	28
2.5 Example	33
3 Experiments with paraffin multilayers under compression	35
3.1 Setup	35
3.2 Results of the experimental study	36
3.3 Conclusions and open questions	41
4 Imperfection and burial-depth sensitivity of the initiation and development of kink-folds in laminated rocks	43
4.1 Abstract	43
4.2 Introduction	45

4.3	Initiation of compaction bands and reverse faults	48
4.3.1	Geometry of the prototype, maximum strength domain and support function	49
4.3.2	Failure mode with a single velocity discontinuity	52
4.3.3	Special case: onset of compaction bands, no imperfection.	55
4.3.4	Special case: onset of reverse faults, no imperfection.	56
4.3.5	Influence of the burial depth on the selection of the dominant failure mode.	57
4.3.6	Imperfection sensitivity.	57
4.4	Onset, development and arrest of the kink-fold	62
4.4.1	Prototype for the kink fold	62
4.4.2	The upper bound in tectonic force	67
4.4.3	Initiation of kink-fold	69
4.4.4	The failure-mechanism maps	77
4.4.5	Evolution based on the upper bound in tectonic force	81
4.4.6	Arrest of kink development	83
4.5	Conclusion	86
References		89
5	The competition between fault-propagation folding and thrusting based on the maximum strength theorem	93
5.1	Abstract	93
5.2	Introduction	95
5.3	The geometry and the velocity field of the FPF	97
5.3.1	The geometrical construction	97
5.3.2	The velocity field	101
5.4	The maximum strength theorem and bounds on the forces	106
5.4.1	The theorem applied to the push-up of a block on an inclined ramp	107
5.4.2	Thrusting through the fault-propagation fold.	110
5.4.3	The least upper bound for the fault-propagation fold	113
5.4.4	Locking of the fault-propagation fold	117
5.5	Competition between folding and thrusting	119
5.5.1	Optimizing the thrust	119
5.5.2	The dominant mode	123
5.6	Conclusion	126
5.7	Appendix 1 : Hadamard's jump condition	129
5.7.1	Geometry and kinematics	129

5.7.2	The jump conditions	131
5.7.3	Application to a simple shear mode of transformation	131
5.8	Appendix 2 : The locking of region no 2 of the hanging wall	132
5.9	Appendix 3 : Faulting in an horizontal layer with friction at the base	134
References		137
II	Fracturing and Joints	139
6	Introduction	141
6.1	Tension fractures and axial splitting	141
6.2	Hobbs and Price’s contributions	144
6.2.1	Frictional coupling model by Price	144
6.2.2	Welded layer model by Hobbs	145
6.3	Fracture spacing as a function of the bed thickness	148
6.3.1	Analogue experiments and field observations	148
6.3.2	Analytical and numerical approaches	152
6.4	Fracture propagation in multilayered sequences	154
6.5	Summary	155
7	Analogue Experiments	157
7.1	Setup	157
7.2	Analogue Materials	159
7.2.1	Gypsum powder	159
7.2.2	Quartz sand	161
7.2.3	Talc powder	161
7.2.4	Tile adhesive	162
7.3	Experiments of Type I	162
7.3.1	Analysis and Interpretation	164
7.4	Experiments of Type II	166
7.4.1	Analysis and Interpretation	166
7.5	Multiple loading of the specimen	168
7.5.1	Analysis and Interpretation	168
7.6	Experiments of Type II in the CT-Scanner	170
7.6.1	Experimental settings for the documentation with the CT-scanner	171

7.6.2	Summary of the observations from the extension-compression-extension experiments	173
7.7	Experiments of Type III	175
7.7.1	Observations	175
7.8	Conclusion	178
8	FE-calculations of gypsum layers under basal extension	181
8.1	Introduction	181
8.2	Constitutive equations	182
8.3	FE calculation	184
8.3.1	Failure in extension or compression of a 2D block	185
8.3.2	The prototype for the experiment with gypsum	190
8.3.3	Frictional interface between a brittle layer and an elastic membrane	200
8.4	Conclusion	203
9	Application of the maximum strength theorem to the experiments with gypsum	207
9.1	Introduction	207
9.2	The support function for the truncated Coulomb criterion	207
9.3	The prototype and the virtual velocity field	209
9.4	The least upper bound to the force	212
9.5	Size effects	214
9.5.1	Application to the experimental work	215
9.6	Modified velocity field	216
III	Bending fractures	221
10	A new experimental device to create bending fractures	223
10.1	Introduction	223
10.2	Experimental device and creating the specimen	225
10.2.1	Preparation of the setup	228
10.3	Results and discussion	228
10.3.1	Bending to an anticline	230
10.3.2	Reverse bending from an anticline to a syncline	230
10.4	Conclusion	231
10.5	Acknowledgements	233

11 Conclusion and Perspective	235
11.1 Kink-folds	235
11.2 Fault-propagation folds	237
11.3 Fractures in a layered sequence	238
11.3.1 Fracture spacing and delamination	238
11.3.2 Perturbation of fracture propagation in multilayers	239
11.3.3 Bending fractures	240
References	241
Annexes	249
A Complementary work/results on the kink-fold	249
A.1 Minimizing the upper bound for compaction band and reverse fault	249
A.1.1 General constraints	249
A.1.2 Constraints for the compaction band:	250
A.1.3 Constraints for the reverse fault:	252
A.2 Kink arrest because of faulting	253
A.2.1 Types of failure modes	254
A.2.2 Reverse fault splitting the kink	255
A.2.3 Upper hinge as the localisation of a thrust	258
A.2.4 Results	259
A.3 The influence of different parameters on the system behaviour	260
A.3.1 Influence of the density of the competent multilayer	260
A.3.2 Influence of the height of the fluid below on the system	261
B CT-Scanner images of gypsum layers under basal extension	265
C Deflection of a polycarbonate plate	273

Chapter 1

Introduction

1.1 Introduction en Français

Le but de cette thèse est de développer une méthode objective pour l'interprétation de profils sismiques et des structures qui sont susceptibles d'être des réservoirs pétroliers. L'apport de ce travail est la prise en compte des concepts d'équilibre mécanique et de la résistance maximale des matériaux. Les structures géologiques qui nous intéressent sont en particulier, des plis de kink et des plis de propagation de rampe (Partie I, Chapitre 2 jusqu'au Chapitre 5). Ces plis sont importants pour l'industrie pétrolière puisqu'ils constituent typiquement des réservoirs d'hydrocarbures. L'existence d'un piège structural est une condition nécessaire mais pas suffisante pour définir un réservoir d'intérêt économique. Pour le stockage et la production de pétrole ou de gaz, la roche doit avoir une certaine perméabilité qui est liée à la porosité et à la présence des fractures ouvertes. C'est la raison pour laquelle la Partie II (Chapitre 6 jusqu'au Chapitre 9) et la Partie III (Chapitre 10) sont concernées par les fractures dans les multicouches, d'un point de vue expérimental, numérique et analytique.

Beaucoup d'efforts ont été investis par le passé afin de comprendre les plis et les failles. La revue du Chapitre 2 fournit les concepts qui sont nécessaires pour comprendre la démarche derrière le choix de l'approche principale préconisée dans cette thèse. On montre qu'il existe, en effet, un outil approprié et économique, développé autour du *Théorème de la résistance maximale*, pour prévoir la durée de vie d'une structure. Ce théorème est équivalent à l'approche externe de l'analyse limite et son nom a été proposé pour souligner que la résistance matérielle de la roche et des interfaces est la pièce maîtresse de la prévision. Le Chapitre 3 présente les résultats des expériences de laboratoire sur des multicouches composées de paraffine sous compression. Le but de ces expériences est d'étudier le début et l'évolution des plis de kink. Le Chapitre 4, publié au *Journal of the Mechanics Physics of Solids* et le Chapitre 5, un manuscrit prêt pour la soumission

à publication, sont concernés par l'initiation, l'évolution et l'arrêt de deux structures différentes, le pli de kink et le pli de propagation de rampe. Pour le pli de kink, nous démontrons que son initiation se fait en compétition avec deux autres modes de ruine que sont la faille inverse et la bande de compaction. On donne les conditions de dominance de chacun de ces modes dans une carte construite dans l'espace de la pression d'enfouissement et l'angle d'inclinaison initiale des couches. Le pli de kink se développe sans pour autant être interrompu par un chevauchement à moins d'introduire un endommagement dans les charnières. Le bilan mécanique du pli de propagation de rampe nous révèle qu'il peut être interrompu par un chevauchement à moins que les charnières soient suffisamment faibles.

La Partie II de cette thèse porte sur la rupture des roches laminées. Après une introduction (Chapitre 6), le travail expérimental avec des matériaux analogues sur des fractures de mode I est présenté (Chapitre 7). L'extension est appliquée aux spécimens ayant une ou plusieurs couches de poudres cohésives et compactantes. Les couches intercalaires se composent de sable ou de matériaux plus cohésifs. La distribution des ruptures et l'espacement moyen des fractures avant et à saturation sont présentés. Le Chapitre 8 suivant a pour but d'aider l'interprétation de ces résultats expérimentaux. Il est basé sur la méthode des éléments-finis et suppose que la réponse matérielle peut être décrite avec une théorie d'élastoplasticité. La résistance matérielle est de type Coulomb avec une coupure en tension pour reproduire la rupture en tension diffuse. L'adoucissement est également utilisé pour localiser la déformation dans des zones équivalentes à des fractures en mode I. Ces calculs numériques nous révèlent la concurrence entre le décollement à la base de la couche et la fracture. Ces deux modes de rupture sont étudiés analytiquement dans le Chapitre 9 qui examine le même système expérimental par l'application du théorème de la résistance maximale. On propose un critère pour estimer le mode dominant en comparant l'angle de friction de l'interface de la base et la résistance à la traction du matériau. Une nouvelle expression analytique pour l'espacement des fractures à saturation est également fournie.

La Partie III de cette thèse, composée d'un seul chapitre, présente des résultats préliminaires obtenus avec un nouveau dispositif expérimental proposé pour créer des fractures dans une couche en flexion. Les fractures ainsi créées ressemblent plus à celles observées dans les plis et montrent un espacement différent à saturation que les fractures obtenues par élongation des couches. L'espacement des fractures en flexion pure n'est pas influencé par l'épaisseur de la couche. Cette conclusion diffère de celle obtenue dans la Partie II. Cette influence est par contre grande si la couche est cintrée et à la fois en extension. Le Chapitre 11 de conclusion fournit un résumé des résultats de thèse et quelques perspectives pour une recherche future tant expérimentale qu'analytique.

1.2 Introduction in English

The aim of this thesis is to contribute to the development of quantitative tools for an objective interpretation, based on the concepts of mechanical equilibrium and material strength, of geological structures and more particularly, of kink-folds and fault-related folds (Part I, Chapters 2 to 5). These folds are important for the oil-industry since they constitute typically hydrocarbon reservoirs. The existence of a structural trap is a necessary but not a sufficient condition to define a reservoir of economical interest. For the storage and production of oil or gas, the rock needs to have a certain permeability which is linked to the porosity and to the presence of opened fractures. It is for that reason that Part II (Chapters 6 to 9) and Part III (Chapter 10) are concerned with the fracturing of layered sequences from the experimental, numerical and analytical point of views.

Much effort has been done in the past to understand folding and faulting. The review in Chapter 2 provides the concepts which are necessary to understand the philosophy behind the choice of the main approach advocated in this thesis. It is shown that there exists indeed a suitable and economic tool, developed around the maximum strength theorem, for predicting the life time of a structure. This theorem is equivalent to the external approach of limit analysis and its name was proposed to emphasize that the material strength of the bulk rock and of the interfaces is central to the prediction. Chapter 3 presents the results of laboratory experiments on multi-layers composed of paraffin and under layer parallel compression. The aim of these experiments is to study the onset and the evolution of kinks and folds. Chapter 4, published in the *J. Mech. Phys. of Solids* and Chapter 5, a manuscript ready for publication, are concerned with the onset, the evolution and the arrest of two different structures, the kink and the fault-propagation fold.

Part II of this thesis is devoted to the fracturing of layered rocks. After a brief introduction (Chapter 6) the experimental work with analogue materials on mode I fractures is presented in Chapter 7. Extensional strain is applied to specimen having one or several layers of compacted cohesive powders. The interlayers are composed of sand or of more cohesive materials. The fracture distribution and the average fracture spacing before and at saturation are reported. The next chapter is proposed to help in the interpretation of these experimental results. It is based on the finite-element method and assumed that the material response can be described with an elasto-plasticity theory. The yield envelop is of a Coulomb type with a truncation in tension to reproduce diffuse tensile fracturing. Softening is also introduced to localize the strain in zones resembling mode I fractures. These numerical calculations reveal the competition between the delamination at the base of the specimen and the mode I fracturing. These two modes of failure are further studied analytically in Chapter 9 which considers the application of the maximum strength theorem to the same experimental setup. A criterion is proposed to estimate which of

the two modes dominates based on a comparison of the frictional angle of the basal interface and the tensile strength of the bulk material. A new analytical expression for the fracture spacing at saturation is also provided.

Part III of this thesis, composed of a single Chapter, introduces preliminary results obtained with a new experimental device proposed to create fractures in a bent layer. The fractures thus created are closer to the ones observed in folds and show a different spacing at saturation than fractures obtained by layer parallel extension. The spacing of pure bending fractures are found not to be influenced by the layer thickness, a conclusion which differs from the one reached in Part II.

The concluding Chapter 11, is not a bankruptcy act, but provides a summary of the thesis results and some perspectives for future research.

Part I

Structural Analysis

Chapter 2

Review on folding and faulting

There is probably no better and complete overview related to the analysis of geological structures than the seminal contribution by Price & Cosgrove in *Analysis of Geological Structures* which was first published 1990. I will not try to repeat their work in this introduction but I would like to provide the elements (rheology and method of analysis) which are necessary to understand the assumptions adopted in this thesis to capture, at least partly, folding in and without the presence of faults.

Within compressional regions, such as fold-and-thrust belts, thrust sequences accommodate the largest amount of shortening. In addition, folds are created which show a strong variety of characteristics depending on several parameters. These parameters include the composition of the mechanical units, their strength properties, their geometrical shape, the burial depth, the history and the strain rate at which layered rocks are deformed. Three major processes are creating folds. They are presented in Figure 2.1: buckling (a), bending (b) and passive folding (c).

Buckle folds are formed by compressional forces which act at an acute angle from the layering of thin plates. Thicker plates under compression have the tendency to create faults to accommodate the applied shortening. Bending can be observed in layers above normal faults or thrusts (forced folding, Stearns 1970) and is caused by a force which acts at an obtuse angle to the layering. Other mechanisms which lead to forced folds can be observed when units are bending in a basin or above an arising dome. Passive folding has its cause in the shape of the sedimentation process itself and is not the result of a deformation mechanism like the buckle or forced folds. However, passive folds are representing irregularities in the geometry of the layering, further referred to as geometrical imperfections, which are able to localize folds and faults in a subsequent deformation stage.

Elliott (1965) proposed a classification of the geometry of folds based on dip isogons, which

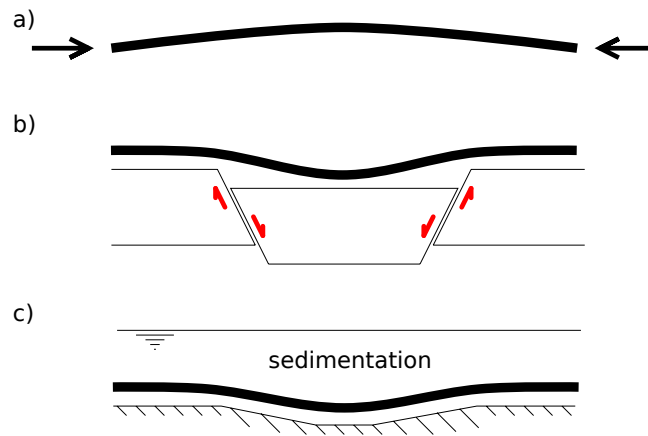


Figure 2.1: Processes which create folds or fold-like structures. (a) buckling, (b) bending and (c) passive folding.

are lines connecting points with the same tangential dip. Fold profiles are then separated in three major classes: convergent (three subclasses: strongly convergent - thinning of the hinge region, parallel, weakly convergent - thickening of the hinge region), similar and divergent fold profiles, see Figure 2.2. In addition, due to their frequent observation in nature, specific names which are not restricted to a particular dip isogon pattern are quite common such as: curved fold, chevron fold, kink band and box fold (Price & Cosgrove J.W. 1990). Examples of curved and chevron folds in the Bude Formation (SW-England) and in layered carbonates in the Coulazou valley (south France) are shown in Figure 2.3.

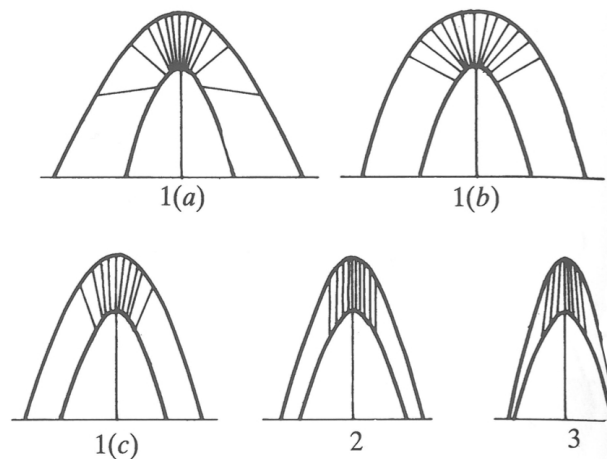


Figure 2.2: Classification of fold profiles using dip isogon patterns. (1) convergent, (2) similar and (3) divergent fold profiles (After Ramsey, 1967, p.365)

The study of geometries, fractures, stylolites, thrusts and lineations in the field give hints but

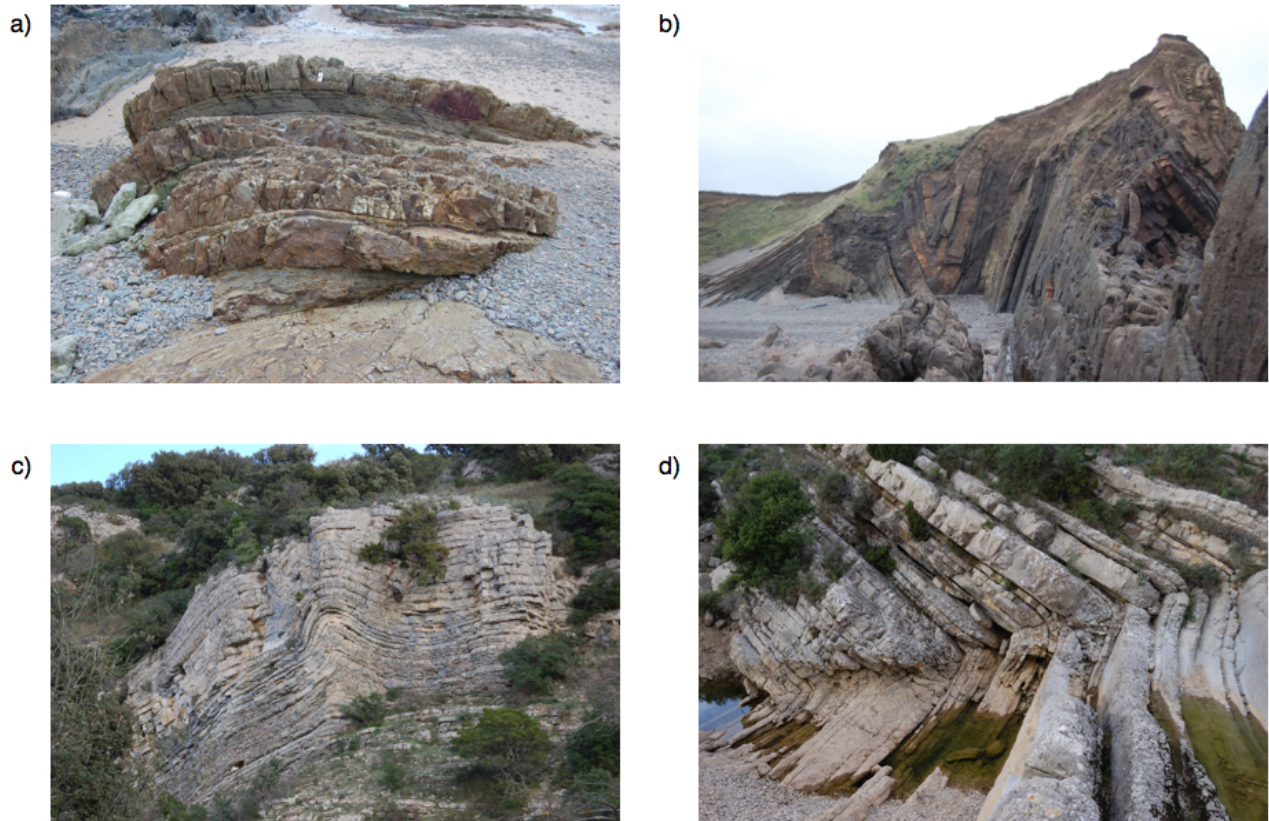


Figure 2.3: (a) curved fold and (b) angular or chevron fold in the Bude formation (sandstone-shale sequences, SW-England), (c) curved fold and (d) angular hinge of a box fold in layered carbonates in the Coulazou valley (south of France)

do not provide a full explanation of the processes involved. Besides the descriptive study, a lot of effort has been done to reproduce folds experimentally in the laboratory or by analytical and numerical means. The objective of the next sections is to provide a short overview of the methods which have been used so far to study folding and faulting.

2.1 Folds and faults in the lab

The most demonstrative way to reproduce folds and to study their evolution is to create them in the laboratory with a properly scaled model (Hubbert, 1937).

Paterson & Weiss (1966) compressed phyllites parallel to their foliation with the application of confining pressure. Reverse kink bands initiate and chevron folds result from their intersection. These kink bands spread during further deformation increasing the size of the chevron folds by flexural slip folding. Weiss (1968) did further analogue experiments with paper card decks,

where chevron folds formed by the same process, as shown in Figure 2.4a.

The experiments reported by Cobbold, Cosgrove & Summers (1971) investigated the behaviour of composite foliated rocks which is described in terms of the average rheological properties of the rock, not the properties of the individual components (Figure 2.4b). Multiple plasticine layers (lubricated with graphite, separated by a film of petroleum jelly or simply unbonded) or only flakes of plasticine, which represented different degrees of anisotropy, were compressed at various angles with respect to the layering. They concluded that compressed rocks which have anisotropic material properties may become unstable internally. This instability, which does not necessarily involve a competence contrast, leads to the development of internal structures whose form is mainly governed by the degree of anisotropy of the rock, rather than by other rheological properties such as elasticity or viscosity. A high degree of anisotropy results in kinks and a low anisotropy results in buckle folds.

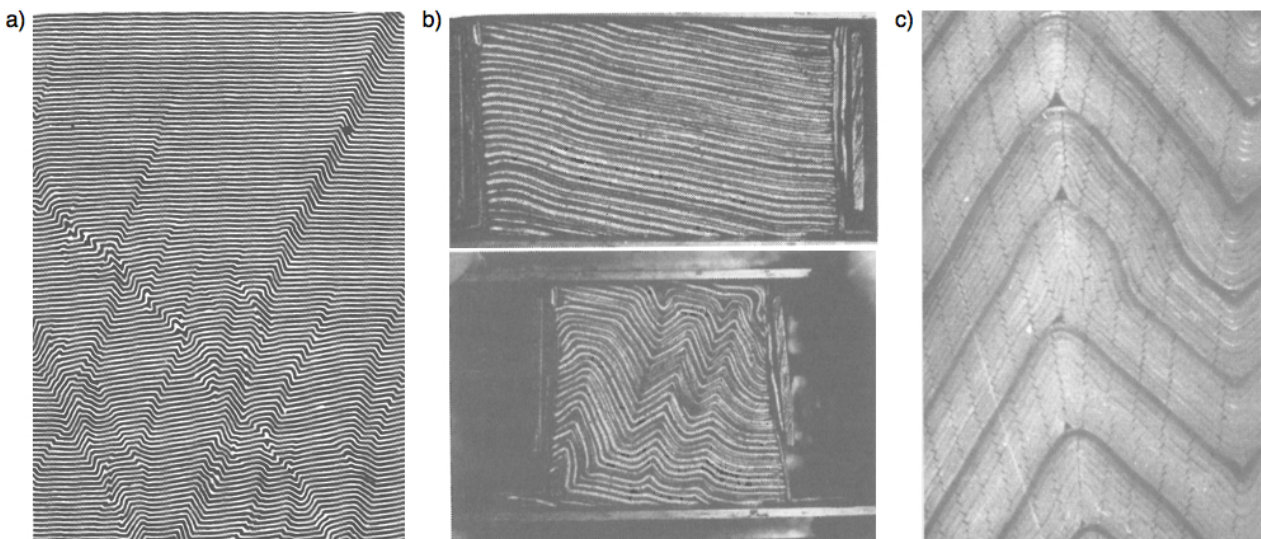


Figure 2.4: Analogue Experiments with paper cards generating folds by Weiss (1968) in (a), plasticine multilayers by Cobbold, Cosgrove & Summers (1971) (b), and with paraffin wax layers by Latham (1983) (c)

Johnson & Ellen (1974) subjected multilayers with various thickness ratios of soft (gelatine) and stiff (rubber strips) elastic layers, to layer parallel shortening in order to examine transitions from one fold type to another. A further objective was to find evidences for discontinuities (faults) oriented along the characteristic directions predicted by a non-linear elasticity theory. These characteristic directions are not predicted when using linear elasticity theory.

Latham (1983) did compressional experiments with 1 mm thick paraffin wax layers, lubricated by liquid soap (Figure 2.4c). He varied the rheological properties by changing the temper-

ature and confining pressures for different set-ups. He observed the creation of folds or faults, depending on the choice of the setup. Low temperatures and low confining pressures create, what he calls a high *intrinsic anisotropy*, being a competence contrast between the layers in terms of the viscosity. A low *intrinsic anisotropy* is obtained at higher temperature and higher confining pressures. Latham's conclusion is the important impact of what he calls the *induced anisotropy*, being the difference between secant and tangent modulus (Figure 2.5), on the resulting structure. If the anisotropy is predominantly *intrinsic*, internal buckles form and if it is predominantly *induced*, shear zones or faults develop. Kink bands form, when there is a certain amount of both *anisotropies*. If there are no *anisotropies*, passive amplification of any initial irregularity occurs. Buckling and faulting are thus end member structures of instabilities caused by lateral compression of multilayers. The term *anisotropy* is not well chosen by Latham, since an anisotropy in a structure is defined as its properties being directionally dependent. It is for that reason why his definitions of anisotropy are indicated with italic letters.

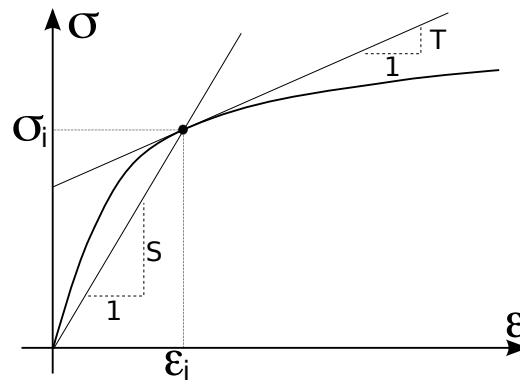


Figure 2.5: Secant (S) and tangent modulus (T) for a given stress σ_i and a strain ϵ_i .

2.2 Geometrical construction of folding and faulting

The restoration of cross sections is necessary to understand the history of the structures. Assumptions of volume and length conservation are then often made and lead to the proposal of geometrical methods. The result of their application is the initial stage of the formations before the folding and thrusting started. Hayes (1891), Chamberlain (1910), Bucher (1933), Goguel (1952) and Laubscher (1962), summarized by Dahlstrom (1969), proposed such geometrical methods to get restored cross sections. The impact in the research community of these simple geometrical constructions had to wait for the seminal work of Suppe (1983) who described the geometrical evolution of fault-bend folds. It is at the basis of many interpretations of seismic sections through fold-and-thrust belts (Mitra, 1990). This geometrical evolution (Suppe &

Medwedeff, 1984) is discussed at length in Chapter 4. These constructions can be done with pencil and ruler on a piece of paper. Figure 2.6 shows an interpreted cross section through the Pine Mountain thrust sheet and below the result of an imbrication of fault-bend folds based on Suppe's geometrical construction. For rather complex sections the work is now done by computers. One of the first systematic constructions with the help of computers has been done by Zoetemeijer & Sassi (1992) making use of a software developed initially by Endignoux & Mugnier (1990). All these methods consider that the material moves through hinges which are fixed or migrating velocity discontinuities. Some of these hinges are fixed, others are migrating in the current configuration of the structure. Erslev (1991) realized that the geometry of folding cannot always be explained by the constructions which were considering only hinge migration. He introduced, with the example of a fault-propagation fold, a theory of a "distributed, strain-compatible shear in a triangular shear zone" migrating with the fault (Figure 2.7). The resulting geometries were, due to their smoother profiles, closer to field observations. The methodology is more sophisticated than the construction proposed by Suppe and requires the use of computers. Zehnder & Allmedinger (2000) described the velocity field within a trishear zone which was also used for an automated forward and backward modelling tool.

Bobillo-Ares et. al. (2000), did an analysis of the geometry of layer profiles folded by tangential longitudinal strain. They took a closer look at the hinges of folds and concluded that the geometry of folded layers involves layer thickening or layer thinning in the hinge region, when migration of the neutral axis is allowed.

The advantage of methodologies which are purely geometrical is evidently the ease with which results are obtained. However, there is a lack of objectivity since two structural geologists may interpret differently the same sequence of thrusting and folding. This missing objectivity results from the absence of any concepts of mechanical equilibrium and rock strength. The goal of a mathematical description of folds and faults is thus to bring an objectivity into the interpretation done by structural geologists. Suitable analytical or numerical approaches help to distinguish between possible and unlikely scenarios which lead to the structures observed within a fold and thrust belt.

2.3 Folding and faulting with analytical and numerical approaches

Modelling techniques rely on different assumptions concerning the material behaviour. Elastic materials are characterized by a reversible stress-strain relationship which may be linear or non-linear and is independent of the rate of deformation. Visco-elasticity includes a time dependency

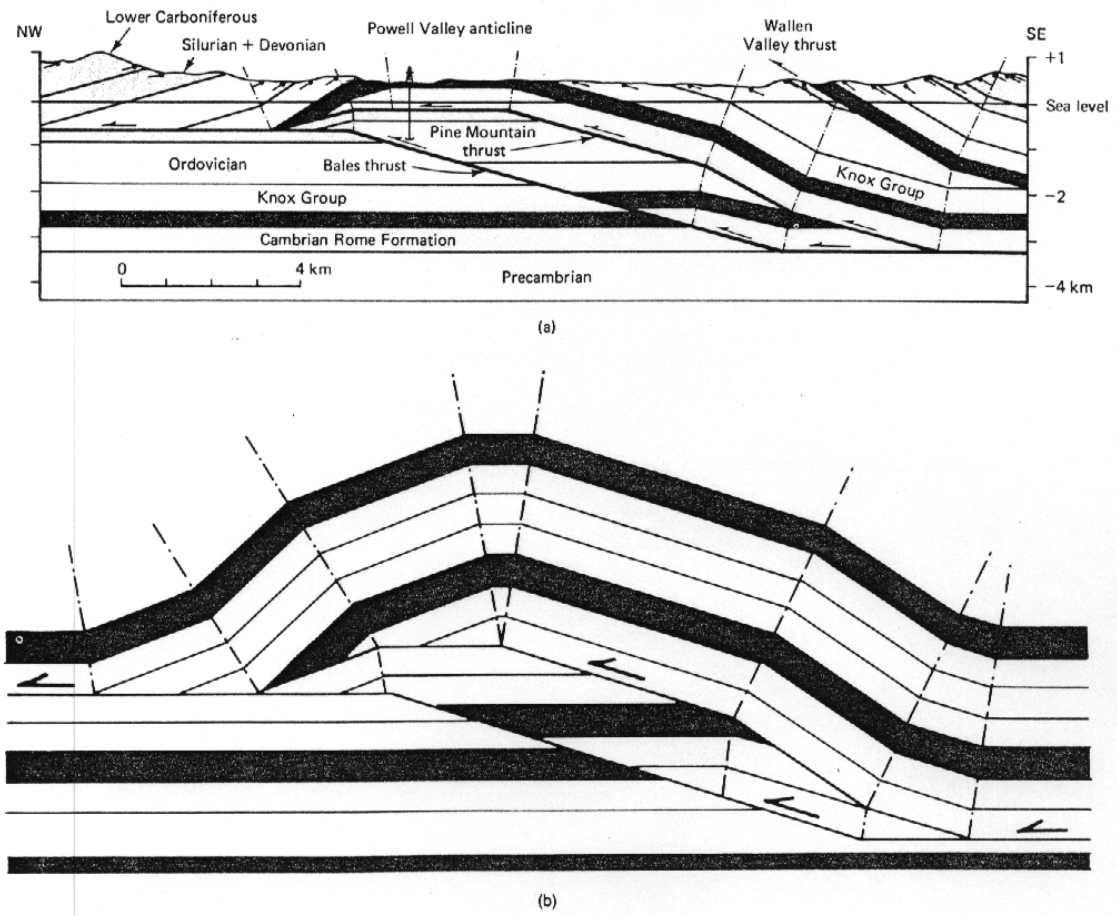


Figure 2.6: Application of Suppe's fault-bend fold to the cross section of the Pine Mountain, southern Appalachians, showing multiple imbrication fault bend folds (Suppe, 1993)

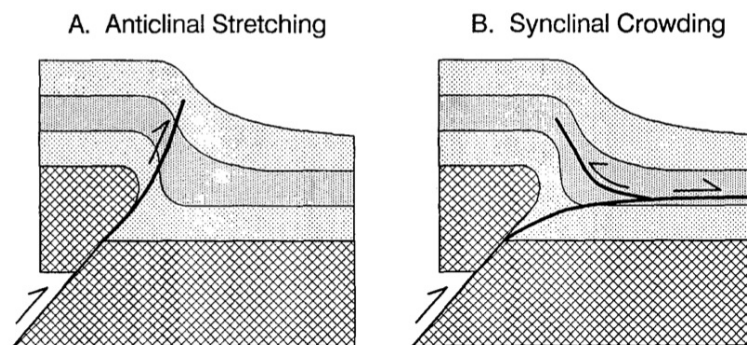


Figure 2.7: Trishear regions ahead of a fault (Erslev, 1991).

	onset	development	
Elasticity	1D solution, buckling no faulting Euler (1757),	folding and characteristic directions of discontinuities based on nonlinear elasticity and folding A. Johnson (1974) post bifurcation analysis, buckling, no faulting Leroy et al. (2002)	folding, no faulting
Visco-elasticity	stability, buckling no faulting Biot (1960s), Ramberg (1960s)	numerical study of buckling no faulting Chapple (1968) Finte Element modelling for buckling no faulting De Braemaecker and Becker (1978)	
Elasto-plasticity	stability, buckling including faulting Triantafyllidis and Leroy (1997)	Finte Element modelling for large deformations, Fault-propagation fold Braun and Sambridge (1994) Finte Element modelling for buckling Massin et al. (1997)	folding and faulting
Limit analysis	onset of kink folding Maillot and Leroy (2006) onset of faulting Cubas et al. (2009) Soloumniac et al. (2009)	evolution of kink folding Maillot and Leroy (2006) evolution of folding and faulting Cubas et al. (2009)	

Figure 2.8: Overview of analytical and numerical methods for the study of folding with and without faulting.

in the material behavior. Elasto-plasticity theories allow the description of irreversible deformation and failure of the material. Numerous yield criteria and flow rules have been used to describe material deformation in the post failure domain. The approach advocated in this thesis which makes only use of the strength of a material and has its origin in limit analysis further referred to as the maximum strength theorem. In the following the applicability of these various material concepts as well as the methods of analysis (finite-element, analytical methods, etc...) are discussed. A summary of this discussion is found in Figure 2.8.

2.3.1 Folding, no faulting

Elasticity

Euler investigated already in the 18th century the buckling of an elastic beam and predicted that the maximum compressive load N_k prior to buckling is

$$N_k = \left(\frac{\pi}{\beta L} \right)^2 EI ,$$

disregarding gravity forces and any confining pressure, E being the Young's modulus of the material and I , the moment of inertia of the cross section ($I = \frac{b h^3}{12}$, with b the width and h the height of the beam, Figure 2.9). The factor βL defines the distance of the inflection points of

the idealized buckled beam and is called the buckle length of the beam. The main result is that the critical stress $\sigma_k = N_k/A$, ($A = bh$, cross section of the beam, Figure 2.9), is a hyperbolic decreasing function with increasing slenderness of the beam (by definition $\lambda = L/h$) and reads:

$$\sigma_k = \frac{E \pi^2}{12 \beta^2 \lambda^2}. \quad (2.1)$$

Four principal cases, depending on the boundary conditions on the beam ends, are defined and shown in Figure 2.9. A beam which is only fixed vertically and horizontally (rotation is allowed) at its ends has a buckle length which is equal to L , case (b). The buckle length is $2L$ or $0.5L$ if rotation, vertical and horizontal displacement are prohibited at one, case (a), or both end points, case (d), respectively. Asymmetric boundary conditions which forbid rotation on one side, vertical and horizontal displacements on both sides, show a buckle length of $0.7L$, case (c).

The buckling instability analysis is valid for an elastic medium and does not account for faulting. However, based on that expression, I would like to propose a simple rule to judge whether buckling or faulting should occur. Assuming an Andersonian stress field and a Coulomb criterion describing the strength domain of the solid (ϕ_s the friction angle and c_s the cohesion of the solid), thrusting will occur at an angle $\pi/4 - \phi_s/2$ with respect to the maximum compressional direction at a force which is equivalent to

$$A(\sigma_1(1 + \sin \phi_s) - 2c_s \cos \phi_s) / (1 - \sin \phi_s). \quad (2.2)$$

Setting the expression for the buckling force (uniaxial compression) equal to the force necessary to create faulting (general case) provides the critical slenderness ratio λ_{cr} at which the transition from thrusting to buckling takes place:

$$\lambda_{cr} = \frac{\pi}{\beta} \sqrt{\frac{E(1 - \sin \phi_s)}{12 [2c_s \cos \phi_s - \sigma_1(1 + \sin \phi_s)]}}. \quad (2.3)$$

if $\lambda_{cr} > \frac{L}{h}$, thrusting,

if $\lambda_{cr} < \frac{L}{h}$, buckling.

Note that a frictional material with $c_s \rightsquigarrow 0$ in combination with $\sigma_1 \rightsquigarrow 0$ leads to $\lambda_{cr} \rightsquigarrow \infty$ which means that without cohesion and without burial pressure no buckling is possible. One should keep in mind that the approach for the buckle load disregards gravity forces and confining pressure, which leads to a slenderness which can be increased or decreased, depending on the confining pressure. An equally distributed confining pressure will stabilize the beam and the critical slenderness will thus be larger than the predicted one by equation 2.3.

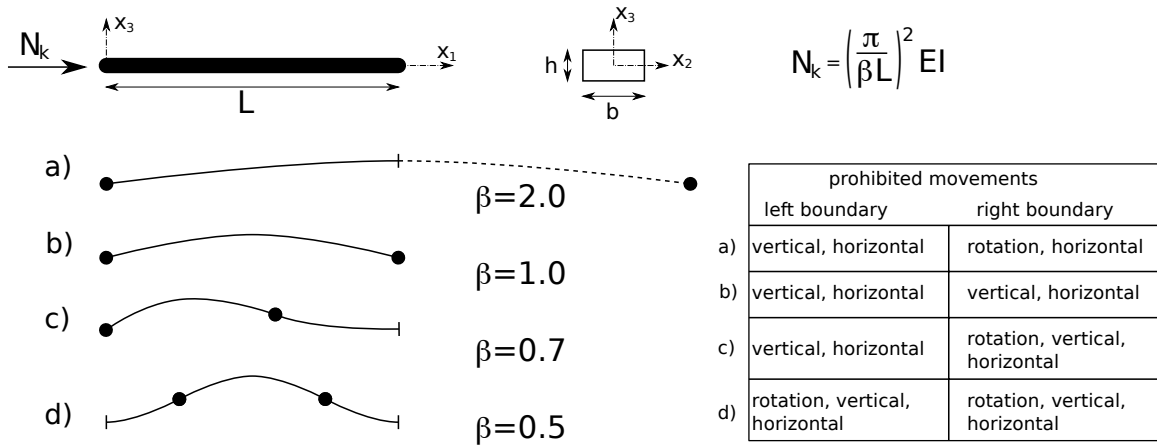


Figure 2.9: Four Euler-cases with buckle lengths, depending on the boundary conditions of the beam ends. The solid dots are marking the inflection points

Handin et al. (1972) deformed limestone and sandstone beams under various confining pressures in the lab. They found out that beams with a length-thickness ratio greater than 30 buckle elastically and the force is in good agreement with the Euler load.

The work of Johnson & Ellen (1974) on folding concentrated on the theoretical conditions under which ideal concentric, chevron, sinusoidal and kink folds as well as monoclin flexures might form. Therefore they used linear and non-linear elasticity. The theory of characteristics which is used for solving hyperbolic partial differential equations is applied to find discontinuities in the geometry. Indeed these directions can be found using non-linear elasticity but not when assuming linear elasticity. They figured out that linear elastic materials create sinusoidal and continuous fold shapes. Kinks and chevron folds are thus results of the deformation of solids which are described with non-linear material response.

Leroy et al. (2002) did asymptotic analysis of the post-buckling of an elastic plate over an inviscid and buoyant fluid. The Lyapunov-Schmidt-Koiter decomposition was applied to construct the bifurcated equilibrium path. The buckling loads result mainly from the bending stiffness at large wave numbers ($n\pi/L$) and from gravity at shorter wave numbers. Beyond the onset of buckling they observed a decrease of the compressive force during further shortening but no faulting could be explained since, again, the beam is elastic.

The following section gives an overview on the development with non-linear materials which have shown results being in line with experiments and field cases.

Visco-elasticity

Ramberg (1963, 1964) and Biot (1957, 1961, 1963, 1964, 1965) have developed in parallel two different approaches to explain the initiation of buckling in multilayered units based on viscous rheologies. Ramberg states that for slow creep under relatively small differential stress, rocks may in a first approximation be treated as viscous fluids and can therefore be described by fluid dynamics. He developed a model for a single layer and also for multilayered sequences of competent and incompetent layers but is basically interested in the behaviour of the individual layer surrounded by another viscous material. This approach is in contrast to Biot, who studied the global behaviour of a multilayered sequence.

2.3.2 Methods for capturing folding and faulting

Elasto-plasticity

A better understanding of folding and faulting requires the introduction of plasticity theory, as the evolution of structures is clearly affected by the failure of materials and the accumulation of irreversible deformation.

Let's assume an Andersonian stress state and a strength domain bounded by a Coulomb failure criterion

$$c_s - \sigma_n \tan(\phi_s) \leq \tau, \quad (2.4)$$

c_s being the cohesion, ϕ_s the angle of internal friction of the solid, σ_n and τ the stress components along normal and tangential directions of the failure plane, respectively. The maximum stress that a beam under axial compression (σ_3) and confining pressure (σ_1) is able to sustain before shear failure, cannot be larger than those given by the graphical solution based on the Mohr circle (Figure 2.10). The orientation of the failure plane with respect to the direction of maximum compression is given by the angle $\pi/4 - \phi_s/2$. The force at shear failure thus reads:

$$F_{thr} = A\sigma_3 = A \frac{\sigma_1(1 + \sin \phi_s) - 2c_s \cos \phi_s}{1 - \sin \phi_s}, \quad (2.5)$$

with A the area of the cross section (tension is positive and compression negative).

Chapple (1969) presents a study on the influence of the plastic zones in the crest regions on the fold-shape. This study is a continuation of his previous work (Chapple, 1968). He investigated the folding of a linear viscous layer and concluded that fold shapes in nature are the result of non-linear material laws. Viscous layers form smoothly rounded folds whereas plasticity localizes the deformation in the crest regions and forms chevron folds.

Rudnicki & Rice (1975) stated that initiation of localized faulting is not necessarily connected to strain softening but is likely to occur also during strain hardening, when using non-associated

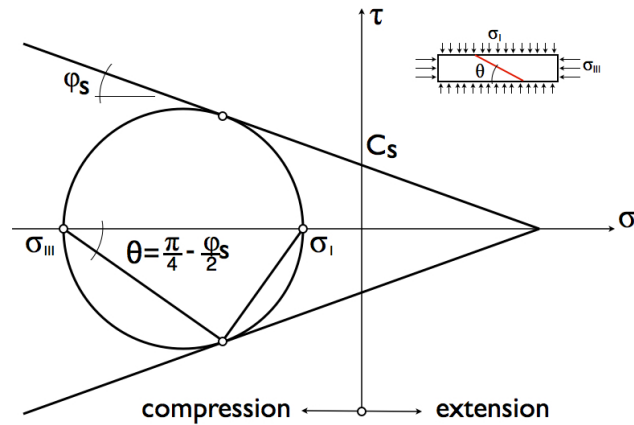


Figure 2.10: Coulomb failure envelope with Mohr circle. The failure plane is dipping with θ

plasticity. More generally, their results support the hypothesis that the inception of faulting can be modelled as a constitutive instability.

Leroy & Ortiz (1989) proposed a special finite element with enhanced deformation modes based on the Rudnicki & Rice criterion as a local failure condition. They could then explore the development of faulting beyond its onset. They concluded that the softening which is observed in plane strain biaxial sand specimens may result entirely from geometrical effects and not from material behaviour. Although the material in their analysis hardens at all times, the force-displacement diagrams show softening as a consequence of strain localization in faults.

Depending on assumptions of small or large strain, dynamical remeshing during the finite element calculations is necessary, as it has been done by Braun & Sambridge (1994) for the example of the development of a fault-propagation fold. They assumed a brittle, frictional material to simulate the propagation of the ramp and the folding, without predefining the rheology of the fault.

Numerical investigations of folding processes by compressing a cohesive, frictional overburden resting on a viscous substratum of lower density is presented by Massin et al. (1996). In a first instance, the layer deformed in a diffuse manner and created a smoothly bended fold. During further shortening, the strain localized within the hinges and formed a chevron fold. There is "loss of ellipticity" at the quadrature points but this local faulting criterion (Rudnicki & Rice, 1975) is not leading to major faulting.

Hardy & Finch 2007 investigated the mechanical stratigraphy and the transition from trishear to kink-band fault-propagation fold forms above blind basement thrust faults with discrete element modelling.

Computation times are decreasing due to faster and parallel working processors. However,

numerical modelling techniques (Finite Elements, Finite Differences, Discrete Element Method) are still time consuming and sensitive to the domain discretization procedure. Calculations are very time intensive when carried out beyond the initiation of failure and the implementation of plasticity theory, when remeshing for capturing strain localization, the handling of contact and surface friction can be quite sophisticated. Those are the reasons why we propose Limit Analysis as an alternative method to capture folding and faulting.

Limit analysis

Limit analysis provides bounds on the failure loads a structure can sustain. This method has its origin in civil and structural engineering and seems to be little used in geology. Its main principle is to construct lower and upper bounds of the load sustainable by a structure by using either a static or a kinematic approach. The application to accretionary wedges and thrust-and-fold-belts is discussed by Souloumiac et al. (2009). They construct the statically admissible stress field by introduction of a linear, spatial discretization. The nodal unknowns are stresses. Taking the example of the wedge shape of the Nankai prism, they tried to distinguish between active and passive faults, depending on the decollement friction angle (Figure 2.11).

The complementary theory which provides an upper bound to the loading is the external or kinematical approach. It consists of the minimization of the power generated by a kinematically admissible velocity field. Maillot & Leroy (2006) extended the external approach to evolution problems which is further referred to as the maximum strength theorem. Defining the geometrical development of a structure and applying the theory at each time or displacement increment, they provide an energy balance, from which an unknown maximum loading is derived. The loading which is necessary for the further development of a failure is compared with the one of another mode of failure. The search for the onset of a new failure mode is done in a systematic manner at each step of advanced deformation. This procedure only compares different failure modes in terms of forces and decides to choose the least force and the corresponding failure mechanism for the further evolution in the post failure domain. No plasticity theory is included in this approach. Cubas et al. (2008) used this approach to study thrusting sequences within accretionary wedges. They compared the onset of a new thrust with the further development of the actual active thrust in terms of forces. The failure mode (new or current thrust) leading to the least upper bound is proposed to be the dominant failure mode. An example of a thrusting sequence with the evolution of the tectonic force is presented in Figure 2.12. Note the force drop in (b), after each initiation of a new thrust. The reason for that is the weakening of the material properties along the fault plane. The amount of weakening defines the life-time of an active ramp, till the next failure plane is favoured.

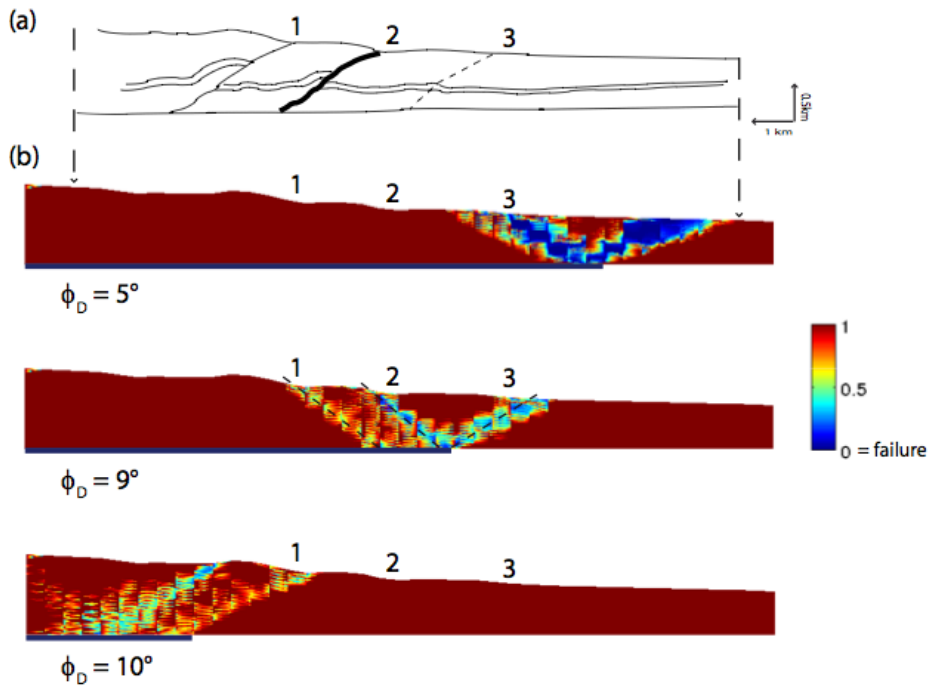


Figure 2.11: The interpretation of the seismic section through Nankai's prism (a) (redrawn from Moore et al., 1991), and the distribution of the distance to the failure criterion, for three different values of the decollement friction angle, (b). The lengths of the activated decollement are marked by blue lines.(from Souloumiac et al., 2009)

Maillot & Leroy (2006) investigated the onset and evolution of a kink in a layered beam under axial compression. Adding burial pressure and geometrical imperfections to a multilayered beam under compression is the subject of Chapter 4. The maximum strength theorem is applied to the fault-propagation fold (Suppe & Medwedeff, 1984) in Chapter 5. The same theorem, although restricted to the onset of faulting, is applied in the second part of this thesis on the fracture development in layered rocks (Chapter 9). This maximum strength theorem is so prominent in this thesis that it is presented in details in the following section.

2.4 The maximum strength theorem

The maximum strength theorem is the external approach of limit analysis as described by Salençon (2002). The name has been chosen to emphasize that the main concept is material strength.

The main ingredients for this theory are mechanical equilibrium and the restriction that the stress remains within a convex strength domain. There is no need for the introduction of a complete plasticity theory as it is often thought. Consequently, the discussion on the selection of a flow

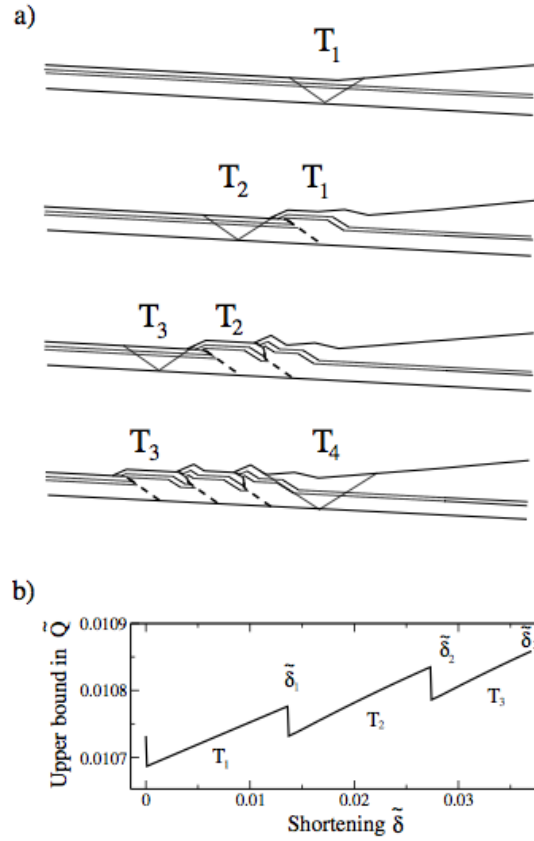


Figure 2.12: Sequence of thrusting T_1 to T_3 ending with the first out of sequence thrust T_4 in (a) and the evolution of the least upper bound on the tectonic force as a function of the amount of shortening $\tilde{\delta}$ in (b). (from Cubas et al., 2008)

rule (associated or non associated) is not relevant to this theorem.

The starting point of the external approach is the construction of a virtual velocity field. The virtual velocity field is not necessarily the actual velocity field and it is only required to satisfy the boundary conditions. Such a velocity field is said to be kinematically admissible (KA) and is identified by a superposed hat (\hat{U}). Consider a general domain Ω occupied by a solid and crossed by a surface of potential in the velocity field Σ_U . The power of the external forces \mathcal{P}_{ext} is the sum of the power in the velocity field of the loading (Q) and of the inertial forces such as gravity. For the example presented in Figure 2.13 this power is:

$$\mathcal{P}_{ext} = \underline{Q} \cdot \hat{U}(\underline{x}_Q) + \int_{\Omega} \rho \underline{g} \cdot \hat{U} \, dV, \quad (2.6)$$

where \underline{x}_Q is the point of application of the force \underline{Q} . The power of the internal forces \mathcal{P}_{int} reads:

$$\mathcal{P}_{int} = \int_{\Omega} \underline{\underline{\sigma}} : \hat{\underline{d}} \, d\Omega + \int_{\Sigma_U} [[\hat{U}]] \cdot \underline{T} \, da, \quad \text{with } \underline{T} = {}^t \underline{\underline{\sigma}} \cdot \underline{n}, \quad (2.7)$$

the first term corresponding to the dissipated energy due to diffuse deformation ($\underline{\underline{\sigma}}$ is the stress tensor and $\underline{\underline{\hat{d}}}$ is the virtual rate of deformation tensor) in the bulk Ω and the second term corresponds to the power along the discontinuity Σ_U of the velocity field and \underline{T} is the traction vector. Note that \underline{n} is the normal to the discontinuity and $[[\underline{\hat{U}}]]$ is the velocity jump over the discontinuity, also referred to as $\underline{\hat{J}}$ which is the difference of the velocity on the plus and minus side. The external and internal power terms are equal by the theorem of virtual power for any choice of the KA velocity field:

$$\mathcal{P}_{ext} = \mathcal{P}_{int} \forall \underline{\hat{U}}. \quad (2.8)$$

The power of the external forces is known, apart from the unknown loading Q for which we seek an upper bound. The power of the internal forces has the unknown terms $\underline{\underline{\sigma}} : \underline{\underline{\hat{d}}}$ and $\underline{T} \cdot \underline{\hat{J}}$. Instead of trying to get the exact values, an upper bound will be defined. If there exists a convex strength domain G , then there exists a function $\pi(\underline{x}, \cdot)$, referred to as the support function, which is an upper bound to the virtual power. They are expressed as:

$$\begin{aligned} \pi(\underline{\underline{\hat{d}}}) &= \text{Sup}\{\underline{\underline{\sigma}}' : \underline{\underline{\hat{d}}} \mid \underline{\underline{\sigma}}' \in G\} \text{ and} \\ \pi(\underline{\hat{J}}) &= \text{Sup}\{\underline{\hat{J}} \cdot \underline{T}' \mid \underline{T}' \in G\}, \end{aligned} \quad (2.9)$$

at every point of the domain or of the discontinuity, respectively. Their derivation is explained in the next subsection. The implementation of the support function provides the power of maximum resistance (\mathcal{P}_{mr}) which reads:

$$\mathcal{P}_{mr} = \int_{\Omega} \pi(\underline{\underline{\hat{d}}}) \, d\Omega + \int_{\Sigma_U} \pi(\underline{\hat{J}}) \, da. \quad (2.10)$$

The theorem of virtual power and 2.8 combined with 2.10 provides the upper bound Q_u to the tectonic force:

$$\underline{Q} \cdot \underline{\hat{U}}(\underline{x}_Q) \leq Q_u \cdot \underline{\hat{U}}(\underline{x}_Q) = \int_{\Omega} \pi(\underline{\underline{\hat{d}}}) \, d\Omega + \int_{\Sigma_U} \pi(\underline{\hat{J}}) \, da - \int_{\Omega} \rho \underline{g} \cdot \underline{\hat{U}} \, dV. \quad (2.11)$$

For the case of a uniform velocity in each subdomain of Ω (Figure 2.13), the virtual power of the stress field is zero because there is no internal initial deformation. Hence, the first term on the right vanishes to zero and only the second term, which represents the dissipated power for the creation of the failure plane, has to be taken into account. This assumption is adopted for the rest of this thesis.

2.4.1 The support function for the discontinuity

The support function $\pi(\underline{\hat{J}})$ is at the core of the maximum strength theorem. This function provides the upper bound on the dissipated power along activated failure planes and interfaces. This upper

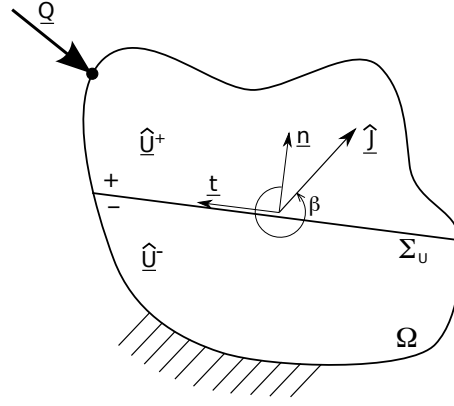


Figure 2.13: A solid domain Ω loaded with the force \underline{Q} . Virtual velocity fields $\hat{\underline{U}}$ on the positive and the negative side of a discontinuity Σ_U , where rupture occurs. The jump in velocity $\hat{\underline{J}}$ is given by $[[\hat{\underline{U}}]] = \hat{\underline{U}}^+ - \hat{\underline{U}}^-$.

bound is function of the orientation of the velocity jump and provides the optimum traction vector \underline{T}^* , so that the work $\underline{T} \cdot \hat{\underline{J}}$ is maximum, as defined in equation 2.9.

Let us consider a strength domain G with a regular, smooth surface. The example of an elliptical shape

$$e = \sqrt{\sigma^2 + 2\tau^2} \leq 1, \quad (2.12)$$

is presented in Figure 2.14. Following Saint Venant's principle of the dual space lets us plot stresses and velocities in the same graph. The virtual power \hat{W} of $\underline{T}(\sigma, \tau)$ due to the jump in the velocity $\hat{\underline{J}}$, combined with the introduced Lagrange multiplier $\hat{\lambda}$ which is necessary to enforce that the selected \underline{T} is on the surface $e = 1$, reads:

$$\hat{W} = \underline{T} \cdot \hat{\underline{J}} + \hat{\lambda}(1 - e). \quad (2.13)$$

For the particular case of the elliptical failure criterion (2.12) the virtual power is:

$$\hat{W} = \sigma \hat{J} \cos \beta + \tau \hat{J} \sin \beta + \hat{\lambda} \left(1 - \sqrt{\sigma^2 + 2\tau^2} \right). \quad (2.14)$$

The maximum power is thus given by setting to zero the partial derivatives

$$\frac{\partial \hat{W}}{\partial \sigma} = 0 \quad \text{and} \quad \frac{\partial \hat{W}}{\partial \tau} = 0, \quad (2.15)$$

which provides for our particular example:

$$\begin{aligned} \frac{\partial \hat{W}}{\partial \sigma} &= \hat{J} \cos \beta - \hat{\lambda} \sigma = 0, \\ \frac{\partial \hat{W}}{\partial \tau} &= \hat{J} \sin \beta - 2\hat{\lambda} \tau = 0. \end{aligned} \quad (2.16)$$

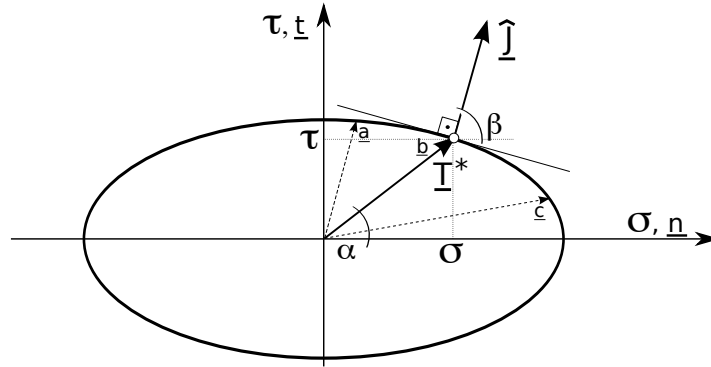


Figure 2.14: Elliptic failure envelope to the strength domain, defined by $e = \sqrt{\sigma^2 + 2\tau^2} = 1$. $\hat{\underline{J}}$ is the velocity jump, oriented with the angle β counter-clockwise from the normal direction \underline{n} and \underline{T}^* is the traction vector reaching the strength of the material and providing the maximum power. The velocity jump is normal to the boundary at \underline{T}^* .

The elimination of the Lagrange multiplier from (2.16) provides the optimum orientation of the stress vector defined by:

$$\tan \beta = \frac{2\tau}{\sigma}. \quad (2.17)$$

The velocity jump is perpendicular to the failure envelope at the optimum stress \underline{T}^* in order to maximise the virtual power. This relation between \underline{T}^* and $\hat{\underline{J}}$ is the one which would have been selected if a plasticity theory had been postulated. However, it has to be pointed out that the velocities which are considered here, are only virtual and are not the real velocity field. The theory of maximum strength is only constructed with the application of equilibrium and the assumption of a convex strength domain.

We do not need to repeat the preceding calculation each time when a new strength domain is defined. Also, when defining a strength criterion which is only piece wise continuous, with corners such as a Coulomb criterion, a geometrical construction provides the support function. First, we have to define the velocity field and thus the velocity jump vectors. $\hat{\underline{J}}$ is the normal of a plane which is presented in Figure 2.15a as a dotted line. In a second step, this plane is moved into the dual space to tangent the strength domain (b). The traction vector at the tangential point defines the traction vector \underline{T}^* which provides the maximum possible power. Figure 2.14 shows three different traction vectors to an elliptic strength domain, indicated as \underline{a} , \underline{b} and \underline{c} . Neither the stress vector \underline{a} , nor \underline{c} are able to provide a larger product on $\hat{\underline{J}}$ than vector \underline{b} . It is observed that the vector \underline{b} provides the maximum for $\underline{T} \cdot \hat{\underline{J}}$.

This statement is valid as long as the strength domain is convex. The strength domain G is

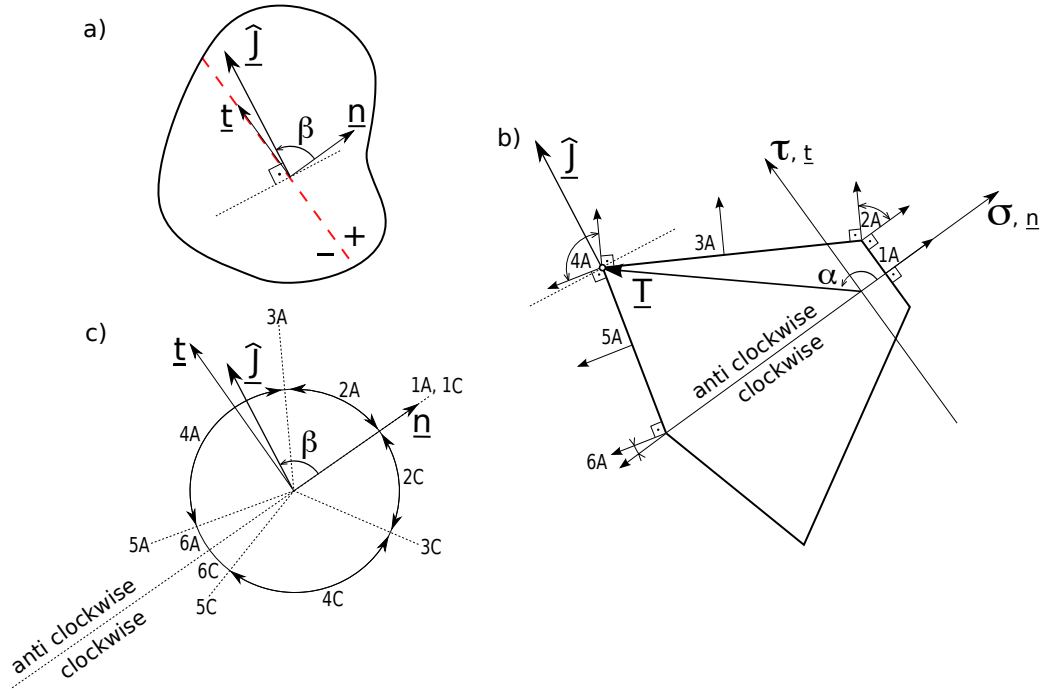


Figure 2.15: A solid, divided in two regions of different velocities by the dotted line, oriented with the normal vector \underline{n} and tangent \underline{t} . A Mohr-Coulomb failure envelope, truncated in tension and closed in compaction which is piecewise linear along the boundary of the strength domain (b). The orientation of the velocity jump along the discontinuity according to the regions of the strength domain are presented in (c).

convex, if

$$\underline{\underline{\sigma_1}}(1 - \zeta) + \zeta \underline{\underline{\sigma_2}} \in G \quad \forall \zeta \in [0; 1], \quad (2.18)$$

for any $\underline{\underline{\sigma_1}}$ and $\underline{\underline{\sigma_2}}$ in G . Applied to the example in Figure 2.16a this convexity condition is equivalently:

$$\tau((1-\zeta)\sigma_2 + \zeta\sigma_1) \leq (1-\zeta)\tau_2 + \zeta\tau_1 \quad \forall \zeta \in [0; 1]. \quad (2.19)$$

The general failure criterion which is used in this thesis is presented in Figure 2.16b. It is of the Coulomb type, truncated in tension and closed in compaction. d is the tensile strength, c the cohesion and ϕ the angle of internal friction. The compaction pressure is P^* and the angle ϕ^* defines the slope of the closure because of compaction (pore collapse, dissolution processes, etc...).

The boundary of the strength domain has corners, indicated as dots in Figure 2.16b. The various T^* along the different parts of the strength domain, presented in Figure 2.15b, are:

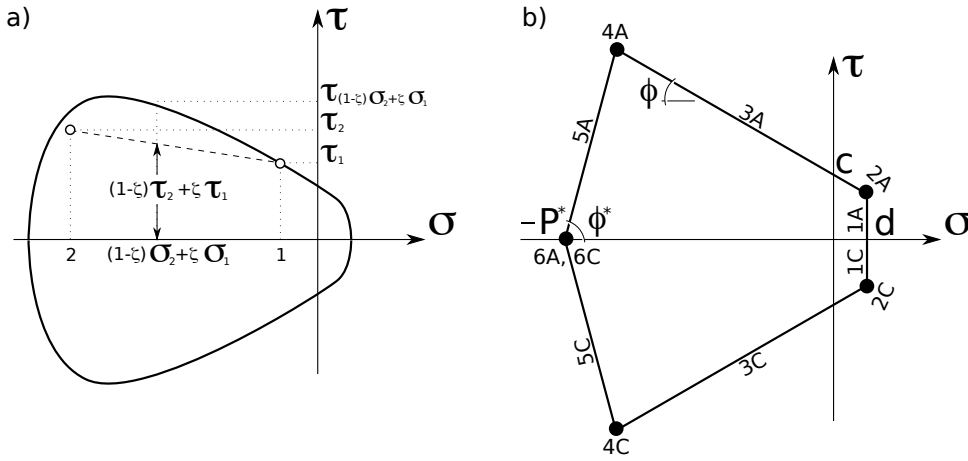


Figure 2.16: A general convex strength domain (a) and of the coulomb type with tension cut off and closure in compaction presented in (b). The points highlight the corners of the boundary of the strength domain.

$$\begin{aligned}
 \underline{T}_{1A}^* &= d\underline{n} + d \tan(\alpha)\underline{t} , \\
 \underline{T}_{2A}^* &= d\underline{n} + (c - d \tan \phi)\underline{t} , \\
 \underline{T}_{3A}^* &= \frac{c \cos \phi}{\sin(\alpha + \phi)} [\cos(\alpha)\underline{n} + \sin(\alpha)\underline{t}] , \\
 \underline{T}_{4A}^* &= (c - P^* \tan \phi^*) \frac{\cos \phi^* \cos \phi}{\sin(\phi^* + \phi)} \underline{n} + (c + P^* \tan \phi) \frac{\sin \phi^* \cos \phi}{\sin(\phi^* + \phi)} \underline{t} , \\
 \underline{T}_{5A}^* &= -\frac{P \sin \phi^*}{\sin(\alpha - \phi^*)} [\cos(\alpha)\underline{n} - \sin(\alpha)\underline{t}] , \\
 \underline{T}_{6A}^* &= -P^* \underline{n} ,
 \end{aligned} \tag{2.20}$$

as one rotates from 0 to π counter clockwise. The six cases correspond to segments or corners of the boundary which are defined in Figure 2.16b. Part 1 along the boundary of the strength domain represents the tension cut-off and part 3 the region, where shear occurs. The transition between opening mode and shear mode occurs in point 2. Region 5 represents a domain where shear in compaction happens which could be also interpreted as the domain, where deformation bands are created. This region is between points 4 and 6. Failure in point 4 is a mixed mode of shear and point 6 represents only a failure due to compaction without any shear. In the linear regions of the failure envelope (1,3 and 5) the jump in velocity is perpendicular to the domain as presented in Figure 2.15b. Various directions of the jump vector are possible at the corners (2, 4 and 6) although the T^* vector keeps the same value for providing the maximum work. Hence, depending on the various orientations of the velocity jump (defined by the angle β from

the normal \underline{n} in Figure 2.15c), there exist six expressions for the support function for clockwise (C) and six for anti clockwise (A) β .

case	β	$\pi(\hat{J}) = \hat{J} \left(\underline{T} \cdot \underline{n} \cos \beta + \underline{T} \cdot \underline{t} \sin \beta \right)$
1A	$\beta = 0$	$\hat{J} d$
2A	$0 \leq \beta \leq \frac{\pi}{2} - \phi$	$\hat{J} (d \cos \beta + (c - d \tan \phi) \sin \beta)$
3A	$\beta = \frac{\pi}{2} - \phi$	$\hat{J} c \cos(\phi)$
4A	$\frac{\pi}{2} - \phi \leq \beta \leq \frac{\pi}{2} + \phi^*$	$\hat{J} \left((c - P^* \tan \phi^*) \frac{\cos \phi^* \cos \phi}{\sin(\phi^* + \phi)} \cos \beta + (c + P^* \tan \phi) \frac{\sin \phi^* \cos \phi}{\sin(\phi^* + \phi)} \sin \beta \right)$
5A	$\beta = \frac{\pi}{2} + \phi^*$	$\hat{J} P^* \sin \phi^*$
6A	$\frac{\pi}{2} + \phi^* \leq \beta \leq \pi$	$-\hat{J} P^* \cos \beta$

There might be cases, when a Coulomb type of strength domain is used, which is not closed in compaction. Regions 5 and 6 will thus not be possible. Instead, the vector T^* will be indefinitely large in region 4, resulting in a support function which is infinite. A meaningful bound has to be limited. For that reason, the velocity jump has a limitation concerning its orientation. It is restricted to be oriented within a cone defined by:

$$-\frac{\pi}{2} + \phi \leq \beta \leq \frac{\pi}{2} - \phi, \quad (2.21)$$

with respect to the normal of the discontinuity. Velocity fields respecting that condition are said to be pertinent.

In the following Chapters 3, 4 and 9 the external approach is applied. Each of these problems needs different parts of the general strength domain which is introduced above. The kink makes use of a strength domain which is closed in compaction, the décollements or faults are described by a simple Coulomb criterion and the opening mode fractures require the tension cut-off.

2.5 Example

A block (length L and heights H) with gravity force ρgHL (ρ is the specific weight and g the gravity acceleration) rests on a flat surface. It is pushed from the right, Figure 2.17, by a force Q which norm is unknown. How large has the force Q to be so that the block moves? For sake of simplicity let us assume a strength domain for the interface between the block and the bottom surface of the Coulomb type, defined in Figure 2.15b without closure in compaction. The strength is thus defined by the cohesion c , the tensile strength d and the friction angle ϕ . We do not need

2.5. Example

the strength of the solid, as we are only interested in the force, which is necessary to activate the interface.

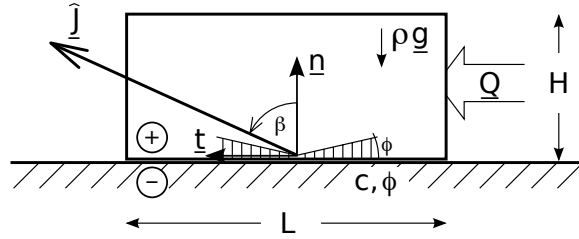


Figure 2.17: Block with length L and gravity force ρgHL on a flat surface. The interface has a Coulomb strength domain with cohesion c and friction angle ϕ .

For the velocity field to be pertinent, the orientation of the jump vector has to be within the cone defined in equation 2.21 and shown in Figure 2.17: the restricted part is highlighted by the dashed region and the angle β will thus be between 0 and $\pi/2 - \phi$. The velocity jump \hat{J} is defined by the difference of the velocity of the positive and the negative side of the discontinuity ($\hat{J} = \hat{U}^+ - \hat{U}^-$). The jump is thus equal to the virtual velocity of the block \hat{U} , since the basement is not moving. The power of the external forces reads:

$$P_{ext} = \hat{U} (Q \sin \beta - \rho gHL \cos \beta) , \quad (2.22)$$

and the maximum resistance is given by:

$$P_{mr} = L\hat{U} (D \cos \beta + (c - d \tan \phi) \sin \beta) . \quad (2.23)$$

The application of the theorem of virtual power provides the upper bound to the force Q

$$Q \leq Q_u = L \cot \beta (\rho gH + d) + L (c - d \tan \phi) , \quad (2.24)$$

after normalization by the virtual velocity \hat{U} .

The minimization of the upper bound leads to the least upper bound of the tectonic force Q_{lu} by varying the only free parameter in our problem, which is the orientation of the jump vector, constrained to be within the interval $[0; \pi/2 - \phi]$. The minimum is reached for the angle $\beta = \pi/2 - \phi$ and the least upper bound then reads:

$$Q_{lu} = L (\rho gH \tan \phi + c) . \quad (2.25)$$

Note that the virtual velocity field for that case implies that the block has to be slightly lifted in order to be pertinent, since a non dilating virtual velocity field would result in a infinitely large tectonic force and is thus not pertinent.

Chapter 3

Experiments with paraffin multilayers under compression

The analogue modelling of multilayered sequences in compression is the objective of this chapter. Experiments performed with phyllites by Paterson & Weiss (1966), plasticine multilayers by Cobbold, Cosgrove and Summers (1971), gelatine-rubber multilayers by Johnson & Ellen (1974) or paraffin wax layers documented by Latham (1983) lead to a better understanding of folding processes in a multilayered setting. More recently, an experimental study with multiple paraffin layers under compression has been done by Bazalgette (2005). His experimental work concentrated on the modelling of two dimensional aspects of folding. The major outcomes were, that the geometrical style of a fold, chevron or curved fold, is depending on the interfacial properties along the bedding planes and on the individual thickness of a single layer which composes a multilayered unit. The extension of his work into the third dimension made possible by a new and larger experimental device has been done in the core shed of the Shell-laboratory in Rijswijk, The Netherlands with the possibility to use a CT-scanner for documenting the deformation.

3.1 Setup

A longitudinal section of the pre-existing loading cell used for this work is shown in Figure 3.1. In the plan view, the cell is approximately one meter long and fifty centimeters wide. The specimen is composed of multiple paraffin plates, the total thickness varying between 30 and 45 mm. This specimen is compressed laterally. To allow for a vertical movement of the multilayer during folding, 25 mm thick layers of plasticine were used to represent soft underlying units and soft overburden. The top plasticine layer has the additional task to prevent the multilayer sequence from being damaged when applying "lithostatic" pressure to the model by inflating a pressure

bag which is placed between the top plate of the loading cell and the upper plasticine layer.

A piston (on the right side of Figure 3.1) applies an horizontal force resulting in a shortening of the plasticine-paraffin-plasticine sequence. The experimental device has the appropriate dimensions to fit into a CT-scanner. After the preparation of the setup, the complete experimental device is placed on the table of the CT-Scanner. The experiments are interrupted at chosen deformation stages and CT-images are taken to get a 4-D evolution of the deformation (i.e., folding and fracture propagation), Figure 3.2. The progress of the deformation is also documented with pictures taken through the transparent sidewalls. Viscous deformation during the CT-Scans were not observed. The interruption of the experiments for scanning the specimen were short (less than five minutes) and the piston did not apply further shortening to the setup.

The specimen unit is composed of paraffin wax plates from Merck-Eurolab, melting point 60–62°, which have the property to form fractures when being deformed at room temperature and strain rates around 10^{-3} s^{-1} . The material is supposed to have a Young's modulus of 18.28 MPa and a uniaxial compressive strength of 2.3 MPa (Bazalgette, 2005). The paraffin plates which are used in the experiments are created by melting a weighted amount of the granular paraffin in a rectangular water filled basin. The water is heated up to 70° Celsius until the paraffin is liquid and forms a flat surface on top of the water. When cooling down the water, the paraffin hardens and can be removed from the surface of the water. It is then cut into the needed dimensions, 650 mm long and 500 mm wide. The paraffin plates are not completely homogeneous but include a certain amount of small bubbles which are distributed rather equally over the whole plate. The air is trapped when the paraffin is swimming as a granulated material on the water surface and begins to melt. In the lab environment, two water basins are available. While one plate is cooling down, the granular paraffin for another one is being melted. The preparation of one experiment, depending on the thickness of the individual layers which compose the mechanical unit of 45 mm height, needs up to five days.

The properties of the plasticine have not been tested. It is in general viscous but it behaves brittle at the nominal strain rates which have been applied during the experiments.

The influence of the friction along the sidewalls on the observed structures is supposed to be small due to the width of the paraffin plates which is slightly smaller than the width of the loading cell. Besides, the sidewalls have been covered with a thin oil film.

3.2 Results of the experimental study

A sequence of pictures visualizing the typical evolution of folding is presented in Figure 3.3. Columns A and E show pictures taken through the transparent side windows of the loading cell

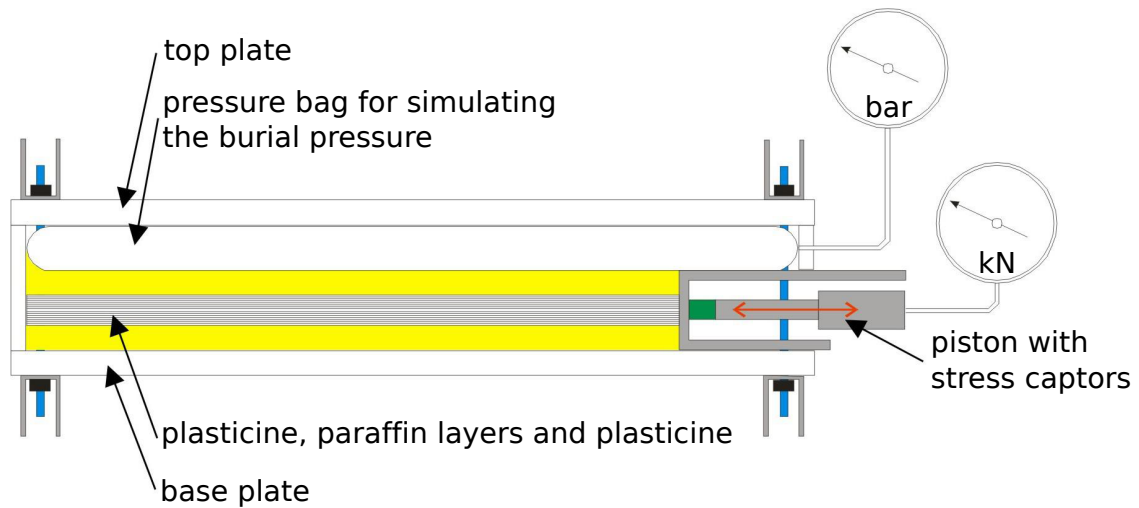


Figure 3.1: Longitudinal section of the loading cell.

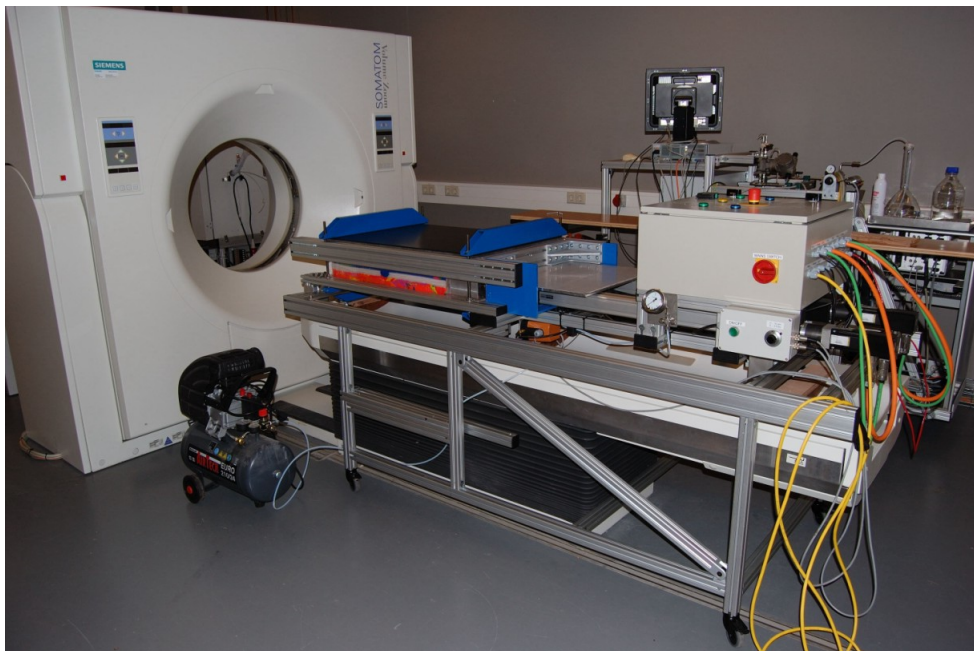


Figure 3.2: The experimental device in front of the CT-scanner in the Shell laboratory in Rijswijk, The Netherlands.

and the columns B, C, and D show longitudinal sections made with the CT-Scanner. The piston pushes from the left side of the longitudinal sections towards the right side.

The results are based on the following experimental setup: The stiff mechanical unit consists of fifteen layers of paraffin, each with an individual thickness of 2 mm. The plasticine layers above and below the multilayer are each 25 mm thick. The length of the specimen is 650 mm

and the applied burial pressure is 0.1 MPa.

Step T1 in Figure 3.3 shows the initial stage of the experiments with almost perfectly flat paraffin layers in column B and slightly tilted in column D. This tilt is referred to as a geometrical imperfection, in what follows. This imperfection was caused by a slight thickness heterogeneity of the underlying plasticine layer in combination with the application of the burial pressure. The geometrical imperfection has visibly triggered the kink initiation in step T2. On the left side of the model, columns A and B respectively, the fold initiated without initial imperfection at almost the same distance from the piston but evolved towards a relatively symmetric geometry until step T3. In columns C, D and E, the fold which has been initiated by the imperfection was asymmetric from the beginning. The further evolution of the fold stopped by the initiation of thrusting in the central part (column C). The fault propagates with further shortening from the central region towards the sidewalls. Hence, the amount of displacement along the fault decreases from the center towards the sidewalls, where no thrusting could be observed through the side windows. On a plan view, not shown here, the shape of the fault would fit to the "Bow and Arrow" rule described by Elliot, 1976.

Figure 3.4 shows a close-up of the geometrical evolution of the fold hinges at three time steps. It is observed that the folded compartment is limited at the initiation stage by parallel fractured zones, acting as dip-domain boundaries. The position of these fractured zones constrains the width of the anticline. Afterwards, the evolution of the fold geometry (with increasing shortening) is related to the development of new sets of parallel fractured dip-domain boundaries while the previously created ones become inactive. The new dip-domain boundaries are rotating around a fixed point on the inner arc with an approximately constant angle increment of 10° . This angle is likely to depend on the internal properties (elastic/plastic parameters, interlayer friction) of the multilayer. This observation of the incremental rotation of the dip-domain boundary has not been reported so far and it would be interesting to look for indicators at the scale of outcrops to find evidences supporting that statement. Furthermore, a theoretical approach such as the maximum strength theorem could be used to investigate these stepwise rotation of the hinges during the fold development. Therefore, weakening of the structure at the hinges will have to be introduced which will give a longer lifespan to an activated hinge before the next one is favoured in terms of forces. This weakening has not been accounted for in Chapter 3 and should be considered in future work.

The oblique top view towards the piston presented in Figure 3.5, shows a folded and thrusting paraffin multilayer after removing the piston and the upper plasticine layer. The amount of shortening in this experiment is larger than in the experiment discussed above and results in a sequence of three folds. The first fold was destroyed when moving back the piston (top of the

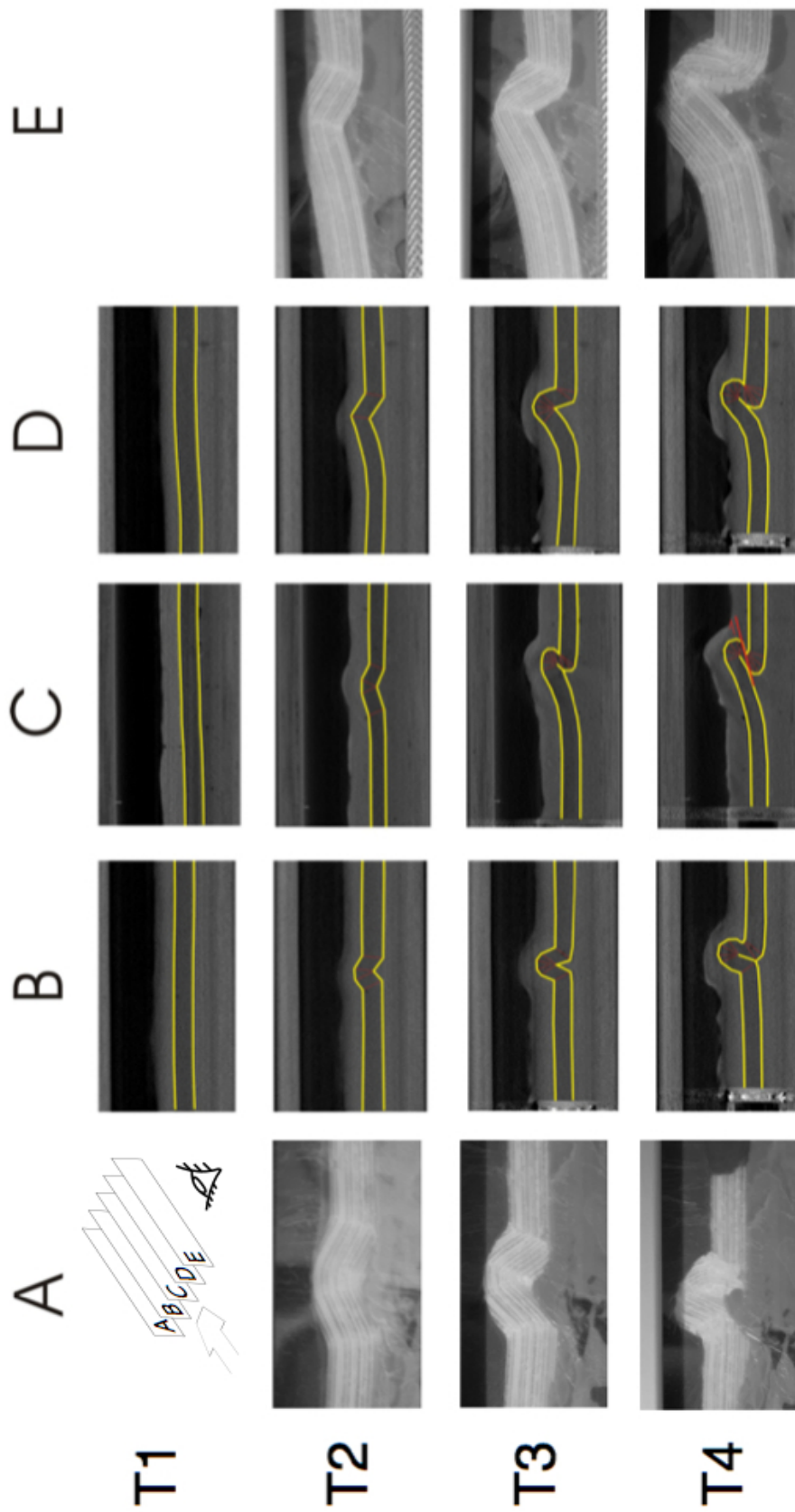


Figure 3.3: Evolution of a fold from the initial non-deformed stage (first row) to a final stage showing a folded structure and related thrust systems. Rows A and E show the view through the transparent side of the loading cell. Columns B, C and D show longitudinal sections made with the CT-Scanner. The limits of the stiff multilayer are highlighted in yellow and the main thrust faults and associated fractures are underlined in red.

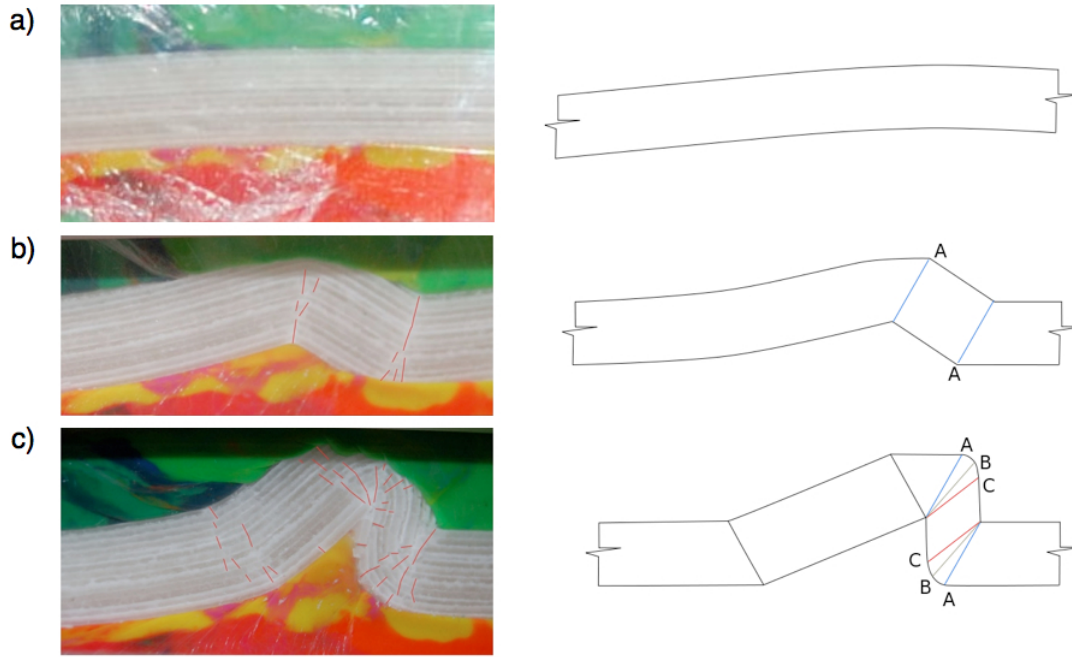


Figure 3.4: Close up showing three stages of the asymmetric fold during its evolution.

picture) and its position is marked as a dashed area. The second fold lead to a thrust but was abandoned for the onset and development of a third fold. The third fold developed but its evolution towards a thrust (dotted line) was interrupted by the end of the experiment. The plasticine filled the opened fractures within the paraffin layers and makes the fracture pattern visible. The red zone on the right-hand side contains fractures which are parallel to the second and third fold axis. The region on the left-hand side, between thrust 1 and 2 has fractures which have a radial distribution in orientation. This distribution is typical of the periclinal termination of folds and results from the 3D character of the experiment. The green fractures between thrust 1 and 2 present a rhomboidal shape resulting from the superposition of the two previously described sets.

Unfortunately, the separation of the plasticine from the paraffin afterwards is almost impossible. For the remaining experiments, the plasticine was put in a thin sheet of plastic, to prevent its penetration in the fractures which are created during folding. However, the contrast between the fractures and the unfractured region in the photographs is not strong enough to get a proper documentation of the fracture pattern.

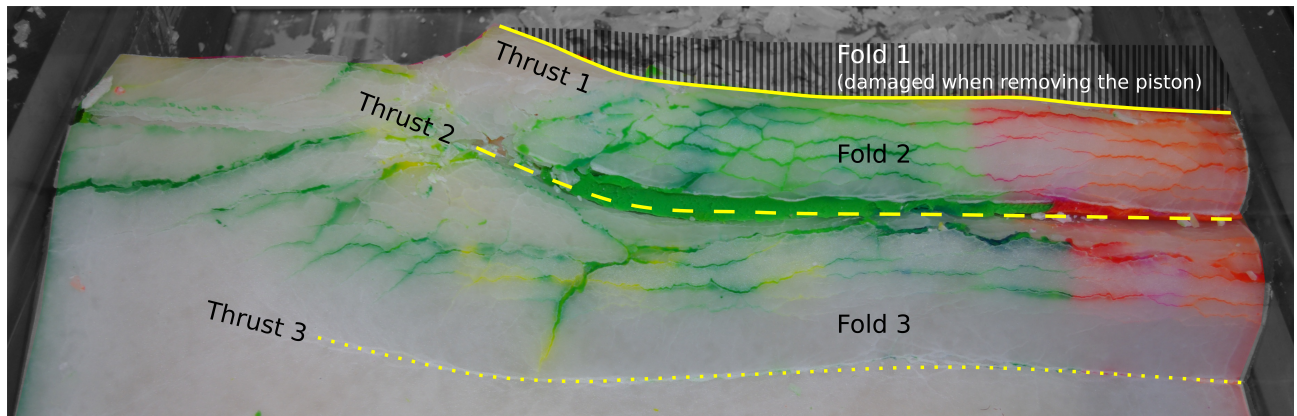


Figure 3.5: Oblique top-view, looking towards the piston, of a folded and thrust paraffin multilayer after removing the upper plasticine layer and the piston. The first generation of folds destroyed when moving back the piston is marked as a dashed area. A thrust stopped the development of the second fold and the evolution of the third fold towards a thrust was interrupted by the end of the experiment. The fracture pattern is seen thanks to the intruded plasticine. The red zone on the right consists of fold-axis parallel fractures changes to a rhomboidal shape towards the left side (region of green fractures). (picture taken by L. Bazalgette).

3.3 Conclusions and open questions

The experiments have shown that the initiation of folding is linked to a geometrical imperfection and the later stage of the evolution is stopped by thrusting. Early fractured zones constitute dip-domain boundaries that define already the final width of the fold. The angles of the following boundaries are rotating incrementally during fold amplification with a center at the inner arc. This rotation causes a radial distribution of the dip-domain boundaries.

Experiments with well aligned paraffin multilayers or with too large burial pressure did not create folds. In that case, the mechanical unit crushed at the piston and created a fold-bend fold over the piston, Figure 3.6. There were also cases, where the experiment had to be stopped because of the limitation in the magnitude of the applicable force, before any failure of the specimen could initiate.

A series of questions are now being formulated based on the qualitative results gained from the experimental work. What is the quantitative influence of an initial geometrical imperfection, the bed-thickness, the interbedding friction and the burial pressure on the fold geometry (potential asymmetry) and the kinematics of folding? The influence of these parameters is investigated in the next chapter which addresses the onset and evolution of kink folds. It is shown that increasing interbedding friction has a similar impact on folding like increasing bed thickness. A failure mechanism map is presented which shows regions of dominant failure modes in

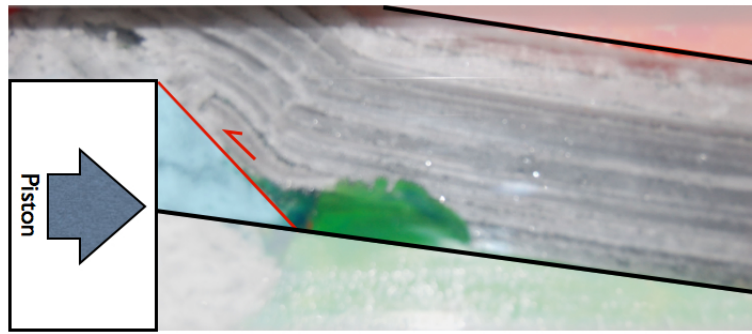


Figure 3.6: Insufficient geometrical imperfections or too large burial pressures lead to thrusting of the mechanical unit at the piston

the space spanned by the geometrical imperfection and the burial pressure. Therefore faulting, compaction bands and kink folds are set in competition with each other in terms of forces. The potential asymmetry of folds remains an open question and is the subject of future theoretical work.

Chapter 4

Imperfection and burial-depth sensitivity of the initiation and development of kink-folds in laminated rocks

G. Kampfer and Y.M. Leroy

Laboratoire de Géologie, CNRS,
École Normale Supérieure, Paris, France,

Published in the *Journal of the Mechanics and Physics of Solids* 57 (2009), 1314-1339.

4.1 Abstract

The first objective is to study the influence of the burial depth and of an imperfection, in the form of a tilt in the inclination of the otherwise straight, laminated beam, on the conditions for the initiation and the development of kink-folds. The beam, typical of sedimentary rocks, is layered with weak interfaces between the competent beds, promoting the onset of kinking by their slip. The results are analytical and based on the upper bound approach of the classical limit analysis, referred to as the maximum strength theorem in the absence of any discussion of plasticity. The weak interface strength is described by the Coulomb criterion whereas the bulk material is also cohesive and frictional but with an additional closure in the compressive stress domain to depict the action of compacting deformation mechanisms. The new twist to the methodology is to extend its application to the development of the failure mode beyond the onset, assuming that the structure finite response is well described by the least upper bound solution. The second

objective is to compare in terms of upper bounds three different failure mechanisms which are the compaction band, the reverse fault and the kink-fold. Their respective domain of dominance is constructed in failure-mechanism maps in the space spanned by the imperfection angle and the burial depth.

Compaction bands are predicted at the deepest end of the beam and the reverse fault and the kink fold at the shallower end. These depth differences are resulting from the geometrical imperfection. It is found that the kink-band mode at its onset, with compaction band dominant conditions, resembles to a slip-enhanced compaction band due to the weak interface activation and the compaction along the two parallel hinges. This hybrid mode migrates suddenly through the competent beam from the deepest towards the shallowest region and develops as a kink fold, after a negligible amount of shortening. The kink fold development, beyond the onset, occurs in two phases, the first corresponding to the rotation of the kink band and the second, to its widening. The associated least upper bound is first decreasing during the development and then increasing, the minimum being controlled more by the increase in the potential energy of the system than by the most favourable orientation of the frictional weak interfaces. It is finally found that the continuous activation of slip over the weak interfaces and the widening of the kink band prevent the rotation of the kink towards the large angles which are necessary to induce its locking. It is proposed that the introduction of damage along the hinges could palliate these two effects and prompt the locking observed experimentally and in the field.

Key words: B (geological material, layered material, rock), C (optimization), kink .

4.2 Introduction

The long-term objective of this research is to develop simplified methods to predict folding and thrusting in layered sedimentary rocks typical of fold-and-thrust belts. This contribution builds on the first attempt by Maillot and Leroy (2006), referred to in what follows as paper no 1, to construct a kink fold with the help of the maximum strength theorem. The new aspects considered here are the introduction of the burial depth and of the mis-orientation of the layers with respect to the compressive force, considered as the geometrical imperfection. These two ingredients are sufficient to define the conditions for the kink fold to dominate at the onset over the compaction band and the reverse fault, the two other potential modes of failure.

The modeling of folding within sedimentary layers is possible from two approaches which are extreme in terms of complexity and efficiency. The first approach, most common in the mechanics literature, is certainly the most complex and computer intensive: a constitutive model is proposed for each lithology and the finite-element method is applied, starting with some initial geometry. The predicted strain localization should reveal the position of the ramps which accommodate subsequently the large displacement jumps, fundamental to thrusting. This approach is of course sensitive to the details of the constitutive relations (Rudnicki and Rice, 1975) and the numerical schemes for strain localization are still debated and require complex bench-marking (Buiter et al., 2006). Efficiency to construct forward models for repeated calculations necessary for statistical analysis are thus not yet possible. The other opposite, extreme approach ignores such complexity and proposes to construct folds from simple geometrical rules such as length and volume conservation (Suppe, 1983). The application of this simple approach to oil-industry exploration questions, completed with a temperature evolution scheme, has had a definite success to explain potential prospects (Zoetemeijer and Sassi, 1992; Sciamanna et al., 2004). Simplicity and efficiency are thus possible but the difficulty remains that this simple geometrical approach to folding is guided only by the experience of the structural geologist. It is impossible to favour one construction from others with quantitative criteria such as mechanical equilibrium and material strength.

A first attempt to bridge the gap between these two extreme approaches was proposed by Maillot and Leroy (2003). They constructed a geometrically simple fault-bend-fold and, instead of postulating the orientation of the back thrust, they found it by the application of the principle of minimum dissipation. A more systematic construction is proposed in paper no 1 where the external approach of limit analysis, as presented by Salençon (1974, 2002), is applied to the formation of kink folds. The kink band orientation (dip) as well as the dip of its two bounding, parallel hinges is selected by optimization of the upper bound in force due to internal dissipation and work against gravity. The difference between classical applications of limit analysis in civil

engineering and in the field of structural geology is that the first failure mode is not sufficient. Its evolution in time defines the fold geometry. It is thus necessary to adapt the geometrical constructions of Suppe (1983) for the fold development proposing that certain degrees of freedom are not postulated but found by optimization of the upper bound in the tectonic force. These degrees of freedom in the present contribution and in paper no 1 include the two dips of the hinges and of the kink band. This yet simple but optimized construction method has been applied to predict the onset and the arrest in the development of every thrust of a normal sequence at the toe of an accretionary prism (Cubas et al., 2008). This kinematics approach does not provide any statically admissible stress field which is at the core of the internal approach of limit analysis. The systematic application of the internal approach via the Equilibrium Element Method, at any step of the thrust development, does provide the optimum stress field as well as an estimate of the lower bound to the applied tectonic force, useful in estimating the error on the tectonic force (Souloumiac et al., 2008). Note that in the application of these two bounding techniques, no reference is made to any plasticity theory, and in particular to flow potentials and dilatancy. This interpretation (Salençon, 2002) of the classical limit analysis explains the reference to the external approach as the maximum strength theorem in paper no 1 and here.

The present contribution concentrates on kink folds with the intention to compare the conditions of dominance at the onset of three failure modes, the kink fold, the reverse fault and the compaction band. These various modes of failure under compression are defined and illustrated in Figure 4.1. The prototype is composed of three regions, the top and bottom occupied by inviscid fluids. The central region is layered with planar weak interfaces between the various beds, tilted with respect to the compressive forces. The reverse fault is possible because of the frictional properties of the competent layers. The compaction band is also a potential mode of failure since the Coulomb criterion of the bulk material is closed in the compressive stress directions. This cap-type strength criterion was found necessary in paper no 1 to initiate kinking with each layer failing partly in compression and partly in extension. The competition between the three modes of failure is controlled by the burial depth (thickness of the top region) and the geometrical imperfection. The larger depths are promoting compaction bands over the reverse faults. The imperfection, which is defined by the layers mis-orientation favours the slip along the weak interfaces and is responsible for the kink development. The comparison of the different upper bounds in tectonic forces provides systematic, quantitative conditions for the dominance of each mode of failure.

The proposed approach to the onset and the development of kinks is rather different from the methods proposed in the engineering and Earth sciences literature and a comparison is now in order. Kinks will be predicted here without recourse to the introduction of elastic or elasto-

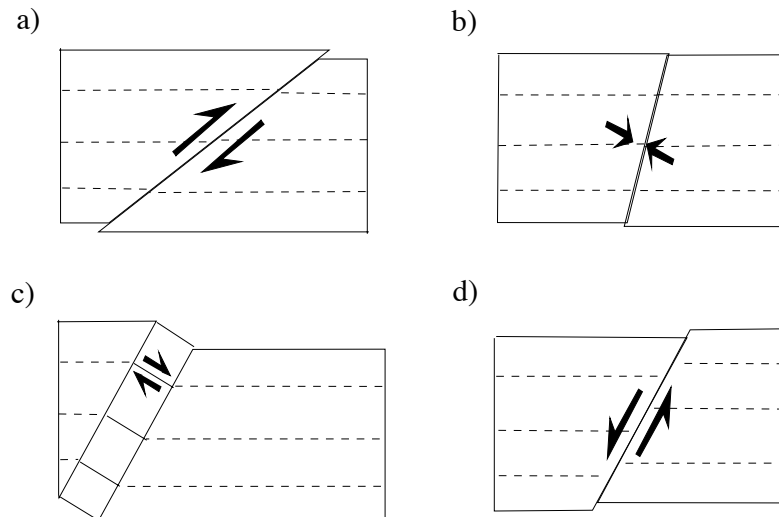


Figure 4.1: The various modes of failure under compression are the reverse fault, top block sliding up the lower block in a), the compaction band defined by a sub-vertical contraction b) and the kink fold c). The fourth mode is the normal fault in c) where the upper block is sliding down on the lower block during extension. It is introduced to compare its orientation with the dip of the compaction band. The normal and reverse fault dips are expected to be at $\pi/4 \pm \phi/2$ for a rock with internal friction angle ϕ . The compaction bands are sub-vertical. The weak interfaces are sub-horizontal and illustrated by solid segments if slipping, as in the kink band, or by dashed segments otherwise. The offset for the two faults and the compaction bands is for sake of illustration only since these modes are studied only at their onset.

plastic buckling. Such instability analyzes were essential for fiber composites, started with the early work of Rosen (1965) and reviewed by Budiansky and Fleck (1994), as well as for the multi-layered structures considered by Biot (1965). The kink band is then seen as a new solution which develops during the post-bifurcation and is captured by numerical means (Vogler et al., 2001). This buckling is imperfection sensitive and unstable due to the rotation of the weak interfaces or of the fiber in the composite materials. Experimental work reviewed by Lankford (1995) suggested that the unstable buckling occurs only once the failure of the fiber-matrix interphase and the tensile fracture of the fibers take place. The unstable character of the kink propagation was further considered by Sutcliffe and Fleck (1993) with a fracture mechanics argument. In paper no 1, it was noted that failure in compression (equivalent to the compressive failure of the fibers in composite) was a necessary deformation mode for the kink onset in the absence of any tilt of the weak interfaces due to either initial imperfection or flexure by buckling. The bifurcation analysis of Nestorović and Triantafyllidis (2004) comes to the same conclusion. The present introduction of the initial imperfection should render this compressive failure however less crucial, allowing for tensile failure over part of each layer at the onset. These two aspects,

the limited compressive strength and the tensile strength solicited over each layer, and the imperfection, render the onset of kinking possible as an independent failure mode which develops rather similarly to the buckling mode: it is unstable and imperfection sensitive. This development is explored here by proposing a family of kinematics for the kink based on simple construction rules, in the spirit of the work of Suppe (1983).

The paper contents are as follows. The next section presents the conditions for the onset of reverse faults and of compaction bands, described as single discontinuities in the virtual velocity field. This section is also found useful to define the maximum strength theorem which is applied to the more complex kink mode of failure. An analytical expression for the critical lithostatic pressure (burial depth) which marks the transition between the reverse fault and the compaction band for zero imperfection is proposed. The influence of the imperfection on this critical pressure is also explored. Section three is devoted to the onset, development and potential arrest of the kink fold. The comparison of the conditions for the onset of the kink with those necessary for the reverse fault and the compaction band are presented in failure-mechanism maps spanned by the imperfection angle and the lithostatic pressure. Those maps are of course reminiscent of the deformation maps of Ashby (1972) and are similar to the extension to the failure of structures considered by Bart-Smith et al. (2002) for the design of sandwich panels. It is found that the kink fold could, under conditions of compaction band dominance, initiate as a slip-enhanced compaction band. This new mode makes use of the activation of slip along every weak interface within the kink band and of the compressive failure along the two hinges which collapse to a single discontinuity. This slip-enhanced compaction band develops after a small shortening of the structure into a kink of finite thickness. The rest of the section four is devoted to the two-step development of the kink: rotation of the band and its hinges followed by its widening, and to a discussion of its potential arrest because of the onset of reverse faulting. The conclusion provides a complete summary of these results as well as a discussion of potential future development geared towards the study of damage in sedimentary layers prompt to kinking.

4.3 Initiation of compaction bands and reverse faults

The objective of this section is to study the onset of two failure modes, the reverse fault and the compaction band (Figure 4.1a and b), and to determine the conditions of dominance of each mode in terms of burial depth and imperfection. These two modes are particular cases of a general failure mode defined by a single discontinuity in the velocity field. This general case is presented to illustrate the application of the maximum strength theorem, once the prototype and the concepts of strength domain and of support function have been introduced.

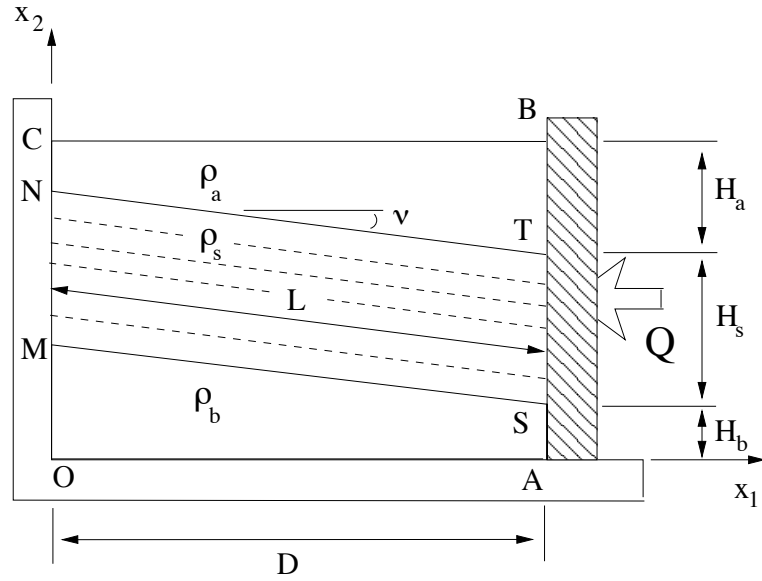


Figure 4.2: The geometry of the prototype.

4.3.1 Geometry of the prototype, maximum strength domain and support function

The prototype considered in this paper is presented in Figure 4.2. It consists of a rectangular domain OABC limited by two vertical rigid walls and lying on a rigid base. The right side is displaced towards the left resulting in an overall compression requiring the force of magnitude Q . The compressed rectangular domain consists of three regions. First, the region OASM is composed of unconsolidated sediments or of material such as shales or salts, which rheology is described as an inviscid, incompressible fluid. The material density is ρ_b and the region thickness at the contact of the right wall is H_b (the subscript b is for bottom). Second, the region MSTN is made of a layered competent rock of material density ρ_s (the subscript s is for the solid region). This domain, as well as the interfaces between the multiple layers which compose it, illustrated as dashed lines in Figure 4.2, have the dip ν , which is the geometrical imperfection. Third, the region NTBC above the multi-layers is of the same type as in the bottom region and also composed of an inviscid fluid of material density ρ_a (the subscript a is for above). The last two material regions have the thicknesses H_s and H_a , respectively, measured at the contact to the right wall. The horizontal length of the structure is D . Note that there is no time scale in this problem except for the shortening induced by the right-lateral wall.

Dissipation occurs along two types of surfaces, which are the weak interfaces and planar surfaces intersecting them and cutting through the competent layer MSTN. They are potential velocity discontinuities. These two types of surfaces have specific material properties and are

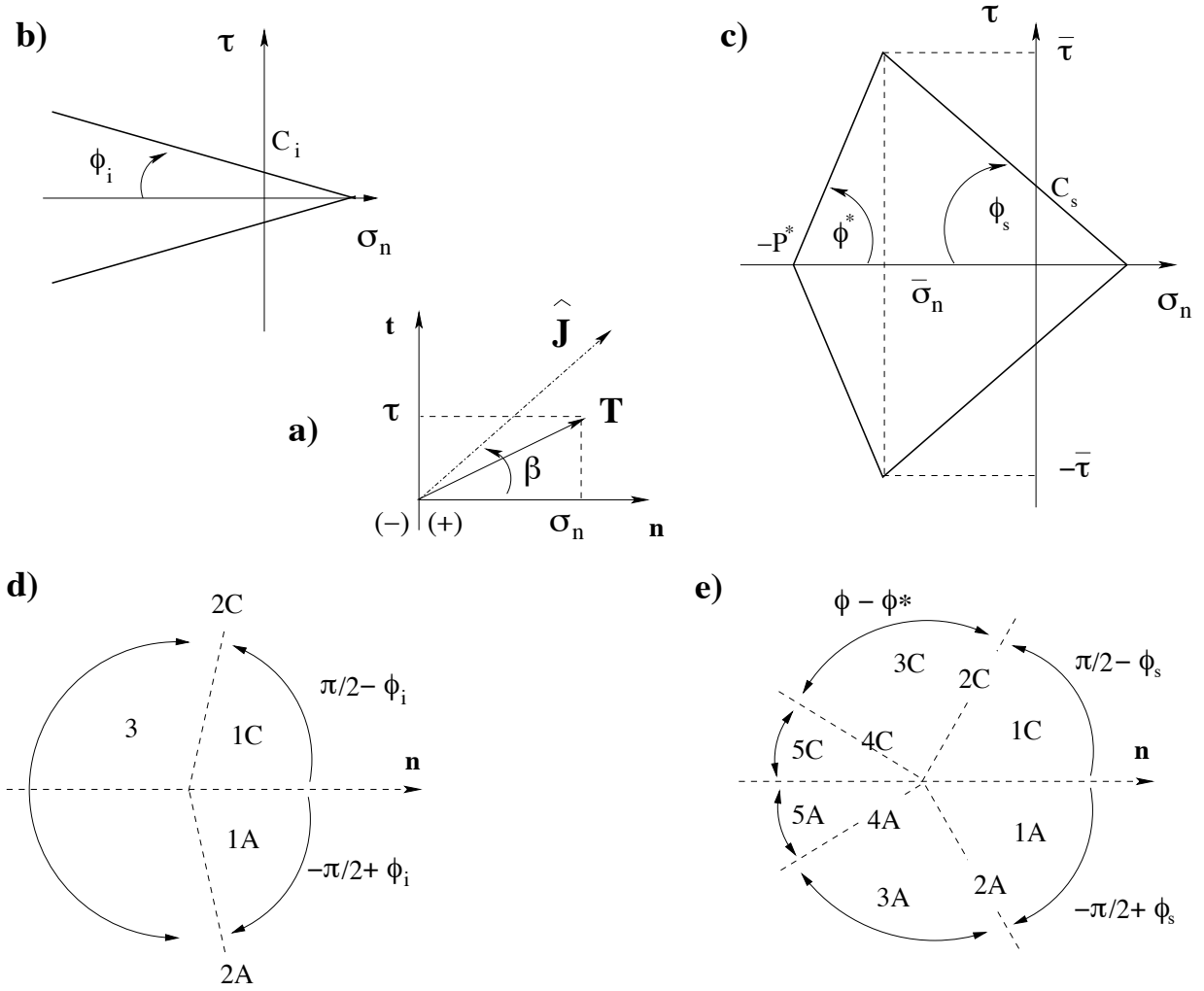


Figure 4.3: The strength domain and the corresponding angular dependence of the support function. The general decomposition of the stress vector and the orientation of the jump in velocity are presented in a). The weak interfaces strength domain is limited by the Coulomb criterion, b). For the hinges, the strength domain is similar with the addition of the closure in compression due to compaction, c). The construction of the support function depends on the orientation of the jump vector with respect to the normal to the discontinuity. The two cases defined in d) and e) are for the weak interfaces and any surface through the competent region, respectively.

oriented by their normal \mathbf{n} and tangent vector \mathbf{t} , such that $\{\mathbf{n}, \mathbf{t}\}$ is a direct basis in the plane of study. Vectors, and subsequently second-order tensors, are represented in bold. The stress vector \mathbf{T} acting on these surfaces is decomposed in a normal $\sigma_n \mathbf{n}$ and a tangential part $\tau \mathbf{t}$, Figure 4.3a. It is in the (σ_n, τ) space that the strength domain of the two types of surfaces is defined. First, the weak interfaces have the strength domain presented in Figure 4.3b, which is bounded by the Coulomb criterion and is defined by

$$G_i = \{\mathbf{T} \mid |\tau| + \sigma_n \tan \phi_i \leq C_i\} , \quad (4.1)$$

in which ϕ_i and C_i are the friction angle and the cohesion of the weak interface, respectively. Second, the discontinuity surfaces through the competent rock have the strength domain shown in Figure 4.3c. The Coulomb criterion is also present, as for the weak interfaces, with the friction angle ϕ_s and the cohesion C_s . In addition, the admissible compressive region is closed by two straight segments, defined by their intersection with the normal stress axis, $-P^*$, and the angle ϕ^* . These additional constraints due to the compaction criterion, are identical to the ones proposed in paper no 1. They reflect the limited strength in compression due to fluid-assisted dissolution processes, pore-collapse compaction or cataclasis flow. The simplified geometry proposed for the cap in compression is certainly attractive for analytical development but is also motivated by laboratory experiments leading to failure in compaction band in sandstone (Fortin et al., 2006), as predicted by Issen and Rudnicki (2001). This second strength domain is defined by

$$G_s = \{\mathbf{T} \mid |\tau| + \sigma_n \tan \phi_s \leq C_s \quad \text{and} \quad |\tau| - (\sigma_n + P^*) \tan \phi^* \leq 0\} . \quad (4.2)$$

The application of the maximum strength theorem is based on the determination of the maximum dissipation $\mathbf{T} \cdot \hat{\mathbf{J}}$ which could occur along failure surfaces accommodating jumps in virtual velocities $\hat{\mathbf{J}}$. This jump is oriented with respect to the normal \mathbf{n} by the angle β in Figure 4.3a. This maximum does exist because the two strength domains are convex and contain the zero stress vector in the (σ_n, τ) space. This maximum is denoted $\varpi(\hat{\mathbf{J}})$ and referred to as the support function (Salençon, 1974, 2002). It reads for the weak interfaces

$$\begin{aligned} \text{case (1A) and (1C)} : 0 \leq |\beta| < \pi/2 - \phi_i , \quad \varpi_i(\hat{\mathbf{J}}) &= \hat{J} C_i \cotan(\phi_i) \cos \beta , \\ \text{case (2A) and (2C)} : |\beta| = \pi/2 - \phi_i , \quad \varpi_i(\hat{\mathbf{J}}) &= \hat{J} C_i \cos \phi_i , \\ \text{case (3A) and (3C)} : \pi/2 - \phi_i < |\beta| \leq \pi , \quad \varpi_i(\hat{\mathbf{J}}) &= +\infty , \end{aligned} \quad (4.3)$$

and was constructed in paper no 1 for the frictional and compacting discontinuities

$$\begin{aligned}
 \text{case (1A) and (1C): } 0 \leq |\beta| < \pi/2 - \phi_s, & \quad \varpi_s(\hat{\mathbf{J}}) = \hat{J}C_s \cotan(\phi_s) \cos \beta, & (4.4) \\
 \text{case (2A) and (2C): } |\beta| = \pi/2 - \phi_s, & \quad \varpi_s(\hat{\mathbf{J}}) = \hat{J}C_s \cos \phi_s, \\
 \text{case (3A) and (3C): } \pi/2 - \phi_s < |\beta| < \pi/2 + \phi^*, & \quad \varpi_s(\hat{\mathbf{J}}) = \hat{J}(\bar{\sigma}_n \cos \beta \pm \bar{\tau} \sin \beta), \\
 \text{case (4A) and (4C): } |\beta| = \pi/2 + \phi^*, & \quad \varpi_s(\hat{\mathbf{J}}) = \hat{J}P^* \sin \phi^*, \\
 \text{case (5A) and (5C): } \pi/2 + \phi^* < |\beta| \leq \pi, & \quad \varpi_s(\hat{\mathbf{J}}) = -\hat{J}P^* \cos \beta.
 \end{aligned}$$

The various cases introduced by pairs depend on the orientation of the velocity jump. If β is positive, the jump is anti-clockwise (A) and is clockwise (C), if β is negative. Note that the stresses $\bar{\sigma}$ and $\bar{\tau}$ used in (4.4c) define the intersection of the Coulomb and the compaction criterion in Figure 4.3c and are given by

$$\bar{\sigma}_n = \frac{C_s - P^* \tan \phi^*}{\tan \phi^* + \tan \phi_s} \quad \text{and} \quad \bar{\tau} = (C_s + P^* \tan \phi_s) \frac{\tan \phi^*}{\tan \phi^* + \tan \phi_s}. \quad (4.5)$$

These various cases are presented in Figure 4.3d and e) for the weak interfaces and the cohesive, compacting discontinuities, respectively.

The final remark concerns the necessity for these support functions to be finite in the construction of an upper bound to the dissipation. Therefore the virtual velocity jump for the weak interfaces has to be in the cone of internal angle $\pi/2 - \phi_i$ and centered on the normal to the discontinuity, as can be judged from (4.3). Consequently, the velocity jump has a normal component which could be seen as a virtual dilatancy. This interpretation in the context of a plasticity theory for frictional material would be problematic and is not necessary. It is for this reason that we restrain this presentation to the concept of material strength and referred to this bound construction as the maximum strength theorem.

4.3.2 Failure mode with a single velocity discontinuity

The common features of the two particular failure modes to be examined in this section are that there is a single straight discontinuity in the virtual velocity field. This discontinuity, segment PQ, is positioned at αD from the left wall, with the unknown scalar α within the range $[0, 1 - H_s \cos \nu \cos \theta / (D \sin(\theta + \nu))]$, and is dipping at the angle θ , Figure 4.4a. Furthermore, this discontinuity separates two blocks in the competent region which are assigned each a uniform velocity field. This analysis of the general case is now used to introduce the maximum strength theorem decomposed in five steps.

The first step is the construction of the virtual velocity field with the constraints due to the fluid incompressibility. The solid multi-layer region is divided into a lower (right) and upper

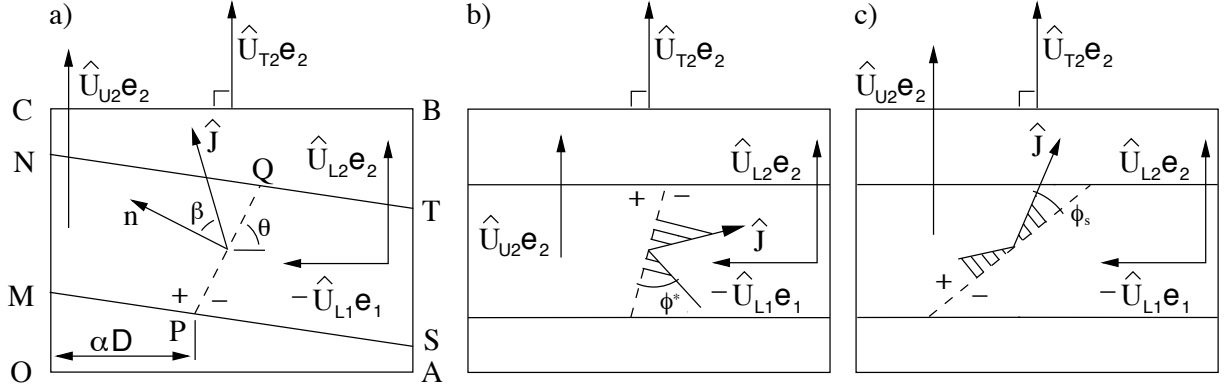


Figure 4.4: The characteristics of the general failure mechanism with a single velocity discontinuity a), and the particular cases of the compaction band b) and of the reverse fault, c). No imperfection is considered.

(left) block by a discontinuity in the virtual velocity field. The lower block sustains the uniform horizontal velocity $-\hat{U}_{L1}\mathbf{e}_1$ imposed by the rigid wall and is displaced upwards with the unknown velocity $\hat{U}_{L2}\mathbf{e}_2$ (subscript L for lower). The upper block of the competent layer has only a vertical velocity component \hat{U}_{U2} (subscript U for upper) because the wall OC to the left is fixed. The velocities of the two blocks of the competent region are also the velocities of the fluid boundary along PS and QT , for the lower block, and along MP and NQ , for the upper block. The top surface of the fluid mass above remains horizontal at all times and its vertical velocity is \hat{U}_{T2} (with T for top). The fluids incompressibility and the mass conservation provide

$$\int_S \hat{\mathbf{U}} \cdot \mathbf{n} \, dS = 0, \quad (4.6)$$

in which S is the constant, closed boundary of the sub-domain occupied by one of the two fluids. The distribution of the velocity within the fluid regions is not specified and not necessary. Equation (4.6), applied to the bottom region, together with the description of the velocities on the boundary provided above, provides the constraint

$$\hat{U}_{L2}(1 - \alpha) + \hat{U}_{U2}\alpha = \hat{U}_{L1}\left(\frac{H_b}{D} + \tan \nu(1 - \alpha)\right). \quad (4.7)$$

Similarly, application of the mass conservation (4.6) to the fluid in the region above provides an expression for the top velocity

$$\hat{U}_{T2} = \hat{U}_{L1}\left(\frac{H_a + H_b}{D} + \frac{H_s \cos \theta \sin \nu}{D \sin \theta + \nu}\right) + (\hat{U}_{U2} - \hat{U}_{L2})\frac{H_s \cos \theta \cos \nu}{D \sin \theta + \nu}, \quad (4.8)$$

once (4.7) has been used.

The second step in the presentation of the maximum strength theorem consists in computing the power of the external forces

$$\mathcal{P}_{\text{ext}}(\hat{\mathbf{U}}) = \mathcal{G}_{\text{ext}}(\hat{\mathbf{U}}) + \int_{S^T} \mathbf{T}^d \cdot \hat{\mathbf{U}} dS \quad \text{with} \quad \mathcal{G}_{\text{ext}} = \int_V \rho \mathbf{g} \cdot \hat{\mathbf{U}} dV, \quad (4.9)$$

which is the sum of the power of the body force \mathcal{G}_{ext} , the gravity is $-\mathbf{g}\mathbf{e}_2$, and of the force distribution \mathbf{T}^d over the boundary S^T (the rigid wall to the right). For the competent region, the power of the body force is computed over the lower and the upper blocks, which have the vertical velocities \hat{U}_{L2} and \hat{U}_{U2} . The power of the compressive force is restricted to the section ST of the right wall. The end result is

$$\mathcal{P}_{\text{ext}(s)}(\hat{\mathbf{U}}) = \mathcal{G}_{\text{ext}(s)}(\hat{\mathbf{U}}) + Q_s \hat{U}_{L1}, \quad (4.10)$$

$$\text{with} \quad \mathcal{G}_{\text{ext}(s)}(\hat{\mathbf{U}}) = -\hat{U}_{L1} \rho_s g D H_s \left[\frac{H_b}{D} + (1 - \alpha) \tan \nu \right] - (\hat{U}_{U2} - \hat{U}_{L2}) \rho_s g \frac{H_s^2 \cos \theta \cos \nu}{2 \sin(\nu + \theta)},$$

having made use of (4.7). The subscript s (for solid) marks the evaluation of (4.9) over the region composed of the competent rock only. For the two fluid regions, the power of the body force needs to be transformed since the velocity field is not defined internally but only on the boundary. For that reason, note that \mathbf{g} is the gradient of the scalar $\mathbf{g} \cdot \mathbf{x}$, in which \mathbf{x} is the position of any material point, so that the volume integral in (4.9), for an isochoric velocity field, is also expressed as

$$\mathcal{G}_{\text{ext}}(\hat{\mathbf{U}}) = \int_S \rho \mathbf{g} \cdot \mathbf{x} \hat{\mathbf{U}} \cdot \mathbf{n} dS, \quad (4.11)$$

in terms of the normal component of the velocity on the boundary. The computation of the body force power for the fluid below is then

$$\mathcal{G}_{\text{ext}(b)}(\hat{\mathbf{U}}) = -\hat{U}_{L1} \frac{1}{2} \rho_b g H_b \left(H_b + (1 - \alpha) D \tan \nu \right) - \hat{U}_{U2} \frac{1}{2} \rho_b g \alpha D^2 \tan \nu, \quad (4.12)$$

having again made use of (4.7). A similar calculation over the region above yields

$$\begin{aligned} \mathcal{G}_{\text{ext}(a)}(\hat{\mathbf{U}}) &= -\hat{U}_{L1} \frac{1}{2} \rho_a g \left\{ H_a^2 + (H_b + A)(A + 2H_a - (1 - \alpha) D \tan \nu) \right\} \\ &\quad + \hat{U}_{U2} \frac{1}{2} \rho_a g D (D \alpha \tan \nu + A) \\ &\quad + (\hat{U}_{U2} - \hat{U}_{L2}) \cotan(\nu) \frac{A}{2} \rho_a g \left\{ (1 - \alpha) D \tan \nu - A - 2H_a \right\}, \\ &\text{with} \quad A = H_s \frac{\cos \theta \sin \nu}{\sin(\nu + \theta)}. \end{aligned} \quad (4.13)$$

The third step of this presentation of the maximum strength theorem concerns the internal virtual power defined by

$$\mathcal{P}_{\text{int}}(\hat{\mathbf{U}}) = \int_{\Sigma_U} \mathbf{T} \cdot \hat{\mathbf{J}} dS, \quad (4.14)$$

and which results from the action of the stress vector over the velocity jump across all failure surfaces Σ_U . There is no internal power within the fluids which are assumed inviscid. Dissipation occurs thus only over the discontinuity PQ , Figure 4.4a, for our example. However, the exact stress vector \mathbf{T} acting on that surface is unknown and the only possibility to progress is to introduce an upper bound to the power $\mathbf{T} \cdot \hat{\mathbf{J}}$, the support function $\varpi_s(\hat{\mathbf{J}})$ in (4.4). The internal power in (4.14) is thus bounded by

$$\mathcal{P}_{\text{int}}(\hat{\mathbf{U}}) \leq \varpi_s(\hat{\mathbf{J}}) \frac{H_s \cos \nu}{\sin(\nu + \theta)} \quad \text{with} \quad \hat{\mathbf{J}} = \hat{U}_{L1} \mathbf{e}_1 + (\hat{U}_{U2} - \hat{U}_{L2}) \mathbf{e}_2. \quad (4.15)$$

The fourth step consists in applying the theorem of virtual power $\mathcal{P}_{\text{int}}(\hat{\mathbf{U}}) = \mathcal{P}_{\text{ext}}(\hat{\mathbf{U}})$, for any kinematically admissible velocity field $\hat{\mathbf{U}}$, in combination with the bound on the internal power proposed in (4.15). Combining the contributions to the external work in (4.10) to (4.13) and the bound(4.15), we obtain

$$Q \leq Q_{\text{upper}}(\tilde{\mathbf{U}}) = \varpi_s(\tilde{\mathbf{J}}) \frac{H_s \cos \nu}{\sin(\nu + \theta)} - \mathcal{G}_{\text{ext}(a)}(\tilde{\mathbf{U}}) - \mathcal{G}_{\text{ext}(s)}(\tilde{\mathbf{U}}) - \mathcal{G}_{\text{ext}(b)}(\tilde{\mathbf{U}}) \quad (4.16)$$

in which Q_{upper} is the upper bound to the tectonic force Q defined as the sum of the forces applied on the three sections of the right boundary AB . Note that the two sides of the inequality in (4.16) have been divided by the velocity \hat{U}_{L1} , a positive scalar, such that the normalized velocity $\tilde{\mathbf{U}}$ is simply $\hat{\mathbf{U}}/\hat{U}_{L1}$.

The fifth and final step of the presentation of the maximum strength theorem concerns the minimization of the bound on the right-hand side of (4.16) with respect to three parameters. There is first a single free velocity scalar, either \hat{U}_{U2} or the orientation β of the velocity jump, because of the two equalities in (4.7) and (4.8). The other scalars are the position (α) and the orientation (dip θ) of the discontinuity PQ . This exercise, providing the least upper bound to the tectonic force, is conducted next for the two particular cases of interest, the compaction band and the reverse fault.

4.3.3 Special case: onset of compaction bands, no imperfection.

The first special case of failure is by compaction band (CB) for a zero imperfection ($\nu = 0$). The band thickness is not determined in this analysis and is set to zero. The jump in velocity is oriented within the cone (5A) or (5C) in (4.4) so that the support function is $\varpi_s(\tilde{\mathbf{J}}) = -\tilde{J} P^* \cos \beta$. The normalization of the velocity jump with respect to the horizontal virtual velocity leads to the following relation

$$\tilde{J} \cos(\beta + \theta) = \tilde{U}_{U2} - \tilde{U}_{L2}, \quad \tilde{J} \sin(\beta + \theta) = -1, \quad (4.17)$$

with the obvious constraint that $\theta + \beta$ is in the interval $[\pi; 2\pi](\text{mod } 2\pi)$ since \tilde{J} is a positive scalar. The upper bound to the tectonic force is then

$$\begin{aligned} \tilde{Q}_{CB \text{ upper}} = & \tilde{H}_s \tilde{P}^* + \frac{1}{2} \tilde{\rho}_b \tilde{H}_b^2 + \frac{1}{2} \rho_a \tilde{H}_a (\tilde{H}_a + 2\tilde{H}_b) + \tilde{H}_s \tilde{H}_b \\ & + \cotan \theta \cotan(\theta + \beta) \tilde{H}_s (\tilde{P}^* - \tilde{P}_l) \quad \text{with} \quad \tilde{P}_l = \tilde{\rho}_a \tilde{H}_a + \frac{1}{2} \tilde{H}_s, \end{aligned} \quad (4.18)$$

combining (4.17) and (4.16) and using the specific value of the support function provided above. Note that in (4.18) and in what follows, dimensionless quantities are introduced and are marked by a superposed tilde. Lengths are normalized by the structure length D and stress-like quantities by $\rho_s g D$. Note also that the upper bound in (4.18) is not sensitive to the scalar α : the position of the compaction band is undetermined in the absence of imperfections.

The kinematics sketched in Figure 4.4b precludes horizontal or sub-horizontal compaction bands since the segment PQ is not cutting through the right nor the left boundary. It turns out that this choice corresponds to the case of a compaction strength P^* larger than the lithostatic pressure P_l , defined in (4.18). This scalar is an outcome of the analytical development and corresponds to the lithostatic pressure at mid-depth of the competent layer. The least upper bound \tilde{Q}_{CB} of (4.18) is found by minimization with respect to the velocity jump orientation and the dip of the discontinuity, with the constraints (4.7) and (4.8). Two conjugate orientations are solutions

$$\begin{aligned} \theta &= \frac{\pi}{4} + \frac{\phi^*}{2} \quad \& \quad \frac{3\pi}{4} - \frac{\phi^*}{2}, \\ \beta &= \frac{3\pi}{4} - \phi^* \quad \& \quad \frac{\pi}{2} + \phi^*. \end{aligned} \quad (4.19)$$

A complete presentation of this optimization is found in Kampfer (2010). The reader accustomed to the Mohr construction will recognize in (4.19) the orientations of the faults which would be found assuming a negative friction coefficient ($-\tan \phi^*$). Note that the orientation of the conjugate compaction bands in (4.19) are close to sub-vertical similar to normal fault dips obtained in extension (this is the fourth mode of failure, presented in Figure 4.1c). For example, the compaction band is at $\theta = 75^\circ$ and 105° for $\phi^* = 60^\circ$ and the normal fault dips at $\theta = \pi/4 + \phi_s/2$ and $\theta = 3\pi/4 - \phi_s/2$, corresponding to 65° and 115° for $\phi_s = 40^\circ$. The sense of virtual displacement for the compaction band is even consistent with normal faulting. In the absence of micro-structural observations to reveal the compaction mechanism, such bands could thus easily be confused with normal faults despite the compressive regime.

4.3.4 Special case: onset of reverse faults, no imperfection.

The second special case of failure is by reverse fault (RF). The normalized velocity discontinuity between the two blocks of the solid region is still defined by (4.17) and is assumed to be within

case (2C) and (2A) in (4.4). The support function is thus $\varpi_s(\tilde{J}) = \tilde{J}C_s \cotan \phi \cos \beta$. The upper bound to the tectonic force is then

$$\begin{aligned} \tilde{Q}_{RF \text{ upper}} = & -\tilde{C}_s \tilde{H}_s \cotan \phi + \frac{1}{2} \tilde{\rho}_b \tilde{H}_b^2 + \frac{1}{2} \tilde{\rho}_a \tilde{H}_a (\tilde{H}_a + 2\tilde{H}_b) + \tilde{H}_s \tilde{H}_b \\ & - \cotan \theta \cotan(\theta + \beta) \tilde{H}_s (\tilde{C}_s \cotan \phi_s + \tilde{P}_l), \end{aligned} \quad (4.20)$$

which is similar to (4.18) with $-P^*$ replaced by $C_s \cotan \phi_s$. The minimization, leading to the least upper bound \tilde{Q}_{RF} , which is not sensitive to the position of the reverse fault, is presented in details in Kampfer (2010). The final results in terms of discontinuity and velocity jump orientations read

$$\begin{aligned} \theta &= \frac{\pi}{4} - \frac{\phi_s}{2} \quad \& \quad \frac{3\pi}{4} + \frac{\phi_s}{2}, \\ \beta &= -\frac{\pi}{2} + \phi_s \quad \& \quad \frac{\pi}{2} - \phi_s. \end{aligned} \quad (4.21)$$

The classical orientations are obtained: the conjugate faults are at low angles with respect to the direction of compression. Typically, the dips are 30° and 150° for a friction angle ϕ_s set to 30° .

4.3.5 Influence of the burial depth on the selection of the dominant failure mode.

The two modes of reverse faulting and compaction banding are sensitive to the burial depth, the thickness of the fluid layer above. This burial depth is measured by the lithostatic pressure P_l . To analyze this sensitivity, one could first check that \tilde{Q}_{RF} is smaller than \tilde{Q}_{CB} at shallow depths where the failure mode in reverse faulting is indeed expected to dominate. Compaction bands are steeper than the reverse faults, leading to less work against gravity. They thus should be preferable at larger depths. The lithostatic pressure for the transition is defined by the equality of the two bounds and reads

$$\tilde{P}_l^T = \frac{\tilde{P}^* [1 - \cotan^2(\frac{\pi}{4} + \frac{\phi_s^*}{2})] + \tilde{C}_s \cotan \phi_s [1 - \cotan^2(\frac{\pi}{4} - \frac{\phi_s}{2})]}{\cotan^2(\frac{\pi}{4} - \frac{\phi_s}{2}) - \cotan^2(\frac{\pi}{4} + \frac{\phi_s^*}{2})}. \quad (4.22)$$

For the typical values of the material properties reported in Table 4.1, this pressure would be 26 MPa corresponding to the depth of 1240 m.

4.3.6 Imperfection sensitivity.

The imperfection should have a minor influence on the selection of the dominant failure mode since the deformation mechanisms by shear and compaction are not dependent on the angle

4.3. Initiation of compaction bands and reverse faults

Symbol	definition	value	unit
C_s	cohesion of competent layer	5.	MPa
C_i	cohesion of interfaces	0.	MPa
P^*	compaction strength (competent layer only)	100.	MPa
ϕ_s	friction angle of competent layer	30.	deg
ϕ_i	friction angle of interface	10.	deg
ϕ^*	compaction angle of competent layer	70.	deg
ρ_a	material density for fluid above	2100.	kg/m ³
ρ_b	material density for fluid below	2800.	kg/m ³
ρ_s	material density for competent rock	2500.	kg/m ³
g	gravity acceleration	9.81	m/s ²
H_a	thickness of fluid above (measured on r.h.side)	1500.	m
H_s	thickness of competent layer (measured on r.h.side)	100.	m
H_b	thickness of fluid below (measured on r.h.side)	100.	m
D	length of the prototype	1000.	m
n	number of layers in the competent region	100	–

Table 4.1: Material properties and geometrical characteristics of the prototype: symbols, definitions, units and typical values.

ν . This influence will be of course very different in the next section since the slip along the weak interfaces is favoured initially by the tilting of the competent layer. The imperfection has however an influence on the position of the compaction band or the reverse fault which was left indeterminate for $\nu = 0$. The imperfection breaks the symmetry of the structure and its loading and will thus promote one of the two solutions found above for the two particular cases.

To study this influence, for small imperfections, the following regular asymptotic development in terms of the angle ν of the least upper bound, obtained from the right-hand side of (4.16), is proposed

$$\tilde{Q}_{\text{Mode}} = \tilde{Q}_{\text{Mode}}^0(\theta_0, \beta_0) + \nu \tilde{Q}_{\text{Mode}}^1(\theta_0, \beta_0, \alpha) + \mathcal{O}(\nu^2). \quad (4.23)$$

The zeroth-order term $\tilde{Q}_{\text{Mode}}^0$ has been studied for the two particular modes (Mode = CB or RF) above, providing the critical orientations of the discontinuity (θ_0) and of the velocity jump vectors (β_0) found in (4.19) and (4.21). These orientations are used in the first-order term $\tilde{Q}_{\text{Mode}}^1$ and only the position scalar α remains unknown. This first-order term reads

$$\begin{aligned}
 \tilde{Q}_{\text{Mode}}^1(\theta_0, \beta_0, \alpha) = & -\tilde{\omega}_s(\tilde{J}) \frac{\cos \theta_0}{\sin^2 \theta_0} \tilde{H}_s + \tilde{H}_s \left[(1 - \alpha) + \frac{\tilde{H}_s}{2} \cotan(\theta_0 + \beta_0) \cotan^2 \theta_0 \right] \\
 & + \tilde{\rho}_b \frac{1}{2} \left[\tilde{H}_b - \alpha(1 - \alpha) \cotan(\beta_0 + \theta_0) \right] \\
 & + \tilde{\rho}_a \frac{1}{2} \left\{ \tilde{H}_s \cotan \theta_0 [2\tilde{H}_a + 2(1 - \alpha) \cotan(\theta_0 + \beta_0) \right. \\
 & \left. - (\tilde{H}_s - 2\tilde{H}_a) \cotan \theta_0 \cotan(\theta_0 + \beta_0)] - \tilde{H}_b + \alpha(1 - \alpha) \cotan(\theta_0 + \beta_0) \right\}.
 \end{aligned} \quad (4.24)$$

It is a quadratic function of the scalar α and its first partial derivative with respect to α set to zero provides the critical scalar

$$\alpha_c = \frac{1}{2} + \frac{\tilde{\rho}_a}{\tilde{\rho}_b - \tilde{\rho}_a} \tilde{H}_s \left(\cotan \theta_0 + \frac{\tilde{\rho}_s}{\tilde{\rho}_a} \tan(\theta_0 + \beta_0) \right). \quad (4.25)$$

This scalar defines a minimum or a maximum in the upper bound depending on the sign of the second derivative of (4.24) with respect to α

$$(\tilde{\rho}_b - \tilde{\rho}_a) \cotan(\theta_0 + \beta_0). \quad (4.26)$$

The range of admissible values for α is $[\alpha_{min}; \alpha_{Max}]$ set by possible geometrical constraints due to the dip of the velocity discontinuity. If θ_0 is less than $\pi/2$, α_{min} is zero, and it is $1 - \tilde{H}_s \cotan \theta_0$ otherwise. If θ_0 is less than $\pi/2$, α_{Max} is $1 - \tilde{H}_s \cotan \theta_0$, and it is one otherwise. If the second derivative in (4.26) is negative, the solution in (4.25) is a maximum and the critical α_c is either α_{min} or α_{Max} . If the second derivative is positive, the solution in (4.25) does provide α_c , if contained in the interval of search. The formula in (4.25) indicates that the discontinuity is positioned to either side of the competent layer, measured from its mid length. Three factors on the right-hand side of (4.25) determine this distance to the center. The first factor is related to the density contrast. A density stratified structure is assumed and the sign of this factor is thus positive. The second factor is determined by the ratio H_s/D which is smaller than one. The third term is function of the orientation of the discontinuity and the velocity jump. It takes the same value with a difference in sign for the two orientations of a given mode of failure (4.19, 4.21).

For the geometrical and material parameters in Table 4.1, the reverse fault is on the left ($\alpha_c = 0, \theta_0 = \frac{\pi}{4} - \frac{\phi_s}{2}$) and the compaction band on the right ($\alpha_c = \alpha_{Max}, \theta_0 = \frac{\pi}{4} + \frac{\phi_s^*}{2}$) for non-zero, small imperfection. The selection of the orientation for each mode is done by inspection of Figure 4.5. The solid lines are the solution to the optimization problem which is obtained by numerical means. The dotted lines are the first-order asymptotic solutions. The four curves for a given mode initiate from the same point on the vertical axis because the two orientations are equivalent in the absence of imperfection. The solid curves diverge even in the presence of a minute amount of imperfection. The curve providing the lowest upper bound determines the

4.3. Initiation of compaction bands and reverse faults

active failure orientation. Comparing the solid curves for the two failure modes, we conclude that the compaction band oriented at $\theta_0 = \frac{\pi}{4} + \frac{\phi^*}{2}$ (for $\nu = 0$) is the dominant failure mode. Note that the orientation of the discontinuity changes with the imperfection in a linear way. It is found that $\theta = \theta_0 - \nu/2$ for the four orientations studied here. Comparing solid and dashed curves in Figure 4.5 provides us with an additional information concerning the validity of our first-order asymptotic development. The approximation is excellent for the compaction band which is rather insensitive to the imperfection angle. For the reverse fault, the error is less than 2.5% for $\nu = 10^\circ$.

The last point of discussion in this section is the influence of the imperfection on the selection of the dominant mode of failure. Figure 4.5 reveals that the compaction band is dominant for imperfection angles smaller than 6° (point T on that figure). For larger angles, it is the reverse fault which is the dominant mode of failure. These results are obtained for specific geometrical parameters and we question now the influence of ν on the mode transition for varying burial depth. Results obtained by numerical means, solid curve, are presented in Figure 4.6. The lithostatic pressure has been normalized by the transition value P_l^T for $\nu = 0$ defined in (4.22). The solid curve partitions the (P_l, ν) space in two regions. In the top region, it is the compaction band which is the dominant failure mode. To the contrary, failure is by reverse faulting in the

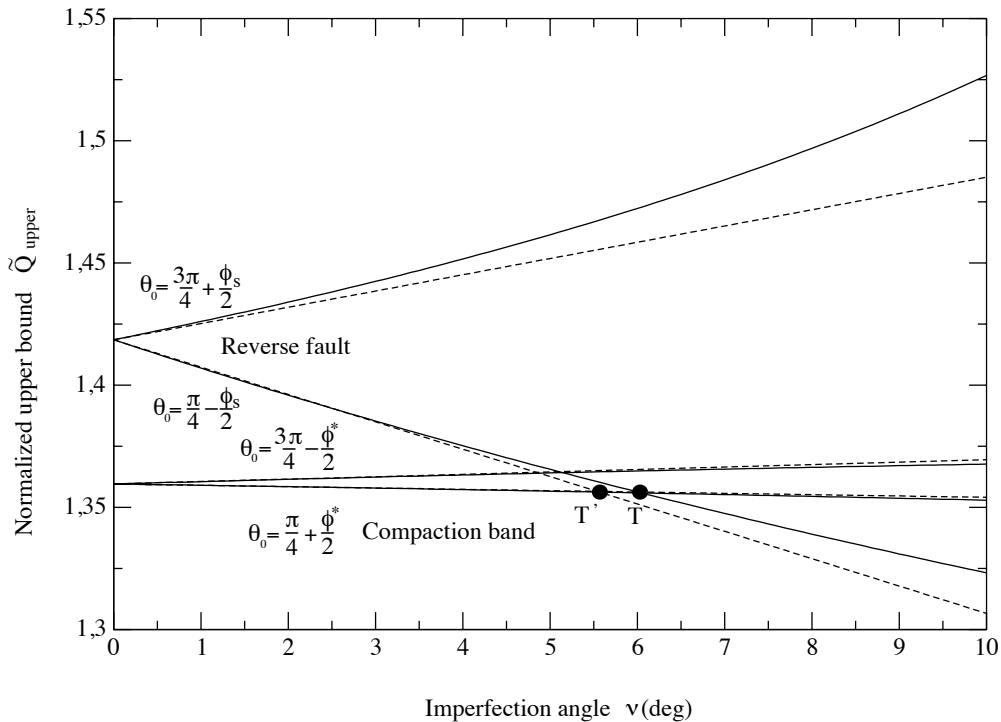


Figure 4.5: The upper bound in tectonic force as a function of the imperfection angle ν , for the failure modes in compaction band and in reverse fault. The first-order asymptotic solution, dashed lines, is compared to the numerical solution, solid curves.

region below the solid curve. Note that this curve is increasing with the imperfection angle. An approximation to this transition boundary obtained with the first-order asymptotic approximation (4.23) is now discussed. Equating \tilde{Q}_{RF} and \tilde{Q}_{CB} at the transition and using (4.23), one obtains

$$\nu_T = \frac{\tilde{Q}_{RF}^0 - \tilde{Q}_{CB}^0}{\tilde{Q}_{CB}^1 - \tilde{Q}_{RF}^1}. \quad (4.27)$$

The two zeroth-order and the two first-order terms in (4.27) are now seen as functions of the burial depth thus of P_l . Consequently, the transition imperfection ν_T in (4.27) is readily seen as a function of the same variable and provides the dashed curve in Figure 4.6. Note that the two zeroth-order terms are quadratic functions of the overburden height (H_a) and thus of the lithostatic pressure whereas the first-order terms are linear functions. The surprising observation in Figure 4.6 is that the asymptotic approximation turns out to be more curvy than the exact solution. The error is however negligible for ν less than 5° and is less than 6% for 10° . This error is illustrated in Figure 4.5 by comparing the position of the point T (exact transition) and T' (first-order approximation).

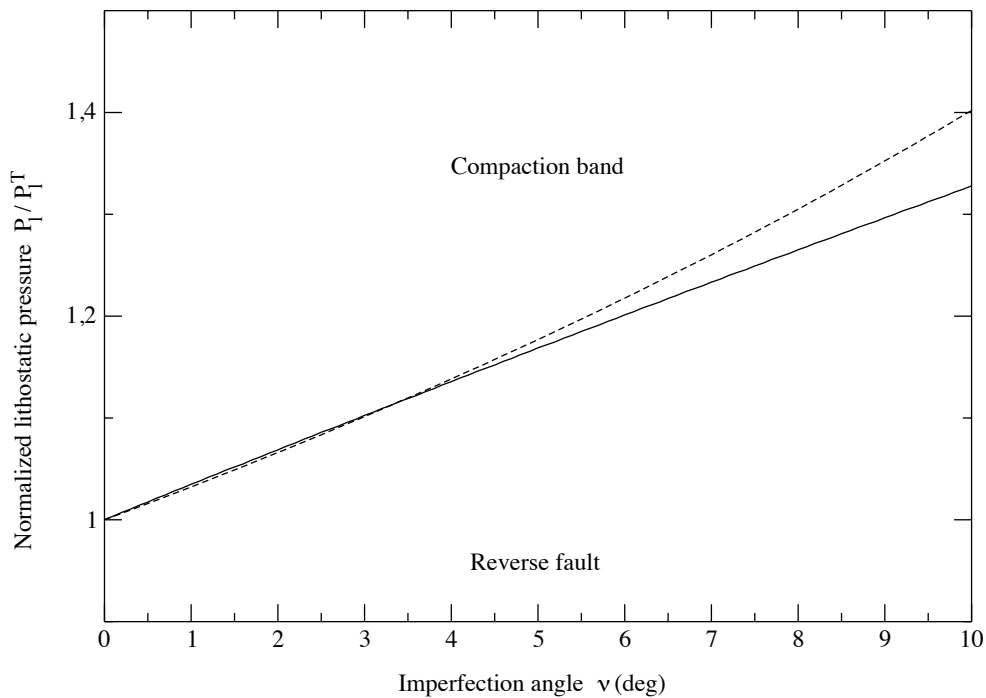


Figure 4.6: The lithostatic pressure for the transition between the dominance of the reverse fault and the compaction band. The dashed curve is obtained with the first-order asymptotic analysis.

4.4 Onset, development and arrest of the kink-fold

The same prototype applies to the three stages, onset development and arrest, and is first presented in details including the proposed virtual velocity field. The upper bound to the tectonic force is then computed before analysing the three stages.

4.4.1 Prototype for the kink fold

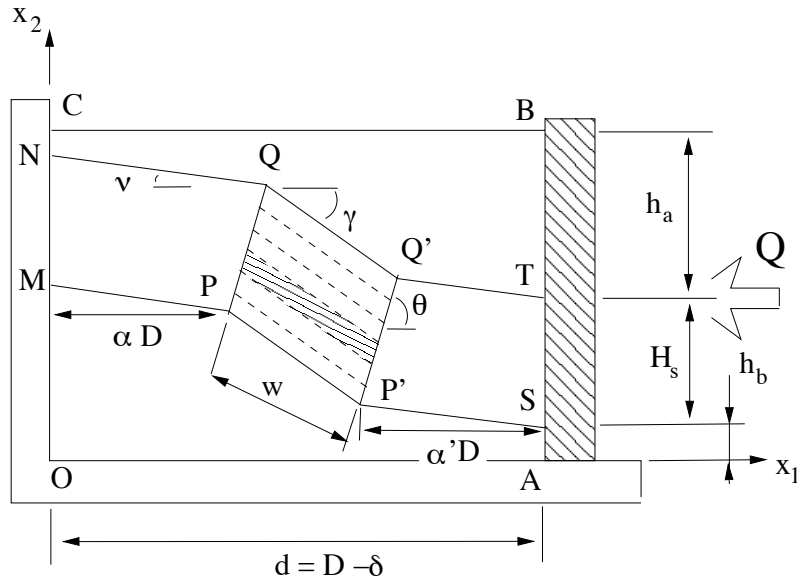


Figure 4.7: The kink fold is characterized by a band limited laterally by two hinges PQ and $P'Q'$. Slip occurs along the weak interfaces within the band (dashed lines). The position αD , the width w of this band, as well as the dips of the hinges θ and of the band γ are the unknowns which are optimized to get the least upper bound in tectonic force. The virtual velocity in the hashed area is presented in the next figure.

The prototype for the failure mode in kink band is presented in Figure 4.7 at an arbitrary stage of the development. The kink band occupies the region $PP'Q'Q$ of width w , with points P and P' positioned at αD and $\alpha' D$ from the left and the right structure boundary, respectively. The kink is dipping at the angle γ and its internal boundaries, the segments PQ and $P'Q'$, are parallel and dipping at the angle θ . These two segments are referred to as the hinges of the kink and constitute the first source of internal dissipation. Outside the band, material points in regions $MPQN$ and $P'STQ'$ sustain rigid translations. Within the kink band, the weak interfaces, illustrated by the dashed lines in Figure 4.7, are activated and constitute the second source of internal dissipation. There are n layers within the competent region. Note that the kink develops because of the displacement to the left of the rigid wall by δ , resulting in the structure current

length $d = D - \delta$ and current thicknesses of the fluid region below and above denoted by h_b and h_a , respectively.

These geometrical parameters describing the prototype during its development are not independent or are constrained by various hypotheses. There is first the condition that the sum of the projections of the segments MP, PP' and P'S over the horizontal direction is equal to the current length d . Furthermore, the length of any weak interface within the competent layer is preserved during shortening, an assumption commonly made in geometrical models of folding. These two conditions provide

$$\begin{aligned}\alpha + \alpha' + \frac{\cos \gamma}{\sin(\theta + \gamma)} \tilde{w} &= \tilde{d}, \\ \alpha + \alpha' + \frac{\cos \nu}{\sin(\theta + \gamma)} \tilde{w} &= 1.\end{aligned}\quad (4.28)$$

The sum $\alpha + \alpha'$ is eliminated from this system of equations to provide the relation between the dimensionless kink width and shortening

$$\tilde{w} \frac{\cos \nu - \cos \gamma}{\sin(\theta + \gamma)} = \tilde{\delta}.\quad (4.29)$$

The mass conservation in the regions above and below is now invoked to determine the two current heights of the fluids

$$\begin{aligned}\tilde{h}_b \tilde{d} &= \tilde{H}_b + \frac{1}{2} \tan \nu (1 - \alpha^2) - \alpha' \tan \nu (\tilde{d} - \frac{1}{2} \alpha') - \frac{\tilde{w}}{2} \frac{\sin \gamma}{\sin(\theta + \gamma)} (\tilde{d} + \alpha - \alpha'), \\ \tilde{h}_a \tilde{d} &= \tilde{H}_a + \tilde{H}_b - \tilde{h}_b \tilde{d} - \tilde{H}_s \frac{\cos \theta}{\sin(\theta + \nu)} \left[\sin \nu (\tilde{d} - \alpha) + \tilde{w} \frac{\sin \gamma \cos \nu}{\sin(\gamma + \theta)} \right],\end{aligned}\quad (4.30)$$

having made use of (4.28a). Another information on the geometry is due to the first of the two lessons learned from paper no 1 and it concerns the relation between the two angles θ and γ . It was found that these two angles are related by $\gamma + \theta = \pi/2 - \phi_i$ to minimize work against gravity. This information is now taken as a fundamental assumption in our construction reducing the number of unknown angles. As a consequence, the hinges must be dipping at $\pi/2 - \phi_i - \nu$ at the onset if γ is then equal to ν . This sub-vertical orientation is close to the one predicted for a compaction band. However, the deformation mechanisms activated by these two modes are different and will be discussed at length in the rest of the paper.

The virtual field proposed for the onset and the development of the kink fold is as follows. The lower block P'STQ' is displaced rigidly to the left with the velocity $-\tilde{U}_{L1}\mathbf{e}_1 + \tilde{U}_{L2}\mathbf{e}_2$. The upper block, section MPQN, moves up with the velocity $\tilde{U}_{U2}\mathbf{e}_2$. The segment CB of the top surface moves vertically with the velocity $\tilde{U}_{T2}\mathbf{e}_2$ to preserve the internal volume of the structure. The

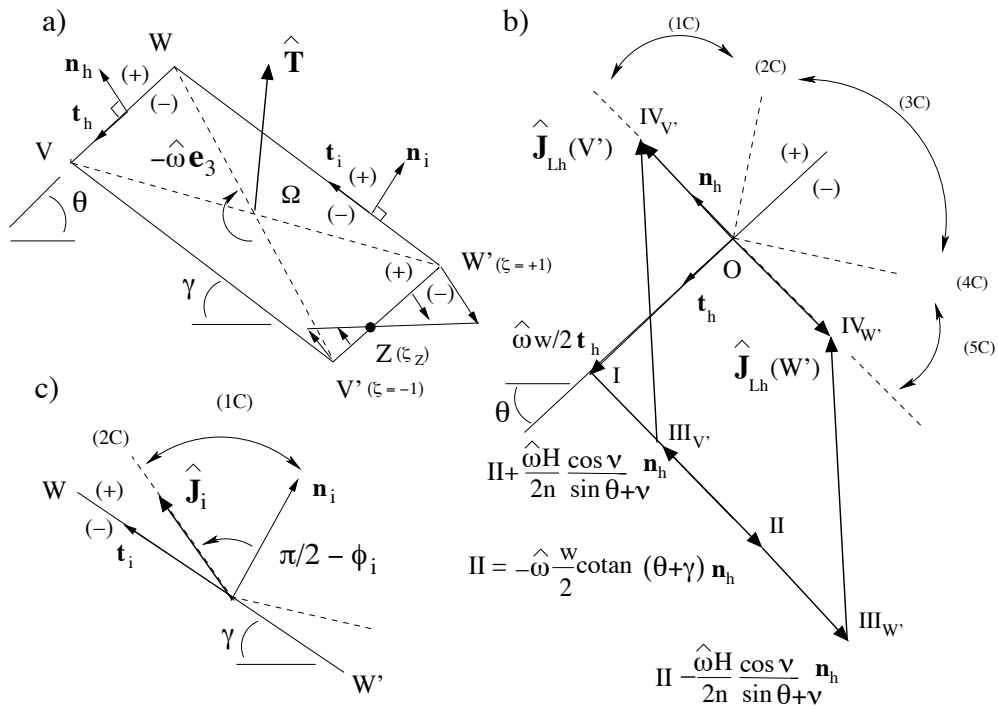


Figure 4.8: The virtual velocity field for a thin layer within the kink bounded by two weak interfaces and the hinges, a). The hodograms of the virtual velocities are in b), for the weak interface and in c) for the hinges.

virtual velocity within the kink band is defined identically for every layer, corresponding to the dashed zone within the kink band in Figure 4.7, and to the parallelogram $VV'W'W$ in Figure 4.8a. The virtual velocity is a rigid body motion described by the clockwise rotation $-\hat{\omega}\mathbf{e}_3$ (positive scalar $\hat{\omega}$) around the center Ω , and the translation $\hat{\mathbf{T}}$. This translation is chosen such that the two hinges sustain the same velocity jump in the absence of any rotation leading to the condition

$$\hat{\mathbf{T}} = -\frac{1}{2}\hat{U}_{L1}\mathbf{e}_1 + \frac{1}{2}(\hat{U}_{U2} + \hat{U}_{L2})\mathbf{e}_2 . \quad (4.31)$$

The segments VW and $V'W'$ along the upper and lower hinges are oriented by the normal \mathbf{n}_h and tangent vector \mathbf{t}_h , Figure 4.8a. The jumps in virtual velocities across the upper and lower hinges are then readily calculated and read

$$\begin{aligned} \hat{\mathbf{J}}_{Uh} &= \frac{1}{2}\hat{U}_{L1}\mathbf{e}_1 + \frac{1}{2}(\hat{U}_{U2} - \hat{U}_{L2})\mathbf{e}_2 + \hat{\omega}\frac{w}{2}\left[\mathbf{t}_h - \left(\cotan(\theta + \gamma) - \frac{H_s}{nw}\frac{\cos\nu}{\sin(\theta + \nu)}\zeta\right)\mathbf{n}_h\right] , \\ \hat{\mathbf{J}}_{Lh} &= \frac{1}{2}\hat{U}_{L1}\mathbf{e}_1 + \frac{1}{2}(\hat{U}_{U2} - \hat{U}_{L2})\mathbf{e}_2 + \hat{\omega}\frac{w}{2}\left[\mathbf{t}_h - \left(\cotan(\theta + \gamma) + \frac{H_s}{nw}\frac{\cos\nu}{\sin(\theta + \nu)}\zeta\right)\mathbf{n}_h\right] . \end{aligned} \quad (4.32)$$

The dimensionless scalar ζ in (4.32) varies between -1 and +1 and defines the position of any point between V and W , for the upper hinge (Uh), and between V' and W' for the lower hinge (Lh). The construction of the jump vector over the lower hinge is now explained thanks to the hodogram in Figure 4.8b. The discontinuity is dipping with the angle θ and oriented with its normal and tangent vectors. The jump vector is constructed by adding the contributions in (4.32b) starting with the virtual rotation. The term along the tangent vector corresponds in Figure 4.8b to the segment $O-I$. There are two contributions along the normal vector, the term independent of ζ corresponding to segment $I-II$. Depending on the value of the scalar ζ , the second contribution along the normal vector corresponds to any point between point $III_{W'}$ and point $III_{V'}$. The last contribution to this construction is due to the constant translation in (4.32b) bringing the jump vector tip to any point between points $IV_{W'}$ and $IV_{V'}$. The jump vectors across the lower hinge are thus always directed along the normal to the discontinuity, a result which was proved in paper no 1, and a consequence of the minimization of the external power due to gravity. This is the second lesson from this earlier work which we adopt, implying that the hinges will not sustain any shear. The consequence is that the velocities along the lower hinge in (4.32b) have a zero component along the tangent \mathbf{t}_h requiring

$$\tilde{\omega}\tilde{w} = \cos\theta + (\tilde{U}_{U2} - \tilde{U}_{L2})\sin\theta , \quad (4.33)$$

in which the normalized virtual rotation $\tilde{\omega}$ is defined by $\hat{\omega}D/\hat{U}_{L1}$. The orientation of the jump vector defines the value of the support function, according to the definitions in (4.4) and Figure 4.3e. It is either at the boundary of case 1A-1C or 5A-5C, as can be seen in Figure 4.8b. These

two orientations correspond to the center of the cones at the front and at the back of the strength domain in Figure 4.3c, which will be referred to as case 1 and 5, respectively. They correspond to a mode of deformation either in opening or in compaction with no shear. There is a position along the hinge where the transition occurs between compaction and opening. This point Z is shown as a solid dot along the lower hinge in Figure 4.8a together with an illustration of the linear variation in ζ of the jump in velocity. This point Z could be seen as a pin with position defined by the scalar ζ_Z obtained by setting the jump in (4.32) to zero. This scalar is defined for the lower hinge by

$$\zeta_Z = \frac{n\tilde{w} \sin(\theta + \nu)}{\tilde{H}_s \sin \theta \cos \nu} \left[\frac{\sin \gamma}{\sin(\theta + \gamma)} - \frac{1}{\tilde{\omega}\tilde{w}} \right]. \quad (4.34)$$

The velocities over the weak interfaces VV' and WW' , Figure 4.8a, oriented by the normal \mathbf{n}_i and tangent \mathbf{t}_i , are

$$\begin{aligned} \tilde{\mathbf{U}}_{V'V}(\eta) &= \tilde{\mathbf{T}} + \tilde{\omega} \left\{ \frac{\tilde{H}_s \cos \nu \sin(\theta + \gamma)}{2n \sin(\theta + \nu)} \mathbf{t}_i + \frac{\tilde{w}}{2} \left[-\frac{1 - 2\eta}{\sin(\theta + \gamma)} + \frac{\tilde{H}_s \cos \nu \cos(\theta + \gamma)}{n\tilde{w} \sin(\theta + \nu)} \right] \mathbf{n}_i \right\}, \\ \tilde{\mathbf{U}}_{W'W}(\eta) &= \tilde{\mathbf{T}} + \tilde{\omega} \left\{ -\frac{\tilde{H}_s \cos \nu \sin(\theta + \gamma)}{2n \sin(\theta + \nu)} \mathbf{t}_i - \frac{\tilde{w}}{2} \left[+\frac{1 - 2\eta}{\sin(\theta + \gamma)} + \frac{\tilde{H}_s \cos \nu \cos(\theta + \gamma)}{n\tilde{w} \sin(\theta + \nu)} \right] \mathbf{n}_i \right\}, \end{aligned} \quad (4.35)$$

with the scalar η varying between 0 (points V' and W') and 1 (points V and W). Note that in (4.35) and in what follows, dimensionless quantities are introduced. The jump in the velocity across a weak interface is obtained by subtracting the second vector from the first in (4.35) and reads

$$\tilde{\mathbf{J}}_i = \tilde{\omega} \frac{\tilde{H}_s \cos \nu}{n \sin(\theta + \nu)} \left[\sin(\theta + \gamma) \mathbf{t}_i + \cos(\theta + \gamma) \mathbf{n}_i \right]. \quad (4.36)$$

This jump is thus constant, independent of its position along the weak interface. Furthermore, the jump is oriented exactly along the condition (2C) since the sum $\theta + \gamma$ is assumed equal to $\pi/2 - \phi_i$, as illustrated in Figure 4.8c. It is of note that the orientation of the jump $\tilde{\mathbf{J}}_i$ is directed in the direction of \mathbf{n}_h , the normal to the hinge, which is also the direction of the velocity jump across the hinges.

The last points of this preliminary section are the constraints on the velocity field, due to mass conservation in the two regions containing the fluid-like materials. The incompressibility constraint (4.6) applied to the fluid region below provides

$$\tilde{U}_{L2} \left(\alpha' + \frac{\tilde{w} \cos \gamma}{2 \sin \theta + \gamma} \right) + \tilde{U}_{U2} \left(\alpha + \frac{\tilde{w} \cos \gamma}{2 \sin \theta + \gamma} \right) = \tilde{h}_b + \alpha' \tan \nu + \frac{\tilde{w} \sin \gamma}{2 \sin \theta + \gamma} - \tilde{\omega} \frac{\tilde{w} \tilde{H}_s \cos \nu \cotan \theta + \gamma}{2n \sin \theta + \nu}. \quad (4.37)$$

The same requirement for the fluid above leads to an expression for the top surface virtual velocity

$$\tilde{U}_{T2} \tilde{d} = \tilde{h}_a + \tilde{h}_b - \tilde{H}_s \cotan \theta \cotan(\theta + \nu) - \tilde{\omega} \tilde{w} \tilde{H}_s \frac{\cos \nu}{\sin \theta + \nu} \left(\frac{1}{n} \cotan(\theta + \gamma) - \cotan \theta \right), \quad (4.38)$$

once (4.37) and (4.33) have been used.

4.4.2 The upper bound in tectonic force

The upper bound in tectonic force is composed of several contributions which are the external power of gravity, due to the two fluid regions and the competent layer, the power of the tectonic force and the bound on the internal power. These various contributions are now calculated without recurring to any new concept compared to the ones required for calculations of the upper bounds for the single discontinuity. The reader could thus skip this section and move to the text after equation (4.44), which introduces the next two sub-sections on the onset and development of kink folds.

The contribution of the fluid below due to the gravity power is computed according to (4.11) with the velocity field described above and reads

$$\begin{aligned} \tilde{\mathcal{G}}_{\text{ext}(b)}(\tilde{\mathbf{U}}) \frac{1}{\tilde{\rho}_b} &= \alpha' (\tan \nu - \tilde{U}_{L2}) (\tilde{h}_b + \frac{\alpha'}{2} \tan \nu) - \alpha \tilde{U}_{U2} (\tilde{h}_b + \alpha' \tan \nu + \tilde{w} \frac{\sin \gamma}{\sin \gamma + \theta} + \frac{\alpha}{2} \tan \nu) \\ &\quad - \left[\tilde{\omega} \left(\frac{\tilde{H}_s \cos \nu \cos \theta + \gamma}{n \sin \nu + \theta} - \frac{\tilde{w}}{\sin \theta + \gamma} \right) - \sin \gamma + (\tilde{U}_{U2} + \tilde{U}_{L2}) \cos \gamma \right] \\ &\quad \frac{\tilde{w}}{2 \sin \theta + \gamma} (\tilde{h}_b + \alpha' \tan \nu + \frac{\tilde{w}}{2} \frac{\sin \gamma}{\sin \gamma + \theta}) + \frac{\tilde{\omega}}{6 \sin^2 \gamma} \left[(\tilde{h}_b + \alpha' \tan \nu + \frac{\tilde{w}}{2} \frac{\sin \gamma}{\sin \gamma + \theta})^2 \right. \\ &\quad \left. (\tilde{h}_b + \alpha' \tan \nu - 2\tilde{w} \frac{\sin \gamma}{\sin \gamma + \theta}) - (\tilde{h}_b + \alpha' \tan \nu)^3 \right] + \frac{1}{2} \tilde{h}_b^2. \end{aligned} \quad (4.39)$$

The external power due to gravity over the competent layer is computed directly from the definition in (4.9):

$$\tilde{\mathcal{G}}_{\text{ext}(s)}(\tilde{\mathbf{U}}) = -\tilde{U}_{U2} \tilde{H}_s \left(\alpha + \frac{\cos \nu}{2 \sin \theta + \nu} (\tilde{H}_s \cos \theta + \tilde{w}) \right) - \tilde{U}_{L2} \tilde{H}_s \left(\alpha' + \frac{\cos \nu}{2 \sin \theta + \nu} (-\tilde{H}_s \cos \theta + \tilde{w}) \right). \quad (4.40)$$

The last contribution to the gravity external power is due to the fluid above and is computed as for the fluid below in (4.39) and reads

$$\begin{aligned}
 \mathcal{G}_{\text{ext}(a)}(\tilde{\mathbf{U}}) \frac{1}{\tilde{\rho}_a} &= \tilde{h}_a \left(\frac{1}{2} \tilde{h}_a + \tilde{h}_b + \tilde{H}_s \right) - \tilde{U}_{T2} \tilde{d} (\tilde{h}_a + \tilde{h}_b + \tilde{H}_s) - \frac{1}{2} (1 - \tilde{U}_{L2} \cotan \nu) \quad (4.41) \\
 &\left[\tilde{H}_s \left(\frac{\cos \nu \sin \theta}{\sin \nu + \theta} - 1 \right) + \alpha' \tan \nu \right] \left[\tilde{H}_s \left(1 + \frac{\cos \nu \sin \theta}{\sin \theta + \nu} \right) + 2\tilde{h}_b + \alpha \tan \nu \right] \\
 &+ \left\{ - \left[\tilde{\omega} \left(\tilde{w} \left(\frac{1}{\sin \theta + \gamma} - \frac{\cos \gamma}{\sin \theta} \right) + \frac{\tilde{H}_s \cos \nu \cos \theta + \gamma}{n \sin \theta + \nu} \right) + \frac{\cos \gamma - \theta}{\sin \theta} \right] \frac{\tilde{w}}{2 \sin \theta + \gamma} + \tilde{U}_{L2} (\alpha + \right. \\
 &\left. \tilde{H}_s \frac{\cos \nu \cos \theta}{\sin \nu + \theta} \right) \left[\tilde{h}_b + \tilde{H}_s \frac{1}{\sin \theta + \nu} \left(\cos \nu \sin \theta + \frac{1}{2} \sin \nu \cos \theta \right) + \left(\alpha' + \frac{\alpha}{2} \right) \tan \nu + \tilde{w} \frac{\sin \gamma}{\sin \theta + \gamma} \right] \\
 &+ \frac{\tilde{\omega}}{6 \sin^2 \gamma} \left[\left(\tilde{h}_b + \tilde{H}_s \frac{\cos \nu \sin \theta}{\sin \theta + \nu} + \alpha' \tan \nu + \tilde{w} \frac{\sin \gamma}{\sin \theta + \gamma} \right)^2 \left(\tilde{h}_b + \tilde{H}_s \frac{\cos \nu \sin \theta}{\sin \nu + \theta} + \alpha' \tan \nu \right. \right. \\
 &\left. \left. - 3\tilde{w} \frac{\sin \gamma}{\sin \theta + \gamma} \right) + \left(\tilde{h}_b + \alpha' \tan \nu + \tilde{H}_s \frac{\cos \nu \sin \theta}{\sin \theta + \nu} \right)^3 \right].
 \end{aligned}$$

Attention is now turned to the bound on the internal power. For the weak interfaces, this bound is obtained by multiplying the norm of the velocity jump in (4.36) by the support function for case 2C in (4.3), by the length of a single weak interface within the kink band, and by the number $(n - 1)$ of activated interfaces. The upper bound to the internal power is then

$$\tilde{\mathcal{P}}_{\text{int}(i)}(\tilde{\mathbf{U}}) = \tilde{\omega} \frac{\tilde{H}_s \tilde{w} (n - 1)}{n} \frac{\cos \nu}{\sin(\theta + \nu)} \tilde{C}_i. \quad (4.42)$$

The second source of internal power is due to the two hinges. The velocity field was constructed such that they contribute identically to this power and we can concentrate over the lower hinge. The velocity jump is always directed along the normal to the lower hinge. From points V' to Z , Figure 4.8a, it is oriented positively such that the support function in (4.4) is in case 1 corresponding to an opening mode of failure. Between points Z and W' , the jump vector is oriented towards the negative side of the discontinuity, the relevant support function is in case 5, signalling compaction. The bound to the internal work has thus two contributions which, after integration from points V' to Z or from Z to W' , are

$$\begin{aligned}
 \tilde{\mathcal{P}}_{\text{int(Lh)}}^1(\tilde{\mathbf{U}}) &= -\tilde{C}_s \cotan \phi_s \frac{\tilde{H}_s \cos \nu}{4 \sin \theta \sin \nu + \theta} (1 + \zeta_Z) \left[1 - \tilde{\omega} \left(\frac{\tilde{w} \sin \gamma}{\sin \theta + \gamma} + \frac{\tilde{H}_s \cos \nu \sin \theta}{2n \sin \theta + \nu} (1 - \zeta_Z) \right) \right], \\
 \tilde{\mathcal{P}}_{\text{int(Lh)}}^5(\tilde{\mathbf{U}}) &= \tilde{P}^* \frac{\tilde{H}_s \cos \nu}{4 \sin \theta \sin \nu + \theta} (1 - \zeta_Z) \left[1 - \tilde{\omega} \left(\frac{\tilde{w} \sin \gamma}{\sin \theta + \gamma} - \frac{\tilde{H}_s \cos \nu \sin \theta}{2n \sin \theta + \nu} (1 + \zeta_Z) \right) \right], \quad (4.43)
 \end{aligned}$$

the superscript 1 and 5 on the left-hand side identifying the origin of the contribution. The expression of the pin position in (4.34) provides further simplifications so these two expressions

for the internal power become

$$\begin{aligned}\tilde{\mathcal{P}}_{\text{int(Lh)}}^1(\tilde{\mathbf{U}}) &= \tilde{C}_s \cotan \phi_s \frac{\tilde{H}_s^2}{8n} \frac{\cos^2 \nu}{\sin^2(\nu + \theta)} (1 + \zeta_Z)^2 \tilde{\omega}, \\ \tilde{\mathcal{P}}_{\text{int(Lh)}}^5(\tilde{\mathbf{U}}) &= \tilde{P}^* \frac{\tilde{H}_s^2}{8n} \frac{\cos^2 \nu}{\sin^2(\nu + \theta)} (1 - \zeta_Z)^2 \tilde{\omega}.\end{aligned}\quad (4.44)$$

The upper bound to the tectonic force is now computed. It results from the contribution of the gravity power, found by adding (4.39) to (4.41), and the internal power defined by adding (4.42) to twice (4.44) (two hinges). The end result reads

$$\tilde{Q} \leq \tilde{Q}_{\text{KB upper}} = \tilde{\mathcal{P}}_{\text{int(i)}} + 2\tilde{\mathcal{P}}_{\text{int(Lh)}}^1 + 2\tilde{\mathcal{P}}_{\text{int(Lh)}}^5 - \tilde{\mathcal{G}}_{\text{ext(b)}} - \tilde{\mathcal{G}}_{\text{ext(s)}} - \tilde{\mathcal{G}}_{\text{ext(a)}}. \quad (4.45)$$

The objective of the next two subsections is to minimize this upper bound at the onset and at each step of the kink development with the constraints

$$\begin{aligned}\tilde{\omega} &\geq 0, \\ -1 &\leq \zeta_Z \leq 1.\end{aligned}\quad (4.46)$$

They correspond to the requirement that the kink is rotating clockwise and that the pin remains within the boundary of each layer. For a given geometry $(\theta, \gamma, \alpha, \alpha', \delta)$, the minimization of the velocity field is done numerically choosing the pin position as the basic unknown, in the range found in (4.46). The angular velocity is then found from (4.34), and the scalars \tilde{U}_{L2} , \tilde{U}_{U2} and \tilde{U}_{T2} from the solution of (4.33), (4.37) and (4.38). There are two major differences in this optimization scheme compared to the one considered in paper no 1. First, an additional constraint was considered in this earlier work: the difference in velocity $\tilde{U}_{U2} - \tilde{U}_{L2}$ was necessarily positive to enforce upward motion of the upper block, typical of a fold. Relaxing this constraint has important consequences on the nature of the kink mechanism at the onset and its affinity with compaction bands. Second, the virtual velocity field in paper no 1 was not constrained by the volume conservation in the regions below and above nor by the fluid incompressibility assumption. For example, the velocities \tilde{U}_{U2} and \tilde{U}_{L2} are now sensitive to \tilde{h}_b according to (4.37) and contribute to the virtual power due to gravity in (4.40). This difference has an important consequence on the development of the least upper bound for the kink.

4.4.3 Initiation of kink-fold

The first objective is to study the onset of kink folds and to compare the three mechanisms, kink fold, compaction band and reverse fault in terms of least upper bounds. This comparison, conducted in the space spanned by the imperfection angle ν and the lithostatic pressure P_l provides

a map of dominant failure mechanism discussed in the next subsection. The geometry and the material properties are still found in Table 4.1 unless otherwise stated. The fluid height below H_b is set to 250 m for the rest of this section.

The first results for the onset are presented in Figure 4.9. The graph a) compares the least upper bounds for the kink fold obtained for three different imperfection angles, dotted-dashed curve for 10^{-6}° , dashed curve for 4° and doubly-dotted, dashed curve for 10° , as well as for the initiation of a compaction band, dotted curve. The competition is indeed between the compaction band and the kink fold because the lithostatic pressure at the onset is 1.2 the transition pressure P_l^T , defined in (4.22). A log scale is adopted for the x-coordinate axis which corresponds to the dimensionless shortening of the prototype. For the two smaller imperfection angles, the kink band initiates at a load which is larger than the one required for the compaction band. A dimensionless shortening of 10^{-4} (10 cm for our structure of 1 km length) is required for the load to decrease and the kink to dominate. The onset is however dominated by the kink band for larger imperfections, as shown on the graph for $\nu = 10^\circ$. The transition between the two dominant mechanisms occurs for the angle $\nu = 5^\circ$, approximately. This angle is strongly dependent on the overburden height and will be discussed in the next subsection. One of the conclusion is thus that for imperfections smaller than this 5° , there is a boundary layer effect in the space spanned by the least upper bound and the normalized shortening. This layer is 10^{-4} -thick in terms of $\tilde{\delta}$ and corresponds to the dominance of the compaction band over the kink. The end of the boundary layer with increasing $\tilde{\delta}$ is marked by the shift in the position of the pin along the lower hinge towards the top ($\zeta_Z = +1$) of each sedimentary layer, Figure 4.9b. At the onset, this pin is at the base of each layer ($\zeta_Z = -1$) for the two smaller imperfection angles. The onset is thus purely compacting along the hinge for these angles and the kink is close to respond as a compaction band. This kinematics is referred to as a slip-enhanced compaction band and is illustrated in Figure 4.10 where it is compared to the compaction band single velocity discontinuity. It characterizes the onset of the kink within the boundary layer defined above. For the larger imperfection, the first position of the pin is at -0.24 marking that the bottom 48% of each layer is opening along the lower hinge.

The kink width w is presented in Figure 4.9c and provides further evidence on the influence of the imperfection angle on the kink fold onset. The width of the kink is tending to zero at the onset for the smallest imperfection. The kink is thus behaving essentially as a compaction band with the additional activation of the weak interfaces over a length vanishing with decreasing shortening, as illustrated in Figure 4.10b. The kink mode is thus a slip-enhanced compaction band in this early stage of its development. For the larger imperfection angle of 10° , the kink at the onset has a finite width which is one tenth of the structure length. This results is very

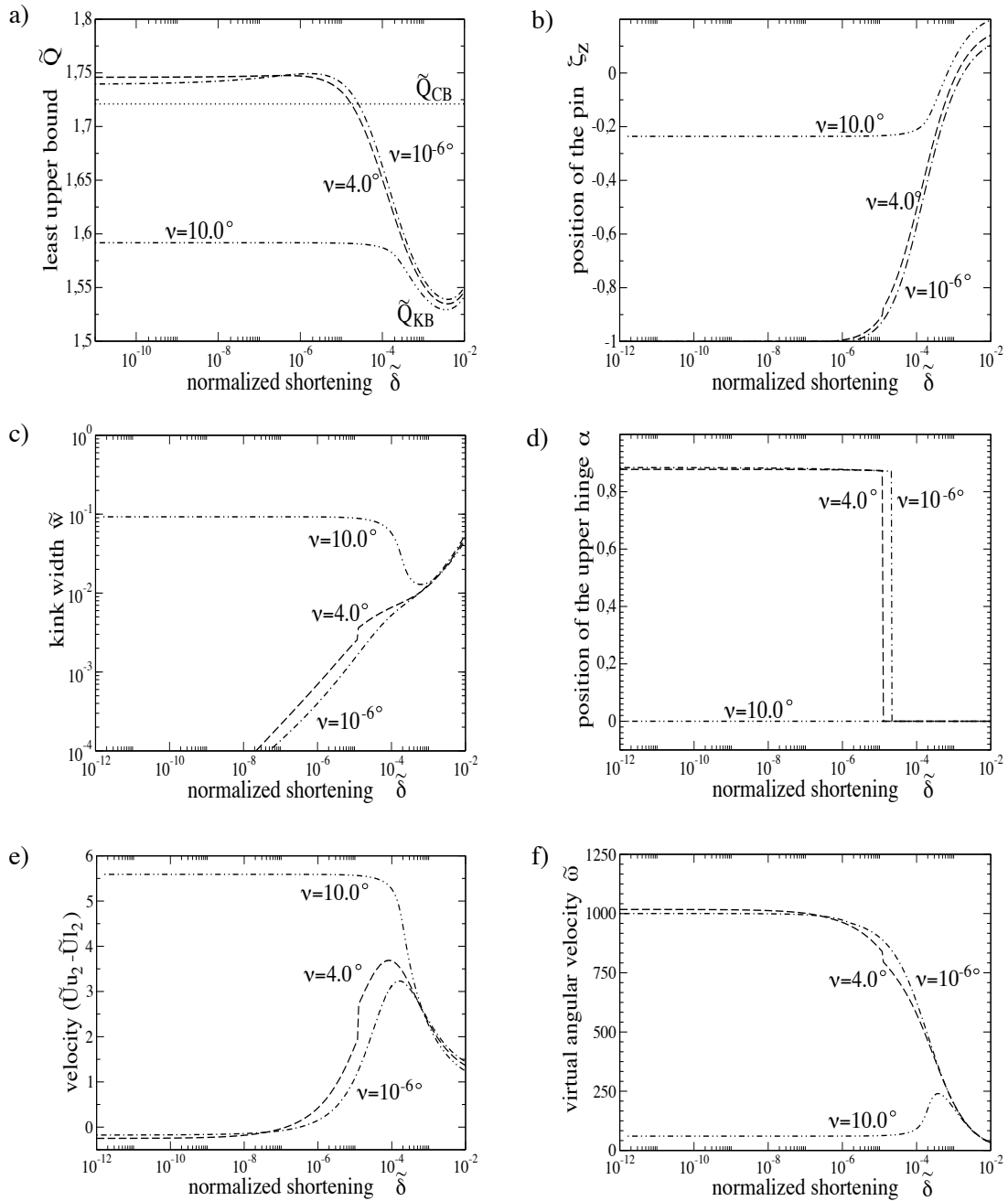


Figure 4.9: Analysis of the kink onset in terms of least upper bound a), position of the pin within the lower hinge b), kink width c), lateral position of the upper hinge d), difference in vertical virtual velocity e) and angular virtual velocity f). The dotted curve in a) depicts the bound for the compaction band. The dotted-dashed, dashed and doubly-dotted, dashed curves are obtained for an imperfection angle of 10^{-6} , 4 and 10° . Results are obtained at a lithostatic pressure $P_l = 1.2P_l^T$ for which the dominant mechanism is a priori the compaction band.

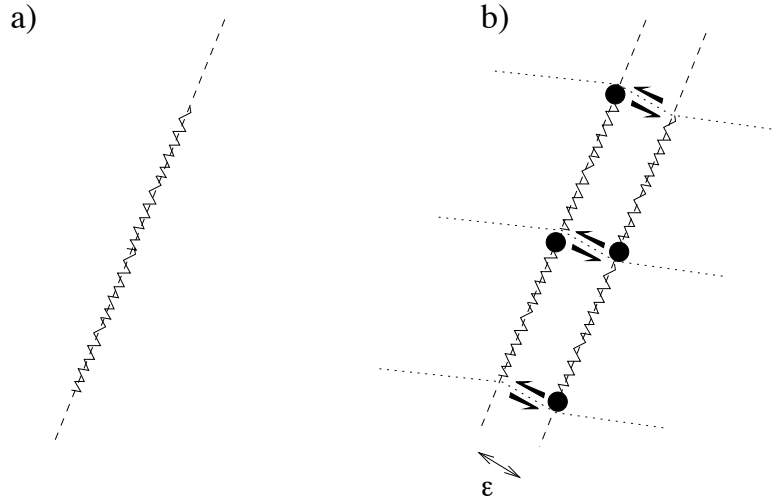


Figure 4.10: Illustration of the compaction band as a single velocity discontinuity, a) and of the slip-enhanced compaction band for vanishing thickness ϵ , b). The pins on the two hinges of each layer are marked by large solid dots.

surprising compared to the solutions found in paper no 1 and is certainly due to the role of the overburden. For normalized shortening larger than 10^{-3} , the three solutions converge to the same response. Note the jump in the kink width for $\nu = 4^\circ$ and a shortening of $\tilde{\delta} \simeq 10^{-5}$ which is now discussed with the help of the position of the failure mode in Figure 4.9d. The failure mode is at $\alpha \simeq 0.9$, so to the right of the structure, for the two smaller imperfection angles. This is the region where compaction bands are found to initiate, according to the results of the previous section. This is the third hint, after the analysis of the position of the pin and of the kink width, that the kink mode does behave like a slip-enhanced compaction bands. Interestingly, there is a sharp transition in the position of the failure mechanism at a shortening of 10^{-5} . The kink mode migrates suddenly to the left of the structure where the kink for $\nu = 10^\circ$ is initiated ($\alpha = 0$). It seems that the kink mode which behaves initially as a slip-enhanced compaction band decides beyond that shortening to resemble more to a real kink, increases its width, uses more opening in the hinge and migrates suddenly to the right where reverse faults initiate and kinks develop.

Figure 4.9e presents the difference between the vertical velocity of the upper block and the lower block. This difference in velocity was constrained to be positive in the optimization proposed in paper no 1, so that the failure mode had the typical positive rotation of a kink. This difference could certainly be negative for a sub-vertical compaction band. The consequence of constraining the velocity difference was that the kink width at the onset is always determined and defined as $(H_s \sin \phi_i)/n$, corresponding to a single competent layer thickness times the sine of the friction angle over the weak interface. In this contribution, the constraint of a positive

difference has been relaxed so that the relation between kink and compaction band could be further explored. The results in Figure 4.9e confirm this interpretation. The velocity difference is negative at the onset for the two smaller imperfection angles since the failure mode is close to a compaction band. This negative difference increases and becomes positive once the kink width starts to increase. For the largest imperfection, the velocity difference is positive from the onset. Note that the kink width is nevertheless not set by the limiting value found in paper no 1 ($H_s/n \sin \phi_i$). This difference is certainly due to the burial depth which was disregarded in this earlier work. Note also and again that beyond the boundary layer, the velocity differences converge to a single response which seems to be independent of the value of the imperfection angle.

The last word on Figure 4.9 concerns graph f) where the kink angle γ is presented as a function of the dimensionless shortening. This angle at the onset is equal to the imperfection angle for $\nu = 4^\circ$ and 10° . The kink starts to rotate significantly only once the boundary layer of the onset has been overcome. For the smallest imperfection angle of $\nu = 10^{-6^\circ}$, the failure mode initiates with an angle γ which is not equal to the imperfection angle. This was never reported in paper no 1 and can certainly be explained by the singularity of the solution for a zero band thickness at the onset in the absence of the constraint on the difference in the velocities $\tilde{U}_{U2} - \tilde{U}_{L2}$.

The second set of results are presented in Figure 4.11 and are obtained at a shallower depth with $P_l = 0.2P_l^T$. The kink-band is now in competition with the reverse fault. Four imperfection angles are considered, 10^{-6° , 0.6° , 0.7° , and 4° and the corresponding results are the dotted, dashed, dotted-dashed, and doubly-dotted dashed curves. The same definitions are used for the reverse fault in Figure 4.11a where the least upper bound for the two mechanisms are compared. The main result of this graph is that there is also a boundary layer effect in terms of shortening, say 10^{-6} thick, during which the kink mode is inhibited. The imperfection has to be larger than, approximately 2.5° , for the kink to dominate the reverse fault at the onset without any delay. The kinks suffering from that inhibition period do not all behave as slip-enhanced compaction bands. This phenomenon occurs only if the imperfection is less than 0.6° . There is indeed a slight opening of each layer during that period for the two examples of $\nu = 0.6^\circ$ and $\nu = 0.7^\circ$, and only the solution for the smallest imperfection is responding at the onset with compaction only, as can be judged from the position of the pin in Figure 4.11b. This trend is confirmed by the band width which vanishes as the imperfection angle tends to zero, Figure 4.11c. Note the non-linear relation between initial kink width and imperfection angle: the initial width for $\nu = 0.7^\circ$ is larger than the width obtained for $\nu = 4^\circ$, Figure 4.11c. This effect will be discussed next. Note also by comparing Figures 4.9b,c and 4.11b,c that more opening is used at the onset and that the

4.4. Onset, development and arrest of the kink-fold

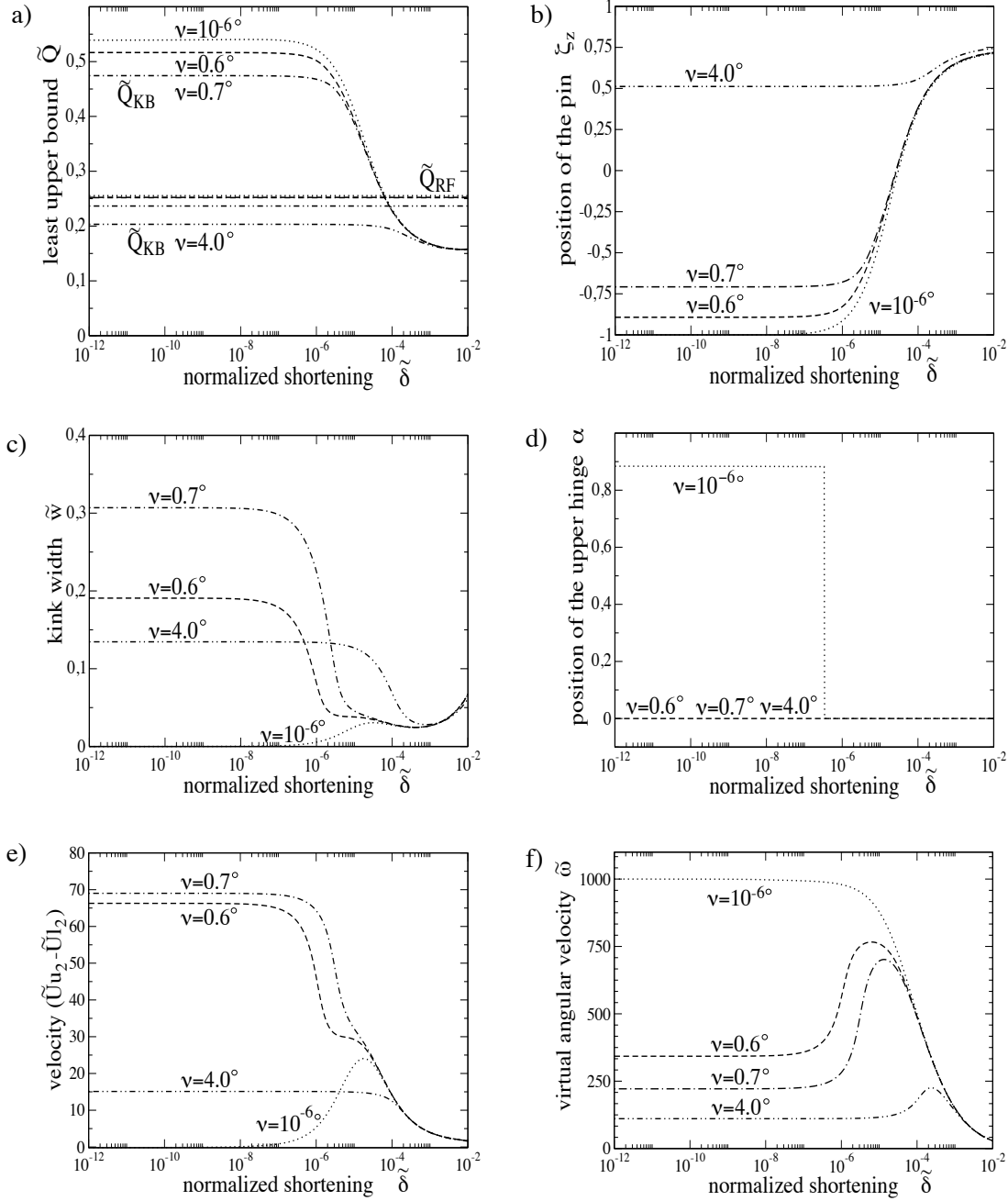


Figure 4.11: Analysis of the kink onset in terms of least upper bound a), position of the pin within the lower hinge b), kink width c), lateral position of the upper hinge d), difference in vertical virtual velocity e) and kink dip f). The dotted curve in a) depicts the bound for the compaction band. The dotted-dashed, dashed and doubly-dotted, dashed curves are obtained for an imperfection angle of 10^{-6} , 4 and 10° . Results are obtained at a lithostatic pressure $P_l = 0.2P_l^T$ for which the dominant mechanism is a priori the reverse fault.

kink width is much larger at shallower depths. The position of the failure mode on the structure, Figure 4.11d, confirms that only the slip-enhanced compaction band is found initially to the right of the structure for $\tilde{\delta}$ within the boundary layer. It migrates to the left once its development is more typical of a kink band. The velocity difference $\tilde{U}_{U2} - \tilde{U}_{L2}$ is positive for all imperfections except for the smallest and during the early stage of the slip-enhanced compaction band, Figure 4.11e. Figure 4.11f reveals that the kink dip is set initially by the imperfection except for the smallest angle for which the first orientation is larger, confirming the singular behaviour at the onset eluded to above.

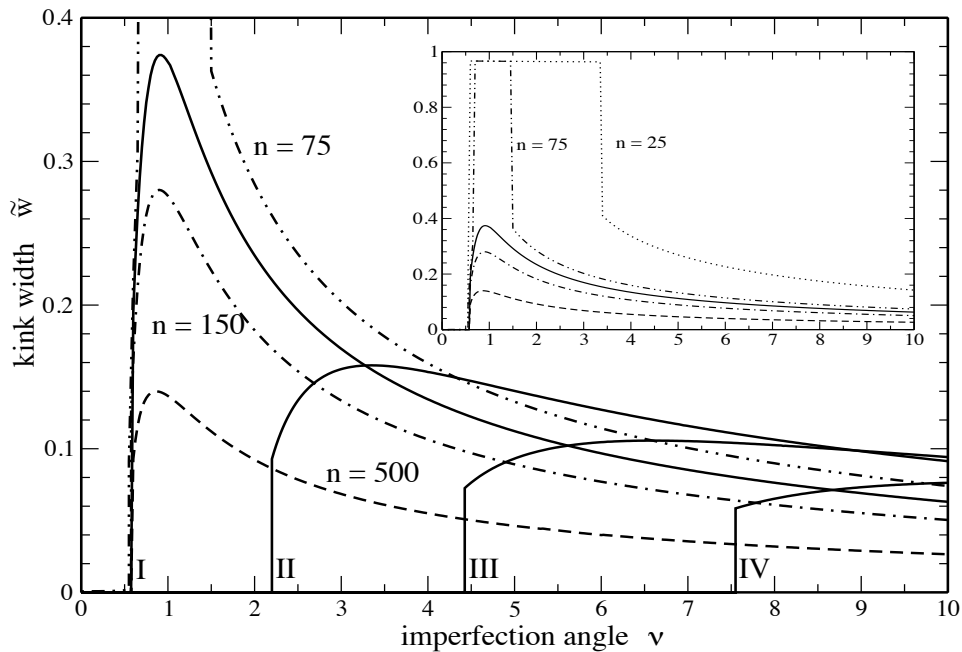


Figure 4.12: The kink width at the onset ($\tilde{\delta} = 10^{-10}$) as a function of the imperfection angle. The four solid curves labeled from I to IV are for burial depths of 200 m, 800 m, 1400 m and 2000 m, respectively. The solid curves are obtained with 100 layers. The dashed, dotted-dashed, doubly-dotted dashed and dotted curves correspond to 500, 150, 75 and 25 layers, respectively, and a burial depth of 200 m.

The kink width at the onset ($\tilde{\delta} = 10^{-10}$) is now further discussed with the help of Figure 4.12 where it is presented as a function of the imperfection angle ν . All widths are measured for $\tilde{\delta} = 10^{-10}$. The solid curves are obtained for 100 layers and are numbered from I to IV for burial depth set to 200, 800, 1400 and 2000 m, respectively. The kink width for small enough imperfection (less than 2° for curve II) is zero and the kink mode is the slip-enhanced compaction band of vanishing thickness discussed above. At the critical angle of 2.2° , the curve jumps to a finite value signalling that the failure mode is a kink of finite thickness. This critical angle increases approximately linearly with the burial depth by comparing curves I to IV. For ν

larger than the critical angle, the kink width at the onset increases first to reach a maximum and then decreases with increasing imperfection angle. These two variations are more important at shallower depths with an initial dimensionless width reaching 0.4 after an increase in the imperfection of 0.5° for curve I. The kink width at the onset has also been plotted on the same Figure for the same burial depth of 200 m but varying the number of layers. The number is 500, 150, 75 and 25 for the dashed, dotted-dashed and doubly-dotted, dashed and finally dotted curves, respectively. The striking result is the jump in the width for a range of imperfection angles of 0.6 to 1.6 for the 75 layers results for example. The kink width in this range is close to one, as can be seen in the inset. The weak interfaces are activated over most of the solid region. The same trend is seen for the results obtained with 25 layers but for a larger range of imperfection angles ($[0.6; 3.4]$). It should be mentioned that the least upper bounds corresponding to these two sets of solutions, fully activated weak interfaces and kink of smaller width, differ relatively by less than 10^{-4} . The solution for smaller width, which would correspond to a continuous width function of the imperfection, as for the curves obtained with 100 layers, is not drawn on the same Figure but could be guessed by extending the curve drawn outside of the interval $[0.6; 1.6]$ for the 75 layers solution, for example. There is thus a resolution issue to decide if the two solutions, fully activated and partly activated weak interfaces, are true, coincident solutions. Improving this resolution would require special numerical treatment. This task remains nevertheless rather academic since the solution with the interfaces fully activated does not persist beyond the onset.

The results obtained at the onset are interesting to define the domain of dominance of a given mode of failure in the space spanned by the imperfection angle and the burial depth of the lithostatic pressure. Such constructions are built in the spirit of the deformation maps proposed by Ashby (1972) although the spaces are different. These failure-mechanism maps are built next by comparing the least upper bounds for the kink-band, the reverse fault and the compaction bands. We choose, for a given value of the imperfection angle, to study these bounds as function of the burial depth. The results are presented in Figure 4.13 for an angle of 2.5° and 5° in a) and b), respectively. The least upper bound for the kink, the reverse fault and the compaction band are the solid, the dashed and the dotted-dashed curves, respectively. Four points ($j = A, B, C$ and D) mark the change in the dominant mode in the first graph and correspond to four burial depths H_j . For depths smaller than H_A the kink has the smallest least upper bound and dominates. Between H_A and H_C , the kink band is overcome by the reverse fault and even the compaction band for depth larger than H_B . The dominant mode is then the reverse fault in that interval. The compaction band has the smallest least upper bound for depths larger than H_C and is in direct competition with the kink band. The results are simpler for 5° in Figure 4.13b. Only the two points E and F mark changes in the dominant modes. For depths smaller than H_E , the kink is

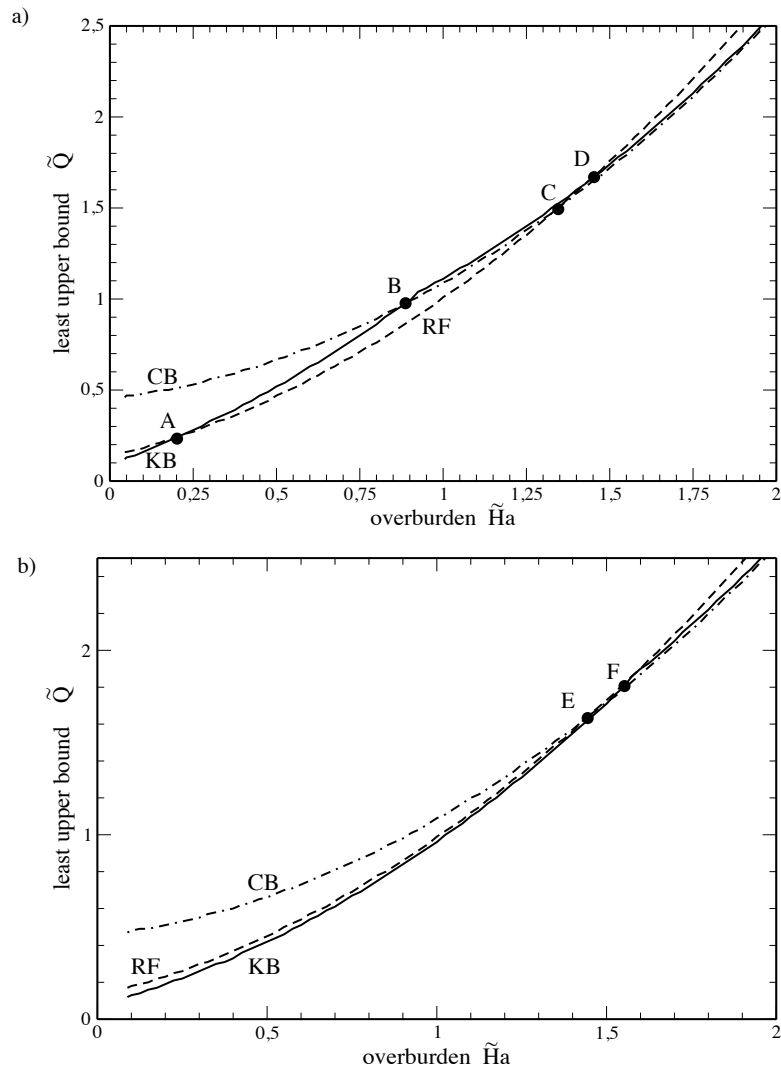


Figure 4.13: Comparison of the upper bound in forces for the reverse fault (dashed curves), the compaction band (dotted-dashed curves) and the kink fold (solid curves) for varying overburden and assuming an imperfection angle of 2.5° and 5° in a) and b), respectively.

dominant. It remains such between H_E and H_F although the competition is with the compaction band from then on. For depths larger than H_F , the compaction band finally dominates.

4.4.4 The failure-mechanism maps

The comparisons just proposed for two imperfection angles are repeated for small intervals in this angle to construct the graph presented in Figure 4.14. The six points A to F defined above are shown to help the reader to understand the graph construction. Note that the vertical axis is not the burial depth but the burial lithostatic pressure, at mid-depth of the competent region,

4.4. Onset, development and arrest of the kink-fold

normalized by the critical pressure defined in (4.22) which marks the transition between the dominance of the compaction band and the reverse fault for zero imperfection. The solid line initiating from the normalized pressure of one and crossing the graph, marks the boundary of the domain of dominance of these two modes. The upper and the lower regions are the compaction band and the reverse fault domains, respectively. The other curves mark also boundaries between two modes except for the dotted curve in the lower part of the graph. The region below that curve is not accessible since the thickness of the fluid above is not large enough to keep the solid layer fully submerged. The dashed and the dotted-dashed curves mark the competition between the reverse fault and the kink band and between the compaction band and the kink, respectively. The limit between the compaction and the kink domains although convex is approximately diagonal to the graph; the compaction domain being in the upper part. The boundary between the reverse fault and the kink band is more complex and again, approximately, the reverse fault domain is in the lower left quadrant of the graph. Note that the three curves intersect at the same point between points B and F. The three modes have the same least upper bound at this point.

The last task is to decide from these three comparisons mode to mode, on the region of dominance of each. This analysis is presented in Figure 4.15a for three friction angles over the weak interfaces (5, 10 and 15° for the curves numbered I to III) and for 100 layers. The compaction

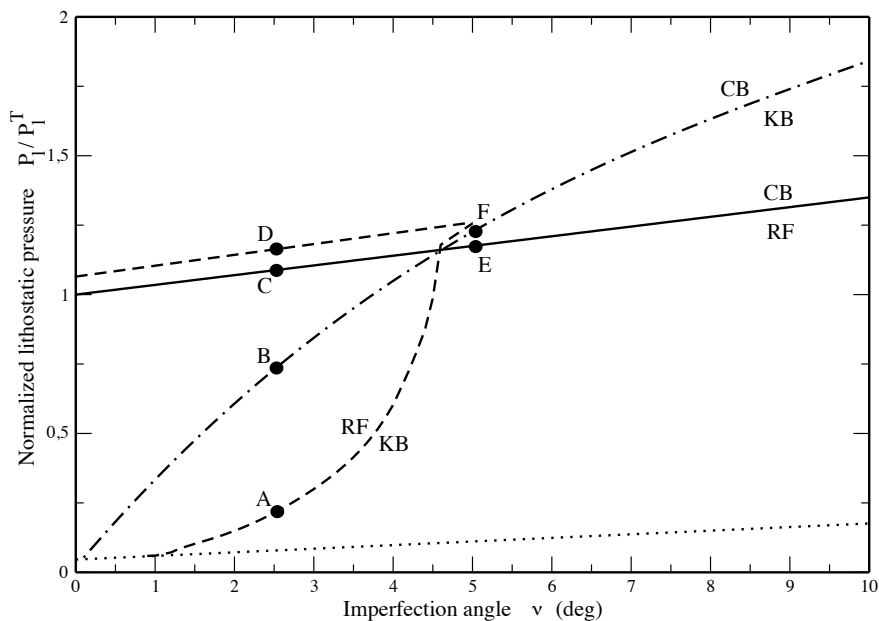


Figure 4.14: The comparisons of the least upper bounds mode by mode, for the reverse fault, the compaction band and the kink fold leads to the construction of regions of dominance in the space spanned by the lithostatic pressure and the imperfection angle.

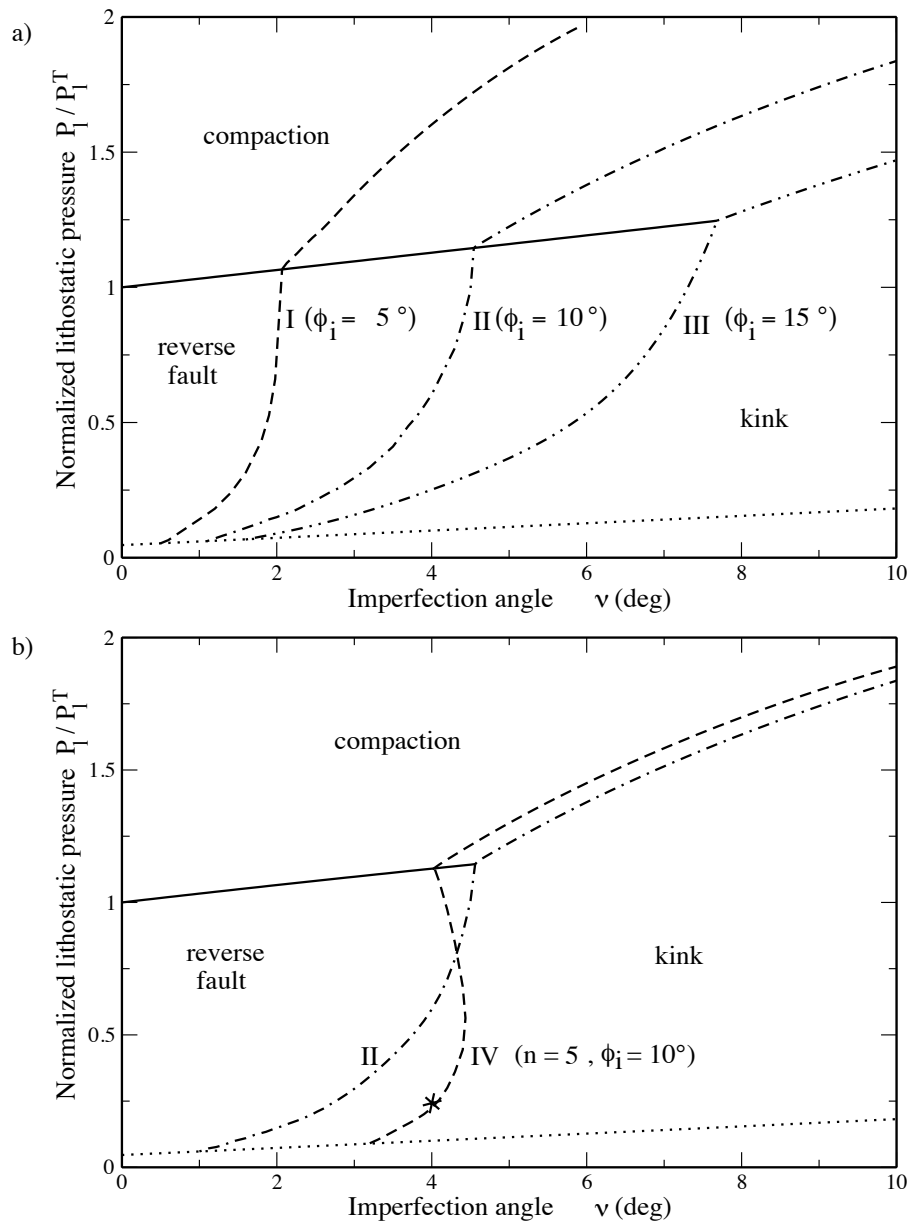


Figure 4.15: The maps of dominant failure-mechanisms in the space spanned by the imperfection angle and the lithostatic pressure. In a), the curves I to III are obtained for a friction angle ϕ_i over the weak interfaces of 5, 10 and 15° and 100 layers. In b), the maps is constructed for 100 layers, curve II (same as in a)) and 5 layers (curve IV). The star defines the initial conditions for the kink discussed in the section on the development.

4.4. Onset, development and arrest of the kink-fold

band domain is in the upper left region of large lithostatic pressures and small imperfection angles. The reverse fault domain is in the lower left area, at lower burial depths and smaller imperfection angles. The kink band dominates the right part of the graph defined for the larger imperfection angles. The size of this domain is very sensitive to the weak interface friction angles and shrinks considerably for 15° .

We are now able to define the conditions for the dominance of the kink band in terms of pressure and imperfection angle. If conditions are selected in the appropriate domain, this mode will develop. It should be remembered, however, that the compaction band region includes also conditions for which the kink band is this slip-enhanced compaction band, only marginally dominated at the onset in the boundary layer in terms of shortening.

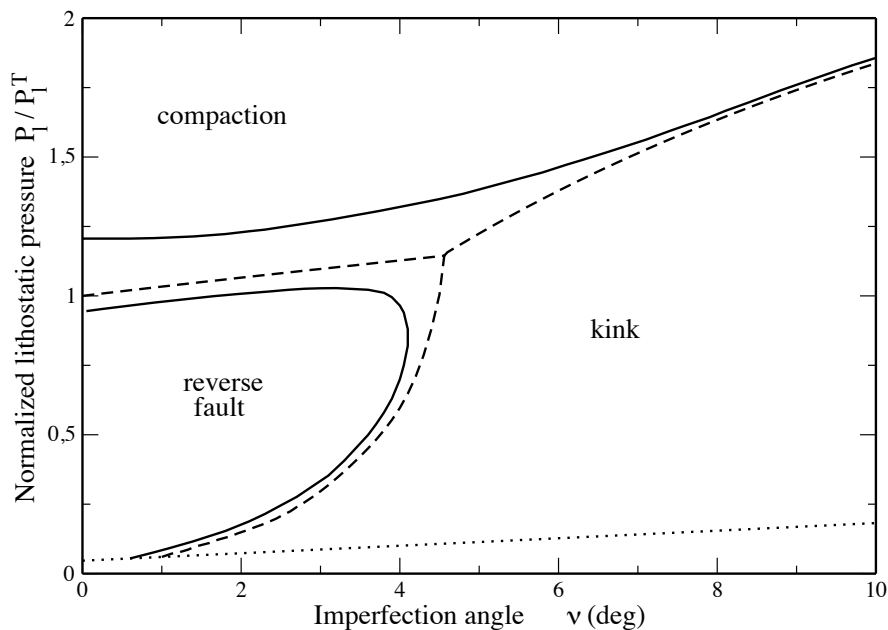


Figure 4.16: The failure-mechanism map based on the shortening of $\tilde{\delta} = 2.5 \times 10^{-5}$, larger than the boundary layer thickness ($\phi_i = 10^\circ$). The dashed curve is curve II in Figure 4.15 obtained for $\tilde{\delta} = 10^{-10}$.

Before developing this idea, let us consider the influence of the number of weak interfaces on the mode selection. The results obtained with 5 layers correspond to curve IV in Figure 4.15b and could be compared with the curve II corresponding to 100 layers. The friction angle ϕ_i is set to 10° for the two sets of results. The domain for reverse faulting is larger for the small number of layers at the shallowest depths (small lithostatic pressure). This trend is reversed for the intermediate pressures and the compaction domain shrinks if the number of layers is reduced. This influence is counter-intuitive since one expects the kink to increase its dominance for larger numbers of layers. This apparent contradiction is again due to the boundary-layer effect where the slip-enhanced compaction band is closer to the compaction band for smaller numbers of

layers.

The influence of the boundary layer on the failure mechanism map is now further explored by comparing the various least upper bounds for a shortening $\tilde{\delta}$ of 2.5×10^{-5} . For that amount of shortening the slip-enhanced compaction band has given place to the kink. Results are presented in Figure 4.16 for 100 layers in the competent region. The dashed curves correspond to the boundaries of the various domains obtained at the onset $\tilde{\delta}$ of 10^{-10} , Figure 4.15a. The main difference between these two sets of results is that the kink domain now extends to the vertical axis, thus even in the absence of any imperfection. This finding is consistent with the dip of the kink band γ which then takes a value of several degrees (Figures 4.9f and 4.11f) and plays the role of the imperfection. Note that the new domain of dominance of the kink is extending more on the compaction band domain than on the reverse fault domain.

4.4.5 Evolution based on the upper bound in tectonic force

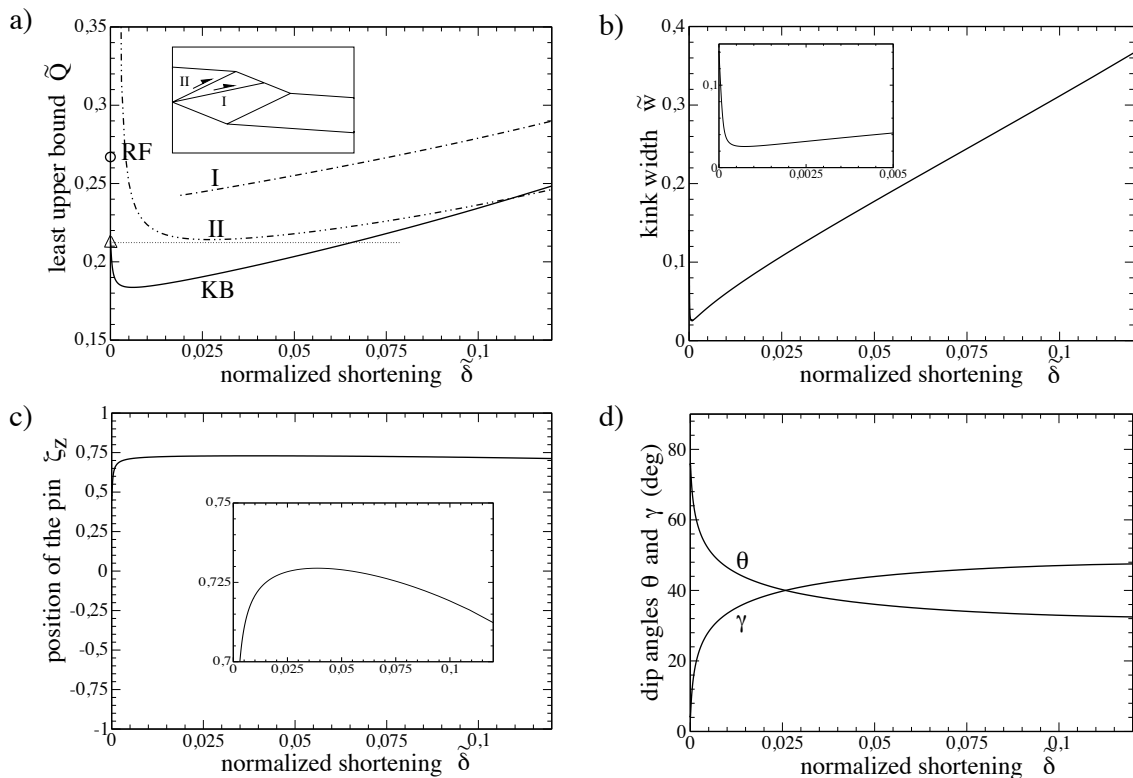


Figure 4.17: The evolution of the kink fold, beyond the onset, in terms of least upper bound, kink width, pin position over the lower hinge, kink dip γ and hinge dip, in a) to d), respectively.

The initial conditions for the results to be discussed are defined by the star in Figure 4.15b and correspond to $(\nu, P_l) = (4^\circ, 0.24P_l^T)$. Curve II marks the relevant boundary between the kink

and the reverse fault regions of dominance. The results for the finite evolution of the kink are presented in Figure 4.17 in terms of the least upper bound, the kink width, the pin position along the lower hinge and the dips of the hinge and of the kink band.

The solid curve in Figure 4.17a is first discussed. It starts at a load marked by the triangle which is indeed below the circle corresponding to the load necessary for the reverse fault. The load decreases drastically, sustains a minimum and rises again, a typical response for imperfection-sensitive structures. During the kink development, the kink width in graph b) decreases first from the values at the onset and then, for a shortening of more than 5×10^{-4} the structure length (see inset), increases linearly, approximately. This decrease in width within the boundary layer in terms of $\tilde{\delta}$ was discussed earlier with Figure 4.11c and 4.12c. The position of the pin in graph c) indicates that the hinges need some compaction even during the development beyond the onset. There is a maximum value attained for a dimensionless shortening of 0.039, see inset, although the decrease for the rest of the development, corresponding to a larger contribution of the compacting mechanism, is marginal. This late increase in the action of compaction could be thought to result from the increase in burial depth due to the finite shortening. It was however observed in paper no 1 where no overburden is accounted for. The effect is thus more likely to be due to the growing width of the kink during its rotation which leads to an increase in the mass contributing to the normal force acting on each weak interface.

Consider now the dip of the kink band γ and of the hinge θ in Figure 4.17d. They are constrained by the relation $\theta + \gamma = \pi/2 - \phi_i$, and show a two-phase evolution. There is first a fast rotation before, say, the point where θ and γ have the common value of 40° . Beyond that point, there is a second period during which the angles remain approximately constant. In this second phase, the kink evolution is marked by its widening.

These results on the development in Figure 4.17 appear to be similar to those found in paper no 1. There are, however, important differences which are worth discussing. The main difference is the conditions corresponding to the minimum in least upper bound. Reches and Johnson (1976) using an Andersonian stress state (two principal stress directions are horizontal and the third is vertical) advocate that the minimum in force coincides with the best orientation of the weak interfaces corresponding to $(\pi/2 - \phi_i)/2$. This criterion was used in paper no 1 and found accurate within an error margin of up to 2° . In the example considered for Figure 4.17, the minimum should be attained accordingly for the shortening of 0.035 approximately, and corresponds to a rotation of the kink band to 40° . It is observed in graph a) that this minimum occurs for 5×10^{-3} , which is thus five times smaller than expected. The kink dip is only 24° at this minimum. This difference between our new findings and the results of paper no 1 cannot be due to the imperfection which essentially set a non-zero initial value to the angle γ . The difference

must be due to the presence of the two fluid layers. The total force which is presented in graph a) is the force necessary to shorten the three regions and not just the solid part. Setting the mass density of the two fluid layers to zero does not change however that verdict. In all cases, the condition for a constant volume below and above are still active. If the assumption of constant volumes is relaxed, the solid region remains at the same height, and the force minimum is indeed at the level found in paper no 1 and corresponding more or less to the value predicted by Reches and Johnson (1976). The difference between this contribution and paper no 1 is thus that we are now working with a closed system and incompressible fluids. The virtual velocity field is thus more constrained in the present contribution. For example, the virtual velocity field is sensitive to the current thickness of the layer below \tilde{h}_b , according to (4.37). Furthermore, the expression for the virtual power due to gravity is now sensitive to the vertical velocity of the lower block, which was zero in the paper no 1.

This influence as well as the one of the burial depth H_a on the kink dip at the minimum compressive force are explored in further details in Kampfer (2010). For thick substratum $\tilde{H}_b = 0.25$, this dip increases by up to 2° for a burial depth changing from zero to $\tilde{H}_a = 2$. Surprisingly, this relation is not monotonic for thin substratum such as $\tilde{H}_b = 0.05$. The dip first increases for shallow overburden with a maximum around $\tilde{H}_a = 0.4$ for all imperfection angles. This dip is varying by up to 2° for an imperfection changing from zero to 10° .

4.4.6 Arrest of kink development

The last point of discussion in this section is the potential arrest of the kink. It is known that kink folds do not accommodate much shortening in nature, typically in regions of fold-and-thrust belts. The kink locks and another failure mechanism, based on a reverse fault, provides the ramp to initiate thrusting.

Various concepts have been put forward to justify the arrest of the kink development and three are discussed. The first is the constant value of the compressive tectonic force. The load at initiation in Figure 4.17a intersects the equilibrium curve for a dimensionless shortening of 0.065 (dotted horizontal line). The kink would develop then unstably from the onset to this shortening and would tend towards this second equilibrium for the same load. The development would then cease because the load is not increasing further (Reches and Johnson, 1976; Collier, 1978). The argument is based on a force control boundary condition which is difficult to justify in nature. Furthermore, that load in our analysis is below the force necessary to initiate a reverse fault so the kink is likely to develop further with an increase in the applied load for a displacement control boundary condition. The second reason often evoked in the same literature to cease the kink development is the critical orientation of the weak interface for which slip is not further possible.

This constraint ($\gamma > \pi/2 - \phi_i$) is never fulfilled here since the virtual velocity construction in paper no 1 and in the present contribution requires: $\theta + \gamma < \pi/2 - \phi_i$. The third reason for the kink locking is based on its geometry. Consider the possibility that the kink band cannot widen and the overall shortening is then accommodated by its rotation. This rotation could exceed the maximum $\pi/2$ so that the kink enters in contact with the left boundary (segment PP' in contact with segment MO in Figure 4.7) stopping further possible shortening with this failure mechanism. The structure would have to select another failure mode. Such locking is often observed in the laboratory but is not captured here for the simple reason that kink widening is permitted. The kink would have to cover the whole structure extent before its rotation would be solicited again to accommodate the shortening.

This scenario is of course possible but at the limit of the validity of our construction. We prefer here to search for the onset of another failure mechanism during the kink development, selecting the reverse fault mode since it provides the ramp for thrusting. Two such reverse faults are considered and illustrated in the inset of Figure 4.17a. The first reverse fault, curve no I, is cutting through the kink. It intersects the rigid back wall at the base of the competent layer and its dip is left as an unknown to be optimized. The solution procedure is rather similar to the one presented in the first part of this contribution and the interested reader is referred to Kampfer (2010) for further information. Fault properties are those of the solid material. The load for this reverse fault is identified in Figure 4.17a with a dotted-dashed curve marked by the roman number I. The values are very large for small shortenings and not presented because the reverse fault dip is then constrained by the small thickness of the kink. The curve increases with shortening in a rather parallel way to the load for the kink fold. This reverse fault does not have the chance to initiate during the kink development. The second reverse fault considered is along the upper hinge of the kink. Its associated load is the dotted-dashed curve labelled II in Figure 4.17a. This load is obtained with the assumption that the cohesion within the reverse fault is zero. In that instance, we do observe that beyond the dimensionless shortening of approximately 0.11, the reverse fault II starts to dominate. Note that the weakening necessary for that change in dominant mode was not used for the kink development.

It thus appears that the proposed prototype does not have the appropriate features to lock the kink during its development and to favour the onset of thrusting. The damage of the kink hinges, which would prevent the kink widening and favour its rotation towards a locking orientation are certainly worth further investigations.

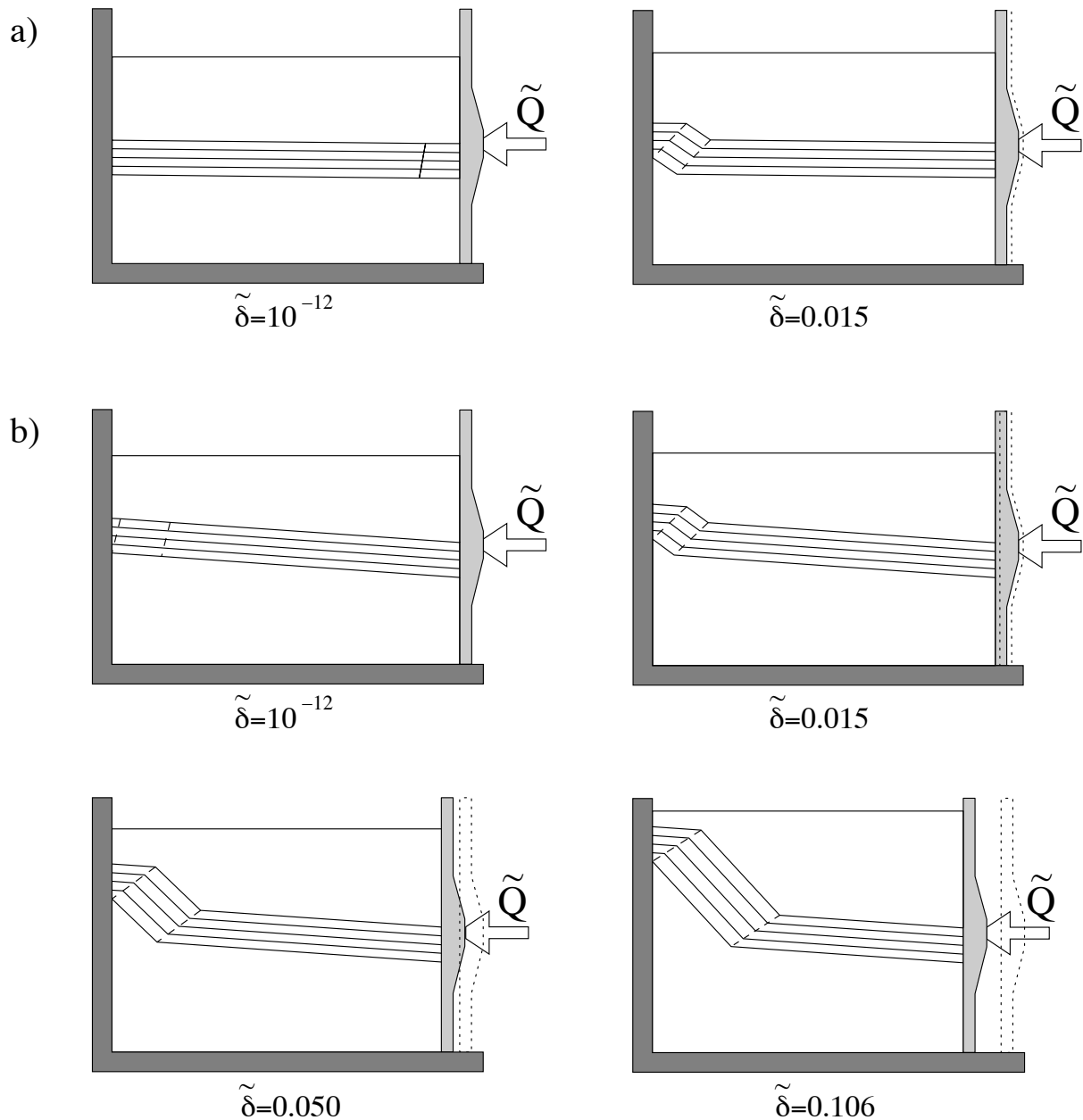


Figure 4.18: Different stages in the development of the kink fold. In a), the imperfection is small (0.6°) and the failure mode initiates as a compaction band to the right and migrates to the left once it develops as a kink. In b), the imperfection is 4° and the failure mode initiates and develops in the left part of the domain with first, the rotation of the kink band and second, the thickening. Only four layers are shown, although the calculations were done with 100; the fluid layers thicknesses are $H_a = H_b = 250m$, other data are found in Table 4.1.

4.5 Conclusion

The first objective was to study the influence of the burial depth and of the imperfection angle on the onset and the development of a kink fold. The second objective was to define the range in these two parameters for which the kink would dominate the reverse fault and the compaction band at the onset.

The prototype considered consists of three parts, the top and bottom occupied by inviscid fluids. The central region is composed of competent layers separated by weak interfaces necessary to ensure easy slip during kinking. The first two modes of failure, the reverse fault and the compaction band, do not make use of these weak interfaces and appear at different locations within the competent layer. The reverse fault is to the left and the compaction band to the right, corresponding to the regions with lowest and greatest burial depth, respectively, in view of the tilt introduced as an imperfection. An analytical expression is provided to express the critical lithostatic pressure which marks the transition in dominant failure mode from the reverse fault to the compaction band, as the burial depth is increased with zero imperfection. The force for compaction band is marginally influenced by the imperfection angle whereas the force for reverse fault is rather sensitive, with a decrease by 10% of its least upper bound for an increase of the imperfection angle up to 10° . These two failure modes are compared with the kink-fold at the onset in terms of least upper bound to decide on the dominant mechanism. The results are presented in maps spanned by the burial depth or lithostatic pressure and the imperfection angle. The sensitivity of the various domain boundaries to the weak interface friction and to the number of layers is explored. Increasing the weak interface friction leads to a marked reduction in the kink dominant region against both the compaction band and the reverse fault. It should be noted that the kinematics of the kink at its onset is often characteristic of a slip-enhanced compaction band. Its thickness is close to zero, although slip along the weak interfaces is contributing to the kinematics dominated by compaction along the two hinges. This hybrid failure mechanism is also found to the right of the beam where the compaction bands are detected. It is only beyond a small amount of shortening (order of 10^{-6} the structure length) that the failure mode starts to thicken and migrates suddenly to the left of the competent layer to develop as a kink, as illustrated in Figure 4.18a. This proposed unifying approach to the onset of compaction band and kinks prompts us to modify the failure-mechanism maps where the comparison between the compaction band and the kink is done just beyond the onset, once the failure mode has revealed its true nature. The kink mode is then found to increase its range of dominant conditions versus the compaction band and the reverse fault, including a range in burial depth for a zero imperfection.

The kink fold development is rather reminiscent of the results obtained in paper no 1. The least upper bound in the tectonic force decreases sharply first although no cusp is monitored in

the load-shortening relation since no stored elastic energy is accounted for. These cusps could be present in the experimental tests on paper cards by Weiss (1968) and are discussed in Wadee and Edmunds (2005) for their experiments on similar material. After this sharp drop, the load-shortening relation presents a minimum followed by an increase for continuing shortening. The kink dip increases sharply beyond the onset and then remains approximately constant. There is thus a two-phase development, characterized by first the kink rotation and, second, the kink widening, as illustrated in Figure 4.18 by the two first graphs and then by the last two, respectively. There is however an important difference between the present results and those of paper no 1, concerning the minimum value in the tectonic force. It is shown that the rotation of the weak interfaces to their most favourable orientation for slip, based on a local stress criterion, does not correspond to the minimum tectonic force. This critical orientation proposed by Reches and Johnson (1976) and found rather accurate in paper no 1 is not observed here because of the hypotheses of closed system and fluid incompressibility which influence the virtual power due to gravity of the solid region. The arrest of the kink development is also studied. The classical arguments for the kink locking, which is observed in nature and experimentally, do not apply. The main reason is the kink band widening in the second phase of development which is favoured to its rotation. The possibility for a second failure mechanism in the form of a reverse fault is further explored. It is shown that no reverse fault could be initiated unless weakening along the hinges is assumed. This weakening could prevent the kink widening and promotes its rotation and deserves further attention.

There are several possibilities to improve this conceptual model of kink folds, the first direction being to capture the discontinuous changes in the fold's curvature observed in the field (Bazalgette, 2005). The continuous variation of the fold curvature is well captured with plasticity, the small-scale fractures providing the basic deformation mechanism, and with the overall flexure associated to a buckling instability (Guiton et al., 2003). The other extreme case is the sharp curvature change, typical of the chevron fold. Of more interest is the intermediate case where the curvature results from a series of kinks with immobile hinges and minor rotations of the band. The first kink is the widest and the successive new kinks appear within the band of the currently active failure system. This complex evolution requires immobile hinges possibly due to damage. The second direction of research is on fault-propagation folds. Field outcrops, such as in the Tamzergout valley (High Atlas, Morocco; Bazalgette 2005), reproduce such folding kinematics on a deca- to hecto-meter length scale and could provide the grounds to study the fractures and the layers rotation ahead of the advancing fault. For these two research directions, it seems necessary to concentrate first on the damage and the fracture development within layered sedimentary rocks, starting very likely from the seminal works of Price (1966) and Hobbs

(1967) discussed at length by Mandl (2005).

Acknowledgements: Bertrand Maillot (University of Cergy-Pontoise) is thanked for his numerous constructive remarks which contributed to the preparation of this manuscript. This work is part of the first author's doctoral thesis which is supported by Shell, Rijswijk, The Netherlands. Authorization to publish was granted by Shell, Rijswijk, The Netherlands.

References

- Ashby, M.F., 1972. A first report on deformation-mechanism maps. *Acta Metallurgica* 20, 887-97.
- Bart-Smith, H., Hutchinson, J.W., Fleck, N.A., Evans, A.G., 2002. Influence of imperfections on the performance of metal foam core sandwich panels. *International Journal of Solids and Structures* 39, 4999–5012.
- Bazalgette, L., 2005. Relations plissement-fracturation multi-échelle dans les multicouches sédimentaires du domaine élastique-fragile. Thèse de doctorat, Université de Montpellier II, Mémoire géosciences Montpellier, v.36.
- Biot, M.A., 1965. Theory of similar folding of the first and second kind. *Geological Society of America Bulletin* 76, 251–258.
- Biot, M.A., 1965. Further development of the theory of internal buckling of multilayers. *Geological Society of America Bulletin* 76, 833–840.
- Budiansky, B., Fleck, N.A., 1994. Compressive kinking of fiber composites: a topical review. *Applied Mechanics Review* 47, part 2, S246—S250.
- Buiter, S.J.H., Babeyko, A.Y., Ellis, S., Gerya, T.V., Kaus, B.J.P., Kellner, A., Schreurs, G. and Yamada, Y., 2006. The numerical sandbox: comparison of model results for a shortening and an extension experiment, in *Analogue and numerical modelling of crustal-scale processes*, edited by Buiter, S.J.H. and Schreurs, G. pp. 29-64, London Geological Society Special Publication.
- Cubas, N., Leroy, Y.M. and Maillot, B., 2008. Prediction of thrusting sequences in accretionary wedges. *Journal of Geophysical Research* 113, B12412, doi:10.1029/2008JB005717.
- Collier, M., 1978. Ultimate locking angles for conjugate and monoclinical kink bands. *Tectonophysics* 48, T1–T6.
- Fortin, J., Stanchits, S., Dresen, G., Guéguen, Y., 2006. Acoustic emission and velocities associated with the formation of compaction bands in sandstone. *Journal of Geophysical Research* 111, B10203.
- Guiton, M.L.E., Leroy, Y.M. and Sassi, W., 2003. Activation of diffuse discontinuities and folding

- of sedimentary layers, *Journal of Geophysical Research* 108, B4, 2183.
- Hobbs, D.W., 1967. The formation of tension joints in sedimentary rocks: an explanation. *Geological Magazine* 104, 550–556.
- Issen, K.A., Rudnicki, J.W., 2001. Conditions for compaction band in porous rock, *Journal of Geophysical Research* 105, B6, 21529–21536.
- Kampfer, G., 2010. Kink folds and mode-I fractures in carbonate rocks. Doctoral thesis, Ecole Normale Supérieure, in preparation.
- Lankford, J., 1995. Compressive failure of fibre-reinforced composites: buckling, kinking, and the role of the interphase. *Journal of Materials Science* 30, 4343–4348
- Mandl, G., 2005. Rock joints, the mechanical genesis. Springer-Verlag, Berlin and Heidelberg.
- Maillot, B. and Leroy, Y.M., 2003. Optimal dip based on dissipation of back thrusts and hinges in fold-and-thrust belts. *Journal of Geophysical Research* 108, B6, 2320–2336.
- Maillot, B. and Leroy, Y.M., 2006. Kink-fold onset and development based on the maximum strength theorem. *Journal of the Mechanics and Physics of Solids* 54, 2030–2059.
- Nestorović, M.D., Triantafyllidis, N., 2004. Onset of failure in finitely strained layered composites subjected to combined normal and shear loading. *Journal of the Mechanics and Physics of Solids* 52, 941–974.
- Price, N.J., 1966. Fault and joint development in brittle and semi-brittle rocks. Pergamon Press, Oxford.
- Rosen, B.W., 1965. Mechanics of composite strengthening. In: *Composite Materials* pp. 37-75. American Society of Metals, Metals Park, OH.
- Reches, Z. and Johnson, A.M., 1976. A theory of concentric, kink and sinusoidal folding and monoclinical flexuring of compressible, elastic multilayers. VI. Asymmetric folding and monoclinical kinking. *Tectonophysics* 35, 295–334.
- Rudnicki, J.W. and Rice, J.R., 1975. Condition for the localization of deformation in pressure-sensitive dilatant materials. *Journal of the Mechanics and Physics of Solids* 23, 371–394.
- Salençon, J., 1974. *Théorie de la plasticité pour les applications à la mécanique des sols*. edited by Eyrolles, Paris, (English translation : *Applications of the theory of plasticity in soil mechanics*, John Wiley & Sons Ltd, Chichester, 1977).
- Salençon, J., 2002. *De l'élasto-plasticité au calcul à la rupture*. Editions École Polytechnique, Palaiseau and Ellipses, Paris.
- Sciamanna, S., Sassi, W., Gambini, R., Rudkiewicz, J.L., Mosca, F., and Nicolai, C., 2004. Predicting hydrocarbon generation and expulsion in the Southern Apennines Thrust Belt by 2D Integrated Structural and Geochemical Modeling: Part I - Structural and thermal evolution.

-
- In: Deformation, fluid flow, and reservoir appraisal in foreland fold and thrust belts, edited by Swennen, R., Roure, F., Granath, J.W., pp.51-67, A.A.P.G. Heldberg series 1.
- Souloumiac, P., Leroy, Y.M., Krabbenhøft, K. and Maillot, B., 2008. Predicting stress in fault-bend fold by optimization, submitted for publication.
- Suppe, J., 1983. Geometry and kinematics of fault-bend folding. *American Journal of Sciences* 283 (7), 684–721.
- Sutcliffe, M.P.F., Fleck, N.A., 1993. Effect of geometry on compressive failure of notched composites. *International Journal of Fracture* 59, 115–132.
- Vogler, T.J., Hsu, S.-Y., Kyriakides, S., 2001. On the initiation of kink bands in fiber composites: Part II. analysis. *International Journal of Solids Structures* 38, 2653–2682.
- Wadee, M.A., Edmunds, R., 2005. Kink band propagation in layered structures. *Journal of the Mechanics and Physics of Solids* 53, 2017–2035.
- Weiss, L.E., 1968. Flexural-Slip folding of foliated model materials. In: Baer, A.J., Norris, D.K., (Eds.), Geological Survey of Canada, GSC paper 68-52, pp. 294–333.
- Zoetemeijer, R. and Sassi, W., 1992. 2D reconstruction of thrust evolution using the fault-bend fold method. In: Thrust tectonics, edited by K. McClay, pp. 133-140, London Geological Society Special Publication.

Chapter 5

The competition between fault-propagation folding and thrusting based on the maximum strength theorem

G. Kampfer and Y.M. Leroy

Laboratoire de Géologie, CNRS,
École Normale Supérieure, Paris, France.

In final preparation before submission

5.1 Abstract

The two concepts, mechanical equilibrium and maximum material strength, are associated to the geometrical constructions of folds and thrusts to decide on the dominance of one of these two modes of deformation, classical in fold-and-thrust belts and accretionary wedges. The theory used to support this statement is the maximum strength theorem, for cohesive and frictional materials, which has its origins in the limit analysis developed initially in soil mechanics. It is the classical geometrical construction of the fault-propagation fold (Suppe and Medwedeff, 1984), with the addition of a fluid-like overburden, which is considered to illustrate our proposition. The fault-propagation fold (FPF) is composed of a kink fold with migrating hinges on top of the region where the ramp propagates. These hinges are assigned frictional properties and small values of the friction angle are necessary to ensure that the FPF development is not stopped by the onset of thrusting. The amount of shortening at the transition from folding to thrusting is mildly

influenced by the thickness of the overburden unless the fold can pierce the weak overburden during its development. It is also shown that the ramp of the thrust and the ramp of the fold, the former extending the latter, have different dips if they are assigned different friction coefficients. The smaller friction coefficient is typical of the fold ramp because of accumulated damage and its dip is larger than the dip predicted for the thrust ramp crossing the pristine rock.

5.2 Introduction

Most of the practical constructions of folds in structural geology relies on sets of simple geometrical rules following the seminal work of Suppe (1983) on fault-bend folds. These constructions are easily modified to account for specific field observations and are not computer intensive. This efficiency and simplicity are certainly not features of the numerical methods necessary to construct folds in the presence of ramps such as the finite-element method (eg. Braun and Sambridge, 1994) or the discrete element method (Hardy and Finch, 2007). The methodology advocated by the authors is that a compromise could be reached between these two extreme approaches thanks to the application of the maximum strength theorem. To prove our claim, it is proposed to study the geometrical construction of the fault-propagation fold (Suppe and Medwedeff, 1984; 1990). It is shown that the fault-propagation fold development is interrupted by the onset of thrusting thrust at a critical shortening which can be predicted based on the geometrical and the material properties. This transition signals the beginning of the late-stage evolution by transport on the flat discussed by Mercier et al. (1997).

The maximum strength theorem corresponds to the kinematics approach of the limit analysis developed initially for predicting bearing capacities of civil engineering structures. This theorem relies on a weak form of the equilibrium equations obtained by integration over the studied structure of the local equilibrium equations multiplied by a virtual velocity field. This theorem requires also the existence of the strength domain, convex in the appropriate stress space, which contains the set of admissible stresses that can be sustained by a given material. The case of frictional and cohesive materials is considered here and the strength domain is bounded by the Coulomb criterion. These two concepts, mechanical equilibrium and maximum material strength, permit to bound by above the internal dissipation, and to obtain an upper bound to the force applied to the structure of interest. The main difference between the maximum strength theorem adopted here, following Salençon (1974, 2002), and the more classical approach in soil mechanics is that no reference is made to a complete plasticity theory, leaving aside the challenge to interpret the rate of deformation obtained from the virtual velocity field as a plastic strain rate.

This maximum strength theorem was applied to kink folds by Maillot and Leroy (2006) and Kampfer and Leroy (2009) not only at the onset of the structure failure but during the whole development of the structure. The upper bound to the applied force is minimized by selecting the optimum virtual velocity fields and the optimum dip and width of the kink band as well as its position in the compressed laminated structure. The same theorem was applied by Cubas et al. (2008) who could predict the complete development of a sequence of forward thrusts at the front of accretionary wedges. These results are obtained for simple geometries which are inspired by the numerous geometrical constructions of thrusts and folds found in the literature. The new idea

of this contribution is to show that any geometrical construction of folding could be considered for the application of the maximum strength theorem and the now classical example of the fault-propagation fold (FPF) proposed by Suppe and Medwedeff (1984) is considered for that purpose. This geometrical construction explains the often observed steep limb close to the propagating fault. Two sets of rules are proposed for the construction of this asymmetric fold (Jamison, 1987; Suppe and Medwedeff, 1990) and the choice is made here to assume conservation of bed thickness and bed length. The fold is characterized by a kink fold, bounded by several propagating hinges, ahead of the region where the fault propagates. It is shown here how the non-material propagating velocities are determined with the help of Hadamard's jump condition. Also, restrictions on the geometry of the FPF based on the frictional properties of the hinges are established.

This initial work of Suppe and Medwedeff (1984) has attracted a lot of attention from the structural geology community and the following review is certainly not complete. Jamison (1987) discusses the geometrical rules to be adopted by comparing the final fold geometries and field examples. Chester and Chester (1990) extended the FPF construction to start from a ramp of finite length. The implications of the details of the geometry of the FPF to position hydrocarbon traps are discussed by Mitra (1990). Mosar and Suppe (1992) propose to include simple shear within the internal layers of the FPF resulting in a rotation of the kink fold ahead of the propagating fault. The generalization to 3D of the FPF construction with lateral variations in the fault geometry and slip rates was proposed by Wilkerson and Medwedeff (1991). These 3D effects due, for example, to variations in the efficiency to activate the décollement, includes en-échelon folds separated by tear faults, as in the South Atlas front of Algeria and Tunisia, still described with the FPF geometrical construction (Outtani et al., 1995). Salvini and Storti (2001) studied the consequences of the migration of the hinges in terms of local history of the activated deformation mechanisms preparing the grounds for a comparison between field observations and theoretical predictions.

The paper contents are as follows. Section 2 is devoted to the presentation of the geometrical construction of the fault-propagation fold. The maximum strength theorem is presented in Section 3, with the simple example of a rigid block pushed-up an inclined ramp, before it is applied to the thrusting through and to the development of the FPF. Analytical expressions are provided for the upper bounds to the forces necessary for thrusting and folding and the theorem ensures that the smaller of two loads determines which deformation mode dominates. This competition is explored in Section 4 where the upper bound to the force for thrusting is first minimized by selecting the appropriate ramp and back-thrust dips to obtain the least upper bound. The upper bound to the force for the fold is the least, since there are no free degree of freedom in the ge-

ometrical construction. Section 4 continues with a comparison of the two least upper bounds to decide on the dominant mode of deformation. In particular, it is shown that the friction angle of the fold hinge is the key parameter to warrant some finite amount of shortening before the development of the FPF is interrupted by the onset of thrusting.

5.3 The geometry and the velocity field of the FPF

The 2D structure includes an initially horizontal, competent layer $A''OG'B''$ of length L , thickness H_s and material density ρ_s which rests in equilibrium, Figure 5.1a. The surface OG' is weak along GG' which acts as a décollement. Shortening is initiated by displacing the back-wall towards the left. The application of the maximum strength theorem provides an upper bound to the force Q necessary to displace this wall. An inviscid fluid-like material of density ρ_f is on top of the competent layer to account for the effect of burial. This second layer has the initial thickness H_f . The fluid is connected to an external reservoir of infinite extent, illustrated on the left-hand side of Figure 5.1a, so that the fluid-layer thickness H_f remains constant during the compression. The objective of this section is to describe the geometry of the FPF development. Further insight on this geometry is gained by considering the velocity field associated to this construction in the second part of this section.

5.3.1 The geometrical construction

At the onset, a ramp of zero length dipping at the angle γ_B is considered at point G . The material to the right of this point, in the back-stop, is displaced to the left by the increasing shortening δ . The left boundary of the back-stop is the hinge \mathcal{B} , Figure 5.1b. This hinge is dipping at the angle θ_B which is half the complementary angle of γ_B ($2\theta_B = \pi - \gamma_B$). This assumption on the angle θ_B is classical in the geometrical constructions of folds and implies the conservation of the thickness of the beds crossing the hinge. Material points coming from the back-stop and crossing the hinge \mathcal{B} are entering the region $GBB'RS$ which is the sub-domain no 1 of the hanging wall. Note that all the geometrical attributes defined so far are summarized in Table 5.1.

The development of the fold is marked by the propagation of the ramp with the same, constant dip γ_B . Point S in Figure 5.1b marks the limit of the material initially on the décollement now found on the ramp of the hanging wall. The dotted line SS'' dipping at θ_B was initially on the hinge \mathcal{B} and is bounding to the left all the material coming from the back-stop. The selection of θ_B to conserve bed thicknesses means also that the distance SG is equal to the shortening δ . The ramp has propagated further than this distance and its tip is now at point P . The distance of this point to the bottom line OG' is h . The bed passing through point P is marked by the dashed

5.3. The geometry and the velocity field of the FPF

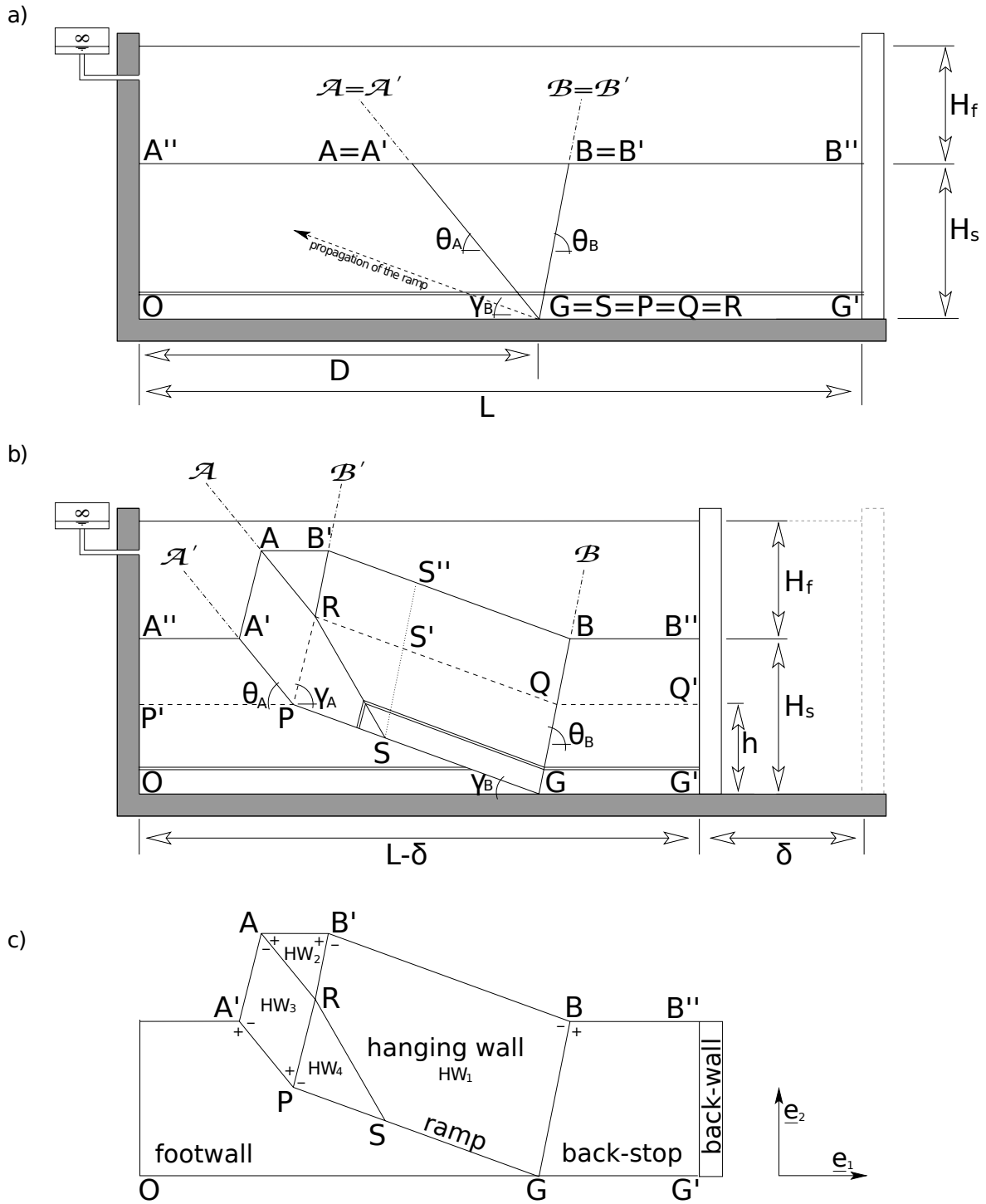


Figure 5.1: The geometry of the structure at the onset a) and during the development of the fault-propagation-fold, b). Definition of the adopted terminology and of the four sub-domains of the hanging wall, c).

Symbol	Fault-propagation fold	value	unit
δ	Shortening	var.	m
h	Current height of ramp tip P	var .	m
γ_B	Ramp dip	var.	deg
θ_B	Hinges \mathcal{B} and \mathcal{B}' dip	var.	deg
γ_A	Interface PR dip	var.	deg
θ_A	Hinges \mathcal{A} and \mathcal{A}' dip	var.	deg
ϕ_H	Friction angle of all hinges	var.	deg
ϕ_B	Friction angle of the bedding	10.	deg
	Thrust		
γ_T	Thrust PP' dip	var.	deg
θ_{Tu}	Upper back-thrust dip	var.	deg
θ_{Tl}	Lower back-thrust dip	var.	deg
ϕ_s	Friction angle of competent layer	30.	deg
	Common properties		
L	Initial length of structure	1500	m
H_s	Thickness of competent layer	250	m
H_f	Thickness of fluid-like layer	var.	m
g	gravity acceleration	9.81	m/s^2
ρ_s	Material density for solid layer	2500.	kg/m^3
ρ_f	Material density for fluid-like layer	2000.	kg/m^3
ϕ_i	friction angle of a generic interface		
ϕ_R	friction angle of ramp GP	20	deg
ϕ_D	friction angle of décollement GG'	10	deg

Table 5.1: Material properties and geometrical characteristics of the fault-propagation fold and of the thrust. The interfaces and hinges cohesions are not indicated; they are denoted by the letter C and the same subscript as for the friction angle in the text. The data which are varied in the analysis are indicated as "var."

line in Figure 5.1b. Material points above and below this line have different kinematics. Region $P'PRS'S''B'AA'A''$ deforms in a kink mode by the propagation of hinges. Hinge \mathcal{A}' is dipping at θ_A an angle chosen to be half the dip of the kink band $PRAA'$, a choice made again to preserve bed thickness ($2\theta_A = \pi - \gamma_A$). Hinges \mathcal{A} and \mathcal{B}' are parallel to hinges \mathcal{A}' and \mathcal{B} , respectively.

This geometry is discussed in further details by computing the distance h and the angle γ_A . They are found by application of the rule of bed length conservation, a fundamental assumption in this construction. The conservation of the bed length passing through the tip of the fault imposes that its current length is identical to its initial length:

$$PR + RQ = PQ + \delta . \quad (5.1)$$

The distance PQ is found by studying the triangle PGQ :

$$PQ = \frac{h}{\sin \gamma_B} . \quad (5.2)$$

Conservation of bed thickness implies that the distance of bed PR to point S and the distance of bed RS' to point S are identical to h . Consequently, the triangle PRS is equilateral with principal summit at P and the distance PR reads

$$PR = \frac{h}{\sin(\gamma_A + \gamma_B)} , \quad (5.3)$$

where γ_A is the dip of the kink band $PRAA'$, the angle yet undetermined. The distance RQ is obtained from the analysis of the trapeze $PGQR$ of height h

$$RQ = h \left(\frac{1}{\sin \gamma_B} - \frac{\cos(\gamma_A + \gamma_B/2)}{\sin(\gamma_A + \gamma_B) \cos(\gamma_B/2)} \right) . \quad (5.4)$$

Combining (5.2) to (5.4) in (5.1) provides

$$h = \delta \frac{\sin \gamma_B \sin(\gamma_A + \gamma_B)}{\sin(\gamma_A + \gamma_B) - \sin \gamma_B} . \quad (5.5)$$

It is now proposed to compute RQ from the sum of $RS' + S'Q$, the distance $S'Q$ being equal to δ . The distance RS' is found from the triangle $RS'S$ noting that RS is bisecting the angle $\widehat{PRS'}$

$$RS' = h \frac{\sin(\gamma_A/2)}{\cos(\gamma_B/2) \cos(\frac{\gamma_A + \gamma_B}{2})} . \quad (5.6)$$

This second expression for RQ is used in the conservation of bed length relation (5.1) which becomes independent of δ and such that every term is proportional to h . The elimination of the scalar h from this modified equation provides the definition of the angle γ_A in terms of γ_B

$$\frac{1}{\sin \gamma_B} = \frac{1}{\sin(\gamma_A + \gamma_B)} + \frac{\sin(\gamma_A/2)}{\cos(\gamma_B/2) \cos(\frac{\gamma_A + \gamma_B}{2})} . \quad (5.7)$$

This is an implicit equation and the non-trivial solution γ_A for the kink band dip which is independent of the shortening. It is found by numerical means. The dip of the kink ahead of

the propagating fault is thus fully determined by the knowledge of the ramp dip, as shown in Figure 5.2, with the scale on the right-hand side of the graph. The kink is overturned on the segment $A''A'$ ($\gamma_A = 180^\circ$) for a flat ramp ($\gamma_B = 0$) and this angle γ_A decreases to zero for a ramp dip increasing to 60° , the maximum value of interest. The kink band dip would be vertical for $\gamma_B = 24.5^\circ$, approximately.

The knowledge of height h in (5.5) yields also the propagation ratio k

$$k \equiv \frac{PG}{SG} = \frac{\sin(\gamma_A + \gamma_B)}{\sin(\gamma_A + \gamma_B) - \sin(\gamma_B)} . \quad (5.8)$$

where PG is the total length of the fault and $SG = \delta$, the length of the part of the ramp where the material was initially on the décollement. This ratio is constant during the FPF development and fully determined by the knowledge of the ramp dip, since γ_A is a function of γ_B . This relation between k and γ_B is presented in Figure 5.2 (axis on the left-hand side of the graph). The ratio varies from the value of 1.5 to infinity for γ_B varying from zero to 60° .

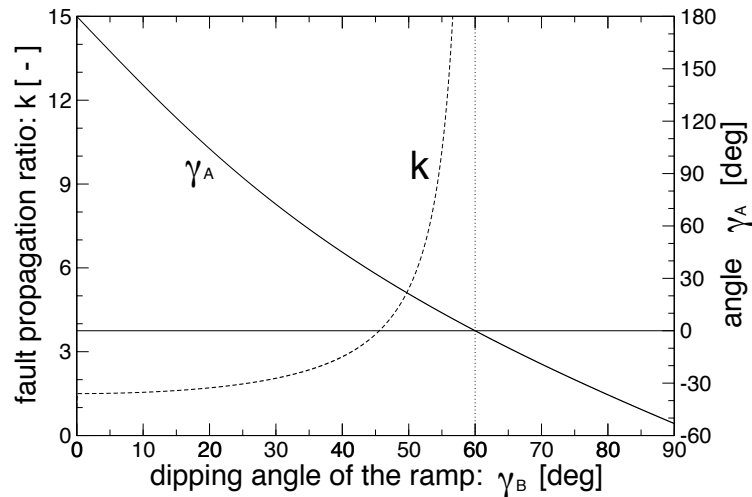


Figure 5.2: The dip γ_A of the kink ahead of the propagating fault and the propagation ratio $\frac{PG}{SG}$ as a function of the ramp dip γ_B

5.3.2 The velocity field

The objective is now to complement our understanding of this geometrical construction by describing the velocities of the four sub-domains of the hanging wall numbered from 1 to 4, Figure 5.1c. The difficulty is the relation between the non-material velocity of the propagating hinges and the material velocities of the four sub-domains. These relations are established with the help of Hadamard's jump condition explored in Appendix 1, generalizing the velocity analysis of Hardy (1997).

The back-stop has the constant velocity $\underline{U}_{BS} = -\dot{\delta}\underline{e}_1$ corresponding to the sliding of this material region over the décollement. Note that the only time scale of this problem is related to the rate of shortening $\dot{\delta}$. Region 1 in the hanging wall has a velocity of same magnitude $\dot{\delta}$ because there is conservation of fluxes (or bed thickness according to the geometrical rules) through the hinge \mathcal{B} . This velocity is uniform in sub-domain no 1 and parallel to the growing ramp SG .

The norm of this velocity could also be found by application of Hadamard's jump condition which is now summarized. The hinges are considered as singular surfaces of order 1 so that the displacement is continuous but the transformation gradient is not. A generic hinge is presented in Figure 5.3 where its normal is oriented by the angle β . Note that β and all the angles to be introduced in this section are measured from the horizontal direction (defined by the vector \underline{e}_1) and are positive in the anti-clockwise sense of rotation. The normal \underline{N} to the hinge points to the + side of the domain which is yet undisturbed (undeformed). The speed of propagation of this hinge is $U_N \underline{N}$ and the sweeping through the + region leads to the deformation in a simple shear mode of intensity marked by the angle s , defined in the - region, Figure 5.3. This angle is determined from the measurements of the dips of the micro-structure on the two sides of the hinges, denoted ψ^+ and ψ^- . This micro-structure is presented in Figure 5.3 by a network of two sets of parallel, dotted lines on each side of the discontinuity. For each network, one of the two sets of lines would correspond typically to the sedimentary bedding directions. The relation between the four angles just introduced is

$$\tan s = \frac{\sin(\psi^+ - \psi^-)}{\cos(\beta - \psi^-) \cos(\beta - \psi^+)}, \quad (5.9)$$

and is valid as long as the two sets of markers of interest are not parallel to the hinge.

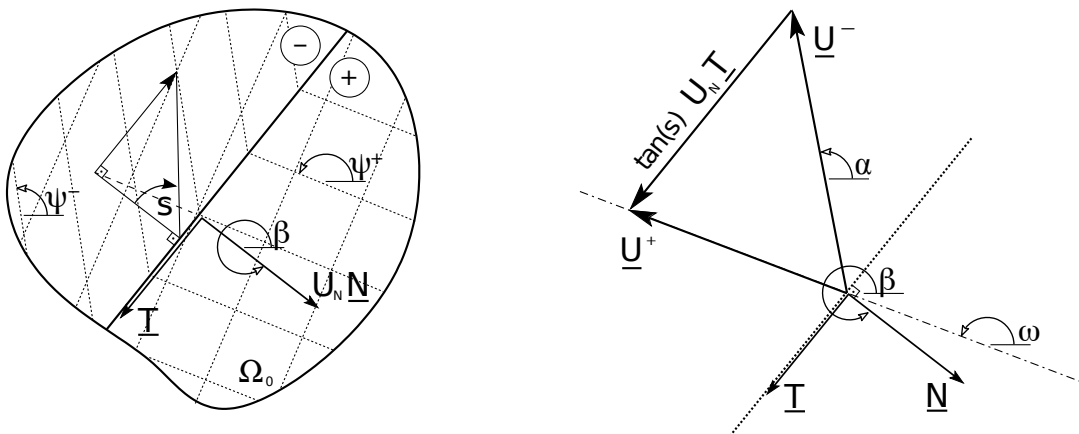


Figure 5.3: The basic mode of deformation in a fault-propagation fold is in simple shear and results from the propagation of a hinge.

The velocities in the two regions separated by the hinge are oriented in the directions dipping at ω and α , and have the norm U^+ and U^- , respectively. Hadamard's jump condition for this simple shear mode of deformation stipulates that the jump in the velocity field is $\tan s \underline{T} U_N$ where \underline{T} is the tangent vector to the hinge (such that $\{\underline{T}, \underline{N}\}$ is a direct basis). This relation is shown in the hodogram construction of Figure 5.3. The application of the law of sines to this triangular construction provides

$$\frac{U_n \tan(s)}{\sin(\alpha - \omega)} = \frac{U^+}{\cos(\beta - \alpha)} = \frac{U^-}{\cos(\beta - \omega)}, \quad (5.10)$$

which is valid if the two material velocities are not parallel to the hinge.

It is this relation which is now applied to the hinge \mathcal{B} and which will be used repeatedly in the rest of this section. Hinge \mathcal{B} dips at θ_B ($\beta = 2\pi - \gamma_B/2$) and separates two regions, the + regions being the back-stop since it is undeformed. The velocities on the two sides of \mathcal{B} are oriented by the angle $\omega = \pi$ and $\alpha = \pi - \gamma_B$. The bedding has the orientation $\psi^+ = \pi$ and $\psi^- = \pi - \gamma_B$ providing the value of $\tan s = 2 \tan(\gamma_B/2)$ by application of (5.9). This information inserted in the two equations of (5.10) provides

$$U^- = U_{HW1} = \dot{\delta}, \quad U_{N\mathcal{B}} = \dot{\delta} \cos \frac{\gamma_B}{2}. \quad (5.11)$$

These results were partly known but the calculation provides a first, simple application of Hadamard's jump condition.

The same jump condition is now applied to the hinges \mathcal{A}' , \mathcal{A} and \mathcal{B}' . The definitions of the + and - regions for each discontinuity are provided in Figure 5.1c. The information required for or obtained from the application of (5.9) and (5.10) is summarized in Table 5.2.

Hinge \mathcal{A}' separates the kink band, region no 3, from the footwall which is yet undisturbed. The bedding is tilted at the angle γ_A and flat in these two regions, respectively. The intensity of shear is thus $\tan(s) = -2 \tan(\gamma_A/2)$. The velocity of the foot-wall is zero so that the velocity of the minus region must be $U^- \equiv U_{HW3} = 2 \tan(\gamma_A/2) U_{N\mathcal{A}'}$. The speed of propagation needs to be determined directly and this is possible because the footwall and its boundary, including the hinge \mathcal{A}' , are yet in the reference configuration. This non-material velocity is computed from the velocity of point P which is always on the hinge. The ramp is extending at the rate $\dot{P}G = \dot{h}/\sin\gamma_B$ in the direction dipping at γ_B . This ramp makes the angle $\gamma_B + \gamma_A/2$ from the normal to the hinge so that its non-material velocity is $U_{N\mathcal{A}'} = \dot{h} \cos(\gamma_B + \gamma_A/2) / \sin\gamma_B$. In conclusion, the velocity of region no 3 and of the hinge \mathcal{A}' are

$$U_{HW3} = \dot{\delta} \frac{\sin(\gamma_A + \gamma_B)}{\cos(\frac{\gamma_A}{2})}, \quad U_{N\mathcal{A}'} = \dot{\delta} \frac{\sin(\gamma_A + \gamma_B)}{2 \sin(\frac{\gamma_A}{2})}. \quad (5.12)$$

5.3. The geometry and the velocity field of the FPF

Hinge	β	ω	α	ψ^+	ψ^-	$\tan s$	U_N/\dot{s}	U^+/\dot{s}	U^-/\dot{s}
\mathcal{B}	$2\pi - \frac{\gamma_B}{2}$	π	$\pi - \gamma_B$	π	$\pi - \gamma_B$	$2 \tan \frac{\gamma_B}{2}$	$\cos\left(\frac{\gamma_B}{2}\right)$	1	1
\mathcal{B}'	$\pi - \frac{\gamma_B}{2}$	$\frac{\pi + \gamma_A}{2}$	$\pi - \gamma_B$	π	$\pi - \gamma_B$	$2 \tan \frac{\gamma_B}{2}$	$\frac{\cos\left(\frac{\gamma_A}{2} + \gamma_B\right)}{2 \sin\left(\frac{\gamma_A + \gamma_B}{2}\right) \tan\left(\frac{\gamma_B}{2}\right)}$	$\frac{\cos\left(\frac{\gamma_B}{2}\right)}{\sin\left(\frac{\gamma_A + \gamma_B}{2}\right)}$	1
\mathcal{A}	$\frac{\gamma_A}{2}$	$\frac{\pi + \gamma_A}{2}$	$\frac{\pi + \gamma_A}{2}$	π	γ_A	$-2 \tan \frac{\gamma_A}{2}$	$\frac{1}{2 \tan\left(\frac{\gamma_A}{2}\right)} \left(\frac{\sin(\gamma_A + \gamma_B)}{\cos\left(\frac{\gamma_A}{2}\right)} - \frac{\cos\left(\frac{\gamma_B}{2}\right)}{\sin\left(\frac{\gamma_A + \gamma_B}{2}\right)} \right)$	$\frac{\sin(\gamma_A + \gamma_B)}{\cos\left(\frac{\gamma_A}{2}\right)}$	$\frac{\cos\left(\frac{\gamma_B}{2}\right)}{\sin\left(\frac{\gamma_A + \gamma_B}{2}\right)}$
\mathcal{A}'	$\pi + \frac{\gamma_A}{2}$	—	$\frac{\pi + \gamma_A}{2}$	π	γ_A	$-2 \tan \frac{\gamma_A}{2}$	$\frac{\sin(\gamma_A + \gamma_B)}{2 \sin(\gamma_A/2)}$	0	$\frac{\sin(\gamma_A + \gamma_B)}{\cos\left(\frac{\gamma_A}{2}\right)}$
PR	$\gamma_A + \frac{\pi}{2}$	$\frac{\pi + \gamma_A}{2}$	$\pi - \gamma_B$	—	—	—	$\frac{\sin \gamma_B \sin(\gamma_A + \gamma_B)}{\sin(\gamma_A + \gamma_B) - \sin \gamma_B}$	$\frac{\sin(\gamma_A + \gamma_B)}{\cos\left(\frac{\gamma_A}{2}\right)}$	1

Table 5.2: For each hinge or interface present in the FPF, dipping at β , the orientation of the velocities (ω and α) and of the micro-structure (ψ^+ and ψ^-) on its + and - sides, the intensity of shear $\tan s$, the non-material velocity of the interface U_N and the norm of the velocity on the two sides (U^+ and U^-) are provided. The notation is defined in Figure 5.3.

Consider now hinge \mathcal{A} , parallel to hinge \mathcal{A}' , separating the region no 3 and the region no 2 which is supposed undisturbed, an hypothesis which will be questioned later on. This assumption relies on the observation that the bedding is dipping at γ_A and is horizontal in these two regions. The intensity of shear induced by the hinge migration is $\tan(s) = -2 \tan(\gamma_A/2)$. We have already found that the velocity of region no 3 U_{HW3} is parallel to hinge \mathcal{A} so the velocity of region no 2 must have the same orientation and the norms of these two velocities are related by

$$U_{HW3} - 2 \tan \frac{\gamma_A}{2} U_{N\mathcal{A}} = U_{HW2}, \quad (5.13)$$

where $U_{N\mathcal{A}}$ and U_{HW2} are yet undetermined.

These two scalars are found by inspection of hinge \mathcal{B}' propagating from region no 1 within region no 2 where the beddings are dipping at γ_B and 0, respectively. The intensity of shear due to the propagation of the hinge is thus $\tan(s) = 2 \tan(\gamma_A/2)$. The velocities in region no 2 and no 1 are oriented at $\omega = (\pi + \gamma_A)/2$ and at $\alpha = \pi - \gamma_B$ so that (5.10) provides

$$U_{HW2} = \dot{\delta} \frac{\cos \frac{\gamma_B}{2}}{\sin(\frac{\gamma_A + \gamma_B}{2})}, \quad U_{N\mathcal{B}'} = \frac{\dot{\delta}}{2} \frac{\cos(\gamma_B + \frac{\gamma_A}{2})}{\sin(\frac{\gamma_A + \gamma_B}{2})} \cotan \frac{\gamma_B}{2}. \quad (5.14)$$

Combine now (5.13) and (5.14) to determine the remaining unknown

$$U_{N\mathcal{A}} = \frac{\dot{\delta}}{2} \cotan \frac{\gamma_A}{2} \left[\frac{\sin(\gamma_A + \gamma_B)}{\cos \frac{\gamma_A}{2}} - \frac{\cos \frac{\gamma_B}{2}}{\sin(\frac{\gamma_A + \gamma_B}{2})} \right]. \quad (5.15)$$

This equation reveals that the sign of the speed of propagation could be negative depending on the geometry. This sign could be guessed from the geometrical construction in Figure 5.1c and the observation of the segment GR. The dip of this segment is independent of the amount of shortening so that point R is propagating within the direction of this segment. Since that point is always on hinge \mathcal{A} , we can conclude that the hinge migrates within region no 3 and not within region no 2 for the specific value of γ_B chosen to construct this figure. Consequently, the material of region no 3 encountered by hinge \mathcal{A} is sustaining a second stage of deformation in simple shear, the first event being due to the earlier passage of hinge \mathcal{A}' , of same magnitude but different sense. The assumption made above that the hinge \mathcal{A} was moving within region no 2 was thus incorrect. It was based on the observation of the bedding in region no 2 which is horizontal. The deformation gradient in this region results from the composition of two transformations in simple shear with equal intensity but opposite sign. The composition is thus the identity tensor as if the medium was undisturbed. The derivation proposed above is thus correct although the physical interpretation had to be amended.

The last region to be considered is the region no 4 separated from region no 3 by the segment PR. This interface is along the bedding and thus its normal in the reference configuration is $\underline{N} = \underline{e}_2$. Its non-material speed of propagation in that configuration is simply \dot{h} since it contains parts of the bedding passing through the tip of the propagation fault. The difficulty is that this propagation in the current configuration occurs through regions which are already deformed so that (5.10) does not apply. However, if the propagation of the interface PR results in a difference in the deformation gradient between region no 3 and no 4 in a simple shear mode, then it is inferred from the results of Appendix 1 that $\underline{U}_3 - \underline{U}_4 = \dot{\Gamma} \underline{t}$, where \underline{t} is the tangent vector to PR and $\dot{\Gamma}$ is the product of the shear deformation induced by the propagation and its speed of propagation. Without determining this scalar, and noting that \underline{U}_{HW4} is parallel to the ramp, the law of sines applied to this difference provides

$$\frac{U_{HW4}}{\cos \frac{\gamma_A}{2}} = \frac{U_{HW3}}{\sin(\gamma_A + \gamma_B)}. \quad (5.16)$$

The comparison of (5.16) and (5.12) reveals that

$$U_{HW4} = \dot{\delta}. \quad (5.17)$$

The velocity of the region no 4 is thus identical to the velocity of region no 1. These two regions compose a single domain. Region no 4 is merged to region no 1 in what follows. The segment PR just analyzed is, consequently, not a source of dissipation during the FPF development. This is an important information for the bounding of the force applied to the back-wall of this structure considered next.

5.4 The maximum strength theorem and bounds on the forces

The objective of this section is to obtain an upper bound to the force Q which is necessary for the development of the fault-propagation fold by application of the maximum strength theorem. This theorem is also applied to the simpler case of a thrust extending the FPF ramp to the top surface of the competent layer. These two modes of deformation, folding or thrusting, are in competition and the dominant mode is the one requiring the least force according to the maximum strength theorem. This theorem is presented in preliminary with the support of the simple problem of a block pushed up an inclined ramp, a structure reminiscent of the central part of the hanging wall for both the fault-propagation fold and the thrust.

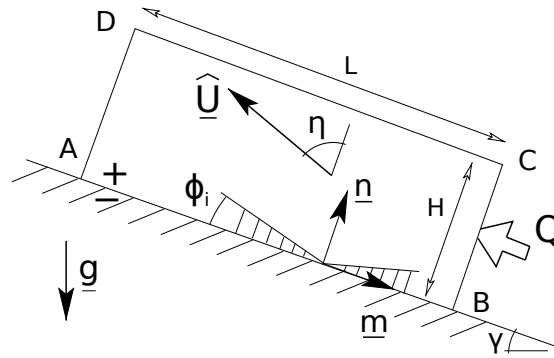


Figure 5.4: A block sliding up an inclined ramp by application of a force Q .

5.4.1 The theorem applied to the push-up of a block on an inclined ramp

Consider a rigid block occupying the rectangular domain $(L \times H)$, denoted Ω_t and pushed up a frictional and cohesive ramp AB inclined at the angle γ , Figure 5.4. The objective is to find an upper bound to the force necessary to initiate sliding and applied on the right boundary with an unknown distribution, and in the direction parallel to the ramp. The ramp sustains from the block a force of an unknown distribution given by the stress vector $\underline{T} = \tau \underline{m} + \sigma_n \underline{n}$ in which τ and σ_n are the shear and the normal components in the orthonormal direct basis $\{\underline{m}, \underline{n}\}$. At every point of the ramp, this vector has to be in the set

$$G_i = \{ \underline{T} \mid |\tau| + \sigma_n \tan \phi_i \leq C_i \}, \quad (5.18)$$

in which ϕ_i and C_i are the friction angle and the cohesion of this interface, respectively. This set G_i is the strength domain of the Coulomb interface which will be used throughout this contribution.

Essential to the maximum strength theorem, which could be seen as the kinematics approach of limit analysis (Salençon, 2002), is the definition of virtual velocity fields. Any field, and not necessarily the exact velocity field, could be considered. It is only required that the velocity satisfies the boundary conditions. Any velocity field having this property is said to be kinematically admissible (KA). In our example, the velocity field over the block is chosen to be uniform with the norm \hat{U} and oriented in the direction which is at the angle η measured from the direction of the normal, Figure 5.4. The superposed hat indicates that the velocity is virtual in the sense, again, that it is not necessarily the exact velocity. Moreover, we will see that the exact velocity field is not desirable for the construction of the proposed theorem. In this problem, there are no specific boundary conditions in terms of velocity, except for the constraint that the points on the wall BC are displaced to the left at the same velocity. The proposed field is thus kinematically admissible.

The derivation of an upper bound to the force Q is based on the theorem of virtual power which stipulates the equality between the external and the internal powers for any KA virtual velocity field

$$\mathcal{P}_{\text{ext}}(\hat{U}) = \mathcal{P}_{\text{int}}(\hat{U}) \quad \forall \hat{U} \text{ KA} . \quad (5.19)$$

This theorem expresses in a weak form the equilibrium conditions as we will see next from the definitions of the external and internal powers.

The external power is

$$\mathcal{P}_{\text{ext}}(\hat{U}) = \int_{\Omega_t} \hat{U} \cdot \rho \underline{g} dV + \int_{\partial\Omega_t^T} \hat{U} \cdot \underline{T}^d dV + Q \sin \eta \hat{U} , \quad (5.20)$$

and results from the power of the velocity field \hat{U} on the gravity force (ρ is the material density and the vector \underline{g} directed vertically has the magnitude g corresponding to the gravity acceleration). The second term in the right-hand side of (5.20) is the surface integral over the part of the boundary $\partial\Omega_t^T$ where distributed forces denoted \underline{T}^d are specified. No such distribution is provided in this example although the third term of the same equation corresponds to the power of the tectonic force of intensity Q by the velocity of the wall BC .

The velocity field has a spatial gradient which symmetric part $\hat{\underline{d}}$ is the rate of deformation tensor. The double bar identifies second-order tensors. The velocity field can also sustain jumps $[[\hat{U}]] \equiv \hat{U}^+ - \hat{U}^-$, defined as the difference between the velocity on the + and - side of the discontinuity (the normal points to the + side). Several discontinuities could exist in a structure including its boundary and they are referred to, collectively, as the set Σ_U . The internal power developed by the velocity field is defined by

$$\mathcal{P}_{\text{int}}(\hat{U}) = \int_{\Omega_t} \underline{\underline{\sigma}} : \hat{\underline{d}} dV + \int_{\Sigma_U} \underline{T} \cdot [[\hat{U}]] dS . \quad (5.21)$$

The double dots between two second-order tensors $\underline{\underline{A}}$ and $\underline{\underline{B}}$ is the sum $\sum_{ij} A_{ij} B_{ji}$ in a cartesian coordinate system. The two contributions in the right-hand side of (5.21) correspond to the diffuse power of the stress ($\underline{\underline{\sigma}}$) on the rate of deformation and the localized power of the stress vector on the velocity jump across the interfaces or discontinuities of Σ_U . In our problem, the tensor $\hat{\underline{d}}$ is zero since the velocity is uniform and only the second term in the right-hand side of (5.21) contributes to the internal power. The ramp is the only interface defining the set Σ_U .

The exact stress field required to define the internal power in (5.21) is unknown and no attempt is made to determine it in this contribution. It is proposed to find an upper bound to the internal power and, for that purpose, we search for the maximum power $\underline{T} \cdot [[\hat{U}]]$ which can be dissipated at every point of the surfaces in Σ_U . It can be shown (Salençon, 1974, 2002 and more recently Maillot and Leroy, 2006) that there is indeed a maximum power because the strength

domain G_i in (5.18) is convex in the stress space. This maximum is called the support function and is defined for the Coulomb strength domain (5.18) by

$$\begin{aligned}
 \text{case (1): } & 0 \leq |\eta| < \pi/2 - \phi_i, \quad \pi_i(\llbracket \hat{U} \rrbracket) = \hat{J} C_i \cotan(\phi_i) \cos \eta, \\
 \text{case (2): } & |\eta| = \pi/2 - \phi_i, \quad \pi_i(\llbracket \hat{U} \rrbracket) = \hat{J} C_i \cos \phi_i, \\
 \text{case (3): } & \pi/2 - \phi_i < |\eta| \leq \pi, \quad \pi_i(\llbracket \hat{U} \rrbracket) = +\infty,
 \end{aligned} \tag{5.22}$$

in which \hat{J}_i is the norm of the velocity jump on the interface of interest. In this example, this jump is simply the block velocity since the footwall below the ramp is assumed rigid. Three cases are defined in (5.22) depending on the angle η which orientates the velocity jump with respect to the normal. Case 1 and 2 are of interest since the support function is finite. The velocity jump vector for those two cases is oriented within or at the boundary of the cone of direction \underline{n} and internal angle $\pi/2 - \phi_i$. Choosing a velocity jump outside this cone (the dashed region in Figure 5.4) leads to an upper bound which is infinite and thus of no interest, case no 3 in (5.22). The velocity jumps which are oriented within or at the boundary of the cone are the only ones of interest and are said to be pertinent. Note that the exact velocity field for the sliding block is not pertinent for our analysis since in that instance $\eta = \pi/2$.

The maximum, resisting power is defined by the integral of the support function over the surfaces of Σ_U and is defined by

$$\mathcal{P}_{\text{mr}}(\hat{U}) = \int_{\Sigma_U} \pi_i(\llbracket \hat{U} \rrbracket) ds \geq \mathcal{P}_{\text{int}}(\hat{U}). \tag{5.23}$$

It is independent of the exact, unknown stress field. For our particular problem, this resisting power is simply $\hat{U} C_i \cotan \phi_i \cos \eta L$, considering case no 1 in (5.22) with (5.23). Combining the inequality (5.23) with (5.20) and (5.19) leads to

$$Q \sin \eta \hat{U} \leq \int_{\Sigma_U} \pi_i(\llbracket \hat{U} \rrbracket) - \int_{\Omega} \hat{U} \cdot \rho \underline{g} dV. \tag{5.24}$$

The normalization of the two sides of (5.24) by the horizontal velocity at the wall BC transforms the right-hand side in an upper bound to the exact, unknown tectonic force Q . This upper bound Q_{u} is function of the angle η which is now selected to minimize it and to obtain the least upper bound Q_{lu} . The upper bound in our particular problem has two contributions, the first due to gravity and the second due to the friction on the interface. It can be shown that the least upper bound is obtained by minimizing the power against gravity which means that the angle η is set to $\pi/2 - \phi_i$, corresponding to case no 2 in (5.22). The least upper bound Q_{lu} is then

$$Q_{\text{lu}} = \frac{\sin(\phi_i + \gamma)}{\cos \phi_i} \rho g H L + L C_i \geq Q, \tag{5.25}$$

a result which is of no surprise to the reader. The exact tectonic force will not be greater than Q_{lu} since that least upper bound is sufficient to initiate failure by sliding on the ramp. It could happen that another failure mode, for example a reverse fault through the block, occurs for a force less than the least upper bound just computed. One can estimate the bound to the force necessary for this second failure mode using the methodology proposed here. The mode requiring the least force is the one which dominates. It is this reasoning which is applied in the rest of this section where we estimate the upper bound for thrusting, Q_u^T and the least upper bound for the fault-propagation fold development, Q_{lu}^{FPF} . The least of the two bounds determines which mode dominates and how the structure develops.

5.4.2 Thrusting through the fault-propagation fold.

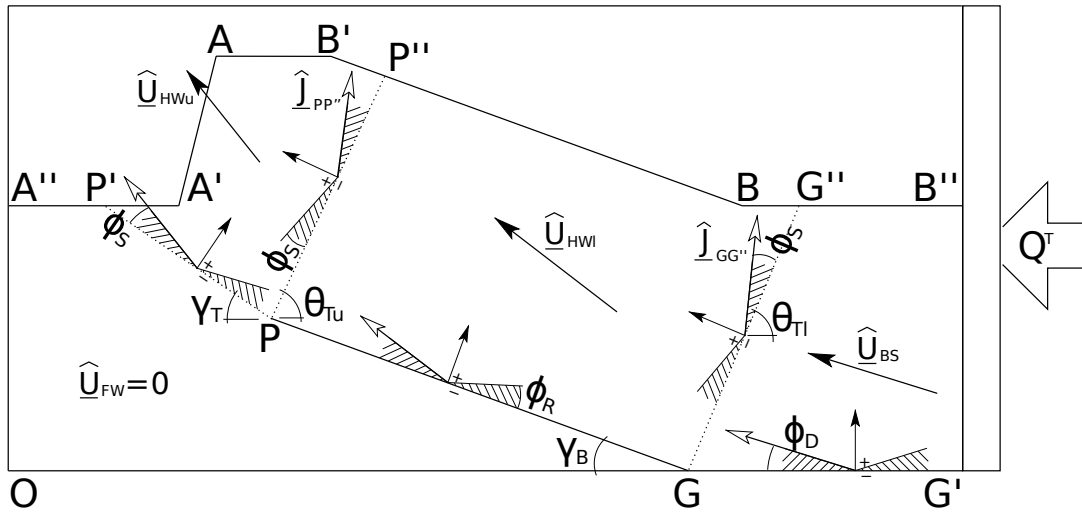


Figure 5.5: The kinematics and the virtual velocity field of the thrusting through the fold-propagation fold. Each dissipative interface is oriented and the cones for pertinent velocities are defined. The jumps are presented with arrows having white heads.

Thrusting is defined by the instantaneous propagation of the ramp GP which is extended by the new segment PP', the point P' being at the top of the competent layer, Figure 5.5. The dip of this last segment could differ from the dip of the fold ramp γ_B and is denoted γ_T . The thrust is composed of four regions, the back-stop (region $GG'B''G''$ denoted BS), the lower and upper hanging walls (region $PGG''P''$ and region $P'PP''$ denoted HWl and HWu, respectively) and the footwall (region $OGPP'A''$). The boundaries between these different regions are dissipative interfaces and they constitute the set of surfaces Σ_U defined above. The virtual velocity within each region is uniform and chosen such that the velocity jump over every interface is pertinent.

The cone of pertinent velocity jump directions is bounded by a dashed area for each dissipative discontinuity in Figure 5.5.

The velocity field is strongly dependent on the frictional properties of the interfaces which have to be discussed. It is assumed here that the new ramp PP' is crossing a pristine material having the friction angle ϕ_s of the solid, competent layer. The ramp GP developed during the folding has the frictional angle ϕ_R assumed to be less than ϕ_s because of the accumulation of damage during its activation, following the proposition of Cubas et al. (2008). The décollement GG' is weak and has the friction angle ϕ_D . These three interfaces have also cohesive properties which are accounted for in the computation of the upper bound although all cohesions are set to zero in the parametric study which follows this section. Note that all the material properties defined so far are summarized in Table 5.1.

The virtual velocity field of the thrust is constructed as follows. The velocity \hat{U}_{BS} of the back-stop is oriented to be pertinent with respect to the décollement GG' . Its angle η with respect to the normal to the décollement needs to be less or equal to $\pi/2 - \phi_D$. It is proposed to set $\eta = \pi/2 - \phi_D$, case no 2 for the support function in (5.22), to minimize the power against gravity, as in the introductory problem of the sliding block. The same reasoning is applied to the lower part of the hanging wall. Its velocity \hat{U}_{HWl} is oriented in the direction dipping at $\gamma_B + \phi_R$. The

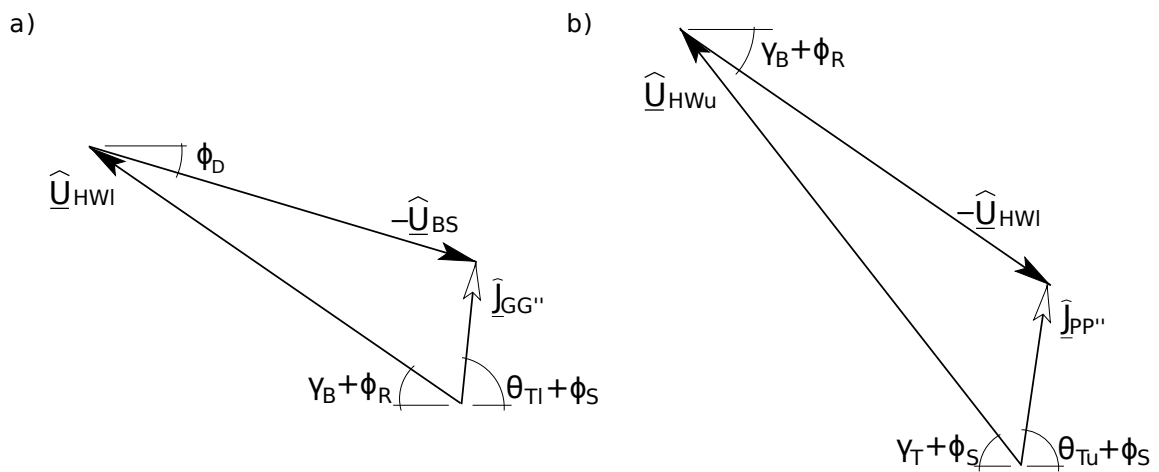


Figure 5.6: The hodogram of the jumps in the velocity over the hinge GG' in a) and the hinge PP' , b) for the thrusting through the fold-propagation fold with the velocity field defined in 5.5.

intensity of this velocity is determined by inspection of the back-thrust GG'' , the boundary of the lower part of the hanging wall and of the back-stop. This back-thrust is dipping at the unknown angle θ_{Tl} which could differ from θ_B since the points G'' and B do not necessarily coincide. Consequently, this interface will be assigned the friction angle ϕ_s as for the new part of the ramp, segment PP' . The back-thrust accommodates the jump in virtual velocity $(\hat{U}_{HWl} - \hat{U}_{BS}) = \hat{J}_{GG''}$,

a vector which is oriented to be pertinent according to case no 2 of the support function (5.22), as illustrated in the hodogram of Figure 5.6a. A mathematical proof that this particular orientation of the back-thrust jump is optimum for the force necessary to initiate thrusting is found in the electronic supplement of Cubas et al. (2008). The law of sines on the triangular construction of the hodogram in Figure 5.6a provides

$$\frac{\hat{U}_{HWl}}{\sin(\phi_D + \theta_{Tl} + \phi_s)} = \frac{\hat{U}_{BS}}{\sin(\gamma_B + \phi_R + \theta_{Tl} + \phi_s)} = \frac{\hat{J}_{GG''}}{\sin(\phi_R + \gamma_B - \phi_D)}. \quad (5.26)$$

The same reasoning is applied to the upper region of the hanging wall separated from the lower part by the back-thrust PP'' dipping at the unknown angle θ_{Tu} . The velocity of the upper region is \hat{U}_{HWu} and corresponds also to the jump on the ramp PP' since the velocity of the footwall is zero. This vector is oriented at the angle ϕ_s from the ramp. Its norm $\hat{J}_{PP''}$ is set by considering the back-thrust PP'' such that the jump in velocity is oriented according to case no 2 of the support function for the friction angle ϕ_s . The corresponding hodogram presented in Figure 5.6b reveals

$$\frac{\hat{U}_{HWu}}{\sin(\gamma_B + \phi_R + \theta_{Tu} + \phi_s)} = \frac{\hat{U}_{HWl}}{\sin(\gamma_T + 2\phi_s + \theta_{Tu})} = \frac{\hat{J}_{PP''}}{\sin(\gamma_T + \phi_s - \gamma_B - \phi_R)}. \quad (5.27)$$

The maximum resisting power, defined in (5.23), is obtained by integration of the support function (all in case no 2 in(5.22)) over the lengths of the back-thrusts, the two segments of the ramp and the décollement

$$\begin{aligned} \mathcal{P}_{mr}(\hat{U}) = & \hat{U}_{HWu} C_s \cos(\phi_s) L_{PP'} + \hat{J}_{PP''} C_s \cos(\phi_s) L_{PP''} \\ & + \hat{U}_{HWl} C_R \cos(\phi_R) L_{PG} + \hat{J}_{GG''} C_s \cos(\phi_s) L_{GG''} + \hat{U}_{BS} C_D \cos(\phi_D) L_{GG'} , \end{aligned} \quad (5.28)$$

in which L_{AB} denotes the distance between any two points A and B . This maximum resisting power is larger than the internal power which is equal to the external work defined in (5.20). The first of the three contributions in this definition is due to the power of the velocity field on the gravity field and the third to the power of the velocity on the tectonic force on the back-wall. The second contribution is the distributed external forces which are due here to the pressure exerted by the fluid-like layer. The pressure at any point A of the top of the competent layer is $\rho_f g D_A$ where D_A is the depth of this point, measured from the stress-free top surface. The depth of each point is found directly from the geometrical description of the fault-propagation fold given in

section 2. The final expression for the external work reads

$$\begin{aligned}
 \mathcal{P}_{\text{ext}}(\hat{U}) &= - \left(p_{A'} L_{P'A'} \sin(\phi_s + \gamma_T) + \frac{p_{A'} + p_A}{2} L_{AA'} \sin(\phi_s + \gamma_T + \gamma_A) + p_A L_{AB} \sin(\phi_s + \gamma_T) \right. \\
 &\quad \left. + \frac{p_{B'} + p_{P''}}{2} L_{B'P''} \sin(\phi_s + \gamma_T - \gamma_B) \right) \hat{U}_{HWu} - \left(\frac{p_{P''} + p_B}{2} L_{P''B} \sin(\phi_R) \right. \\
 &\quad \left. + p_B L_{BG''} \sin(\phi_R + \gamma_B) \right) \hat{U}_{HWl} - p_B L_{G''B''} \sin \phi_D \hat{U}_{BS} + Q \cos \phi_D \hat{U}_{BS} \quad (5.29) \\
 &\quad - S_{HWu} \hat{U}_{HWu} \rho_s g \sin(\phi_s + \gamma_T) - S_{HWl} \hat{U}_{HWl} \rho_s g \sin(\phi_R + \gamma_B) - S_{BS} \hat{U}_{BS} \rho_s g \sin(\phi_D) ,
 \end{aligned}$$

in which S denotes the surface of the area identified by the subscript. We now combine the inequality (5.24) to the theorem of virtual power (5.19) with the expressions (5.28) and (5.29) to obtain the upper bound to the force for thrusting

$$\begin{aligned}
 Q &\leq Q_u^T \quad \text{with} \quad Q_u^T \cos \phi_D = \quad (5.30) \\
 &\left(p_{A'} L_{P'A'} \sin(\phi_s + \gamma_T) + \frac{p_{A'} + p_A}{2} L_{AA'} \sin(\phi_s + \gamma_T - \gamma_A) + p_A L_{AB} \sin(\phi_s + \gamma_T) \right. \\
 &\quad \left. + \frac{p_{B'} + p_{P''}}{2} L_{B'P''} \sin(\phi_s + \gamma_T - \gamma_B) \right) \tilde{U}_{HWu} + \left(\frac{p_{P''} + p_B}{2} L_{P''B} \sin(\phi_R) \right. \\
 &\quad \left. + p_B L_{BG''} \sin(\phi_R + \gamma_B) \right) \tilde{U}_{HWl} + p_B L_{G''B''} \sin \phi_D \\
 &+ S_{HWu} \tilde{U}_{HWu} \rho_s g \sin(\phi_s + \gamma_T) + S_{HWl} \tilde{U}_{HWl} \rho_s g \sin(\phi_R + \gamma_B) + S_{BS} \tilde{U}_{BS} \rho_s g \sin(\phi_D) \\
 &\quad + \tilde{U}_{HWu} C_s \cos(\phi_s) L_{PP'} + \tilde{J}_{PP''} C_s \cos(\phi_s) L_{PP''} \\
 &\quad + \tilde{U}_{HWl} C_R \cos(\phi_R) L_{PG} + \tilde{J}_{GG''} C_s \cos(\phi_s) L_{GG''} + \tilde{U}_{BS} C_D \cos(\phi_D) L_{GG'} ,
 \end{aligned}$$

in which the jumps and the velocities with a superposed tilde have been obtained by the normalization with the arbitrary velocity of the back-stop $\tilde{U}_\alpha = \hat{U}_\alpha / \hat{U}_{BS}$. Note that the last two equations (5.29) and (5.30) were set up for the thrusting defined in Figure 5.5. The new segment of the ramp reaches the competent layer at point P' between A'' and A' . Similarly, point P'' and G'' are presented to the right of point B' and B , respectively. These particular choices have consequences on the exact pressure at these series of points which is used in (5.29) and (5.30). The results presented in the next section could rely on different geometries and proper modification of these two expressions are accounted for in a straight forward manner which is not discussed further here. Note also that the contribution of the fluid-like pressure on the back-wall over the depth H_f ($\rho_f g H_f^2 / 2$) has been disregarded from the bound in (5.30) for thrusting. The reason is that the same term contributes to the least upper bound determined next for the fold and what is of interest is not the exact value of these bounds but their difference.

5.4.3 The least upper bound for the fault-propagation fold

The least upper bound to the force necessary for the development of the fault-propagation fold is now computed using the same methodology considered for the two examples above.

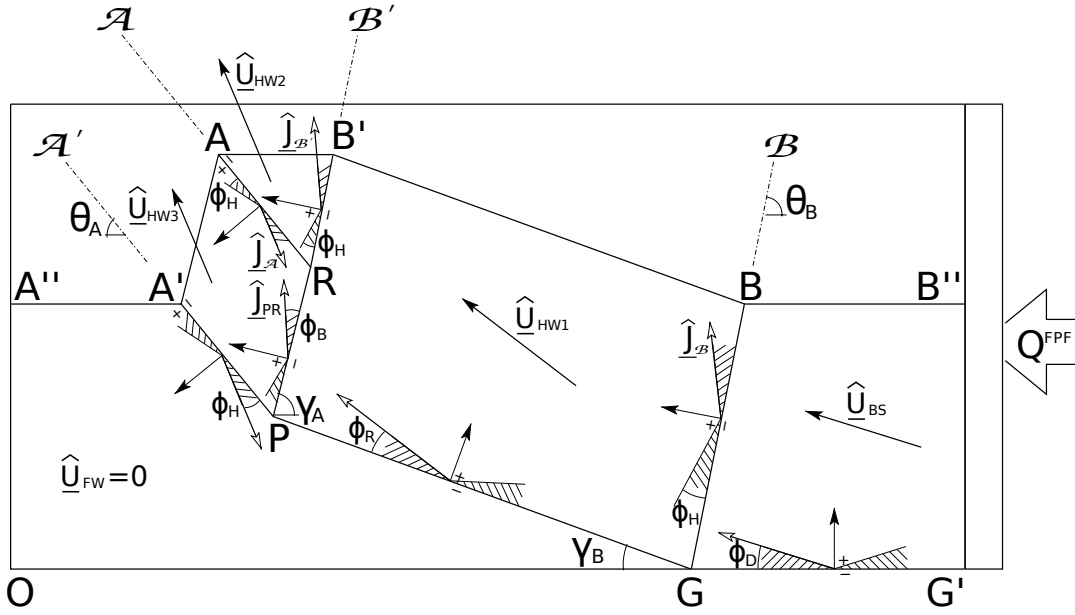


Figure 5.7: The virtual velocity field of the fault-propagation fold. The dashed region, plotted for each surface of dissipation, indicates the cone of admissible directions for the velocity or the jump in velocity to be pertinent. The velocity jumps are presented with arrows having white heads.

The frictional properties of the interfaces composing the fold are first discussed. The ramp has the friction angle ϕ_R assumed again to be lower than the friction angle of the pristine material because of damage accumulation. It is also assumed that the competent rock is layered. The rock composing each layer has the friction angle ϕ_s considered in the previous section for thrusting. The layers are separated by weak interfaces corresponding to the bedding planes, typically composed of shales and having the smaller friction angle $\phi_B \leq \phi_s$. The existence of these two materials facilitate the activation of the hinges, a detailed discussion of the hinge mechanism being given by Maillot and Leroy (2003). It is assumed here that the effective properties of the hinge are cohesive and frictional, the friction angle being denoted ϕ_H and assumed smaller than ϕ_s . The décollement GG' is also assumed weak with the friction angle ϕ_D . All interfaces are cohesive for the theoretical development which follows although these cohesions are set to zero in the parametric study of the next section.

The virtual velocities of the back-stop and of the region no 1 in the hanging-wall are constructed similarly to the velocities of the back-stop and of the lower hanging-wall of the thrust, respectively. The velocities \hat{U}_{BS} and \hat{U}_{HW1} are oriented at the angle ϕ_D and ϕ_R from the directions of the décollement GG' and of the ramp, respectively. The norm of \hat{U}_{HW1} is found from the application of the law of sines to the hodogram for the velocity jump across hinge \mathcal{B} , of norm $\hat{J}_{\mathcal{B}}$, presented in Figure 5.8a

$$\frac{\hat{U}_{HW1}}{\sin(\phi_D + \theta_B + \phi_H)} = \frac{\hat{U}_{BS}}{\sin(\gamma_B + \phi_R + \phi_H + \theta_B)} = \frac{\hat{J}_{\mathcal{B}}}{\sin(\phi_R + \gamma_B - \phi_D)}. \quad (5.31)$$

The velocity of the region no 3 of the hanging-wall is oriented in the direction at the angle ϕ_H from the hinge \mathcal{A}' . Its norm is found by requiring that the velocity jump over the hinge PR dips at $\phi_B + \gamma_A$. It is indeed the bedding friction angle which is used here since the surface PR is parallel to the bedding. The application of the law of sines to the hodogram corresponding to the jump across PR , of norm \hat{J}_{PR} , presented in Figure 5.8b, yields

$$\frac{\hat{U}_{HW3}}{\sin(\gamma_B + \phi_R + \gamma_A + \phi_B)} = \frac{\hat{U}_{HW1}}{\sin(\theta_A + \phi_H + \phi_B + \gamma_A)} = \frac{\hat{J}_{PR}}{\sin(\theta_A + \phi_H - \gamma_B - \phi_R)}. \quad (5.32)$$

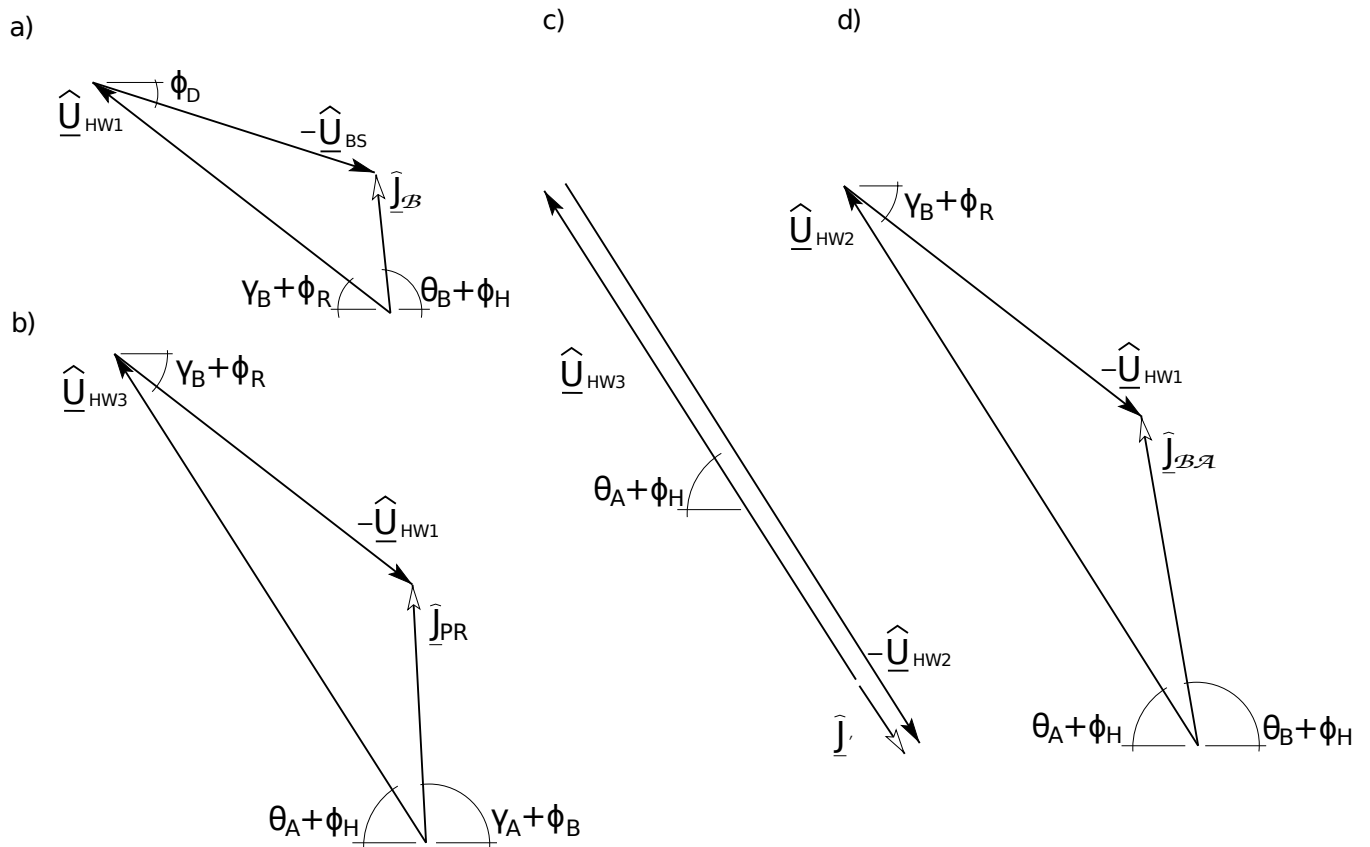


Figure 5.8: The hodogram for the velocities and the velocity jumps of hinges \mathcal{B} , PR , \mathcal{A} and \mathcal{B}' of the fault-propagation fold in a) to d), respectively.

The velocity of the region no 2 in the hanging wall is found by studying the hinges \mathcal{A} and \mathcal{B}' . The jump in velocity across the hinge \mathcal{A} is oriented with the dip $\theta_A + \phi_H$. This vector is thus parallel to the velocity vector \hat{U}_{HW3} and, consequently, the unknown velocity vector \hat{U}_{HW2} has to have the same direction, as it is illustrated in Figure 5.8c. The norm of this last vector remains unknown and is determined by inspection of the hinge \mathcal{B}' . The velocity jump over the hinge \mathcal{B}'

has the norm $\hat{J}_{\mathcal{B}'}$ and is dipping at $\theta_B + \phi_H$. The corresponding hodogram is presented in Figure 5.8d and the application of the law of sines reveals

$$\frac{\hat{U}_{HW2}}{\sin(\gamma_B + \phi_R + \theta_B + \phi_H)} = \frac{\hat{U}_{HW1}}{\sin(\theta_B + 2\phi_H + \theta_A)} = \frac{\hat{J}_{\mathcal{B}'}}{\sin(\theta_A + \phi_H - \gamma_B - \phi_R)}, \quad (5.33)$$

providing the unknown \hat{U}_{HW2} .

The virtual velocity field just constructed only exists under certain constraints which are deduced from the four hodograms of Figure 5.8. These constraints will be presented in the next sub-section and the derivation of the least upper bound on the force is now continued following the same lay out as in the two previous applications of the maximum strength theorem.

The maximum resisting power defined in (5.23) is

$$\begin{aligned} \mathcal{P}_{\text{mr}}(\hat{U}) &= \hat{U}_{HW3} C_H \cos(\phi_H) L_{A'P} + \hat{J}_{PR} C_B \cos(\phi_B) L_{PR} \\ &\quad + \hat{J}_{\mathcal{A}} C_H \cos(\phi_H) L_{AR} + \hat{J}_{\mathcal{B}'} C_H \cos(\phi_H) L_{RB'} \\ &\quad + \hat{U}_{HW1} C_R \cos(\phi_R) L_{PG} + \hat{J}_{\mathcal{B}} C_H \cos(\phi_H) L_{GB} + \hat{U}_{BS} C_D \cos(\phi_D) L_{GG'}. \end{aligned} \quad (5.34)$$

The external power defined in (5.20) reads

$$\begin{aligned} \mathcal{P}_{\text{ext}}(\hat{U}) &= -\frac{P_{A'} + P_A}{2} L_{AA'} \sin(\phi_H + \gamma_A + \theta_A) \hat{U}_{HW3} - P_A L_{AB'} \sin(\phi_H + \theta_A) \hat{U}_{HW2} \\ &\quad - \frac{P_{B'} + P_B}{2} L_{B'B} \sin(\phi_R) \hat{U}_{HW1} + \left(Q \cos(\phi_D) - P_B L_{BB''} \sin(\phi_D) \right) \hat{U}_{BS} \\ &\quad - S_{HW3} \hat{U}_{HW3} \rho_s g \sin(\phi_H + \theta_A) - S_{HW2} \hat{U}_{HW2} \rho_s g \sin(\phi_H + \theta_A) \\ &\quad - S_{HW1} \hat{U}_{HW1} \rho_s g \sin(\phi_R + \gamma_B) - S_{BS} \hat{U}_{BS} \rho_s g \sin(\phi_D). \end{aligned} \quad (5.35)$$

The theorem of virtual power (5.19), the inequality (5.23) and the expressions (5.34) and (5.35) provides the least upper bound

$$\begin{aligned} Q &\leq Q_{lu}^{FPF} \quad \text{with} \quad Q_{lu}^{FPF} \cos \phi_D = \\ &\frac{P_{A'} + P_A}{2} L_{AA'} \sin(\phi_H + \gamma_A + \theta_A) \tilde{U}_{HW3} + P_A L_{AB'} \sin(\phi_H + \theta_A) \tilde{U}_{HW2} \\ &\quad + \frac{P_{B'} + P_B}{2} L_{B'B} \sin(\phi_H) \tilde{U}_{HW1} + P_B L_{BB''} \sin(\phi_D) \tilde{U}_{BS} \\ &\quad + S_{HW3} \tilde{U}_{HW3} \rho_s g \sin(\phi_H + \theta_A) + S_{HW2} \tilde{U}_{HW2} \rho_s g \sin(\phi_H + \theta_A) \\ &\quad + S_{HW1} \tilde{U}_{HW1} \rho_s g \sin(\phi_R + \gamma_B) + S_{BS} \rho_s g \sin(\phi_D) \\ &\quad + \tilde{U}_{HW3} C_H \cos(\phi_s) L_{A'P} + \hat{J}_{PR} C_B \cos(\phi_B) L_{PR} \\ &\quad + \tilde{J}_{\mathcal{A}} C_H \cos(\phi_H) L_{AR} + \hat{J}_{\mathcal{B}'} C_H \cos(\phi_H) L_{RB'} \\ &\quad + \tilde{U}_{HW1} C_R \cos(\phi_R) L_{PG} + \hat{J}_{\mathcal{B}} C_H \cos(\phi_H) L_{GB} + n C_D \cos(\phi_D) L_{GG'}, \end{aligned} \quad (5.36)$$

in which again all virtual velocities have been normalized by the arbitrary velocity of the back-stop. The bound defined in (5.36) is the least since there is no free degree of freedom either in the geometry nor in the velocity field which could be optimized.

5.4.4 Locking of the fault-propagation fold

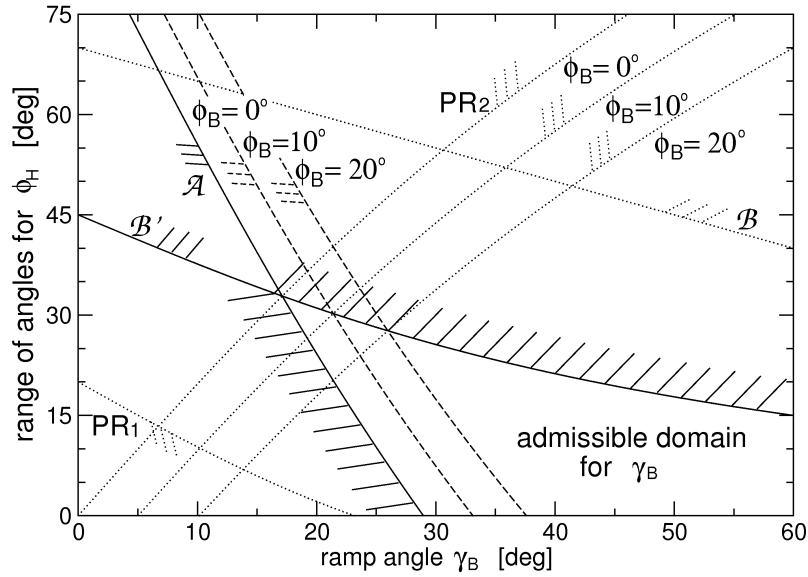


Figure 5.9: The various constraints obtained from the hodograms of the virtual velocity jumps (Figure 5.8) are defining an admissible domain for the selection of the ramp angle and of the hinge friction angle.

This last sub-section of section 3 is devoted to the constraints due to the construction of the virtual velocity field of the fault-propagation fold. The hodograms presented in Figure 5.8 were plotted for realistic orientations of the sense of shear on all the interfaces. The reversal of a sense of shear would not be consistent with the development of the structure and the velocity field would loose its relevance. It is said that in this instance, the fault-propagation fold would *lock*. The condition for this locking to occur is, typically, that two of the three vectors used for one of the triangular construction become linearly dependent. These conditions are now presented and the consequences for the development of the fault-propagation fold discussed.

For the first hodogram in 5.8a for the hinge \mathcal{B} , the three conditions are

$$\begin{aligned} \phi_D - \phi_R &\leq \gamma_B, \\ \phi_H + \phi_R &\leq \frac{\pi + \gamma_B}{2}, \\ \phi_H + \phi_D &\leq \frac{\pi + \gamma_B}{2}. \end{aligned} \tag{5.37}$$

The décollement friction angle is less than the ramp friction angle and the first condition is always met. Small values are thought for ϕ_H and ϕ_R so that the second condition is also not restrictive. Consequently, only the third condition remains. It is presented in Figure 5.9, where the hinge friction angle is plotted as function of the ramp dip, as a dotted line labelled with the letter \mathcal{B} . The series of barbs mark the region which is restricted.

The second hodogram in 5.8b corresponds to the interface PR and the three conditions to ensure its validity are

$$\begin{aligned}\phi_R - \phi_H &\leq \frac{\pi - \gamma_A}{2} - \gamma_B \\ \phi_H + \phi_B &\leq \frac{\pi - \gamma_A}{2}, \\ \phi_R + \phi_B &\leq \pi - \gamma_A - \gamma_B.\end{aligned}\tag{5.38}$$

The first and second conditions correspond to the dotted curve $PR1$ and $PR2$ in Figure 5.9, the second being plotted for three values of the bedding friction angle. The third condition is always respected.

The third hodogram in 5.8c for the hinge \mathcal{A} is based on three co-linear vectors and the appropriate sense of shear requires that $\hat{U}_{HW3} \geq \hat{U}_{HW2}$. Comparing the two hodograms in Figure 5.8b and 5.8d, it is concluded that this condition is equivalent to

$$\theta_B + \phi_H \geq \gamma_A + \phi_B.\tag{5.39}$$

This constraint is presented in Figure 5.9 where it is labeled \mathcal{A} and plotted for three values of ϕ_B .

The fourth hodogram is for hinge \mathcal{B}' and the first of the three conditions for its validity is identical to the first in (5.38). The two others read

$$\begin{aligned}\phi_H &\leq \frac{\gamma_A + \gamma_B}{4} = \phi_H^c, \\ \phi_R + \phi_H &\leq \frac{\pi - \gamma_B}{2}.\end{aligned}\tag{5.40}$$

The first of these two conditions is the only relevant one and is plotted in Figure 5.9 with the label \mathcal{B}' .

These various inequalities define the admissible domain for the couple (γ_B, ϕ_H) . It is found that for a ramp dip between 17° and 29° there is a minimum and a maximum value for ϕ_H to avoid the fold locking. The minimum value is zero for $\gamma_B \geq 29^\circ$ and the maximum decreases significantly for large γ_B .

The physical interpretation of these constraints are better explained in the space of forces than in the virtual velocity space. The example of the first constraint in (5.40), which is characteristic of the region no 2, is chosen to illustrate this point. For $\phi_H > \phi_H^c$, the forces on the two hinges \mathcal{A} and \mathcal{B}' cannot balance the vertical weight of the region no 2. There is thus a locking of this region if the friction angle is larger than the critical, maximum value ϕ_H^c . This locking is found here by inspection of the virtual velocity fields. The proof of this statement in terms of forces is presented in the Appendix 2 with a force balance analysis of the free body diagram of this region.

The fact that the restrictions based on forces and on virtual velocities are the same provides a non-trivial illustration of the equivalence between the force approach and the maximum strength theorem.

5.5 Competition between folding and thrusting

The main outcome of the preceding section is the provision of upper bounds Q_u^T and of the least upper bound Q_{lu}^{FPF} to the forces necessary for thrusting and for the development of the fault-propagation fold, respectively. The bound for folding is the least since there is no free degrees of freedom in the proposed velocity field. Only bounds were obtained for the force required to thrust because several angles necessary to describe the failure mode and the velocity field are yet undetermined. This section has two objectives, the first consisting in obtaining the least upper bound for thrusting Q_{lu}^T . The second objective is to compare Q_{lu}^T and Q_{lu}^{FPF} to decide on the dominant mode, thrusting or folding.

5.5.1 Optimizing the thrust

The need to optimize the thrust is first assessed by considering the upper bound Q_u^T obtained for a thrust where the ramp PP' extends the initial ramp GP with the same dip ($\gamma_T = \gamma_R$) and the upper and lower back-thrusts coincide with the segments PB' and GB, respectively. The optimized thrust is obtained by numerical means searching among all possible orientations γ_T , θ_{Tu} and θ_{Tl} the set of three angles leading to the smallest upper bound for thrusting according to (5.30). The comparison between the two bounds Q_u^T and Q_{lu}^T is presented in Figure 5.10a and 5.10b, with dotted-dashed and dashed curves, obtained for the two values of the fluid-like layer thickness of zero and 500 m. The bounds are compared during the whole development of the folding defined by the increase in the shortening δ . Note that dimensionless quantities are marked by a superposed tilde. Dimensionless lengths are obtained by dividing the physical quantity by the competent layer thickness H_s . The dimensionless forces have been divided by $\rho_s g H_s^2$. There is a reduction by 45 % of the bound by optimizing the thrust during the whole development of the fold, in the absence of the fluid layer. The magnitudes of these forces are rather independent of the amount of shortening. This reduction between the upper and the least upper bound for thrusting is of the order of 15 % only for the 500 m thick overburden. This is simply the consequence of the dominant role played by the fluid-like pressure on the top of the competent layer. This dominant effect is also seen by the slight decrease in the forces for thrusting with increasing shortening which is due to the reduction in the effective thickness of the fluid layer over the main part of the fold.

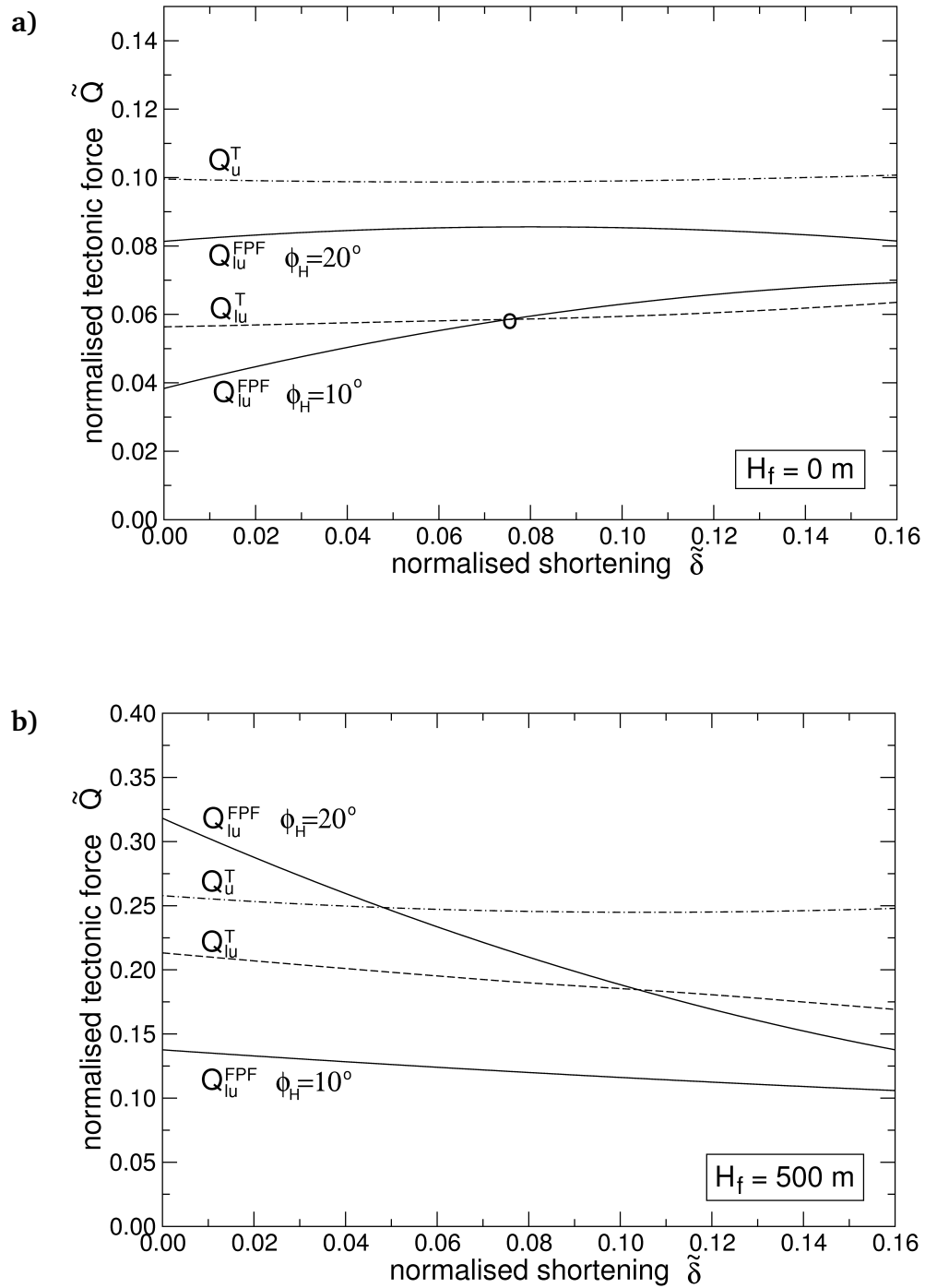


Figure 5.10: Comparison between the dimensionless upper bound \tilde{Q}_u^T , the least upper bound \tilde{Q}_{lu}^T for the thrust and the upper bound \tilde{Q}_{lu}^{FPF} for the fault-propagation fold during shortening. Two values of the fluid-like layer thickness are considered in a) and b). The circle in a) indicates the transition from folding to thrusting for the dimensionless shortening of 0.075.

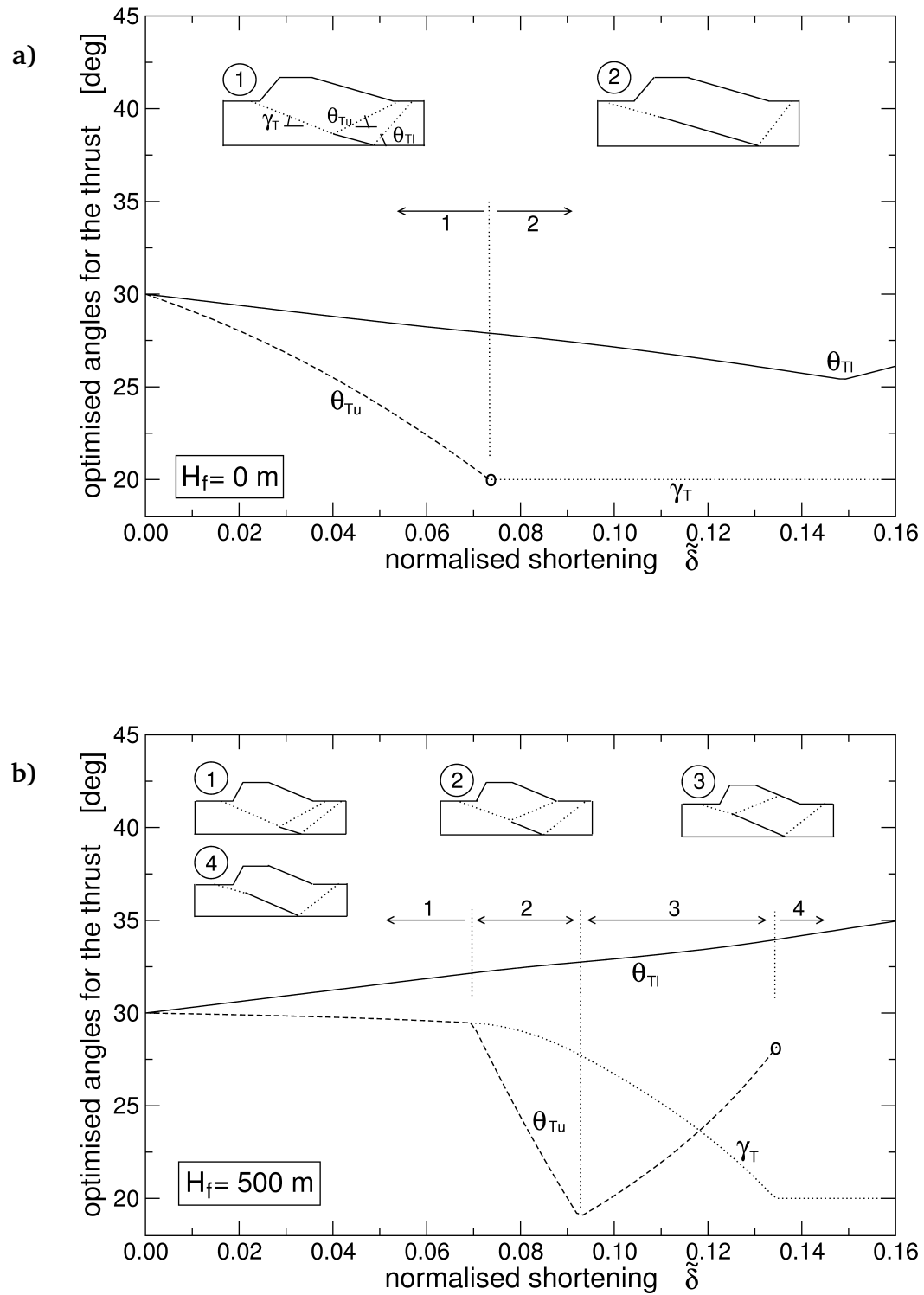


Figure 5.11: The optimized dips of the ramp γ_T , the lower and the upper back-thrust (θ_{Tl} and θ_{Tu} of the thrust during the shortening of the fold. Two values of the fluid-like layer are considered in a) and b), 0 and 500 m, respectively.

The geometry of the optimised failure mode for thrusting is defined by three angles, the ramp dip γ_T and the upper and lower back-thrust dips, θ_{Tl} and θ_{Tu} , Figure 5.5. These optimized angles are presented in Figure 5.11 with dotted, solid and dashed curves, respectively. Results were obtained with γ_B , the fault dip of the fold, set to 30° . The three angles are found to have the same value, corresponding to $\pi/4 - \phi_s/2$, for zero shortening. This result is not influenced by the friction angle of the décollement nor the length $L - d$ of the back-stop. An analytical proof of this surprising result is presented in Appendix 3. It is during the fold development that these various angles change drastically. The case with no overburden ($H_f = 0$) in Figure 5.11a is first discussed. The evolution of the angles is partitioned in two phases. In phase 1, the upper back-thrust and the thrust ramp are conjugate faults with the same dip decreasing to reach the critical value of 20° , marking the beginning of phase 2. At the transition and in phase 2, the upper hanging wall virtual velocity \hat{U}_{HWu} and the virtual velocity of the lower part of the hanging wall \hat{U}_{HWl} (see Figure 5.5 for these definitions) are identical. It implies that $\gamma_T + \phi_s = \gamma_B + \phi_R$ and means that the hanging wall is acting as a single region. The upper back-thrust is thus not existing anymore in this phase 2, as it can be seen by the two insets in Figure 5.11a. The small circle at the boundary between phase 1 and 2 marks the end of the existence of the upper back-thrust. In this phase 2, the thrust ramp keeps the same dip. The lower back-thrust dip does not appear to be influenced by the transition between these two phases, with and without the upper back-thrust. Its dip decreases steadily during the fold development until the lower back-thrust intersects the back-wall, resulting in the kink in the curve for the dimensionless shortening of 0.15, approximately.

The evolution during the FPF development of the three dips of the thrust geometry is more complex in the presence of an overburden, Figure 5.11b, and is now partitioned in four phases. Phase 1 is identical to the one described above except that the lower back-thrust is now increasing its dip. In phase 2, the upper back-thrust and the ramp are not conjugate anymore, the upper back-thrust dip decreasing more than the ramp dip. It is found that the upper back-thrust is intersecting the top of the competent layer exactly at the transition from the back-stop to the hanging wall of the fold (point B in Figure 5.5). In phase 3, the selection of this special point B ceases and the upper back-thrust remains within the hanging wall. Its dip increases sharply. During that same phase, the dip of the ramp continues to decrease to reach the conditions $\gamma_T + \phi_s = \gamma_B + \phi_R$ for which the upper back-thrust ceases to function. Phase 4 is thus identical to phase 2 in Figure 5.11a where the hanging wall of the thrust behaves as a single region.

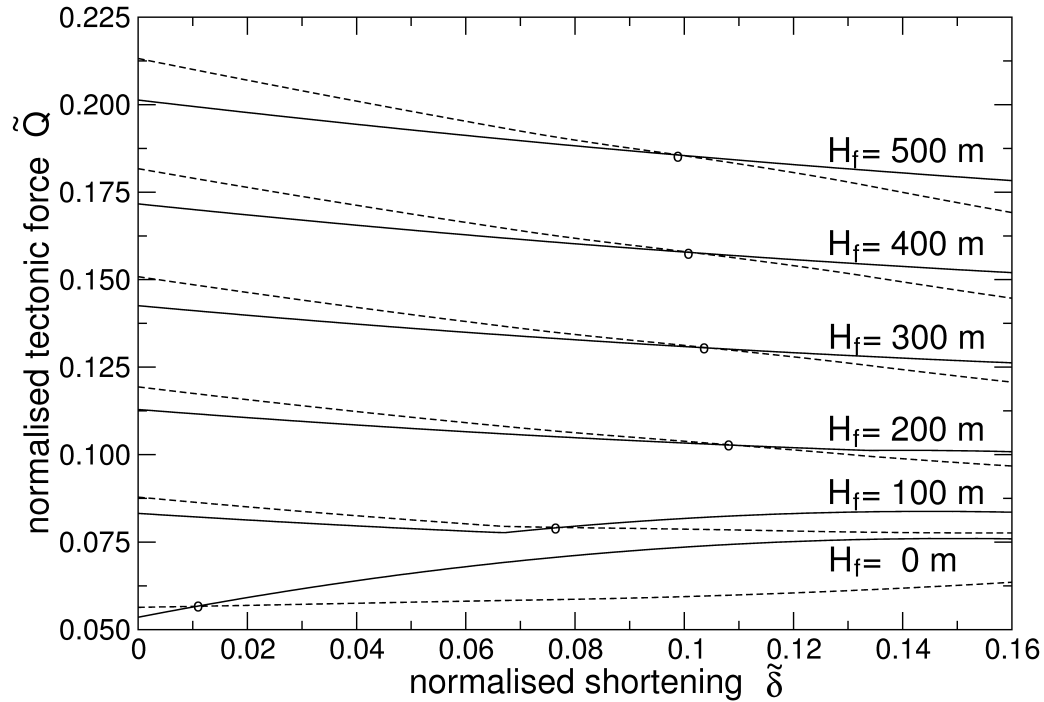


Figure 5.12: The least-upper bounds for the fault-propagation fold (solid curves) and for the thrust (dashed curves) for different thickness of the fluid-like layer. The circles indicate the cross over of the two curves and signal the end of the fold development replaced by the thrust.

5.5.2 The dominant mode

The objective is now to compare the least upper bound for thrusting with the least upper bound for folding to decide on the life expectancy of the latter. This life-span is defined by the amount of accumulated shortening at the transition between folding and thrusting.

This comparison in terms of bounds is presented in Figure 5.10 where the force for the fault-propagation fold \tilde{Q}_{lu}^{FPF} is presented as solid curves; the least upper bound for the thrust \tilde{Q}_{lu}^T corresponds to dashed curves. For the two cases of a fluid-like layer thickness $H_f = 500$ m and $H_f = 0$, the force for folding is initially less than the force for thrusting, if the fold hinge are given the weak friction angle of 10° . The two curves for the bounds intersect for a dimensionless shortening close to 0.08, for $H_f = 0$. Note that for a friction angle of 20° , the thrust dominates initially and thus a fault-bent fold is likely to developed instead of the fault-propagation fold. For a 500 m thick overburden and the hinge friction set to 10° , the fold-propagation fold develops completely (the fold ramp reaches the top of the competent layer) for the shortening of 0.16 without being interrupted by the onset of thrusting. For the same value of H_f but $\phi_H = 20^\circ$, the bound to the force necessary to fold is more than the least upper bound for thrusting from the start until a dimensionless shortening of approximately 0.05. The thrust dominates the early part

of the shortening and the proposed fold kinematics does not apply.

The sensitivity of the dominance of the fold or the thrust on the thickness of the fluid-like layer is further explored in Figure 5.12. The least upper bounds for these two mechanisms are plotted as dashed and solid curves, respectively. The circles mark the transition with increasing shortening between the dominance of the fold and of the thrust. Results are obtained for $\phi_H = 16^\circ$, a value intermediate between the two values considered to produce the results presented in Figure 5.10. The least upper bound with no overburden is an increasing function of the shortening because of the increasing relief. For $H_f = 100$ m, the same least upper bound is first decreasing with the accumulated shortening corresponding to a phase where the fluid pressure on the top of the competent layer is decreasing on average. The kink on that curve is marking the shortening for which the relief is piercing the fluid layer. The least upper bounds for the thicker overburden are rather similar with intersections, marking the end of the dominance of the fold and pinpointed by the circles, decreasing slightly with increasing H_f . This dependence is opposite to the trend observed for H_f less than 200 m.

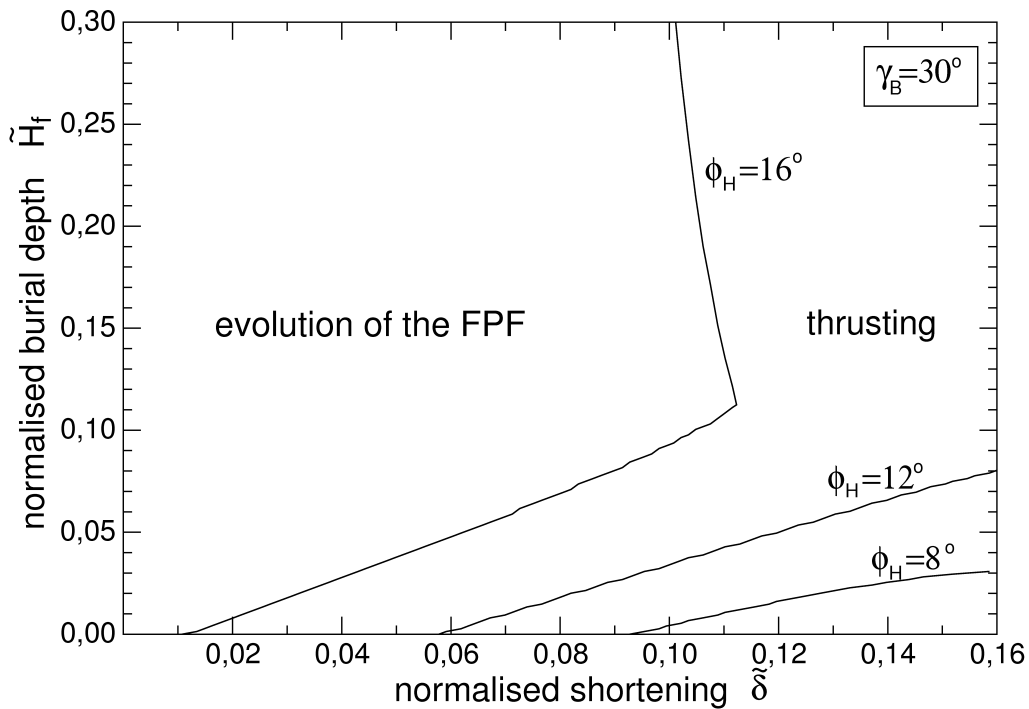


Figure 5.13: The competition between the fault-propagation fold and the thrust are presented in the map spanned by the shortening and the initial burial depth defined by the thickness of the fluid-like layer. The boundary between the domain of the fold and the thrust are obtained for three values of the fold hinges friction angles. Each boundary is found by collecting the circles defined in Figure 5.12.

These comparisons to define which of the two mechanisms dominates are now summarized in

Figure 5.13 in a map spanned by the dimensionless shortening and thickness of the overburden. They partition the map in two domains, one to the left where the fold develops and one to the right where the thrusting has stopped this development. The boundary between the two regions is the collection of the circles found in Figure 5.11. These curves are obtained for different values of the hinge friction angle. The larger the hinge friction angle, the smaller is the region of dominance of the fold. Note the kink in the domain boundary for $\phi_H = 16^\circ$ corresponding for the lower H_f conditions for which the fold pierces the weak overburden. The influence of H_f is weak in the absence of this piercing mechanism.

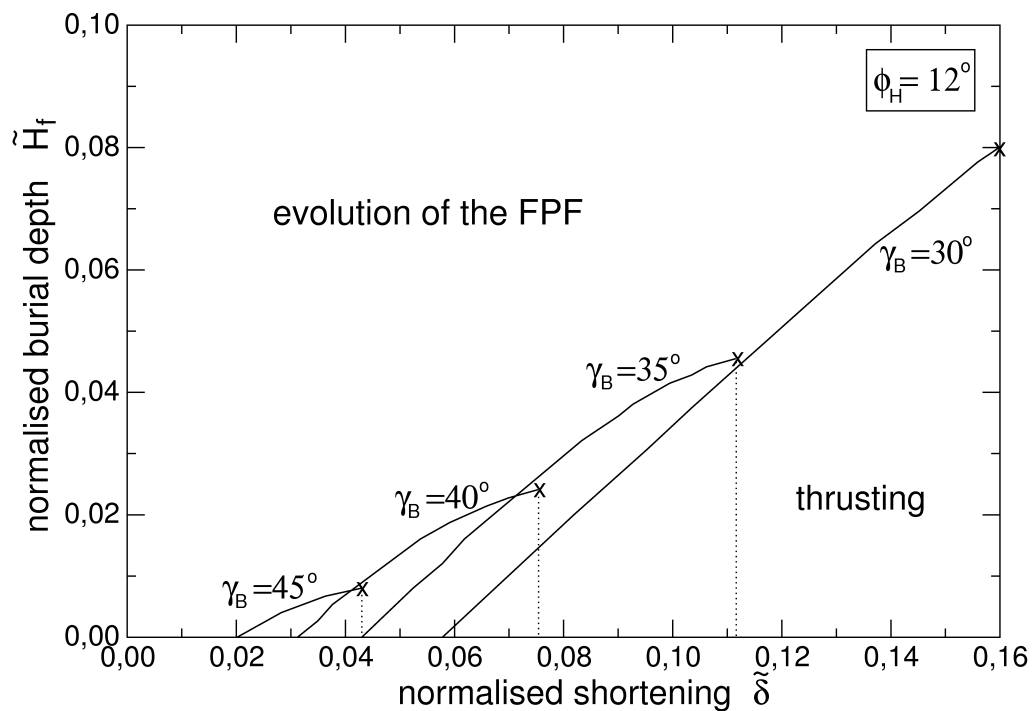


Figure 5.14: The competition between the fault-propagation fold and the thrust is seen to be sensitive to the orientation of the fault ramp γ_B in this map spanned by the shortening and the burial depth defined by the thickness of the fluid like layer. Reducing the fault dip decreases the shortening necessary for thrusting to dominate although less shortening is also required for the completion of the fold development, as marked by crosses.

The geometry of this map is further explored in Figure 5.14 by varying the dip of the fold ramp setting $\phi_H = 12^\circ$. The curve for $\gamma_B = 30^\circ$ is the one found in Figure 5.13. The cross marks the shortening for which the fold development is completed without being interrupted by the onset of thrusting. It is observed that an increase in the ramp angle from the 30° , which is the initial optimum dip for faulting, leads to a reduction in the size of the region of dominance of the fold. Also, note the associated reduction in the amount of shortening necessary to complete the

fold development.

5.6 Conclusion

The two objectives of this contribution were first, to show that one could estimate the tectonic force necessary for the development of folds constructed with classical geometrical rules and second, to predict when this fold development is interrupted by the onset of thrusting. This prediction is based on a comparison of the least upper bounds on the forces necessary for thrusting and folding which are obtained by application of the maximum strength theorem.

The fault-propagation fold (FPF) is composed of a kink-fold bounded by several hinges which are migrating during the fold development ahead of the region of the propagating fault. It is shown how these migrations could be computed by application of Hadamard's jump conditions providing a rather systematic construction of the exact velocity field. The application of the maximum strength theorem to the FPF, thus the account of mechanical equilibrium and of the Coulomb maximum material strength, shows that there are some restrictions on the range of admissible fault dips according to the possible values for the hinge friction angles. There are no ramp dips less than, approximately 20° . For ramp dips varying between 20° and 60° , the maximum hinge friction angle decreases from 30° to 20° , approximately.

The comparison between the least upper bounds on the force to thrust and to develop the FPF is directly interpreted in terms of life span of the fold defined by the accumulated shortening prior to the thrust onset. These verdicts on the life span are summarized in Figure 5.15 for various values of the fold hinges friction angle ϕ_H . The top layer is composed of a fluid-like layer connected to a remote reservoir of infinite extent so that its thickness is constant during the compression. The grey line is a marker. For the largest value of the hinge friction angle, thrusting dominates as soon as shortening is initiated and the dashed segments in Figure 5.15a are marking the ramp and the back-thrust, both dipping at 30° . This particular angle corresponds to the classical orientation for faulting $\pi/4 - \phi_s/2$ in compression, where ϕ_s is the friction angle of the bulk material. This orientation at 30° is independent of the friction on the décollement, as it is shown analytically in the Appendix 3. Figure 5.15b and 5.15c show that the fold develops until it is stopped by the onset of thrusting at a critical shortening which is increasing with decreasing values of the hinge friction angle. Note the difference between the thrusting mechanisms in these two examples. In Figure 5.15b, the ramp for thrusting is sub-parallel to the ramp used for the fold and is associated to two back-thrusts, the first at the base of the fold ramp and the second at its tip. In Figure 5.15c, a single back-thrust exists at the base of the fold ramp and the thrust ramp dip γ_T satisfies the relation $\gamma_T + \phi_s = \gamma_B + \phi_R$ where ϕ_R is the friction angle of the damaged

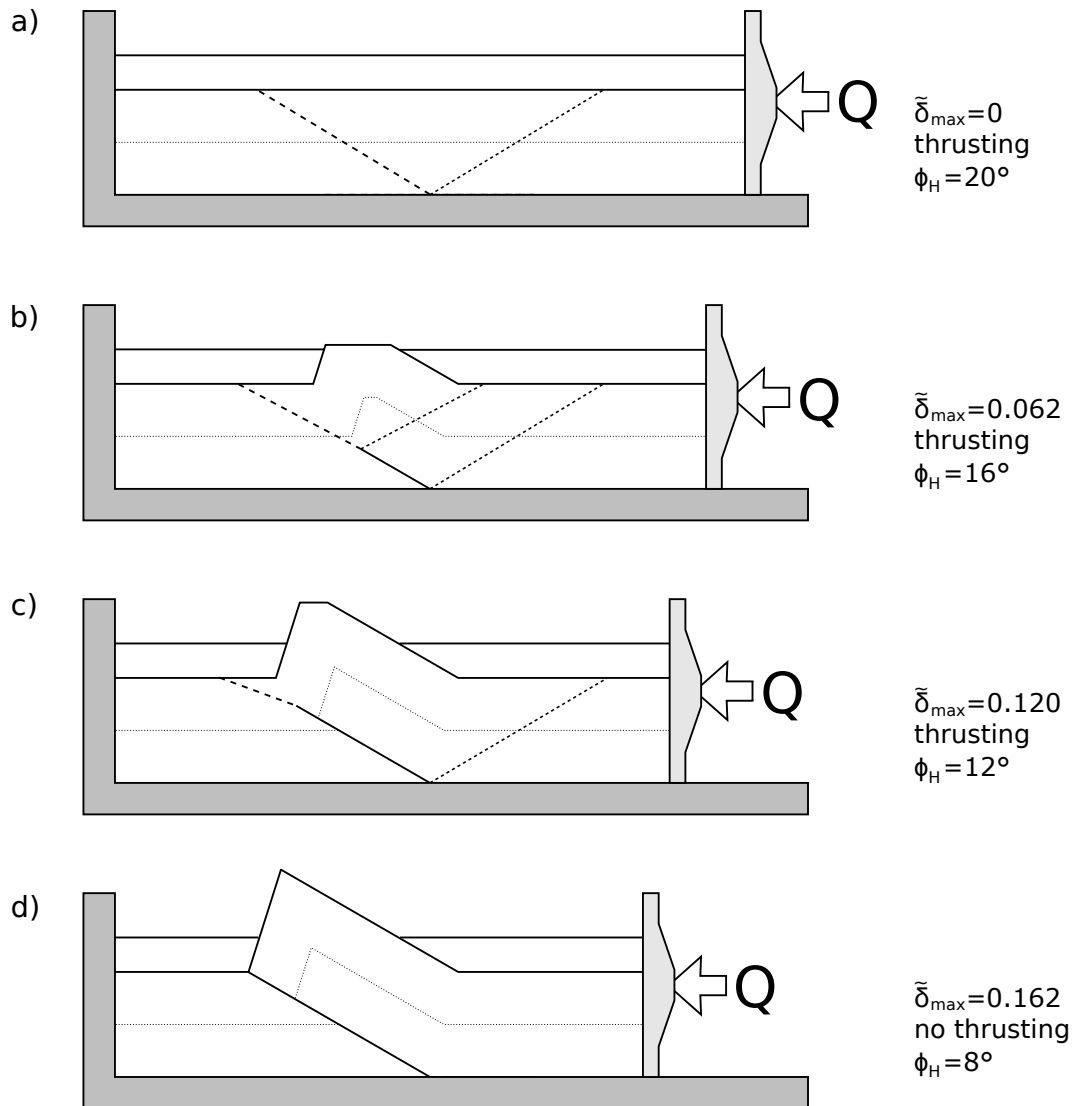


Figure 5.15: Thrusting interrupts the fault-propagation fold development at different amount of shortening depending on the fold hinge friction angle, except for case d) for which the fold development is completed before thrusting could occur. Note in c) that the thrust ramp dip is less than the fold ramp dip and that there is no upper back-thrust.

ramp after the accumulation of some amount of slip ($\phi_R \leq \phi_S$). It is thus observed that, in certain instances, the ramp dip of the thrust is influenced by the reduced friction angle of the weakened ramp of the FPF. In the last example, Figure 5.15d, the fold develops completely without being interrupted by the onset of thrusting, thanks to the small value of the hinge friction angle. In the last two examples of Figure 5.15, the fold pierces the fluid-like overburden. The thickness of this overburden has little influence on the shortening marking the end of the FPF development unless piercing of the overburden occurs.

One of the main outcomes of these comparisons is the importance of the friction angle of the hinges which are composing the fault-propagation fold. It is argued that this friction angle could be significantly smaller than the classical Coulomb friction angle of a pristine rock if slip parallel to the bedding is activated during the propagation of the hinges. This mechanics has been studied in details by Kampfer and Leroy (2009) for the development of a kink fold as well as by Maillot and Leroy (2003) for the back-thrust of a fault-bend fold. Key to the weak hinges of the kink fold was the introduction of a compacting deformation mechanism in the intrados of every bed crossed by the hinge. Here we are assuming simply that the hinge friction angle is smaller than the pristine rock friction angle without introducing explicitly the details of the hinge mechanisms nor any compaction mechanism. Extending the present analysis to include the detailed hinge geometry and property could certainly be done in the future especially if field data were available to constrain the spacing of the bedding and laboratory experiments to quantify the bedding friction and the exact nature of this compaction mechanism.

In the meanwhile, it could be argued that the necessity to reduce our hinge friction angle is needed to palliate to the fact that the kinematics of the fold-propagation fold is not yet optimized. Such optimization is certainly important since we have seen here that an optimized thrust could lead to the reduction in the applied force by up to 45 %. An optimized fault-propagation could thus be more competitive with respect to the thrust with yet a large hinge friction angle. Optimizing the fault-propagation fold is a work by itself beyond the scope of the present contribution and it will require to relax some of the assumptions adopted for the geometrical constructions. Choosing which assumption to relax, or which set of geometrical rules to choose, should be guided by comparisons with field examples (Jamison, 1987; Suppe and Medwedeff, 1990). One assumption which is known not to be optimum is the choice of orienting the back-thrust at half the complementary angle of the ramp. This point was discussed by Maillot and Leroy (2003) from the theory and Maillot and Koyi (2006) and Koyi and Maillot (2007) from the results of laboratory analogue experiments and field observations. The second assumption is the rate of propagation of the ramp. This rate in this contribution is either controlled by the FPF construction or is instantaneous if thrusting is dominant. A continuous transition from fold-control to

thrust-control would be of interest.

The optimization of the FPF could be unsuccessful or the field evidences for weak hinges missing pointing to a limited applicability of the FPF geometrical construction. In that instance, it is reasonable to study other folding mechanisms that the FPF such as the tri-shear (Erslev, 1991) where there is a smooth transition in the velocity field in a triangular zone ahead of the propagating thrust instead of the FPF hinges. The velocity field was provided by Zehnder and Allmendinger (2000). The mechanics of this tri-shear construction was considered by Johnson and Johnson (2002) for a viscous-fluid rheology but the equivalent analysis for frictional, cohesive and compacting materials is yet to be considered. The maximum strength theorem considered in this contribution does provide the appropriate framework for this purpose.

Acknowledgments: This work is part of the first author's doctoral thesis which is supported by Shell, Rijswijk, The Netherlands. Authorization to publish was requested from Shell, Rijswijk, The Netherlands.

5.7 Appendix 1 : Hadamard's jump condition

The objective of this Appendix 1 is to study the structure of the jump in the velocity field across a propagating hinge analysed as a singular surface of order 1. The general concepts are first introduced to obtain Hadamard's jump condition and the consequences for the velocity field across a hinge propagating a simple shear mode of deformation is then studied

5.7.1 Geometry and kinematics

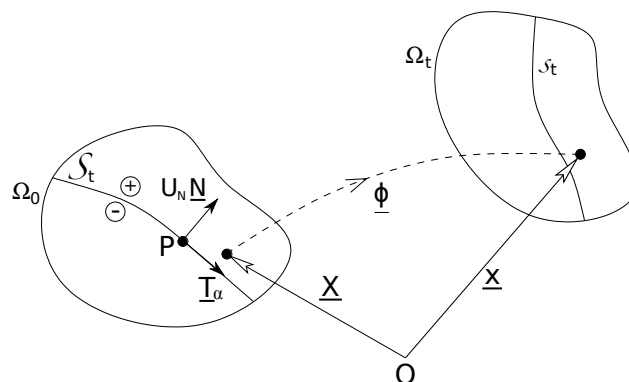


Figure 5.16: The singular surface \mathcal{S}_t in the current domain Ω_t is mapped back in the reference domain Ω_0 to the surface \mathcal{S}_t which has the local propagating speed U_N in the direction of the unit normal \underline{N} .

Consider the material domain Ω_t , in the current configuration κ_t , which was occupying initially the domain Ω_0 , in the reference configuration κ_0 . Material points in the current and reference configurations are located by the vectors \underline{x} and \underline{X} , respectively, Figure 5.16. The mapping between the two configurations

$$\begin{aligned}\Omega_0 &\rightarrow \Omega_t \\ \underline{X} &\rightarrow \underline{x} = \underline{\phi}(\underline{X}, t),\end{aligned}\tag{5.41}$$

is continuous in space and thus invertible at any time. The smooth surface \mathcal{S}_t is propagating in the domain Ω_t and is mapped back to the reference configuration by $\underline{\phi}^{-1}$ to correspond to the surface \mathcal{S}_t migrating locally in the direction of the unit normal \underline{N} at the speed of propagation U_N , Figure 5.16. The surface \mathcal{S}_t is singular of order 1: the function $\underline{\phi}$ is continuous across \mathcal{S}_t and its spatial gradient and time derivative are discontinuous. The first objective of this Appendix is to define these discontinuities or jumps. Non-material points on this surface are positioned by the vector \underline{p} which must respect the condition

$$\mathcal{S}_t(\underline{p}, t) = 0,\tag{5.42}$$

defining the geometry of the surface in the reference configuration. This surface is smooth so that

$$\mathcal{S}_t(\underline{p} + \epsilon l^\alpha \underline{T}_\alpha, t) = 0 \quad \text{for } \epsilon \ll 1,$$

for any set of two scalars l^α , \underline{T}_α denoting the two tangent vectors to \mathcal{S}_t at point \underline{p} . Repeated greek indices imply summation from 1 to 2. A first-order development of this relation provides:

$$\mathcal{S}_t(\underline{p}, t) + \epsilon \underline{\nabla}_0 \mathcal{S}_t(\underline{p}, t) \cdot l^\alpha \underline{T}_\alpha = 0,\tag{5.43}$$

with $\underline{\nabla}_0$ the gradient operator in the reference configuration. Relation (5.43) with (5.42) apply to any set of scalar l_α and consequently the Lagrangian gradient $\underline{\nabla}_0 \mathcal{S}_t(\underline{p})$ is a vector parallel to the normal \underline{N} to the surface. During the propagation of the surface, condition (5.42) is also enforced at time $t + dt$

$$\mathcal{S}_t(\underline{p} + d\underline{p}, t + dt) = 0 \quad \text{with } d\underline{p} = U_N \underline{N} dt,$$

at a non-material point which is distant from \underline{p} by the vector $d\underline{p}$ defined by the speed of propagation times the time interval dt . A first-order development of this relation provides

$$\underline{\nabla}_0 \mathcal{S}_t(\underline{p}, t) \cdot \underline{N} U_N + \frac{\partial}{\partial t} \mathcal{S}_t(\underline{p}, t) = 0,$$

from which the propagation speed is defined by

$$U_N = -\frac{\frac{\partial \mathcal{S}_t}{\partial t}}{\nabla_0 \mathcal{S}_t \cdot \underline{N}}. \quad (5.44)$$

5.7.2 The jump conditions

The continuity of $\underline{\phi}$ across the surface \mathcal{S}_t in the current configuration, using a Lagrangian description, implies

$$\llbracket \underline{\phi}(\underline{X}, t) \rrbracket = \underline{0} \quad \text{for} \quad \underline{X} = \underline{P} \quad \text{at time } t \quad \text{and} \quad \mathcal{S}_t(\underline{P}, t) = 0. \quad (5.45)$$

The double brackets denotes the difference in the argument on the two sides of the discontinuity, oriented by the normal \underline{N} , Figure 5.16. Consider now the transformation gradient $\underline{\underline{F}}$ (also denoted $\underline{\underline{\nabla_0 \phi}}$), which is defined as the second-order tensor relating the material vector $d\underline{X}$ in the reference configuration to $d\underline{x}$ found in the reference configuration ($d\underline{x} = \underline{\underline{F}} \cdot d\underline{X}$). The jump in the transformation gradient $\underline{\underline{F}}(\underline{X}, t)$ across the surface \mathcal{S}_t is known to have the structure

$$\llbracket \underline{\underline{F}} \rrbracket = \underline{a} \otimes \underline{N}, \quad (5.46)$$

in which \underline{a} is the jump amplitude vector. Note that the vector \underline{a} can be expressed as $\underline{a} = \llbracket \underline{\underline{F}} \rrbracket \cdot \underline{N}$.

The time derivative of the jump condition in (5.45) has to be zero since it is true at all times. This derivative is computed assuming first the discontinuity at a constant position in time and second accounting for its evolution in time

$$\frac{d}{dt} \llbracket \underline{\phi}(\underline{X}, t) \rrbracket = \frac{d}{dt} \llbracket \underline{\phi}(\underline{X}, t) \rrbracket|_{\mathcal{S}_t \text{ fixed}} + \nabla_0 \llbracket \underline{\phi}(\underline{X}, t) \rrbracket \cdot U_N \underline{N} = 0. \quad (5.47)$$

The first term in the right-hand side of (5.47) is the jump in the material velocity \underline{U} since the interface is fixed in space. In the second term, the gradient operator can be moved within the difference bracket thus introducing the transformation gradient. These two remarks transform (5.47) in

$$\llbracket \underline{U}(\underline{X}, t) \rrbracket = -\llbracket \underline{\underline{F}}(\underline{X}, t) \rrbracket \cdot U_N \underline{N} = -\underline{a} U_N, \quad (5.48)$$

using the definition for the jump in the transformation gradient in (5.46).

5.7.3 Application to a simple shear mode of transformation

The transformations in the fault-propagation fold are of a simple-shear mode which propagates in undisturbed media by migration of hinges. This generic transformation is presented in Figure 5.3. The undisturbed media is on the plus side of the discontinuity and its transformation gradient is

the identity tensor $\underline{\underline{\delta}}$. The deformed region is the minus region and its transformation gradient is $\underline{\underline{\delta}} + \tan s \underline{T} \otimes \underline{N}$ in which \underline{T} is the unitary tangent vector in the plane of study (such that $\{\underline{T}, \underline{N}\}$ is a direct basis) and s the angle determining the intensity of the shear (note that $\tan s$ is a negative scalar in the example of Figure 5.3). This angle corresponds to the rotation of the dotted markers across the discontinuity. The jump in the transformation gradient is $\llbracket \underline{F} \rrbracket = \tan s \underline{T} \otimes \underline{N}$ and the amplitude vector defined in (5.46) is $\underline{a} = -\tan \alpha \underline{T}$. The jump condition (5.48) becomes in this particular case

$$\llbracket \underline{U}(\underline{X}, t) \rrbracket = \tan s \underline{T} U_N . \quad (5.49)$$

The main conclusion is that the difference in velocity between the undisturbed and the sheared regions is a vector which is directed along the tangent to the hinge and of norm equal to the product of the intensity of shear $\tan s$ times the speed of propagation of the interface U_N . This conclusion is used repeatedly in the main text to construct the velocity field of the fault-propagation fold. For that purpose consider that the minus region has the uniform velocity \underline{U}^- , a vector of norm U^- oriented along the direction dipping at the angle α ($\underline{U}^- = U^-(\cos \alpha \underline{e}_1 + \sin \alpha \underline{e}_2)$) in the orthonormal basis $\{\underline{e}_1, \underline{e}_2\}$ used in Figure 5.3). The velocity in the positive region is also uniform and assumed to be along the direction oriented by the angle at ω ($\underline{U}^+ = U^+(\cos \omega \underline{e}_1 + \sin \omega \underline{e}_2)$). The difference between those two vectors is $\tan s \underline{T} U_N$ according to (5.49) resulting in the hodogram in Figure 5.3. The law of sines for this triangular construction provides the two equations (5.49) in the main text. They define the ratio of the norms of the velocities on the two sides of the hinges as well as the relation between these norms and the product $\tan s U_N$. This law of sines applies only if the velocities are not parallel to the hinges. If one velocity is indeed parallel to the hinge, the other has to be also parallel, and the difference between the two velocities is simply $\tan s U_N$.

5.8 Appendix 2 : The locking of region no 2 of the hanging wall

The objective of this second Appendix is to confirm by a force balance analysis the finding made by the application of the maximum strength theorem that there exists of a maximum friction angle ϕ_H^c defined in (5.40) which cannot be exceeded for the region no 2 of the hanging wall to develop as a pop-up.

Consider the free-body diagram of the region no 2 presented in Figure 5.17. Three forces acts on this isolated region, the action of region no 3, \underline{R}_A , the action of region no 1, \underline{R}_B and of course the external force due to gravity $S_{ARB'} \rho \underline{g}$, where $S_{ARB'}$ is the surface of the triangular region ARB' . The hinges \mathcal{A} and \mathcal{B}' are active if the Coulomb criterion (5.18) is respected point-wise

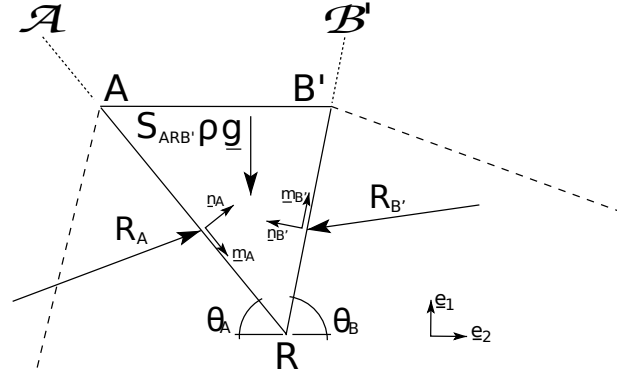


Figure 5.17: The free-body diagram of region no 2 of the hanging wall.

along them. Consequently, the two action forces could be written as

$$\begin{aligned} \underline{R}_A &= -\sigma_n^A \underline{n}_A + (C_s L_A - \sigma_n^A \tan \phi_H) \underline{m}_A, \\ \underline{R}_{B'} &= -\sigma_n^{B'} \underline{n}_{B'} - (C_s L_{B'} - \sigma_n^{B'} \tan \phi_H) \underline{m}_{B'}, \end{aligned} \quad (5.50)$$

in which σ_n^A and $\sigma_n^{B'}$ are the integral of the distribution in normal stress over the corresponding hinge (dimension of N/m). The two direct bases $\{\underline{m}_{B'}, \underline{n}_{B'}\}$ and $\{\underline{m}_A, \underline{n}_A\}$ are defined in Figure 5.17. The lengths L_A and $L_{B'}$ in (5.50) are the lengths of segments RA and RB' , respectively. Equilibrium requires the sum of all external forces to be zero

$$\underline{R}_A + \underline{R}_{B'} + S_{ARB'} \rho \underline{g} = 0, \quad (5.51)$$

which is equivalently written, in terms of the two unknowns $\sigma_n^{B'}$ and σ_n^A introduced in (5.50), as

$$\frac{1}{\cos \phi_s} \begin{bmatrix} \sin(\theta_A + \phi_H) & -\sin(\theta_{B'} + \phi_H) \\ \cos(\theta_A + \phi_H) & \cos(\theta_{B'} + \phi_H) \end{bmatrix} \begin{Bmatrix} \sigma_n^A \\ \sigma_n^{B'} \end{Bmatrix} = \begin{Bmatrix} C_s(L_A \cos \theta_A - L_{B'} \cos \theta_{B'}) \\ S_{ARB'} \rho g - C_s(L_A \sin \theta_A + L_{B'} \sin \theta_{B'}) \end{Bmatrix}. \quad (5.52)$$

There is a solution to this system unless the determinant of the 2×2 matrix is zero, a condition leading to $\sin(2\phi_H + \theta_A + \theta_{B'}) = 0$. This condition is indeed met for the critical friction coefficient ϕ_H^c defined in (5.40). The physical interpretation of this condition is that for $\phi_H = \phi_H^c$ the system of forces applied to the region no 2 is not in equilibrium. The two forces \underline{R}_A and $\underline{R}_{B'}$ are then dependent vectors: they do not balance the vertical weight of the region no 2.

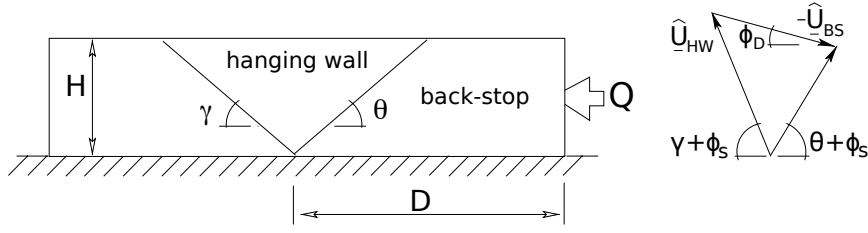


Figure 5.18: Faulting in an horizontal slab with friction on the base

5.9 Appendix 3 : Faulting in an horizontal layer with friction at the base

One of the first results of section 4 is that thrusting at the onset of the fault-propagation fold occurs with a symmetric ramp and back-thrust despite the friction at the base of the fold and the thrust. To validate this result, obtained by numerical means, the simple prototype presented in Figure 5.18 is analysed with, one more time, the maximum strength theorem presented in section 3. The frictional material and interfaces are assumed cohesionless.

The back-stop is sliding over the décollement of length D with the virtual velocity \hat{U}_{BS} of arbitrary magnitude \hat{U}_{BS} and known dip ϕ_D , the décollement friction angle. The hanging wall velocity \hat{U}_{HW} is oriented at the angle ϕ_s from the ramp dipping at the angle γ . The magnitude of this vector is selected such that the difference between these two velocities, the jump over the back-thrust, is oriented in a direction dipping at $\theta + \phi_s$. The corresponding hodogram is presented in Figure 5.18 and the law of sines reads

$$\frac{\hat{U}_{HW}}{\sin(\phi_D + \theta + \phi_s)} = \frac{\hat{U}_{BS}}{\sin(\theta + \gamma + 2\phi_s)}. \quad (5.53)$$

Application of the maximum strength theorem with these velocities provides the following dimensionless upper bound to the force necessary to initiate thrusting

$$\begin{aligned} \tilde{Q}_u &= F(\theta, \gamma) + G(\theta, \gamma) \tan \phi_D \quad (5.54) \\ \text{with } F(\theta, \gamma) &= \frac{1}{2}(\cotan \theta + \cotan \gamma) \frac{\sin(\gamma + \phi_s) \sin(\theta + \phi_s)}{\sin(\theta + \gamma + 2\phi_s)} \quad \text{and} \\ G(\theta, \gamma) &= \tilde{D} - \frac{1}{2} \left(\cotan \theta \frac{\cos(\gamma + \phi_s) \sin(\theta + \phi_s)}{\sin(\theta + \gamma + 2\phi_s)} - \cotan \gamma \frac{\cos(\theta + \phi_s) \sin(\gamma + \phi_s)}{\sin(\theta + \gamma + 2\phi_s)} \right), \end{aligned}$$

where the two functions G and F are function of the friction angle ϕ_s but not of ϕ_D . The superposed tilde in (5.54) marks the normalization with $\rho g H^2$. The minimum to this upper bound is sought in terms of the two angles θ and γ . The numerical results suggest that the partial derivatives of \tilde{Q}_u with respect to these two angles are zero for the specific and classical choice $\theta = \gamma = \pi/4 - \phi_s/2$. The objective of the rest of this appendix is to prove that such is the case.

Note that the arguments θ and γ play the same role in the definition of the function F in (5.54b) so that $F(\theta, \gamma) = F(\gamma, \theta)$. Consequently $F_{,\theta}(\theta, \gamma) = F_{,\gamma}(\gamma, \theta)$. The function G is antisymmetric with respect to its two arguments: $G(\theta, \gamma) = -G(\gamma, \theta)$. Consequently $G_{,\theta}(\theta, \gamma) = -G_{,\gamma}(\gamma, \theta)$ and, along the line $\theta = \gamma$, we find $G_{,\theta} = -G_{,\gamma} = 0$. These partial derivatives are given by

$$\begin{aligned} F_{,\theta} &= - \left(\frac{\sin(\theta + \phi_s)}{\sin(\theta)} - \frac{\sin(\theta + \gamma) \sin(\gamma + \phi_s)}{\sin(\gamma) \sin(\theta + \gamma + 2\phi_s)} \right) \frac{\sin(\gamma + \phi_s)}{2 \sin(\theta) \sin(\theta + \gamma + 2\phi_s)}, \\ F_{,\gamma} &= - \left(\frac{\sin(\gamma + \phi_s)}{\sin(\gamma)} - \frac{\sin(\theta + \gamma) \sin(\theta + \phi_s)}{\sin(\theta) \sin(\theta + \gamma + 2\phi_s)} \right) \frac{\sin(\theta + \phi_s)}{2 \sin(\gamma) \sin(\theta + \gamma + 2\phi_s)}, \end{aligned} \quad (5.55)$$

and

$$\begin{aligned} G_{,\theta} &= \left(\frac{\sin(\theta + \phi_s)}{\sin(\theta)} - \frac{\sin(\theta + \gamma) \sin(\gamma + \phi_s)}{\sin(\gamma) \sin(\theta + \gamma + 2\phi_s)} \right) \frac{\cos(\gamma + \phi_s)}{2 \sin(\theta) \sin(\theta + \gamma + 2\phi_s)}, \\ G_{,\gamma} &= - \left(\frac{\sin(\gamma + \phi_s)}{\sin(\gamma)} - \frac{\sin(\theta + \gamma) \sin(\theta + \phi_s)}{\sin(\theta) \sin(\theta + \gamma + 2\phi_s)} \right) \frac{\cos(\theta + \phi_s)}{2 \sin(\gamma) \sin(\theta + \gamma + 2\phi_s)}. \end{aligned} \quad (5.56)$$

The two partial derivatives $F_{,\theta}$ and $F_{,\gamma}$ are zero for $\theta = \gamma = \frac{\pi}{4} - \frac{\phi_s}{2}$, corresponding to the classical orientations for the failure in compression if principal stresses are Andersonian. Consequently, since $\theta = \gamma$, the two partial derivatives of G are also zero according to the property established before (5.55). The two partial derivatives of \tilde{Q}_u are thus null for this orientation. We need however to prove that it corresponds indeed to a local minimum and apply for that purpose the second partial derivative test. The determinant of the Hessian matrix is

$$M = \begin{vmatrix} F_{,\theta\theta} + G_{,\theta\theta} \tan \phi_D & F_{,\theta\gamma} + G_{,\theta\gamma} \tan \phi_D \\ F_{,\theta\gamma} + G_{,\theta\gamma} \tan \phi_D & F_{,\gamma\gamma} + G_{,\gamma\gamma} \tan \phi_D \end{vmatrix}, \quad (5.57)$$

which is explicitly

$$\begin{aligned} M &= F_{,\theta\theta} F_{,\gamma\gamma} - F_{,\theta\gamma}^2 + \tan \phi_D \left(F_{,\theta\theta} G_{,\gamma\gamma} + F_{,\gamma\gamma} G_{,\theta\theta} - 2G_{,\theta\gamma} F_{,\theta\gamma} \right) \\ &\quad + \tan \phi_D^2 \left(G_{,\theta\theta} G_{,\gamma\gamma} - G_{,\theta\gamma}^2 \right). \end{aligned} \quad (5.58)$$

To study this determinant at $\theta = \gamma = \frac{\pi}{4} - \frac{\phi_s}{2}$ first note that $F_{,\theta\theta} = F_{,\gamma\gamma}$ for any set $\theta = \gamma$. Similarly $G_{,\theta\theta} = -G_{,\gamma\gamma}$ and furthermore $G_{,\theta\gamma} = 0$ for any set $\theta = \gamma$ so that the only second derivatives required are

$$\begin{aligned}
 F_{,\theta\theta} &= \left(\frac{\sin(\phi_s)}{\sin^2(\theta)} + \frac{\sin(\gamma + \phi_s) \sin(2\phi_s)}{\sin(\gamma) \sin^2(\theta + \gamma + 2\phi_s)} \right) \frac{\sin(\gamma + \phi_s)}{2 \sin(\theta) \sin(\theta + \gamma + 2\phi_s)} \\
 &\quad + \left(\frac{\sin(\theta + \phi_s)}{\sin(\theta)} - \frac{\sin(\theta + \gamma) \sin(\gamma + \phi_s)}{\sin(\gamma) \sin(\theta + \gamma + 2\phi_s)} \right) \frac{\sin(\gamma + \phi_s) \sin(2\theta + \gamma + 2\phi_s)}{2 \sin^2(\theta) \sin^2(\theta + \gamma + 2\phi_s)} , \\
 F_{,\theta\gamma} &= \left(\frac{\sin(\theta + \gamma) \sin(\theta + \phi_s)}{\sin(\theta + \gamma + 2\phi_s)} - \frac{\sin(\theta) \sin(\gamma + \phi_s)}{\sin(\gamma)} \right) \frac{\sin(\gamma + \phi_s)}{2 \sin(\theta) \sin(\gamma) \sin^2(\theta + \gamma + 2\phi_s)} \\
 &\quad + \left(\frac{\sin(\theta + \phi_s)}{\sin(\theta)} - \frac{\sin(\theta + \gamma) \sin(\gamma + \phi_s)}{\sin(\gamma) \sin(\theta + \gamma + 2\phi_s)} \right) \frac{\sin(\theta + \phi_s)}{2 \sin(\theta) \sin^2(\theta + \gamma + 2\phi_s)} , \\
 G_{,\theta\theta} &= - \left(\frac{\sin(\theta + \phi_s)}{\sin(\theta)} - \frac{\sin(\theta + \gamma) \sin(\gamma + \phi_s)}{\sin(\gamma) \sin(\theta + \gamma + 2\phi_s)} \right) \frac{\sin(2\theta + \gamma + 2\phi_s) \cos(\gamma + \phi_s)}{2 \sin^2(\theta) \sin^2(\theta + \gamma + 2\phi_s)} \\
 &\quad - \left(\frac{\sin(\phi_s)}{\sin^2(\theta)} + \frac{\sin(\gamma + \phi_s) \sin(2\phi_s)}{\sin(\gamma) \sin^2(\theta + \gamma + 2\phi_s)} \right) \frac{\cos(\gamma + \phi_s)}{2 \sin(\theta) \sin(\theta + \gamma + 2\phi_s)} .
 \end{aligned} \tag{5.59}$$

These second derivatives for the specific orientation $\theta = \gamma = \frac{\pi}{4} - \frac{\phi_s}{2}$ read

$$\begin{aligned}
 F_{,\theta\theta} &= B \sin(\gamma + \phi_s) , \\
 G_{,\theta\theta} &= -B \cos(\gamma + \phi_s) , \\
 F_{,\theta\gamma} &= 0 , \\
 \text{with } B &= \left(\frac{\sin(\phi_s)}{\sin(\gamma)} + \frac{\sin(\gamma + \phi_s) \sin(2\phi_s)}{\sin^2(2\gamma + 2\phi_s)} \right) \frac{1}{2 \sin^2(\gamma) \sin(2\gamma + 2\phi_s)} .
 \end{aligned} \tag{5.60}$$

These results combined in (5.58) provide

$$M = \frac{B^2}{\cos^2(\phi_D)} \left(\sin^2(\gamma + \phi_s) - \sin^2(\phi_D) \right) , \tag{5.61}$$

The determinant is thus positive as long as $\sin^2(\gamma + \phi_s) > \sin^2(\phi_D)$. This relation is always met in practice since $\gamma + \phi_s > \phi_D$ and $\gamma + \phi_s \leq \pi/2$. The former condition is sufficient for the first component of the Hessian in (5.57) to be positive. So we can conclude that the angles $\theta = \gamma = \frac{\pi}{4} - \frac{\phi_s}{2}$ correspond to a local minimum to the bound \tilde{Q}_u , regardless of the value of the friction angle on the décollement.

References

- Braun, J. and Sambridge, M., 1994. Dynamical Lagrangian Remeshing (DLR): A new algorithm for solving large strain deformation problems and its application to fault-propagation folding. *Earth and Planetary Science Letters* 124, 211-220.
- Cubas, N., Leroy, Y.M. and Maillot, B., 2008. Prediction of thrusting sequences in accretionary wedges. *Journal of Geophysical Research* 113, B12412, doi:10.1029/2008JB005717.
- Chester, J.S. and Chester, F.M., 1990. Fault-propagation folds above thrusts with constant dip. *Journal of Structural Geology*, Vol. 12, No. 7, 903-910.
- Erslev, E., 1991. Trishear fault-propagation folding. *Geology*, Vol. 19, 617-620.
- Hardy, S. and Finch, E., 2007. Mechanical stratigraphy and the transition from trishear to kink-band fault-propagation fold forms above blind basement thrust faults: A discrete-element study. *Marine and Petroleum Geology*, 24, 75-90.
- Hardy, S., 1997. A velocity description of constant-thickness fault-propagation folding. *Journal of Structural Geology*, Vol. 19, No. 6, 893-896.
- Jamison, W., 1987. Geometric analysis of fold development in overthrust terranes, *Journal of Structural Geology*, 9, 207-219.
- Johnson, K.M. and Johnson, A. M., 2002. Mechanical models of trishear-like folds. *Journal of Structural Geology*, Vol. 24, 277-287.
- Kampfer, G. and Leroy, Y.M., 2009. Imperfection and burial-depth sensitivity of the initiation and development of kink-folds in laminated rocks. *J. Mech. Phys. Solids*, 57, 1314-1339, 2009.
- Koyi, H.A. and Maillot, B., 2007. Tectonic thickening of hanging wall units over a ramp, *Journal of Structural Geology*, 29, 924-932.
- Maillot, B. and Leroy, Y.M., 2003. Optimal dip based on dissipation of back-thrusts and hinges in fold-and-thrust belts. *Journal of Geophysical Research*, 108, B6, 2320-2336.
- Maillot, B. and Leroy, Y.M., 2006. Kink-fold onset and development based on the maximum strength theorem. *Journal of the Mechanics and Physics of Solids*, 54, 2030-2059.
- Maillot, B. and Koyi, H., 2006. Thrust dip and thrust refraction in fault-bend folds : analogue

- models and theoretical predictions, *J. Struct. Geology* 28, 36-49.
- Mercier, E., Outtani, F. and Frizon de Lamotte, D., 1997. Late-stage evolution of fault-propagation folds: principles and example. *Journal of Structural Geology*, Vol.19, No. 2, 185-193.
- Mitra, S., 1990. Fault-propagation folds: geometry, kinematic evolution and hydrocarbon traps. *Bulletin of the American Association of Petroleum Geologists* 74, 921-945.
- Mosar, J. and Suppe, J., 1992. Role of shear in fault-propagation folding. in *Thrust Tectonics*, edited by K. R. McClay, 123-137, Chapman and Hall, London.
- Outtani, F., Addoum, B., Mercier, E., Frizon de Lamotte, D. and Andrieux, J., 1995. Geometry and kinematics of the South Atlas Front, Algeria and Tunisia. *Tectonophysics* 249, 233-248.
- Salençon, J., 1974. *Théorie de la plasticité pour les applications à la mécanique des sols*. edited by Eyrolles, Paris, (English translation : *Applications of the theory of plasticity in soil mechanics*, John Wiley & Sons Ltd, Chichester, 1977).
- Salençon, J., 2002. *De l'élasto-plasticité au calcul à la rupture*. Editions École Polytechnique, Palaiseau, and Ellipses, Paris.
- Salvini, F., and Storti, F., 2001. The distribution of deformation in parallel fault-related folds with migrating axial surfaces: comparison between fault-propagation and fault-bend folding. *Journal of Structural Geology*, Vol. 23, 25-32.
- Suppe, J., 1983. Geometry and kinematics of fault-bend folding. *American Journal of Sciences* 283 (7), 684-721.
- Suppe, J. and Medwedeff, D. A., 1984. Fault-propagation folding. *geological Society of America Bulletin*, Abstracts with programs 16, 670.
- Suppe, J. and Medwedeff, D. A., 1990. Geometry and kinematics of fault-propagation folding. *Eclogae Geologicae Helvetiae*, 83, 409-454.
- Wilkerson, S. M. and Medwedeff, D. A., 1991. Geometrical modeling of fault-related folds: a pseudo-three-dimensional approach. *Journal of Structural Geology*, 13, No. 7, 801-812.
- Zehnder, A. T. and Allmendinger, R. W., 2000. Velocity field for the trishear model. *Journal of Structural Geology*, 22, 1009-1014.

Part II

Fracturing and Joints

Chapter 6

Introduction

The second part of this thesis is concerned with the development of fractures and joints in layered rocks from the experimental, numerical and analytical point of view. The results presented in Chapter 7 to 9 are preceded by this short introductory chapter to the topic.

The base for the following discussion are three reviews which are essential contributions to the subject of fracturing. The book *Rock Joints, The Mechanical Genesis* written by G. Mandl, first published in 2005, gives a concise overview on the mechanics of several kinds of jointing. Price & Cosgrove (1990) dedicate a full chapter of their book to the subject of fracturing. Pollard & Aydin (1988) provide a detailed review on the understanding of jointing over the past century. I will not even try to repeat their work and prefer to focus on the elements which are the most relevant for the discussion in the next chapters. After explaining the difference between tension and extension fractures, two frequently discussed theories for joint spacing from the mid 1960s are presented. They are at the basis of the development in more recent years, discussed afterwards.

6.1 Tension fractures and axial splitting

Figure 6.1 and a close up in Figure 6.2 are taken from an outcrop in the Bristol Channel at Lilstock Beach, UK. Whittaker & Green 1983 described the 5-40 cm thick limestone beds interlayered with up to 300 cm thick shale layers. The fractures have been extensively studied by Rawnsley et al. 1998 and Engelder et al. 2001. According to the nomenclature of Mandl's book, this kind of fractures are named tension fractures and occur because the maximum principal effective stress exceeds the tension strength (σ_t) of the rocks (Figure 6.4).

A field trip in the SW of England on the topic of folding brought me to Bude. Besides the chevron folds discussed in the first part of this thesis we could also see fractures in layered sandstone-shale sequences. Figure 6.3 shows an interesting alignment of fractures in a sand-

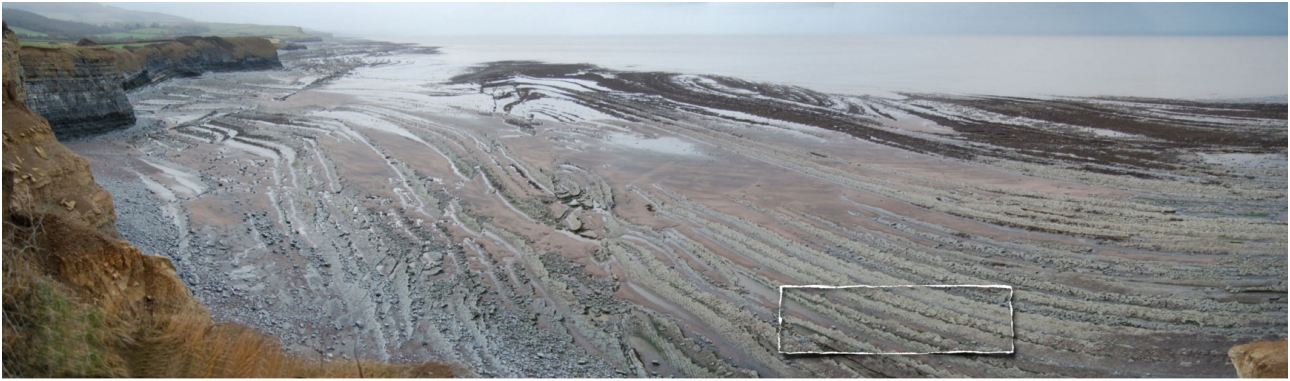


Figure 6.1: Several sets of tensile fractures are exposed in Lilstock/Bristol Channel, UK. The marked region is chosen for a close up in Figure 6.2.



Figure 6.2: Close up of Figure 6.1 showing the different sets of fractures which can be observed in Lilstock /Bristol Channel, UK.

stone layer which cannot be explained by the tensile stress explanation used for the fractures in the Bristol Channel. This dense fracture spacing leads to a second interpretation and is the result of axial splitting, also referred to as extensional fractures. This kind of brittle failure is observed when a principal effective stress is close to zero and the other one reaches the uniaxial compressive strength. The Mohr circle on the left side in Figure 6.4 presents this stress state in uniaxial compression. Looking at this Mohr construction, a paradox is visible. In general, a circle which touches the failure envelope defined by the line dipping with the friction angle ϕ is supposed to result in a fault dipping at $\pi/4 - \phi/2$ with respect to the least principle effective stress. This is not the case, when the maximum stress is almost zero. The reason for that can be found in the micro structure of the rock. Flaws, heterogeneities in the stiffness of grains and matrix and other imperfections are initiating fractures which coalesce to form macroscopic fractures parallel



Figure 6.3: Extension fractures (axial splitting) due to a local increase of the vertical stress in combination with releasing horizontal stress. (Bude, SW-England)

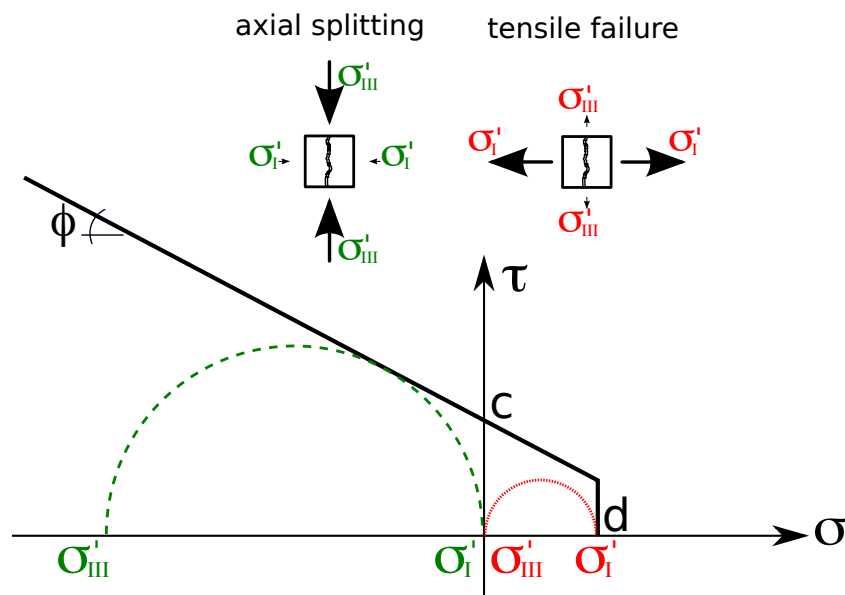


Figure 6.4: Mohr circles for axial splitting and tension fractures. The strength domain is a truncated Mohr-Coulomb criterion, defined by the cohesion c , the tensile strength d and the angle of internal friction ϕ . Axial splitting occurs at effective stress states similar to uniaxial compression as illustrated by the green dashed Mohr circle. The fractures appear parallel to the maximum compression and open in the direction of minimum compression. Tension fractures are observed, when the maximum principal effective stresses are higher than the tensile strength of the material (red Mohr circle on the right).

to the direction of maximum compression. The fractures are opening then in the direction of the maximum effective stress. These kind of fractures can result in very small fracture spacings in a layered stratum. This paradox between micro and macro failure is extensively discussed by Mandl (2005).

My thesis addresses tension fractures in layered sequences, although extensional fractures were also observed in analogue experiments. However, the knowledge of both types of fractures is important for predicting the permeability of fractured reservoirs and hence a lot of efforts have been done to understand these processes.

6.2 Hobbs and Price's contributions

The two, probably most cited approaches which provide the fracture spacing as a function of the bed thickness are the frictional coupling model of Price (1966) and the welded layer model of Hobbs (1967).

6.2.1 Frictional coupling model by Price

Price disregards the construction of the real stress distribution within the fractured layer. He simply states that the sum over the maximum activated shear stress τ along an observed stripe of the bedding plane is $LW\sigma_n \tan \phi$, with L the length, W the width, σ_n the normal stress on that bed and ϕ the friction angle of the interface (Figure 6.5). This resulting shear force acting on the observed stripe of the bedding is applied on the top and lower surface of the confined brittle layer. For equilibrium, the horizontal stress within the layer has to be tensile. The minimum length which is needed to raise the stress up to the tensile strength d within the layer of thickness H and to create a fracture reads

$$L = \frac{dH}{2\sigma_n \tan(\phi)} . \quad (6.1)$$

This simple argument based on mechanical equilibrium and tensile strength defines the fracture spacing as a linear increasing function of the bed thickness (H). One could complain that the stress distribution along the activated interface is not constructed. The description of a statically admissible stress field, satisfying the boundary conditions is thus not established. However, the approach by Price takes into account the *maximum possible shear stress* which can be transferred over an interface. A fully activated bed cannot increase the stress within the fractured layer any more, considering the normal stress on the interface as resting constant. Hence, Price's model provides a minimum for the fracture spacing (Mandl 2005). In the next chapter, when discussing

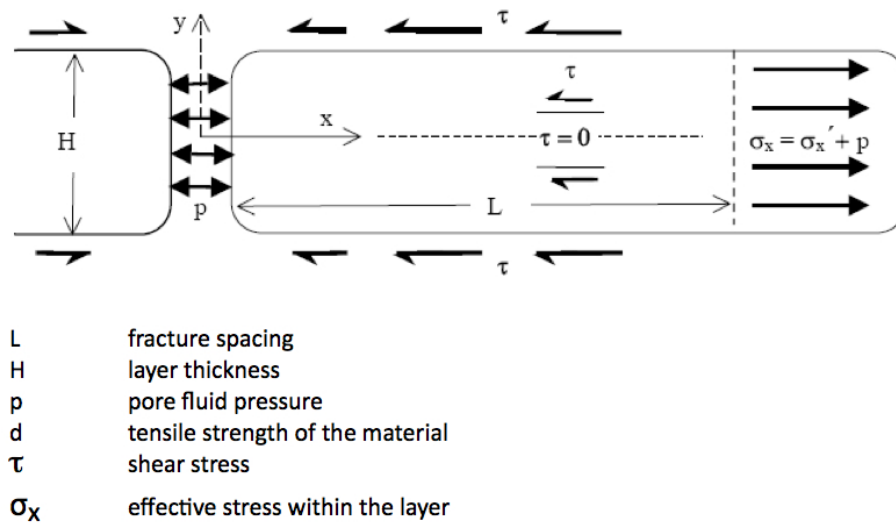


Figure 6.5: Price fracture model assuming frictional coupling and an average shear stress transfer over the bedding (modified from Mandl 2005).

the results of the analogue experiments with gypsum powder, this approach will help us to find a reasoning for reaching the saturated stage of fracturing. The finite element analysis which follows in Chapter 8 will show that although an elastic interface is assumed, delamination occurs next to the interface on the boundary of the brittle layer. The analytical approach which is the subject of Chapter 9 of this thesis will show the importance of delamination along the interface in order to reach a finite minimum fracture spacing.

6.2.2 Welded layer model by Hobbs

Hobbs argued that the physical properties of the fractured layer and of the surrounding rock beds, the thickness of the rock bed and the amount of tectonic deformation define the joint frequency. His prototype consists of a brittle layer surrounded above and below by elastic layers with a thickness much larger than the brittle layer. No slip is accounted for along the interfaces between the brittle and the elastic layers which are supposed to be welded together. The right vertical boundary of the domain is displaced to provide extensional deformation to the layers, Figure 6.6.

The first fracture in the brittle layer is created as soon as the increase in the average horizontal stress due to the elastic extension reaches the tensile strength of the material. The jointed layer tries then to contract horizontally due to the new stress free joint surface. The displacement is prohibited at the contacts of the neighbouring units which results in an additional shear stress $\tau_y(y)$ in the surrounding layers. The shear stress distribution is assumed to be linearly decreasing to become negligible at the depth, assumed to be equal to the thickness of the jointed bed H_1 . The

stress σ_x is assumed to be constant in the x -direction, an assumption which is questioned by Mandl for the sake of equilibrium.

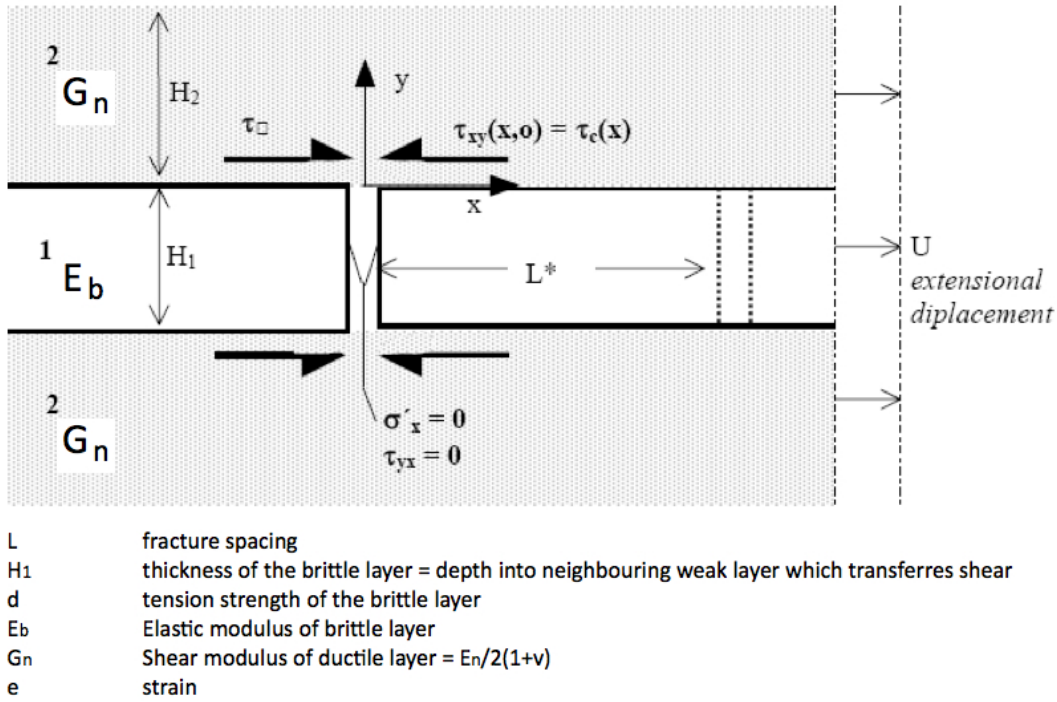


Figure 6.6: Hobbs fracture model assuming welded layers (modified from Mandl 2005).

The stress in the elastic layers increases with further stretching to the prototype. There is a transfer of shear over the interface to the fractured layer till the average horizontal stress reaches again the tensile strength of the brittle material and the next generation of fractures occurs. Between two neighbouring fractures, the increase in the horizontal stress has a hyperbolic distribution with the maximum tensile stress at midway between the two fractures. It is there where the next new fractures will thus appear. Following this approach, fracture spacing is proportional to the bed thickness of the brittle layer, the square root of Young's modulus of the brittle layer (E_b) and the inverse of the square root of the shear modulus of the neighbouring beds (G_n). The spacing of the second fracture L_2 is given by

$$L_2 = H_1 \left(\frac{E_b}{G_n} \right)^{\frac{1}{2}} \cosh^{-1} \left(\frac{e_2}{e_2 - e_1} \right), \quad (6.2)$$

with

$$e_1 = \frac{d}{E_b},$$

e_2 being the applied strain at the creation of the second fracture set and e_1 the strain at which the first fracture occurs. This theory predicts that joint spacing is increasing with increasing tectonic

deformation up to an infinite number of fractures. The formation of fractures does not occur continuously with applied strain but periodically since the stress has to build up repeatedly to reach the tensile strength. This is in contrast to Price's theory which predicts fracture spacing for a stage of deformation, when the whole interface is activated and no further fractures are created.

However, Hobbs welded layer model of fracturing has some weak points which are discussed at length by G. Mandl (2005) and by Bai & Pollard (2000). It is mentioned that the assumed stresses do not respect mechanical equilibrium. Hobbs also disregards pre-stress and pore fluid pressure. Furthermore, he considers stresses and displacements only in cross sectional averages and thanks to the choice of the shear stress penetration depth equal to the bed thickness H_1 of the brittle layer, he obtains that the fracture spacing scales indeed with H_1 .

Mandl extended Hobbs' approach to thin interlayers but also developed a theory which does not average the stress field. He concluded that a compressing zone between two adjacent fractures appears for a small enough spacing because of the relaxation within the fractured layer. This compression zone in the middle of the layer thickness will stop further fracturing as soon as the release of strain energy is less than the energy which is consumed during fracturing.

Mandl also advocates the use of fracture mechanics which was applied by Bai & Pollard, 2000. They measured stress intensity factors in front of a propagating crack through a heterogeneous stress field. The predefined path of the fracture begins in an extensional region and ends in a zone with compressional stresses. The length of the fracture increases during the propagation and thus also the stress intensity factor K_I changes during crack propagation. As long as $K_I - K_{Ic}$ is positive the fracture continues to grow. Negative values for K_I are of course unrealistic and correspond to closing the fractures. Keeping the crack tip constant while increasing the applied strain results in linearly increasing horizontal stress ($\sigma_{xx} = f(K_I)$) within the layer. There will always be a sufficiently large value for the applied strain applicable, due to the welded layer approach, so that the stress raises to a level at which the crack propagates. Hence, the fracture toughness is not relevant for the minimum possible fracture spacing. Note that this statement is valid as long as delamination is disregarded.

The knowledge of the fracture toughness is thus not necessary, as its value will only affect the magnitude of the applied strain at which crack propagation occurs. Mandl concludes, using this remark, that the minimum ratio of fracture spacing and layer thickness is 0.55.

6.3 Fracture spacing as a function of the bed thickness

The following subsections give an overview on the experimental and theoretical outcomes on the fracture spacing and fracture patterns in layered rocks.

6.3.1 Analogue experiments and field observations

The experiments by Garrett & Bailey (1977) were conducted on specimens of a 90° cross-ply glass-reinforced polyester. Different specimen thicknesses were exposed to tension and fracturing occurred. They measured the fracture spacing (see Figure 6.7) and observed that the average distance between two neighbouring fractures increases linearly with the thickness of the transverse-ply.

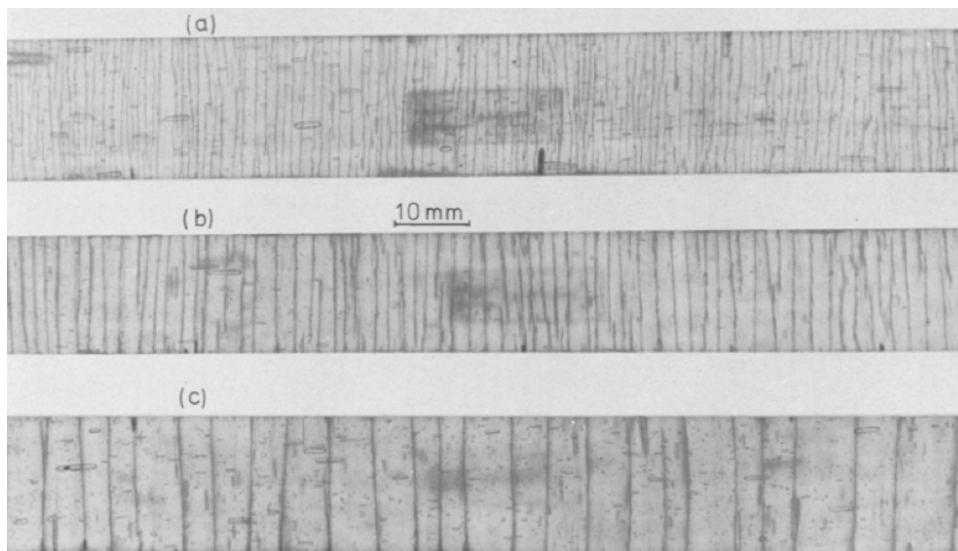


Figure 6.7: Transverse cracking in specimens with transverse-ply thickness of (a) 0.75 mm, (b) 1.5 mm and (c) 2.6 mm, strained to 1.6 % (Garrett & Bailey, 1977).

The relationship between fracture spacing and bed thickness was discussed by Ladeira & Price (1981). They analysed numerous measurements from greywacke (UK and Portugal) and limestone (Portugal) with different interlayer thicknesses consisting of Shales, which are presented in Figure 6.8a. They concluded that the data can be represented by two straight lines (Figure 6.8b) which are the result of two different mechanisms controlling the fracturing. The first relationship (OA) shows a linear increase of fracture spacing with increasing bed thickness. The failure mode which is leading to this trend is due to extensional strain. The second relationship (BC) shows a fracture spacing, which is not sensitive to the bed thickness and is explained by hydraulic fracturing. The distance between fractures created by this second mechanism is thought to be related

to the gradient in fluid pressure, caused by the drop of pressure in the opened fracture. The next fracture can thus only be created at a distance from the existing fractures where the fluid pressure is not affected any more. The gradient and thus the fracture spacing is function of the permeability of the unfractured rock and the rate of fracture propagation. Hence, high rates and a high permeability lead to dense fractures.

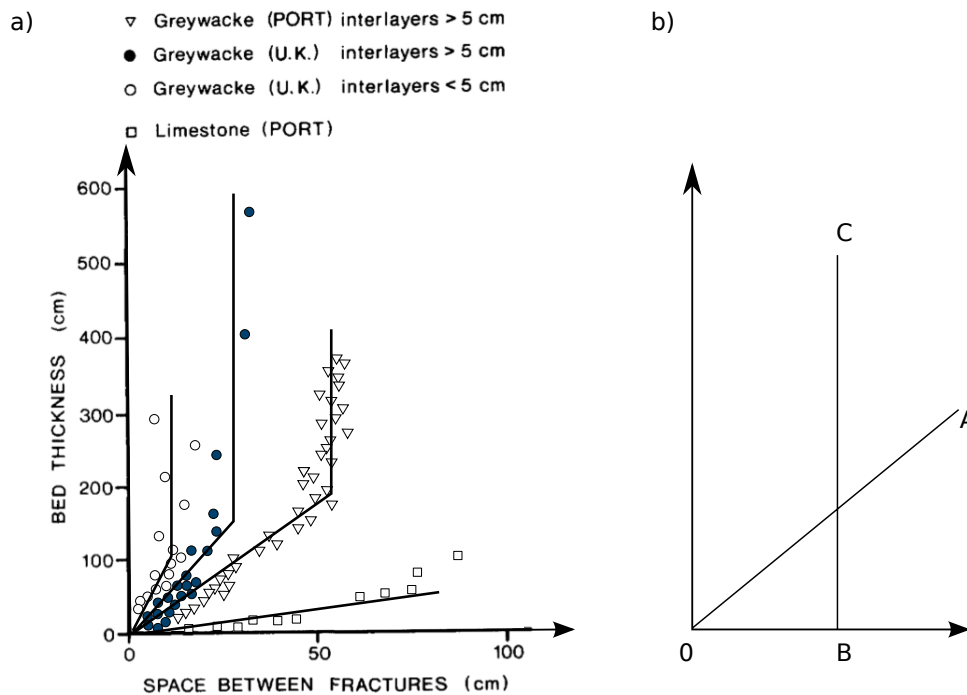


Figure 6.8: In (a) the relationship between fracture spacing and bed thickness for different rock types is presented. Each point represents the mean of at least 50 readings. In (b) two general relationships between fracture spacing on the horizontal axis and the bed thickness on the vertical axis can be seen. The trend (OA) is linearly increasing and represents fracturing due to extensional strain. The second relationship (BC) is not sensitive to the bed thickness and represents a uniform fracture spacing due to hydraulic fracturing (modified from Ladeira & Price, 1981).

Narr & Suppe (1991) investigated the joint spacing in sedimentary rocks at coastal exposures in central California in a sequence of inter-bedded siliceous shale, chert, phosphatic shale, mudstone and dolostone. The measured ratios of layer thickness to joint spacing which is called the fracture spacing index (FSI) is constant at 1.3 for the observed outcrops and the frequency distribution of the fracture spacing is log-normal. The FSI is constant over different lithologies over a substantial region on the surface which means that the fracture spacing is increasing linearly with bed thickness. However, the FSI is much less in an oil field in the same region where the rocks have not undergone uplift and cooling. In addition a simulation with Hobbs' model was

done. Including macroscopic flaws which weaken the fractured layers, the predicted fracture frequency distribution was similar to the one at the outcrops.

Rives et al.(1992) worked on the statistical distribution of fracture spacing based on outcrop studies and analogue experiments. The analogue experiments consisted of applying cylindrical bending to a partly alcohol treated polystyrene plate, Figures 6.9a. They propose that the spacing within a fractured layer follows three different distribution laws, depending on the stage of applied extension. Close to the initiation of the first fracture, the distribution is negative exponential and it is a log-normal distribution in an intermediate stage (Figures 6.9b). When fracturing reaches a saturated stage at which no further fractures are created, the fracture spacing has a normal distribution. Using a statistical approach (geometry of fractures) they were able to recreate fracture patterns numerically under the assumption that fractures initiate randomly and by including a minimum fracture spacing corresponding to fracture saturation. In 1994, Rives et al. reported the simulation of natural orthogonal joint set formation in brittle varnish. which are presented in Figures 6.9c and (d). PVC plates covered with brittle varnish were bended cylindrically, oblique folding was induced by torsion or direct traction was applied. Three modes were identified which can create a second set of fractures: relaxation effects (c), slight tension due to warping of the bands defined by the first parallel fractures or (d) stress inversion. In the analogue experiments with gypsum powder, which are discussed in the next chapter, it is found that the distribution of the fracture spacing is log-normal, when no further fracturing could be observed. In addition, strain inversion resulted in a ladder type pattern which develops to form strike slip faults when further compression is applied to the specimen

The analogue experiments by Wu & Pollard (1995) had the objective to study the influence of the bed thickness on the fracture spacing. A brittle coating was laid on a polymethyl methacrylate substrate (PMMA plate) which were bent. They varied the thickness of the coating between 0.016 and 0.373 mm. The concept of fracture saturation has been confirmed, although spacing to layer thickness ratios were six to twenty times higher than reported from outcrops in literature (Price & Cosgrove 1990, Narr & Suppe 1991, Gross 1993). FE calculations based on fracture mechanics were done to investigate the difference between unconfined and confined layers under extension. Layered sequences under bed parallel extension are usually buried confined respectively which is in contrast to the unconfined layers in the experimental setting. They concluded that fractures in a confined layer would propagate more easily due to the higher stress level on the whole cross section which results in a higher fracture density than in the unconfined specimens in the experiments. The relationship between bed thickness and fracture spacing from the experiments can be interpreted linearly but also exponentially increasing with increasing bed thickness. Hence, there is no conclusion on that topic.

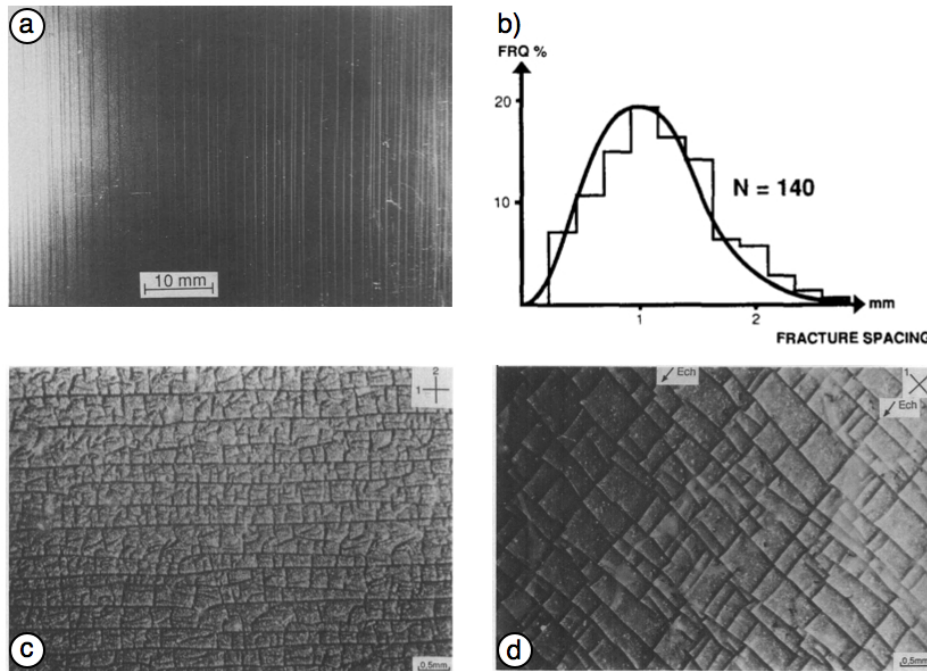


Figure 6.9: (a) shows an analogue fracture set produced by the stress cracking process in a thin plate of polystyrene. In (b) a histogram of the fracture spacing distribution at the end of an experiment is presented which is log-normal (Rives et al.1992). Orthogonal fracture patterns produced in the brittle varnish analogue models are presented in (c) and (d). (c) shows an irregular ladder pattern. The initial set develops normal to direct traction and the second set forms during relaxation. In (d) the second set is orthogonal to the first and can be arranged in stepping arrays which are parallel to the second loading (Rives et al.1994)

Mandal et al. (1994) reported a nonlinear relationship between layer thickness and fracture spacing on the basis of analogue experiments done with rigid plaster layers on a viscous substratum. Based on their study, the fracture spacing increases with the square root of the layer thickness. An experimental study with partly solidified plaster on a foam rubber substrate to study flexure induced fault population was done by Supak et al. (2006). The results lead to the conclusion that the spacing of bending fractures does not scale with the layer thickness and stretching the layers results in power law scaling of the fracture spacing which formed clusters. Chapter 7 will discuss the results of experiments done with layers of compacted gypsum powder resting on a pre-deformed foam plate. The extension is applied to the specimen by releasing the elastic deformation of the foam plate and fracturing in the specimen occurred. The linear relationship between layer thickness and fracture spacing from these experiments are in contrast to the ones reported by Mandal (1994) and Supak et al. (2006) but in agreement with Ladeira & Price (1981) and Narr & Suppe (1991). In Part III of this thesis a new experimental device

and some preliminary experimental results are presented. Specimens of gypsum powder were bent and it is observed that the fracture spacing is not sensitive to the layer thickness. Combined bending and extension showed to be dependent on the layer thickness.

Although not the whole community agrees on the existence of a linear relationship between fracture spacing and bed thickness, our new experimental results in Chapter 7 point to this kind of relationship.

6.3.2 Analytical and numerical approaches

Bai et al. (2000a, b, c) worked on the fracture spacing in layered rocks using FE-methods based on elastic fracture mechanics. Layer parallel extensional deformation is applied to a three layer model with predefined fractures in the central layer. The interface between layers have an infinite strength, corresponding to the welded layer model. They investigate the stresses between the fractures along line AA' in Figure 6.10a and varied the fracture spacing S . At a critical thickness to spacing ratio, compressional stress perpendicular to the fracture surface appears in the middle of the layer as shown in Figure 6.10b. This is further referred to as the shadow effect between two fractures and is observed for thickness to fracture spacing ratios below 0.8 and 1.2. Pre-existing fractures on the boundary of the layer show the tendency to propagate and cut through the structure for ratios of bed thickness to spacing down to 0.3. Ratios larger than 1.2 for confined layers are explained by the layers having not reached a saturated state so far. The two-layer setting with a base and a fractured top layer, both with the same material properties, lead to a fracture spacing approximately three times the layer thickness. If delamination is allowed, the fracture spacing is even larger. These qualitative results are in agreement with the observations on the fracture spacings of confined and unconfined layers by Wu & Pollard (1994).

In contrast, the Finite Element calculations which will be discussed in Chapter 8, show a different behaviour when brittle layers are attached to elastic neighbouring layers which are stretched. Although the interface cannot fail in shear, the calculations based on plasticity theory predict shear and opening failure in the brittle layer next to the interface. It is only in a second step that a tensile fracture is initiated which separates the brittle layer.

Jain et al. (2007) investigated the effects of overburden on the joint spacing in layered rocks. They used a shear-lag model, first introduced by Cox (1952), to derive the characteristic joint spacing. This approach is based on interfacial shear stress transfer between brittle and elastic neighbouring layers under extensional strain. They established a general elastic-slip model for the stress state in a layered rock system which is solved for the characteristic joint spacing as a function of layer thickness, applied strain and burial depth. Their prototype is presented in

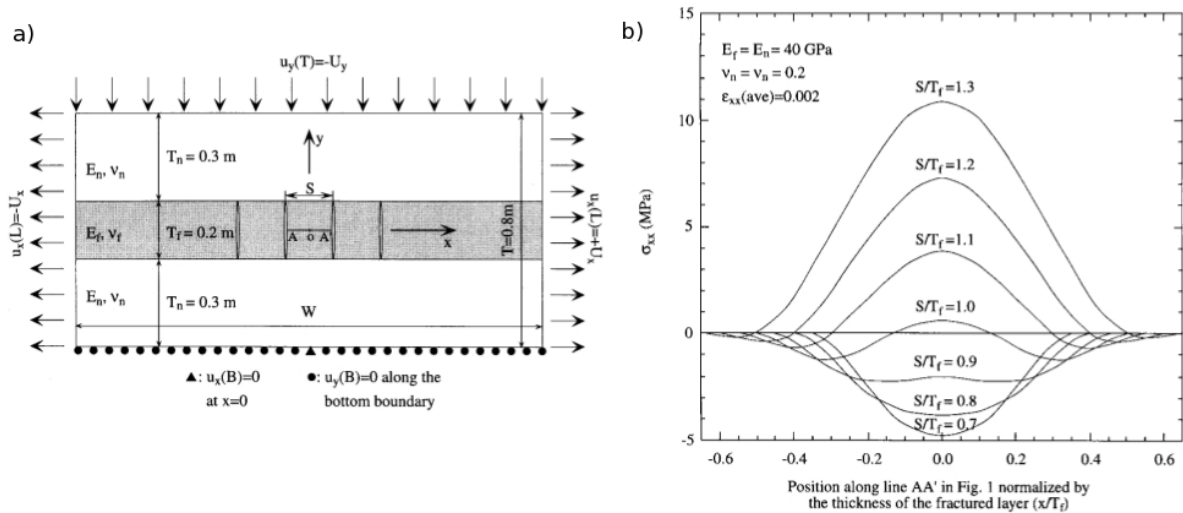


Figure 6.10: (a) FEM model and its boundary conditions of layered rocks with four equally spaced fractures in the fractured layer. The displacements are imposed along the left and right boundaries. A displacement is imposed on the top boundary of the model to simulate the effect of overburden stress. In (b) the distributions of the normal stress component in the direction perpendicular to the fractures along the line AA' in (a) as a function of fracture spacing to layer thickness ratio (S/T_f) is presented. The figure shows that there is a critical spacing to layer thickness ratio between 0.9 and 1.0, which marks the stress state transition. When the spacing to layer thickness ratio (S/T_f) is less than the critical value, the stress is compressive, whereas, when it is greater than the critical value, the stress in the middle of the plot line becomes tensile (from Bai & Pollard, 2000).

Figure 6.11a and considers a region of interfacial slip next to the fracture (region II) and bonded conditions in region I. Their analysis validates a slip-based saturation as soon as the interface between two adjoining layers is failing in shear. Their fracture spacing decreases with depth until a critical depth is reached from which the spacing increases again. The reason is found by decomposing the function for the fracture spacing in a slip-only part and a pre-stress part (Figure 6.11b). Considering only slip along the interface results in a decrease of fracture spacing with increasing depth due to increasing friction. On the other hand, the fracture spacing decreases when taking into account only the pre-stress which increases with depth. The weights of these two complementary factors are thus defining the decrease followed by an increase of the fracture spacing with depth.

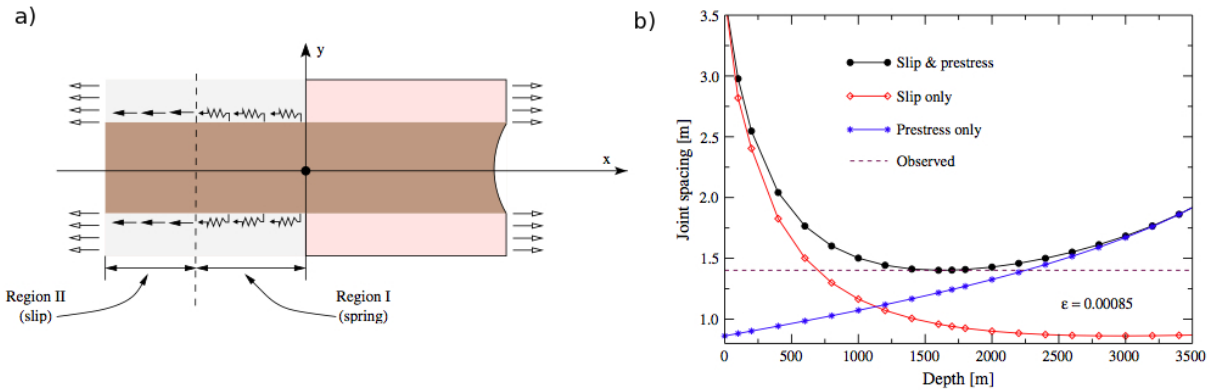


Figure 6.11: The mechanical analogue of the competent layer matrix system can be seen in (a). Notice, that a combination of interfacial slip in region II next to the fracture and bonded conditions in region I are taken into account for the calculations. In (b) the average joint spacing is shown on the basis of calculations using the slip and pre-stress (black curve), slip only (red curve) and pre-stress only (blue curve) solutions (from Jain et al. 2007)

6.4 Fracture propagation in multilayered sequences

It is frequently observed in sedimentary rocks that fractures are stopping or are shifted at the interface between beds of different lithology or mechanical properties. Helgeson & Aydin (1991) studied the behaviour of individual joints near layer interfaces as well as the interaction and communication among joints in different layers. They propose three major elements which are crucial in fracturing across interfaces, which are the strength of the interface, geometric and material properties of the adjoining layers and the loading. Finite element predictions based on elasticity provided the evolution of the stress field on both sides of an interface where a joint propagates towards the interface (Figure 6.12a). The main conclusion was, that the largest stress in the layer ahead of the joint occurs out of the plane of the approaching joint at two symmetric regions. A flaw or any other imperfection in the material decides then at which of the two sides the joint will continue. The out-of-plane offset is found to be generally proportional to the thickness of the weak interlayer. They concluded that joint propagation within a layered sequence of sedimentary rocks is controlled by the contrast of mechanical properties of adjoining lithologies and interfaces.

Cooke et al. (2001) did a numerical study on the types of fracture intersection with bedding contacts. For the simulation of a fracture approaching a frictional interface, they used a boundary element code developed by Cooke (1996). Three types of results are observed as a fracture propagates towards a bedding contact. The observed type depends on the strength properties of the interface between the layers (see Figure 6.12b). Termination of the fracture propagation is

favoured at weak interfaces and the propagation straight through is observed at strong interfaces. Moderate strength of the contact surface results in a step-over to the left or to the right.

A similar effect is observed during analogue experiments (Chapter 7) when stretching layered sequences of gypsum powder separated by different weak materials. Depending on the contrast of the cohesion of the materials straight, wavy or staircase like patterns are observed.

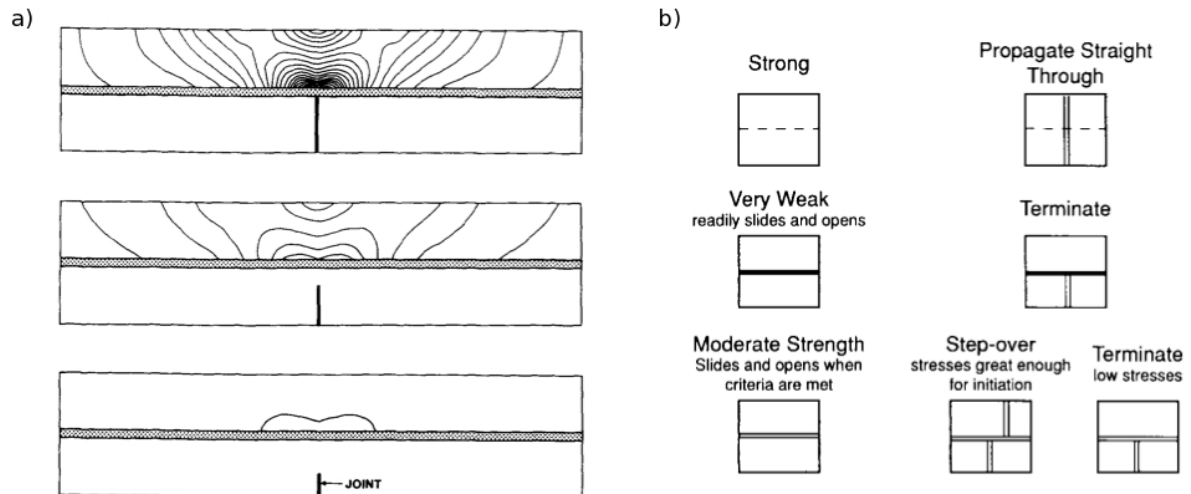


Figure 6.12: (a) Patterns of the normalized maximum principal stress in the upper, unjointed layer due solely to a joint in lower layer for three differing joint configurations is shown. The contours are symmetrical about the plane of the lower joint. It is at one of these two maxima that new joints would likely initiate (from Helgeson & Aydin, 1991). In (b) according to different strength of the bedding contacts on the left, inferred variations in the geometry of fracture-bed contact intersections (right side) are presented (from Cooke et al., 2001).

6.5 Summary

The statistical distribution of fracture spacing measured in analogue experiments reproduces those made in the field (Narr & Suppe, 1991; Rives et al., 1992). However, those statistical distributions do not provide the relationship between fracture spacing and layer thickness. Depending on the origin of the extensional strain there is an influence of the bed thickness (layer parallel extension) or not (bending fractures). In addition, different ways of deforming the specimen (cylindrical bending, torsion) and the change in loading from primary extension to compression lead to multiple sets of fracturing. The specimens showed ladder to grid type fracture patterns which are observed in the field as for example in the Bristol Channel. Theory tries to explain the

fracture saturation. One school of thought advocates the idea that weak and stiff layers within a multilayered sequence are welded. Other research groups consider an interface where slip and opening is possible. It appears that it is essential to know the interlayer or interface properties (Helgeson & Aydin, 1991; Cooke et al., 2001), for explaining the propagation of a joint from one layer to the other with step overs out of the plane of propagation. Analogue experiments did not consider so far the influence of the burial depth, nor the confining pressure of the fractured layers. Jain et al.(2006) have shown that slip along the interface defines the minimum fracture spacing. Fracture spacing is decreasing at depth because of larger stresses which can be transferred over a frictional interface. However, at large burial pressures the horizontal pre-stress cannot be overprinted by the extensional strain and becomes the dominating factor which increases the fracture spacing at saturation.

In Chapter 7, an experimental setting is introduced with cohesive powders as analogue materials. Monolayers with three different thicknesses and multilayers with different weak interlayers are examined under extension. Chapter 8 of this thesis addresses the genesis of fractures with the finite-element method and plasticity theory. A Drucker-Prager criterion truncated in tension in combination with hardening/softening rules for a solid layer is used with the aim to study the influence of delamination along the bedding planes and details of the propagation of fractures in a monolayer setting. In Chapter9, an analytical solution based on limit analysis is presented which is expected to fill the gap between the computer time intensive numerical analysis of fracturing and the analogue experiments.

Chapter 7

Analogue Experiments

This chapter summarizes results from the analogue experiments with cohesive powders performed in the Shell-laboratory in Rijswijk, The Netherlands. The objective of the study is to investigate and quantify the relationship between the loading conditions, the mechanical properties of the composing units and the fracture distribution using different types of brittle, cohesive powders. Quantitative assessments of the mechanical properties of each analogue material remain to be done before proper scaling could be conducted from the laboratory to the field scale. The experimental setup and the analogue materials are first introduced. Section three presents the results of three different types of experiments. The first type is used to investigate the influence of the layer thickness on the fracture spacing and the second type is devised to observe the impact of the number of weak interfaces, which divide a brittle unit. The third type aims at the research of the influence of a contrast in the mechanical properties of layers composing a multilayered sequence, on the fracture pattern. Additional results which have been obtained with a CT-scanner are summarized in Appendix B of this thesis.

7.1 Setup

The principle of the experimental setup is to apply extensional strain at the base of a layer consisting of compacted gypsum powder, representing a stiff mechanical unit. The idea for the used experimental setup came in my mind from the need to create opening mode fractures with the help of a loading cell. Therefore, there are differences between the experimental study by Mandal et al. (1994), Spyropoulos et al. (1999) and Supak et al. (2006) and the one which is reported in this chapter. These differences are found when comparing the used analogue materials and also the experimental protocol has not been published in literature before, as far as my knowledge is.

Longitudinal sections through the experimental setup for three preparation steps and three experimental steps are shown in Figure 7.1. The device consists of a cell 800x500x150 mm (length x width x height). The piston on the right side compresses a foam plate constrained by the back stop on the left hand side (steps T1-T2). The multilayer is built up above the preliminarily compressed foam (step T3). A thin layer of quartz sand distributes the applied deformation from the foam plate to the specimen. During the building of the specimen, two lateral sidewalls are placed temporary (see Figure 7.2). The gypsum powder is poured in the space limited by the sidewalls, the back stop and the piston. The gypsum is compacted stepwise with a 50x50 mm large indenter at an approximate pressure of 0.1 Pa. The pressure was determined by pressing the indenter with the same force on a balance. The final top surface is flattened and compressed with a steel plate with a pressure of same amplitude.

The experiment begins when the compressed foam is progressively released, as the piston moves back to its initial position (T4 in Figure 7.1). The stretching of the foam plate leads to the tensile straining of the multilayer on its top. The applied tensile deformation leads to mode I fractures. The speed of the piston is kept constant, resulting in $4.60 \cdot 10^{-5} \text{ s}^{-1}$ nominal strain rate. It is the same rate in each of the following cases unless otherwise stated. The strain rate is assumed to be uniform through the foam. This material does not behave completely elastically and has also a small viscosity. The velocity of stretching has been chosen to be sufficient small, so that that the viscous response of the foam can be neglected.

Three different types of experiments were done which are presented in Figure 7.3a to (c). Type I has for objective to show the influence of the thickness of an individual layer on the fracturing by testing in parallel three specimens 5, 20 and 40 mm thick. Type II experiments investigate the influence of dividing a mechanical unit with different numbers of weak interfaces but keeping the total thickness constant. Therefore three parallel specimen with 0, 1 and 3 interfaces are tested. Type III experiments consist of alternating sequences of gypsum with other cohesive powders to show the influence of the material properties of the weak interlayers.

The analysis of the experiments is based on photographs which are taken throughout the experiments. In addition, one extensional only and two experiments which include compression (step T5) and re-extension (step T6) were conducted with a CT-scanner. They are discussed in the Appendix B.

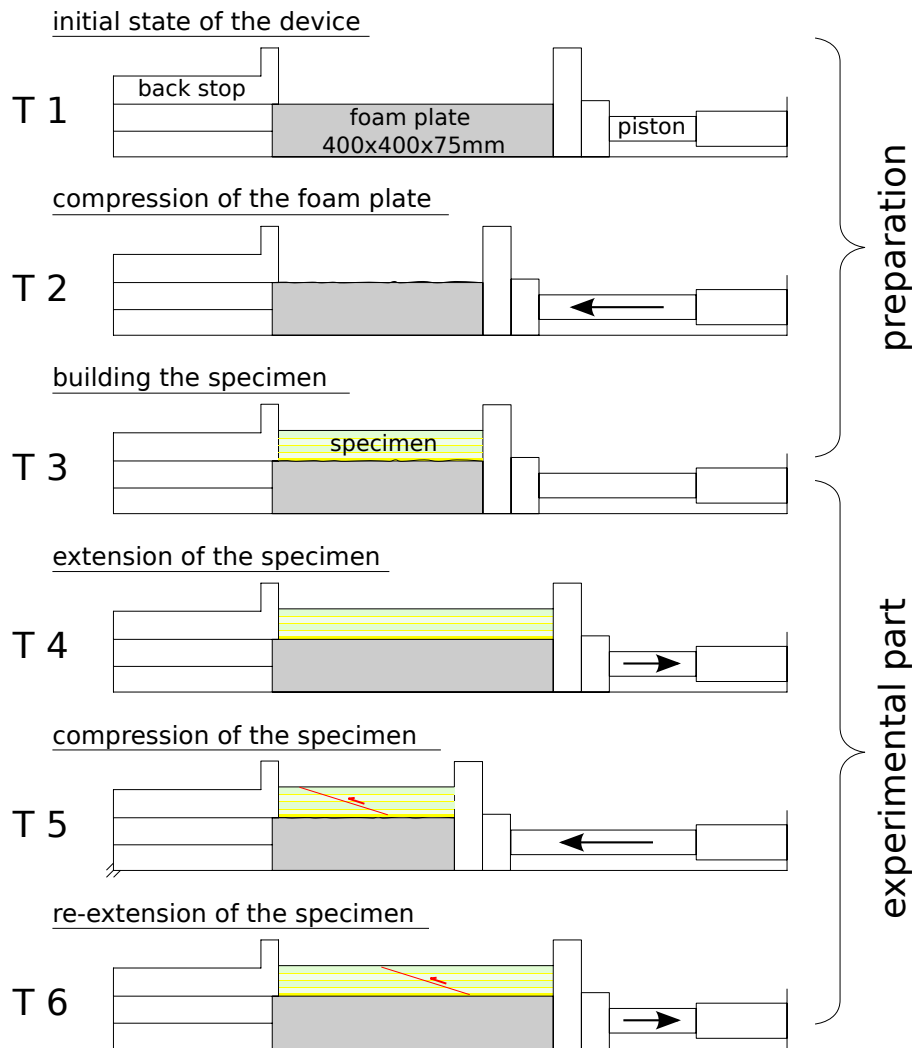


Figure 7.1: Longitudinal sections of the setup at six time steps. T1 to T3 are preparation steps and the experiment itself begins by moving back the piston towards its initial position.

7.2 Analogue Materials

A brief description of the analogue materials is provided now.

7.2.1 Gypsum powder

The stiff units in the multilayer sequences were built with compacted gypsum powder. The cohesion of this material depends on the grade of compaction. The angle of internal friction is 30 to 35° and is estimated from the angle of repose. Van Gent et al. (2009) performed experiments with gypsum powder to study normal faulting in multilayers. They also provide information on the material properties. For the experimental setup, they did not compact the gypsum by hand.

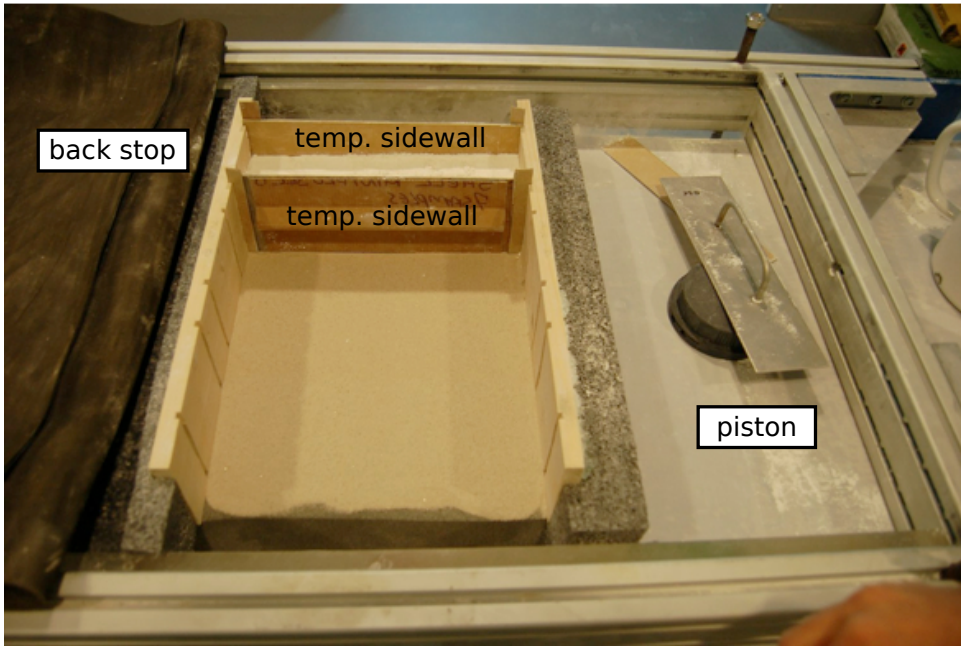


Figure 7.2: Oblique sideview of the experimental setup during preparation of the specimen. A pre-compressed foam plate with a sand layer on its top rests between the back stop on the left and the piston on the right. The specimen is limited in length by the piston and the back stop. During preparation, two temporary sidewalls are placed to ensure the intactness of the specimen during compaction.

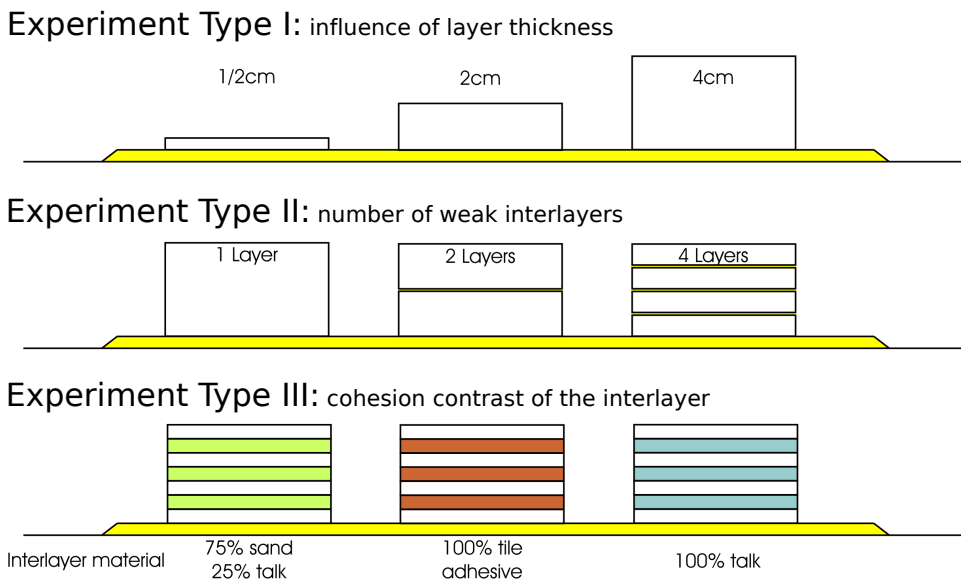


Figure 7.3: The three types of experiments which are described and discussed in the following.

Their powder was compacted by its self-weight without additional forces. Consequently, gravity sets in a vertical gradient in material strength because of the pressure sensitivity of the powder. Strength properties for gypsum powder are provided as a function of the void ratio e based on experiments. The void ratio is a function of the compaction pressure (σ) and is given by

$$e [-] = -0.17\ln(\sigma) + 3.8 , \quad (7.1)$$

the stress having the unit Pa . The cohesion (c) and tensile strength (d) are approximated by

$$\begin{aligned} c [Pa] &= -1014.1e + 2911.7 , \\ d [Pa] &= -127.33e + 391 . \end{aligned} \quad (7.2)$$

The applied compaction pressure in my experimental setting is approximately $0.1kg/cm^2$. The void ratio, the tensile strength and the cohesion are thus 2.23, 107 Pa and 646 Pa, respectively according to equations 7.1 and 7.2. The material density was not reported as a function of the void ratio by Van Gent et al. (2009) and was estimated as follows. A glass is filled with gypsum powder and is compacted. Weighting the empty glass and taking the difference to the full glass with gypsum provides the weight of the powder. The volume within the glass is known by filling it with water and determining the weight. Hence, a specific weight for the compacted gypsum powder is found to be approximately $1g/mm^3$.

7.2.2 Quartz sand

The quartz sand is in the fine sand fraction with a grain size smaller than 0.63 mm. The cohesion is almost zero and the measured angle of repose of 30° is used for the friction angle. The negligible cohesion makes quartz sand to the ideal material for separating the gypsum layers in the experiments of Type II.

7.2.3 Talc powder

For the experiments Type III, talc powder was used for generating weak interlayers. The low angle of internal friction makes this material ideal for decoupling layers of gypsum. However, its cohesion is much larger than that of the gypsum. This talc is also mixed with quartz sand to increase the cohesion and to lower the friction angle of the resulting material.

7.2.4 Tile adhesive

Tile adhesive has also been used to build interlayers. This powder is less cohesive than the gypsum based on observation of the free standing height but forms an angle of repose which seems similar to the one of sand.

7.3 Experiments of Type I

The experiments of Type I investigate the impact of the thickness of the competent mechanical unit on the fracture distribution. Three different monolayers, each $270 \times 70 \times 40/20/5 \text{ mm}^3$ (length x width x height), were built on the same foam plate.

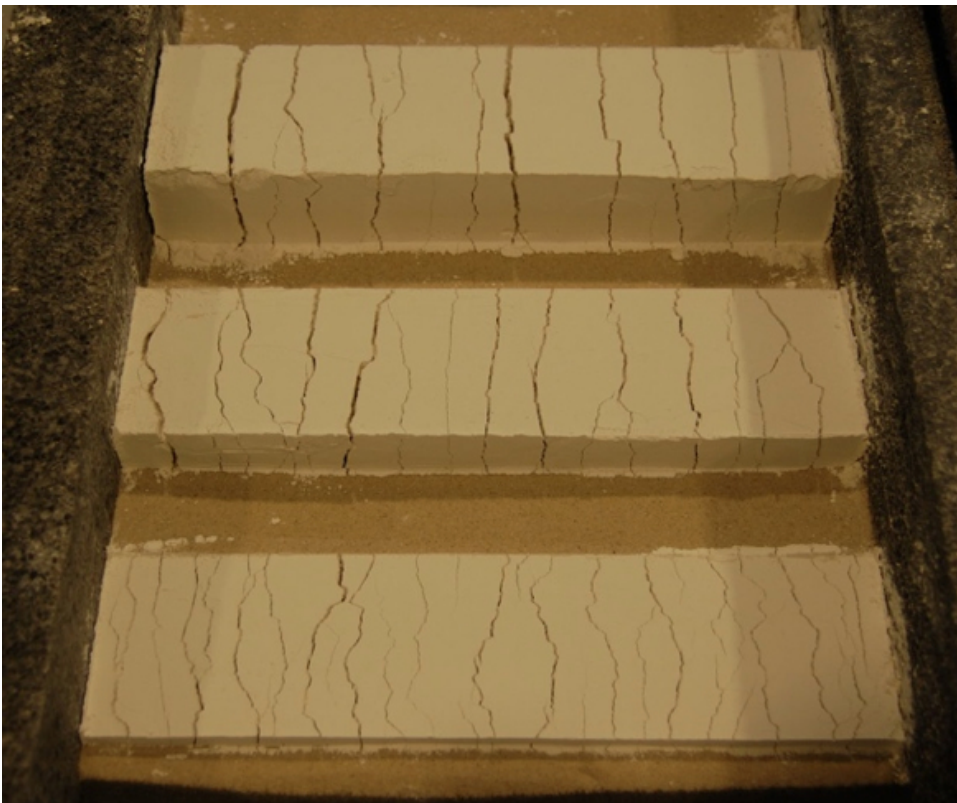


Figure 7.4: Top view taken at the final step of extension after 11% of nominal strain for three blocks of different thickness. The impact of the layer thickness is clearly visible: the thin layer shows systematically denser fracture distributions than the thick one.

Series of pictures were taken during the experiments (e.g. Figure 7.4), to document and investigate the development of fractures. To prove the validity of the observed features and to show the reproducibility of the experiments, the same experiment was repeated 16 times.

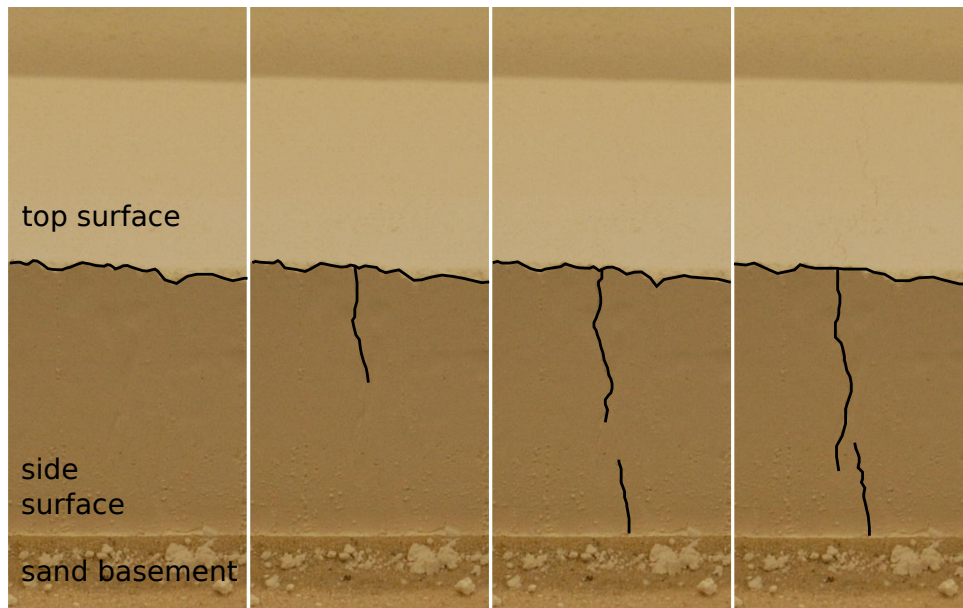


Figure 7.5: Successive images (from left to right) showing the propagation direction of the first fractures in a 40 mm thick layer. Most often first fractures tend to initiate from the top and propagate downwards to the bottom of the mechanical unit. In this example, the fracture initiated at the top, then interacted with another one propagating from the bottom upwards.

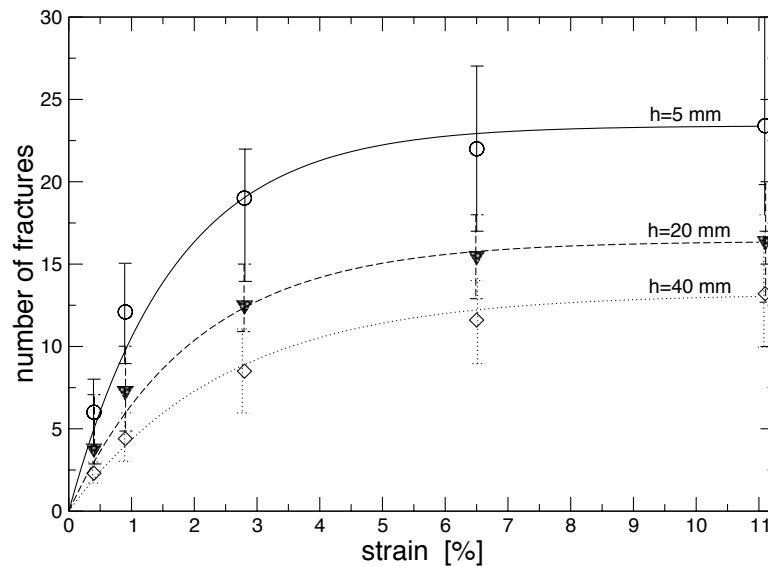


Figure 7.6: Number of fractures versus the nominal extensional strain for 40 mm, 20 mm and 5 mm thick layers of gypsum powder. The lines represent exponential functions fitted to the mean values.

7.3. Experiments of Type I

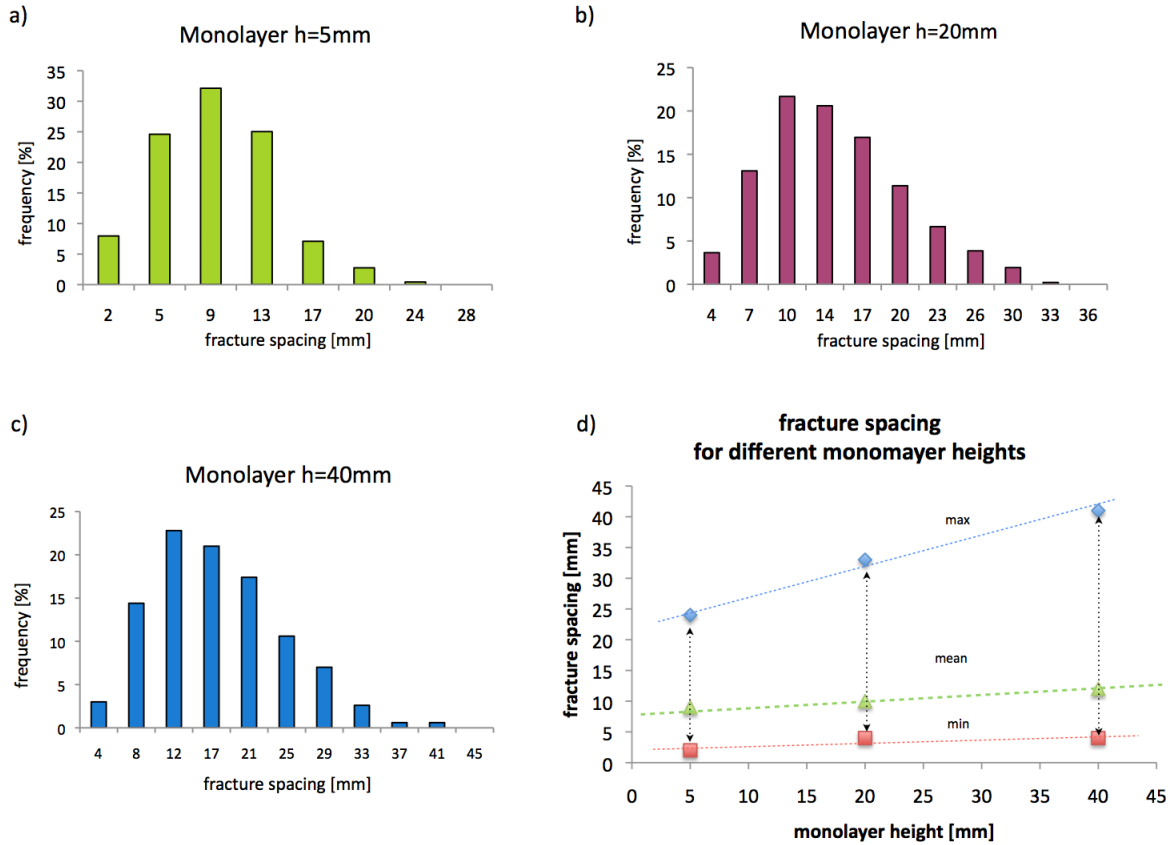


Figure 7.7: (a), (b), (c) Histograms showing the distributions of fracture spacings at saturation for three thicknesses of a single layer. The applied extensional strain is 11%. (d) shows the relationship between min, mean and maximum value of the fracture spacing for monolayers thicknesses of 5, 20 and 40 mm. The fracture spacing is thus increasing with increasing thickness of the layer.

7.3.1 Analysis and Interpretation

The propagation of the very first fractures tends to occur from the top towards the bottom (see Figure 7.5). Conversely, the later fractures tend to initiate at the bottom and migrate towards the top. An explanation could be that the material strength and stiffness of the gypsum layers are very low, inducing the creation of an initial pre-extensional stress field, with already large extensional stresses at the top. Increasing the applied strain overprints the initial stress field, resulting in larger extensional stresses at the bottom than at the top, necessary to initiate fractures at the bottom. Due to the weak tensile strength of the mechanical unit, the first fractures are indeed created at the top, before the applied strain develops the stress which is able to overprint the initial stress field.

Only fractures which completely intersect the layer were considered for the interpretation. These layer crosscutting fractures are counted at different stages of extension on the top surface

of the specimen. The numbers were obtained by the average of three longitudinal lines over the specimen length referred to as scanlines. The fracturing was also captured from photographs which were taken at defined nominal strains and when new fractures were created during the experiment. The graphs in Figure 7.6 show the number of fractures for nominal strains of 0.4, 2.8, 6.5 and 11.1%, respectively. The evolution of the mean values of 16 experiments follows the exponential function

$$D = A \left(1 - B e^{-C\epsilon} \right), \quad (7.3)$$

where D and A are the number of fractures in the specific layer at the applied strain ϵ and the maximum number of fractures in the layer at fracture saturation, respectively. The scalar A in equation 7.3 defines a horizontal asymptote ($D = A$ for infinite strain). The scalar B controls the origin of the curve and should be greater than one to account for the elastic properties of the layer. The scalar C affects the rate at which the fracture number saturates. There is also the possibility to describe the relation between the number of fractures and the nominal strain with a logarithmic function which would not exhibit a saturated level of fracturing. That absence assumes a welded-layer-model (no slip or opening along the interface, Hobbs 1967), since the logarithm grows slowly towards infinity with applied strain. Hobbs approach for explaining fracture spacings is a widely acknowledged theory but not realistic in the observed experiments and is underpinned with the following observation. The fractures are opening also at the contact of the gypsum and the sand layer. This opening can only be explained by shear along a part of the interface, next to the fracture. Hence, the saturation is reached when the whole interface is activated and the fractures are only increasing their aperture to accommodate the applied deformation. This interpretation is further proved by the observation that there are gaps between the specimen and the piston and the specimen and the back stop. These gaps are increasing in size with the unstretching of the foam and are impossible without partial delamination.

Fracture spacings have been analysed for a total strain of 11 % from the pictures taken at several steps of applied strain. The graphs in Figure 7.7 (a), (b) and (c) show the statistical distribution of the fracture spacing for each of the three layer thicknesses (5 mm, 20 mm and 40 mm). The mean values are visible for each of the multilayer thicknesses (respectively 12, 10 and 9 mm for thicknesses of 40 mm, 20 mm and 5 mm). Figure 7.7 (d) illustrates the relationship observed between the fracture spacing and the thickness for the chosen mean as well as for the min and max values. The trends is linear increasing with increasing layer thickness and the maximum spacing is increasing more rapidly than the mean and min values.

7.4 Experiments of Type II

Experiments of Type II have the objective to vary the numbers of layers (1, 2 or 4), keeping the total thickness constant (40 mm). The loading conditions described in the previous section for monolayers were identical.

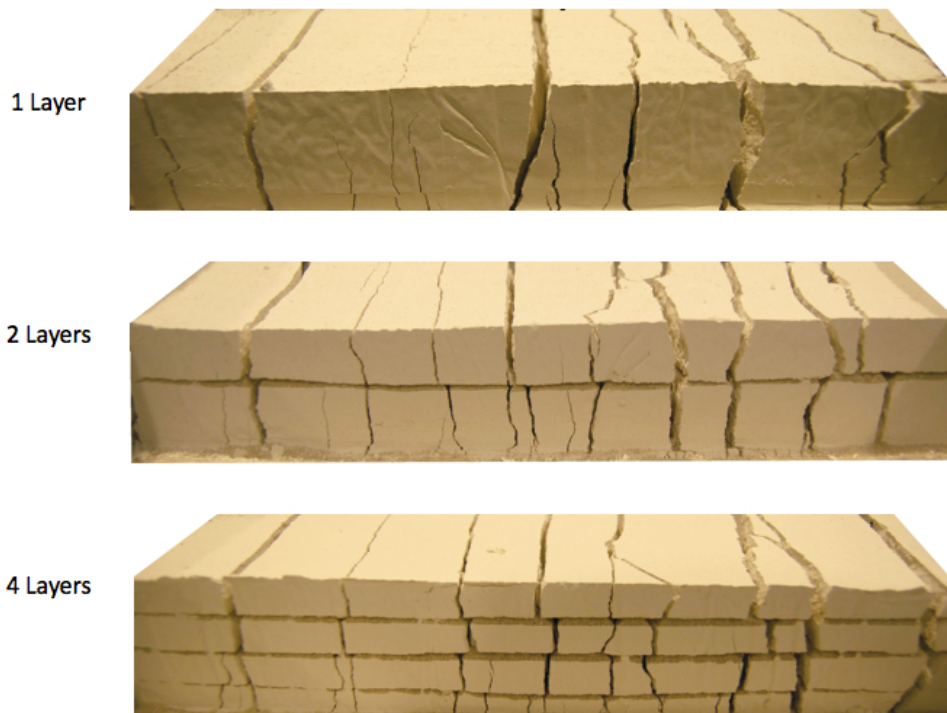


Figure 7.8: Pictures showing an oblique top view of the deformed multilayers taken during experiment Type II after 11% of extensional deformation. The fracture densities on the top surface are almost equal in each case. The difference is in the fracture pattern observed in the profile. In the single layer, the fractures tend to merge towards the top of the sample. In the 2- and 4-layer sequence the weak interlayers behave as barrier for the propagation of fractures that are cutting through the whole thickness of the sample.

7.4.1 Analysis and Interpretation

Oblique views of the three samples at the final step of extension (after 3 cm, corresponding to 11% nominal strain) are presented in Figure 7.8. In the monolayer, several fractures stop within the layer before cutting through the complete unit. They can also reorient slightly to merge with other fractures if they are favourably aligned or located close enough. The bottom layers in the multilayer samples are more densely fractured. The number of fractures towards the top is decreasing. For multilayers, fractures tend not to stop within the competent layers but their propagation is impeded at the interface between the layers. Only few fractures cut straight across

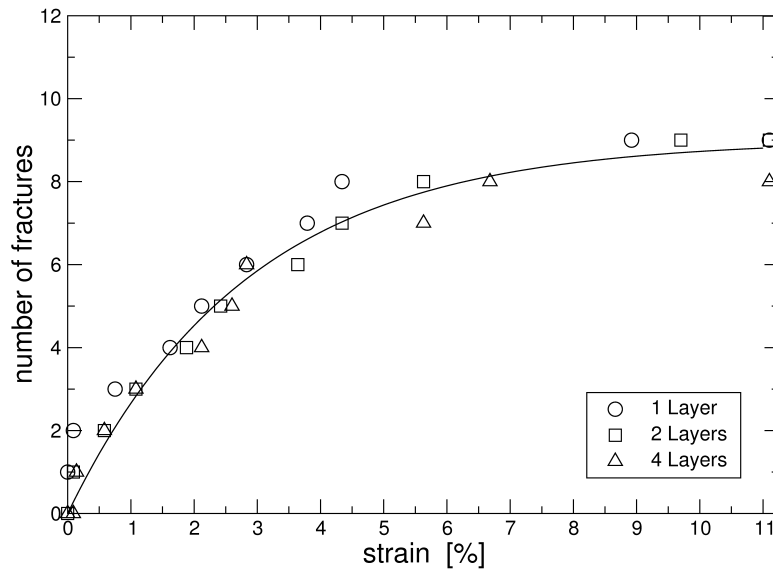


Figure 7.9: Number of fractures (observed on the top layer) plotted against the nominal strain in (b) for the 1, 2 and 4 layers of gypsum powder, with the same total thickness of 40 mm.

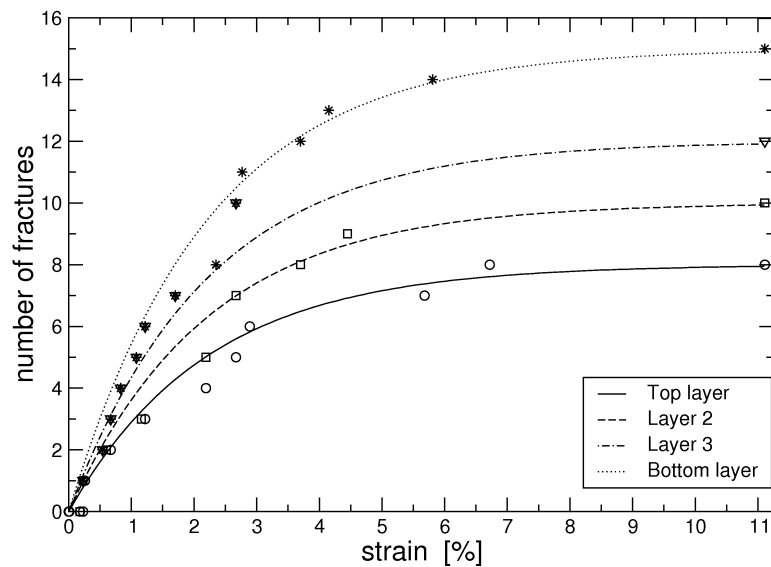


Figure 7.10: Evolution of the fracture number in the four layer experiments. The decreasing number of fractures is clearly visible from the bottom towards the top of the specimen.

the sand interlayers. In most cases, the fractures are off-setted in the propagation direction at the sand interlayers, generating a staircase like pattern.

The number of fractures on the top layer as a function of the nominal strain is presented in Figure 7.9 using circles, squares and triangles for 1, 2 and 4 layers, respectively. It seems that the number of interlayers has an almost negligible effect on the fracturing of the top layer. At best, a slightly smaller number of fractures is found in the top layer for models with three weak interfaces. The reason is probably the weak contrast between the internal friction angles of the two materials used, which are around 30° for the sand and $30 - 35^\circ$ for the gypsum powder. Cohesion and tensile strength which are very different for the two materials thus do not play an important role.

The evolution with nominal strain of the number of fractures in the multilayer with three weak interfaces is shown in Figure 7.10. The offset between the four curves leads to the conclusion that there is a linear relationship between the depth of each layer and its number of fractures.

7.5 Multiple loading of the specimen

The same experimental protocol for the setup, construction and initial extensional step as for the experiments discussed in the two previous sections is applied. A compressional phase followed again by an extensional phase are added to the experimental procedure. The changes in the loading (2x extension, 1x compression) lead to different sets of fractures, which are now discussed.

The following experiment is done with an eight-layer unit composed of repeating three-layer-sequences (thick, medium and thin), ending with a medium layer on the top. The nominal strain rate is $3 \cdot 10^{-4} s^{-1}$. The loading is composed of three stages. The first extensional step is similar to the experiments in the previous sections. In addition, a compressional and a final re-extensional step is applied to the specimen. The progression of the experiment is seen in Figure 7.11 for the initial (a), the first extensional (b), the compressional (c) and the re-extensional steps (d). The sidewalls of the multilayer sequence are not stable during the compressional stage of the experiment as can be judged from the collapses observed in Figure 7.11(c).

7.5.1 Analysis and Interpretation

The first extensional phase leads to the formation of Mode-I fractures (Figure 7.11(b)). The results do not differ from the ones which have been obtained by the experiments in the previous sections for the first step. The following, compressional phase causes the development of a

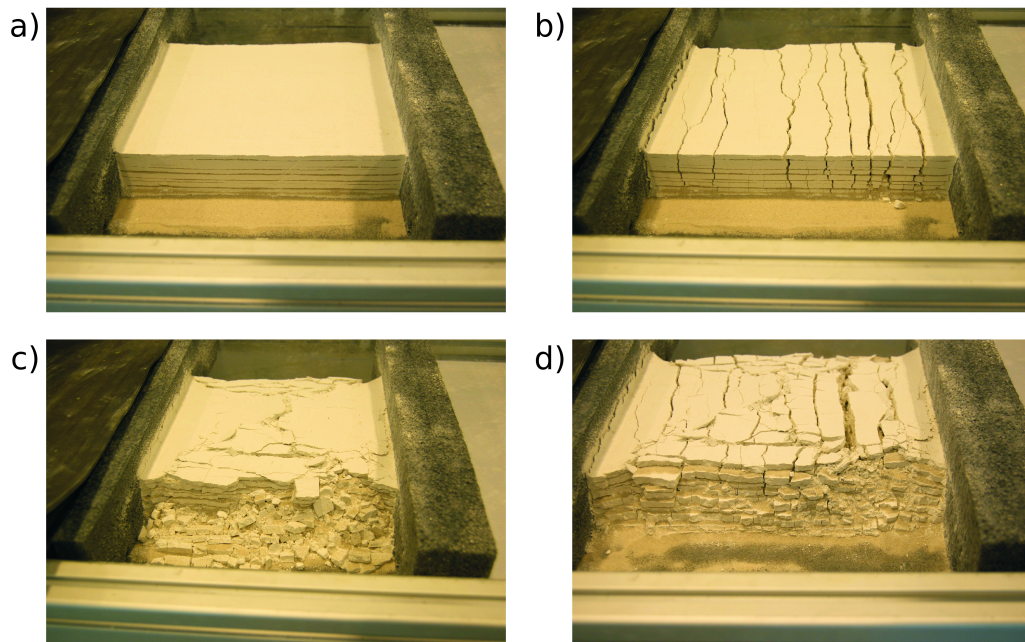


Figure 7.11: Extension, compression and re-extension experiment. Undeformed initial state (a), after 10% nominal extension (b), after strain inversion by 10% nominal compression (c) and after complete relaxation to the initial state (d)

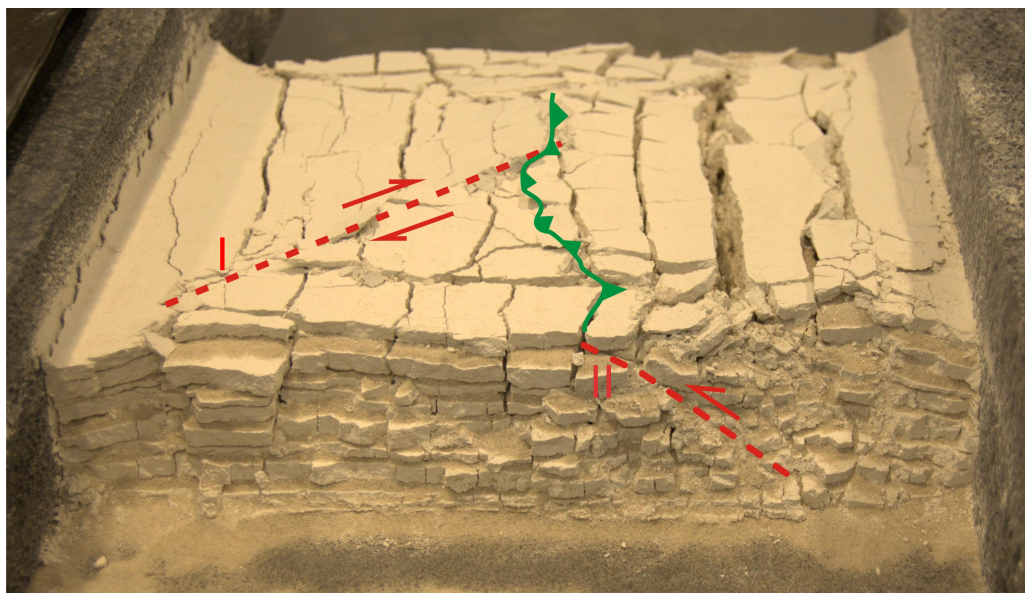


Figure 7.12: Final state of the experiment Type II with strain inversion. Note the strike slip fault (I) and the reverse fault with the green line on the top surface indicating the outcropping thrust (II).

transverse fracture set perpendicular to and limited in length by the first set, which is seen in Figure 7.11(c) and (d). During final compression, the transverse fractures locally form en-echelon arrays that may coalesce to form strike-slip faults, oblique to the direction of maximum compression which are presented in Figure 7.12 with a red dashed line on the top surface marked with *I*. In addition, reverse faults are also observed (red dashed line on the sidewall marked as *II* and a green line for the trace of the thrust on the top).

The slope collapse of the stress free sides during the compressional phase (Figure 7.11c) limits the observation from the top. It is for that reason that the following experiments including strain inversion were conducted in the CT scanner. The number of experiments done was limited by the availability of the machine and the costs of the operating staff.

7.6 Experiments of Type II in the CT-Scanner

The advantage of the documentation with CT-scanner images is that the fracturing and faulting within the specimen can be analysed during the second and third phase of the strain-inversion tests, while the sidewalls collapse and no fracture evolution is visible externally any more. Three experiments have been imaged with the CT-Scanner. Tables 7.1 to 7.3 summarize the geometry of the experimental setups and the nominal strain during the successive phases of extension, compression and final extension referred to as Phase A, B and C, respectively. Details about the settings of CT-I, CT-II and CT-III are provided in the next subsection, followed by the a summary of the outcomes from the documentation by CT-scanner images. A whole series of those CT-scan images which show the 4-D evolution throughout the phases of the fracturing and faulting are presented in Appendix B for all three experiments for the sake of completeness.

Nr.	Dimensions of the model (Length x Width x Height)	Phase A	Phase B	Phase C
CT-1	4-layer unit (27 x 30 x 4cm)	$L_0+11\%$ ext. 5 steps	$L_0-11\%$ comp. 2 steps	$L_0+11\%$ ext. 2 steps
CT-2	4-layers, 2-layers, monolayer, 3x (27 x 7 x 4cm)	$L_0+11\%$ ext. 7 steps	—	—
CT-3	monolayer (27 x 30 x 4cm)	$L_0+11\%$ ext. 5 steps	$L_0-11\%$ comp. 2 steps	$L_0+11\%$ ext. 2 steps

Table 7.1: Description of the specimen dimensions and loading phases for the three experiments done in the CT-Scanner. L_0 is the initial length of the specimen.

	Phase A						
	Step 1	Step 2	Step 3	Step 4	Step 5	Step 6	Step 7
Exp. CT-1 and CT-3	L_0	$L_0+0.9\%$	$L_0+2.8\%$	$L_0+6.5\%$	$L_0+11.1\%$	—	—
Exp. CT-2	L_0	$L_0+0.4\%$	$L_0+0.9\%$	$L_0+2.0\%$	$L_0+2.8\%$	$L_0+6.5\%$	$L_0+11.1\%$

Table 7.2: Nominal strain during Phase A of the experiments. L_0 is the initial length of the specimen. Each step ends with a CT-scan.

	Final step of Phase A	Phase B		Phase C	
		Step 1	Step 2	Step 1	Step 2
Experiment CT-1, CT-2 and CT-3	$L_0+11.1\%$	L_0	$L_0-11.1\%$	L_0	$L_0+11.1\%$

Table 7.3: Applied strain during Phase B and Phase C of the experiments. L_0 is the initial length of the specimen. Each step ends with a CT-scan.

7.6.1 Experimental settings for the documentation with the CT-scanner

Details of the experimental settings are now presented.

Experiment CT-1: The first experiment imaged in the CT-Scanner involved a four-layer model with equal layer thicknesses. The dimensions of the specimen were 270x300x40 mm (length x width x height). 11% nominal strain was applied to the sample at the beginning, with a strain rate of $4.60 \cdot 10^{-5} s^{-1}$. A picture of the experiment after 11% nominal extensional strain is found in Figure 7.13.

Experiment CT-2: The second experiment involving CT-scanner imaging followed the same setup with three parallel testes specimen as they were presented in experiment Type II. It was done with three 70 mm wide and 270 mm long multilayered samples with different numbers of weak interfaces (respectively 3, 1, 0). The applied strain rate was $4.60 \cdot 10^{-5} s^{-1}$. The experiment after 11% applied extensional strain is seen in Figure 7.14.

Experiment CT-3: The third experiment done in the CT-Scanner involved a 40 mm thick monolayer, 300 mm wide and 270 mm long (Figure 7.15). The Experiment followed a 3-phase loading

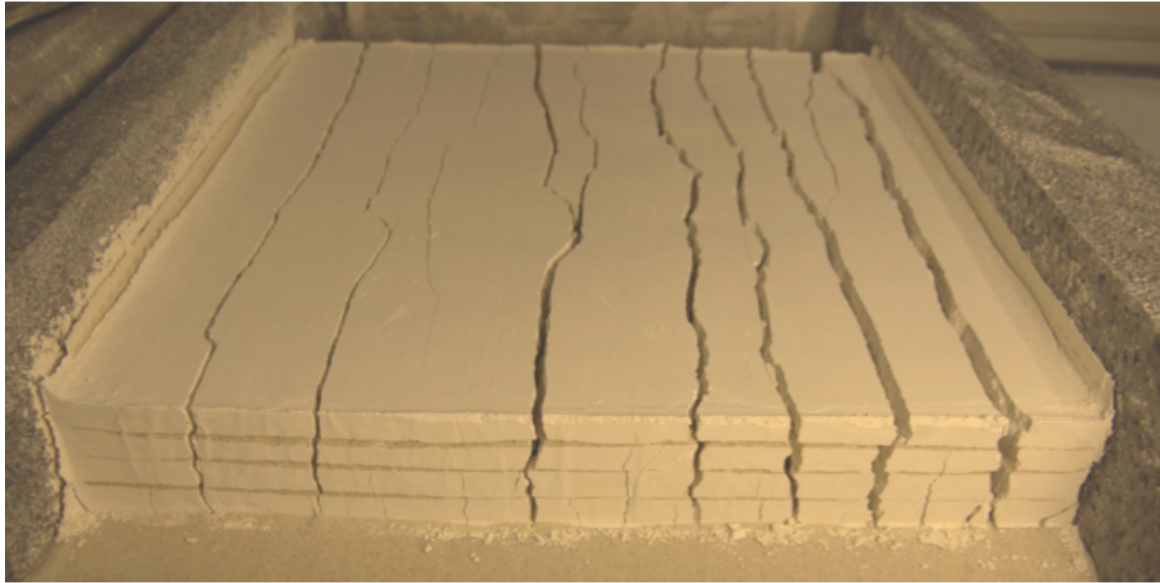


Figure 7.13: 4-layer-unit after step 5 with 11% applied extensional strain.

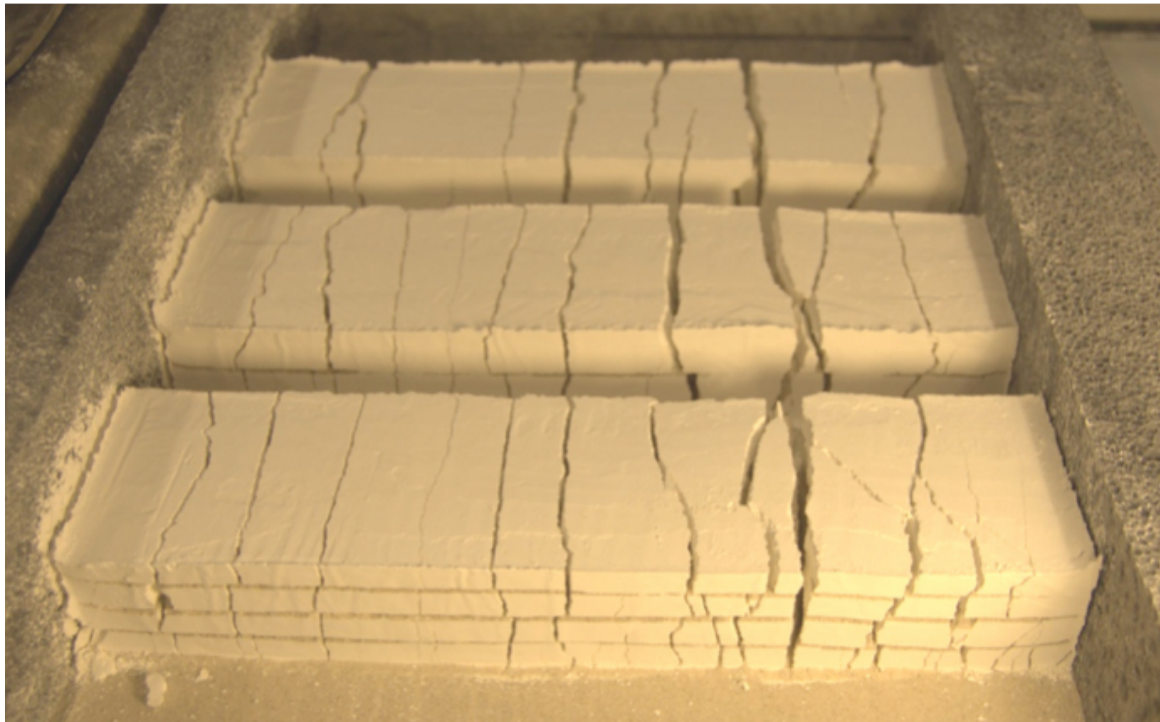


Figure 7.14: Experimental setup CT-2 after step 7 with 11% applied extensional strain.

scenario identical to the first test done in the CT-Scanner (extension, compression, extension, see above).

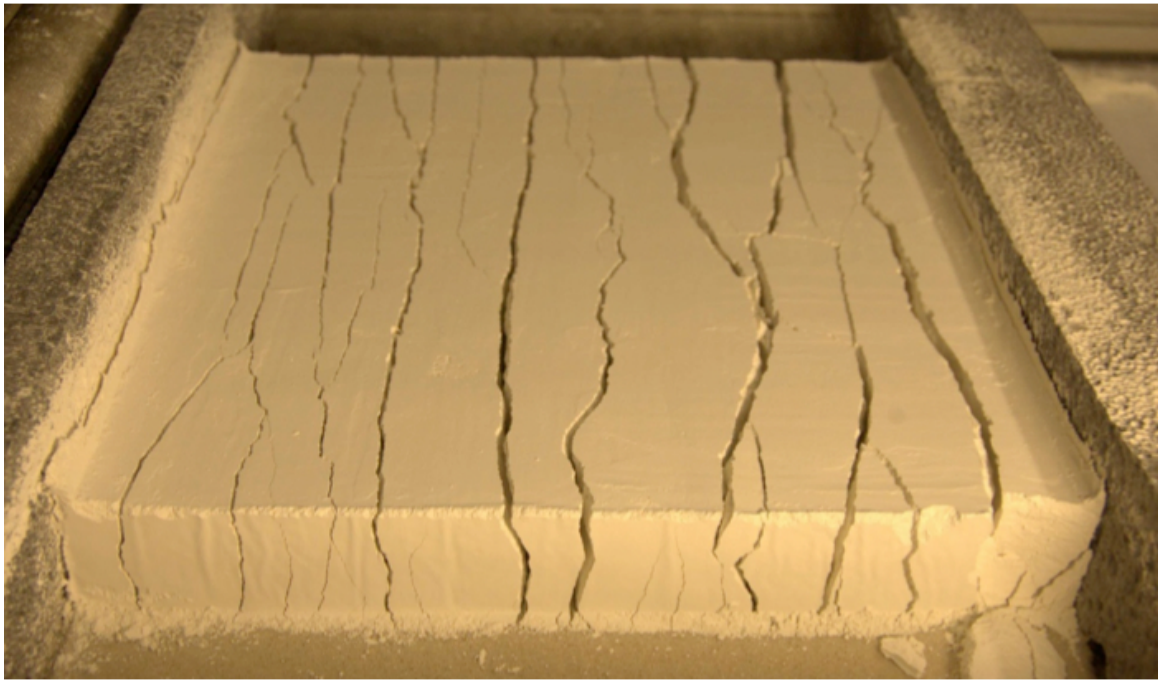


Figure 7.15: Monolayer after step 5 with 11% applied extensional strain.

7.6.2 Summary of the observations from the extension-compression-extension experiments

Phase A: extension

The number of fractures decreases linearly from the top to the bottom of the specimen as has already been described previously.

Phase B: compression

The compressional deformation history is divided in two phases. In phase B_I , the pre-existing opening mode fractures (from the first extensional phase) sub-orthogonal to the compression close progressively. Longitudinal fractures develop, limited in their extension by the previously formed, first fracture set. In Phase B_{II} , some of the en-echelon longitudinal fractures coalesce to form a conjugate pair of strike-slip faults (see also Figure 7.12), oriented oblique to the axis of maximum compression. In addition, reverse faults and pop-up structures are initiated, which are cutting-through the whole unit, without reactivating the fractures inherited from Phase A and

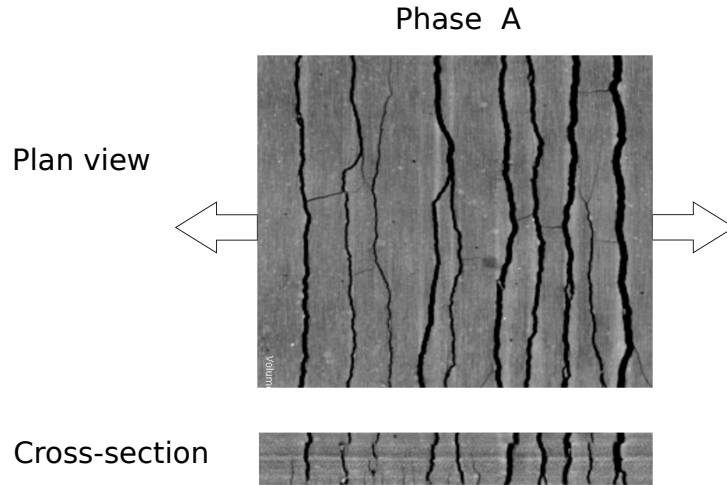


Figure 7.16: Plan view and cross section of the experiment CT-1 after 3 cm extension (11% strain)

Phase B. The reverse faults have a tendency to offset the pre-existing fractures and to change drastically the vertical connectivity of the system.

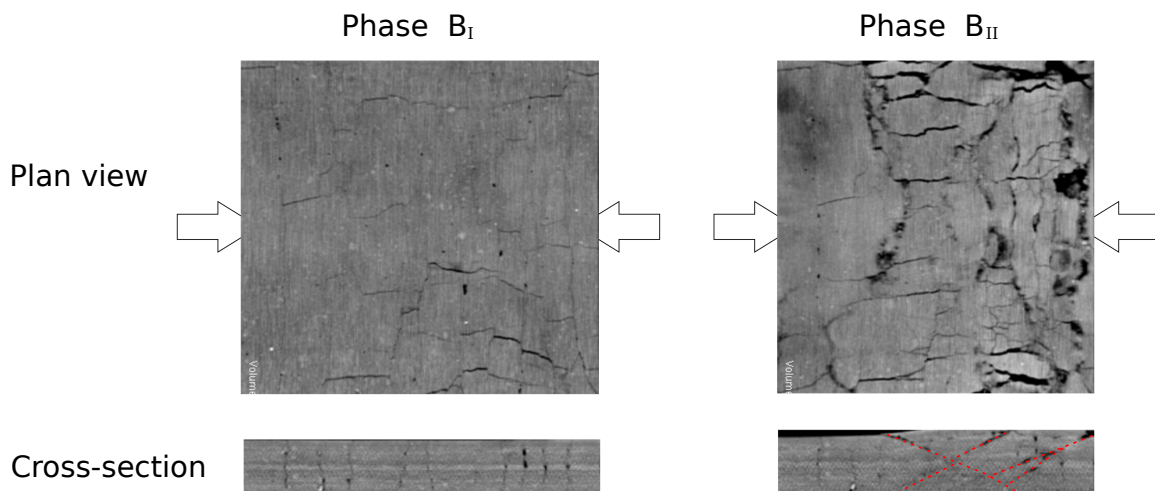


Figure 7.17: plan view and cross section of CT-1 after 3 cm compression (11 % strain) in Phase B_I and after 6 cm compression in Phase B_{II} in addition to the last extensional step in Phase A

Phase C: extension

The last phase leads in general to no initiation of new fractures, but to the activation of normal faults connecting inherited fractures. Simultaneously, other pre-existing fractures reactivate by re-opening or by propagating from their initial position. Due to their unfavourable dip compared to the extension orientation, reverse faults do not tend to reactivate.

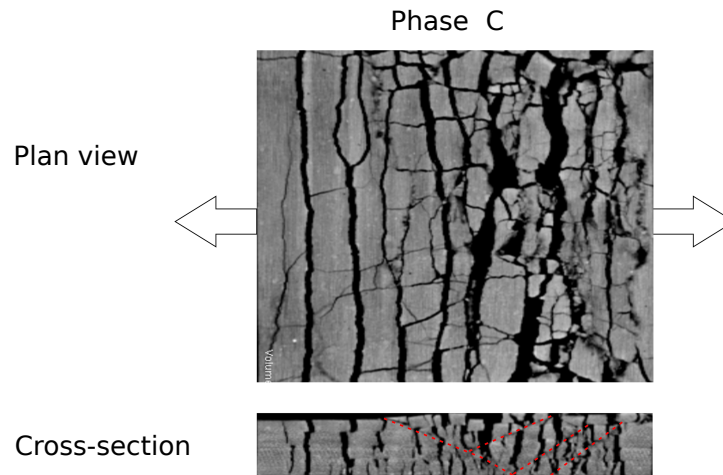


Figure 7.18: Plan view and cross section of CT-1 after 6 cm extension, applied after the final step of compression in Phase B_{II} .

7.7 Experiments of Type III

This experimental setup of Type III is prospected to compare simultaneously three samples with different layering configurations. The multilayers were composed of four layers which consist of pure gypsum powder interspaced by three layers of various materials described previously. The thickness of all the specimens was kept equal at 40 mm. Similar experiments have been repeated three times to test their reproducibility. The first material for the weak layers between the gypsum units is a mixture of 25% talc and 75% quartz sand. The second sample involved pure tile adhesive as interlayers. The angle of internal friction is very close to the one of quartz sand and the cohesion is supposed to be intermediate between the values of quartz sand and talc. In the third specimen, interlayers of pure talc powder are considered. The cohesion is stronger than for the other materials, but talc has the lowest angle of internal friction of all materials which were used.

7.7.1 Observations

Figure 7.19 summarizes the results of the tests involving sand/talc, tile adhesive and pure talc interlayers. Each one of the pictures in the left column shows a specimen after 11% nominal strain. A top view after strain inversion is presented for each multilayer setting in the right column. The first extensional phase did not cause a difference in the fracturing when comparing the three specimens in the left column. The material properties do not seem to influence the fracture intensity. The reason for that is found in the stresses which are involved in the fail-

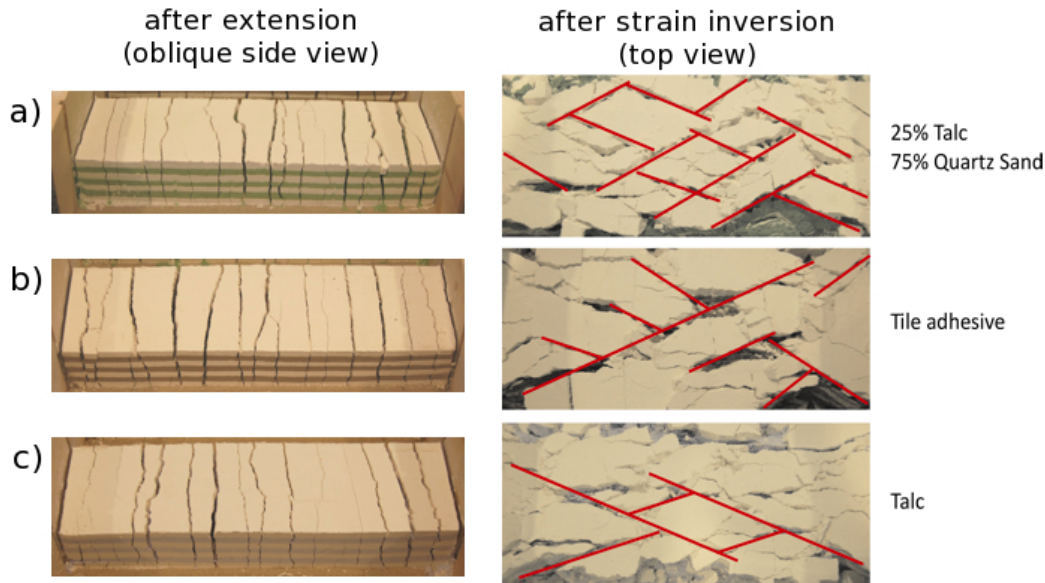


Figure 7.19: On the left, oblique side views of layered sequences of gypsum and either quartz (a), or tile adhesive (b) or talk after 30 mm extension (11% nominal strain). On the right side, top views from the same specimens after strain inversion. No difference in the fracturing is visible after the first extensional phase. That observation changes after the compression since differences in the faulting behaviour are visible. The red lines highlight shear faults.

ure. The stresses are too low to allow the friction angle to play a more important role than the cohesion. Therefore the main mechanical parameter controlling the fracturing is the cohesion, which does not vary significantly within the different interlayer materials which are used for this study. However, during compression differences in the failure mode are visible. The red lines in the pictures in the right column highlight shear faults which result from coalescing longitudinal opening mode fractures organized in en-echelon arrays. In addition, opening mode fractures can be observed on the same top views which are indicated by the horizontal wavy dark lines. The weakest of the three interlayer-powders in (a), which is the talc-quartz sand mixture, shows a dense shear fault system and less opening mode fractures compared to the specimens in (b) and (c) with tile adhesive and talc, respectively. Hence, the stronger units are dominated by mode-I fractures, parallel to the shortening direction and shear faults become scarcer.

Although the first extensional phase of the multilayer sequences showed similar fracture patterns, these patterns are different from the ones which were obtained with specimens in the Type I and Type II experiments. A close-up of a 40 mm thick monolayer, gypsum-talc/quartz sand sequence and a gypsum layer decoupled by three thin layers of quartz sand are presented in Figure 7.20. The fractures in the gypsum monolayer shows a more or less straight pattern. The

failure surface of the interlayer material in (b) tends to be inclined compared to the neighbouring gypsum layers. The measured angle (approx. 60°) fits to the angle predicted by the Mohr construction: $\pm(\pi/4 + \phi/2)$, with respect to the horizontal axis (ϕ is the angle of internal friction). To the contrary, the gypsum (white) layers have the tendency to develop mode-I fractures. The fractures show a wavy geometry in cross section views, which is caused by the shear/opening mode fracture transition from one layer to the other. The same trend is observed for multilayers of gypsum with thin interlayers of quartz sand in Figure 7.20c, which involve also delamination and slip processes. This delamination triggers the localization of slip within the sand interlayers.

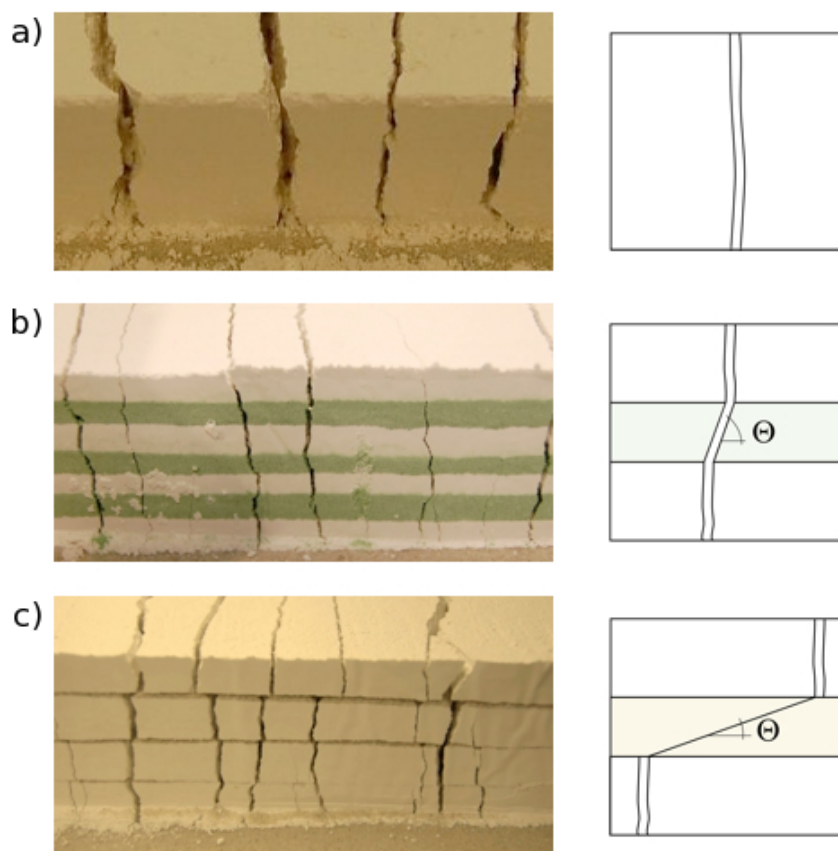


Figure 7.20: Close ups on specimens after 11% nominal strain for a monolayer setting in (a), talk/quartz sand in (b) and thin layers of quartz sand (c) as interlayers decoupling the specimen. On the right side, sketches interpreting the failure are presented. Opening mode, mixed opening/shear and shear failure within the "weak" interlayer are resulting in a straight, wavy and staircase like fracture pattern (from (a) to (c)).

7.8 Conclusion

Three types of experiments with cohesive powders were performed during this study. Types I were done with monolayered gypsum of three different thicknesses. Experiments of Type II differ from Type I by the introduction of dividing a layer of constant thickness by thin layers of sand. In Type III, multilayered specimens (gypsum/talc, gypsum/tile adhesive and gypsum/sand) were studied. The loading consisted in straining the bottom of the samples. The evolution of mainly opening mode fractures was observed. In some of the experiments, a secondary compressional phase was applied to the specimen after the extensional phase, prior to the final extensional phase.

The main outcomes from the experiments are summarized as follows:

The mean values of the measured fracture spacing and layer thickness are related linearly at saturation. The maximum spacing is increasing with layer thickness more rapidly than the mean and minimum values. These findings are in line with the observations reported by Ladeira and Price (1981), who studied in the field Greywacke and Limestone structures. Narr & Suppe (1993) also stated that the relationship between layer thickness and spacing is linear. Experiments by Garrett & Bailey (1977) also lead to the same conclusion. In the literature there are also reported experimental results (Mandal et al. (1994), Supak et al. (2006)), which point to a nonlinear relation between fracture spacing and layer thickness. It could be that these nonlinear effects require a larger thickness to be observed with an experimental setup. A detailed scaling of the material properties in the various experiments is certainly required to provide a theoretical basis to this discussion. It is this lack of scaling, which will establish the relevance of all these experimental work to reproduce the observed fractures in the field. Up to now, it remains unknown which relationship gets closer to reality. Therefore, theoretical studies in combination with field data will be essential to answer that question.

Fracture spacings have been measured in the experiments of Type I. The distribution of fracture spacing seems to follow a log-normal trend in monolayer configurations. Please note that the data is not tested with statistical tools to check whether it actually fits exactly a log-normal distribution. The trend is only interpreted by binning the measured data as it is presented in Figure 7.7. This interpretation is in agreement with the outcrop observations of Rives et al. (1992). This is thus the second evidence, after the linear relationship between the fracture spacing and the layer thickness, that analogue experiments with compacted gypsum powder can be used as a predictive tool.

The evolution of the fracture density during the increase of the applied strain usually follows an exponential and sometimes a logarithmic trend. Exponential fittings are typical for saturation processes whereas logarithmic trends forbid saturation. The dominating factor which defines whether saturation can occur is the possibility of stress/strain transfer over the interfaces within the multilayer sequence. One extreme case would be the welded layer-model (Hobbs 1967), where the number of fractures increases following a logarithmic trend as a function of the applied strain. As soon as delamination along the interface between the stiff unit and the weak adjoining layers is involved in the fracturing process, a saturation level is reached. Hence, no additional fracture can initiate any more and the curve will show an exponential trend. The second extreme case would thus be that of no stress transfer over the interface (zero friction angle and no cohesion along the interface). There is no further fracturing possible, after the first fracture has appeared.

The results of the multilayer experiments (Type II and Type III) showed that fracture patterns strongly depend on the properties of the weak interlayer. The fractures are in general propagating straight through a gypsum layer till they reach the interface (*a* in Figure 7.20). The failure mode changes to shear within the sand layers in Type II which creates a horizontal offset in the fracture propagation over the interface, which gives the fracture pattern a staircase-like appearance (*c* in Figure 7.20). In multilayer sequences of gypsum and sand-talc mixtures, the fractures show a wavy pattern (*b* in Figure 7.20) which has its origin in a mixed opening/shear failure within the sand-talc mixture. The variable refraction of the dip of the fractures is a function of the contrast of mechanical properties of the materials. Due to the low stresses involved during the experiments, the cohesion seems to be the most important parameter influencing the fracture patterns.

In the experiments of Type II and Type III, different materials as weak interlayers have shown that a contrast in cohesion only is not sufficient to get significant differences in fracture spacings, keeping the total thickness constant. This problem is related to the small stresses, which are involved in the failure of the specimens. In the previous experiments the cohesion and tensile strength of the compacted powders are the properties which dominate the stress transfer from one gypsum layer to the other. It is expected by the author that this is a bit in contrast to the fracturing processes in nature, where the friction angle along the interfaces plays a major role. This should be investigated in further experiments with suitable analogue materials.

Chapter 8

FE-calculations of gypsum layers under basal extension

8.1 Introduction

This Chapter summarizes a campaign of 2D non-linear finite-element calculations which had the objective to complement and enrich the interpretation of the experimental results on the extension of gypsum layers reported in the previous chapter. The non-linear character of the calculations is due to the introduction of the plasticity theory for frictional, cohesive materials having also a finite tensile strength. Hardening and softening are introduced to reproduce numerically the localization of the deformation in shear faults and in tensile fracture.

One interesting outcome from the experiments is that the very first fractures initiated from the top of the specimen and propagated towards the interface whereas the later fractures were initiated at the bottom and propagated towards the top. The experimental study has also shown that no new fractures were created after a certain amount of nominal strain. Instead, fracture opening was observed which is only possible, if the layer slips relative to the foam plate. Therefore the interface between the gypsum layer and the foam plate has to be activated in slip and/or opening. This mode of deformation is referred to, in what follows, as delamination. Delamination prohibits further fracturing and is thus an important factor for fracture saturation. This FE study will help us to understand whether a fracture is initiated at the top or the bottom of a layer. It will also shed light on the role of delamination along the base of the specimen and the importance of the interface properties for the saturation process.

The next section provides the main ingredients for the numerical study (material properties, meshing). The results of the FE calculations are discussed in Section 3.

8.2 Constitutive equations

The strength domain of the bulk material is bounded by the Drucker-Prager criterion truncated in tension which is presented in Figure 8.1a. The stress invariants are the hydrostatic stress

$$P = \frac{1}{3} \text{tr}(\underline{\underline{\sigma}}), \quad (8.1)$$

and the von Mises equivalent stress equal to

$$Q^{vm} = \left(\frac{3}{2} \underline{\underline{\sigma}}' : \underline{\underline{\sigma}}' \right)^{\frac{1}{2}} \quad \text{with the deviatoric part of the stress tensor} \quad \underline{\underline{\sigma}}' = \underline{\underline{\sigma}} - P \underline{\underline{\delta}}. \quad (8.2)$$

The cohesion in the $P - Q^{vm}$ space is defined by c_s , the angle of internal friction is ϕ_s and the tensile strength of the material is limited by d_s . The cohesion and also the tensile strength are dependent on the plastic strain γ_m which is defined to be $\max[\gamma^o; \gamma^s]$, γ^o, γ^s being the plastic strain in opening and shear respectively. The trilinear hardening/softening law for d_s and c_s is presented in Figure 8.1b. The implicit algorithm for the update and its consistent tangent associated to these constitutive relations are not presented here for the sake of conciseness.

Since the seminal work of Rudnicki & Rice (1975), it is known that non-associated plasticity under plane-strain conditions leads to the onset of localization in the hardening phase of the cohesion. The same result has been reported by Hallbauer et al. (1973) who did axial compression test on fine grained quartzite specimens. A whole discussion on that topic is presented in G. Mandl's book *Faulting in Brittle Rocks* (2000). However, to ensure that the development of this strain localization is important, we have introduced a softening in the evolution of the cohesion and the tensile strength of the material. These scalars are increasing typically for $\gamma_m < \gamma_{max}$ and decreasing thereafter until γ_m reaches γ_{res} . Beyond this value, the cohesion and the tensile strength are kept constant (Figure 8.1b).

Based on the strength domain which has been defined above, two different modes of plastic deformation are accounted for and for which flow rules are now defined. The flow rule for shear deformation is non-associated without dilation

$$\underline{\underline{\dot{\epsilon}}}^s = \dot{\gamma}^s \underline{\underline{M}}^s, \quad \text{with} \quad \underline{\underline{M}}^s \equiv \frac{\partial Q^{vm}}{\partial \underline{\underline{\sigma}}} = \frac{3}{2Q^{vm}} \underline{\underline{\sigma}}'. \quad (8.3)$$

Tensile deformation is dilatant only

$$\underline{\underline{\dot{\epsilon}}}^o = \dot{\gamma}^o \underline{\underline{M}}^o, \quad \text{with} \quad \underline{\underline{M}}^o \equiv \frac{\partial P}{\partial \underline{\underline{\sigma}}} = \frac{1}{3} \underline{\underline{\delta}}. \quad (8.4)$$

Strain localization consists of a rapid transfer of the initially homogeneous deformation rate to a narrow region of large strain rate. The elastic energy stored in the specimen is the driving force which speeds up this transfer and not the rate at which the displacement is prescribed at

the boundary. To make sure that the localization process is captured numerically, it is found convenient to introduce a time scale in the plasticity theory. It is a visco-plasticity theory which is considered and the enforcement of the yield criterion is replaced by the linear over-stress viscosity law

$$\dot{\gamma}^s = \frac{Q^{vm} + P \tan \phi - c(\gamma_m)}{\eta}, \quad (8.5)$$

for shear failure. For the opening mode, the corresponding viscosity law is

$$\dot{\gamma}^o = \frac{P - d(\gamma_m)}{\eta}. \quad (8.6)$$

The strain rate is proportional to the distance of the current stress point to the boundary of the elastic domain. The parameter η in equation 8.5 and 8.6 is the viscosity and is set to the normalized value 10^{-3} in all the calculations which are reported. The dimensionless nominal strain rate $\dot{\epsilon}$ was set to $2.7 \cdot 10^{-4}$ based on the experimental study reported in the previous chapter, if not explicitly mentioned otherwise.

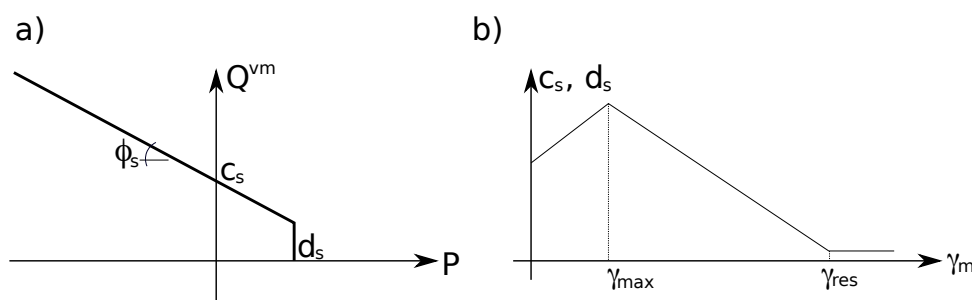


Figure 8.1: (a) The strength domain for the material of the brittle layer is bounded by a Drucker-Prager criterion truncated in tension. The cohesion c_s and the tensile strength d_s follow a trilinear hardening/softening law as a function of the plastic strain. The angle of internal friction ϕ_s is constant.

The values for the material parameters are based on measurements made by Van Gent et al. (2009) on gypsum powder and chosen to be similar to the ones defined in the previous chapter. Hence, the cohesion is 646 Pa and the tensile strength is 107 Pa . The angle of internal friction was approximated from the angle of repose which was estimated in the laboratory to be 30° . The Young modulus is at least of the order of 10^7 Pa . This value was estimated from the observation that the first fractures initiated without obvious elastic pre-deformation of the specimen. However, this value remains questionable. The specific weight of the gypsum powder has been measured during the experiments to be around 1 g/mm^3 . Please note at this point, that these values should be seen only as estimates. Hence, not all the calculations are based on exactly these properties which are also varied. To check the sensitivity of our results to these

material properties, a parametric study will be reported in what follows. Tables are presented in the next sections which provide the relevant material properties for each set of calculations.

The input for the FE-calculations consists of dimensionless numbers using the following reference values for the normalization of the geometry, the material properties and the loading of the specimen:

$$\begin{aligned}
 \text{length } l & 4 \cdot 10^{-2} \text{ m} \quad \hookrightarrow \quad \text{layer thickness from the analogue experiments} \\
 \text{gravity } g & 9.81 \text{ m/s}^2 \\
 \text{specific weight } \rho & 1000 \text{ kg/m}^3 \\
 \text{stress } \sigma & 392.4 \text{ Pa} \quad \hookrightarrow \quad \rho g l
 \end{aligned}$$

The interface with the membrane is assigned specific material properties and its strength domain is described with the Coulomb criterion truncated in tension. The material properties are thus c_i , ϕ_i and d_i , the subscript i identifying the interface (Figure 8.2). The majority of the calculations are based on the assumption that the interface is elastic with a much larger strength than the gypsum which results in welding the membrane and the layer above together. Finally, calculations are presented for a frictional interface with $c_i = 10^{-4}$, $d_i = 1.7 \cdot 10^{-4}$ for which slip and opening occur.

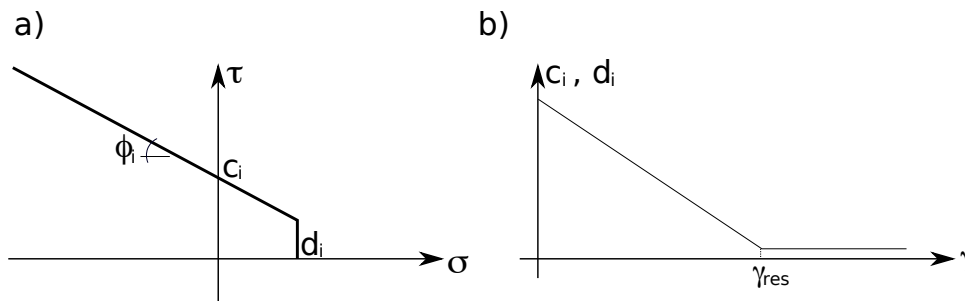


Figure 8.2: The interface has a strength domain bounded by the Coulomb criterion with a tension cut off (a). The cohesion c_i and the tensile strength d_i follow a bilinear hardening/softening law, function of the plastic strain. The friction angle ϕ_i is kept constant.

8.3 FE calculation

The FE-code, used for the application of the plasticity theory presented above is SARPP (Structural Analysis & Rock Physics Program). This code is written in Fortran 77 (compatible 95) and the source code is open to the user. It provides the appropriate platform to develop the above

constitutive algorithm for both the bulk material and the interface. The discretized domains of the structures consist of meshes with 25-noded and 64-noded spectral elements. These elements are Lagrangian for the test and shape functions and rely on Lobatto's quadrature rule such that nodes, where the displacement values are estimated, are also used to compute the strain and stress. These elements have the property to be easily extended to large values of nodes. It is thus relatively easy to study convergence of the numerical scheme based on the p version (increase the degree of the interpolation polynomial) instead of the h version (decrease the size of the elements), see Karniadakis & Sherwin (1999). We will not attempt such convergence analysis here for the simple reason that the shear band or the tensile crack always occurs over a width set by the mesh. Our calculations are thus mesh-dependent, a drawback which should not stop us from analysing the onset and development of strain localization. However, the use of spectral elements with large number of nodes provides two advantages in strain localization problems in plasticity. First, the kinematics of the elements is sufficiently rich to avoid locking once the maximum load is approached and the deformation is close to be isochoric. This locking is well known for simpler 4-noded Lagrange elements. The second advantage is that strain localization which is marked by sharp gradients in the displacement field can be captured with spectral elements. They do not need special mesh design or refinement nor additional modes of deformation, as it was explored in the eighties for the example of simpler Lagrange elements or crossed triangles.

In the next subsection, a parametric study on the gypsum properties is presented with the help of the example of a 2D block in extension or compression. The results presented in the third subsection concerns the prototype considered for the experiments which were reported in the previous chapter. Various geometries in terms of length but keeping the thickness constant were studied. The loading consists in stretching the membrane (elastic foam) which strains the base of the gypsum layer. The third subsection shows the results of a calculation with a frictional interface between the layer and the membrane.

8.3.1 Failure in extension or compression of a 2D block

The geometry of the prototype consists of the rectangular 2D block shown in Figure 8.3. The block has the dimensionless height 6, the width 3 and is asymmetrically tapered in the central section by $\delta = 0.1$, to introduce a geometrical imperfection. This imperfection defines the site for the onset of strain localization. The absence of a taper implies homogeneous deformation in the hardening range. During softening, the strain should localize or not by round-off errors due to the numerical scheme.

The mesh consists of 50 25-noded spectral elements (5 by 10 elements). The vertical displacement of the nodes on the bottom boundary are set to zero. The vertical displacement of the

nodes on the top boundary are all equal and set to a value which is function of time, defining the displacement type of loading. The sign of this displacement defines whether we are in tension or compression.

Five cases of loading and constitutive relations are considered. The first three cases (a, b, and c) are in extension and explore the influence of the tension cut off and of the hardening/softening development of the cohesion and tensile strength on the strain localization process. The fourth case (d) considers compression. In case a and case c the material is described by the Drucker-Prager criterion truncated in tension and in case b no tension cut off is considered. Case a, case b and case d consider strain hardening followed by softening whereas in case c softening is introduced as soon as plasticity appears, with no hardening phase. Case e consists of a single element with the same dimensions of the other cases but without a geometrical imperfection to produce homogeneous deformation. The normalized material properties are found in Table 8.1. Note that in the four following calculations the influence of gravity has been disregarded. The nominal strain rate is set to 1 for these calculations.

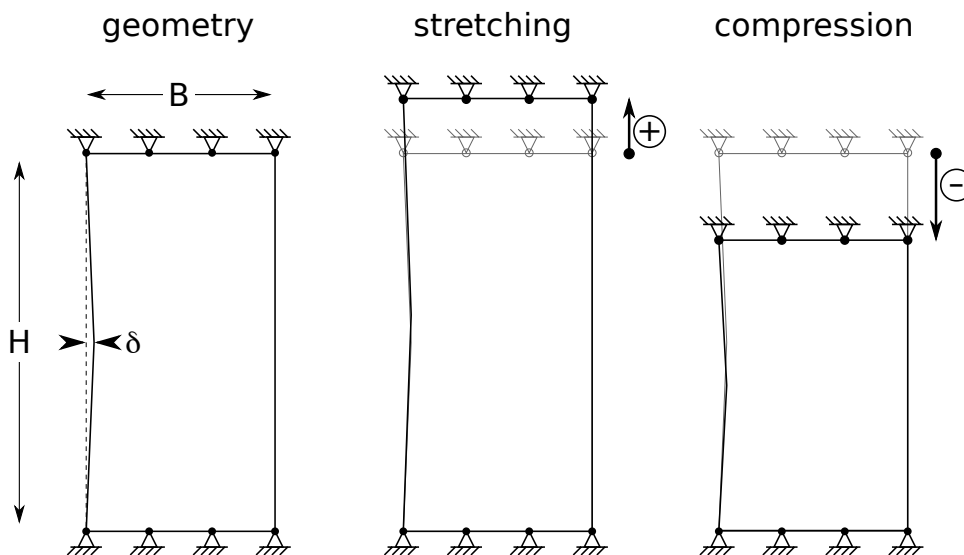


Figure 8.3: The geometry of the blocks with the width B and the height H , tapered in width by δ .

The results of the calculations are summarized in Figure 8.4 and Figure 8.5 for extensional and compressional loading, respectively. The localization initiates at the geometrical imperfection and propagates through the specimen as a narrow band which thickness is limited by up to three neighbouring nodes, in all examples which are reported. The localization in case a and case c appears in a single band, perpendicular to the direction of extension. These bands are interpreted as mode-I fractures. The difference between these two cases is simply the nominal strain at which the localization occurs. Strain hardening followed by softening results in a larger force and larger

case	loading	$\gamma_m = 0$		$\gamma_{max} = 10^{-3}$		$\gamma_{res} = 5 \cdot 10^{-3}$	
		c_s	d_s	c_s	d_s	c_s	d_s
a	extension	1.65	0.27	2.06	0.34	$2.06 \cdot 10^{-2}$	$0.34 \cdot 10^{-2}$
b			2.80	2.06	3.50	$2.06 \cdot 10^{-2}$	$3.50 \cdot 10^{-2}$
c			0.27	$1.65 \cdot 10^{-1}$	$0.27 \cdot 10^{-1}$	$1.65 \cdot 10^{-2}$	$0.27 \cdot 10^{-2}$
d	compression		0.27	2.06	0.34	$2.06 \cdot 10^{-2}$	$0.34 \cdot 10^{-2}$
e	extension		0.27	2.06	0.34	$2.06 \cdot 10^{-2}$	$0.34 \cdot 10^{-2}$

Table 8.1: Values of the elastic and plastic parameters which have been used for testing the constitutive equations and its consequences on strain localization. The results are presented in Figure 8.4 and Figure 8.5. Case e consists of a single element under extension without any geometrical imperfection. The elastic properties ($E = 2.55 \cdot 10^4$ and $\nu = 0.2$) and the friction angle with 30° are the same for all five cases.

strain which is needed to create failure than when introducing immediately softening.

The propagation of the localized region of strain through the block has a certain analogy with the propagation of a fracture through a solid. The difference is the existence of a crack tip when the stress is singular according to linear fracture mechanics. In the plasticity theory the zone in front of the propagating strain localization does not include a tip. There is however a stress concentration in front of the zone of strain localization and its center will be used to define an equivalent crack tip. Hence, for the interpretation of the strain localization in terms of fracturing, the word "crack tip" is used in a loose manner.

One might think that the onset and intermediate stages presented in Figure 8.4b are inverted. The maximum and minimum values for the shadings are independent for each of the figures to make the strain gradient and concentration visible. Unfortunately, there is an intensive local strain concentration in the upper and lower right boundary of the structure which overprint the strain plot. In contrast to (a) and (c), the strain localizes in two conjugate shear bands in case b, where there is no tension cut off in the strength domain. Further extension activates only the upper band while the other rests passive. Compression in case d results also in two conjugate shear planes, where the same transition from two active to a passive and an active failure plane is observed. Classical angles between fault planes and maximum principal stresses should be $\pi/4 + \phi_s/2$ which corresponds to 60° ($\phi_s = 30^\circ$.) In case b the measured angle is 47° and in case d, 46° . The calculations have not been able to reproduce the expected orientations certainly because of a mesh sensitivity which influences the orientation of the bands. This mesh dependency has not been further explored since we are interested here by mode I fractures and the corresponding localization bands will always be parallel to the mesh sides.

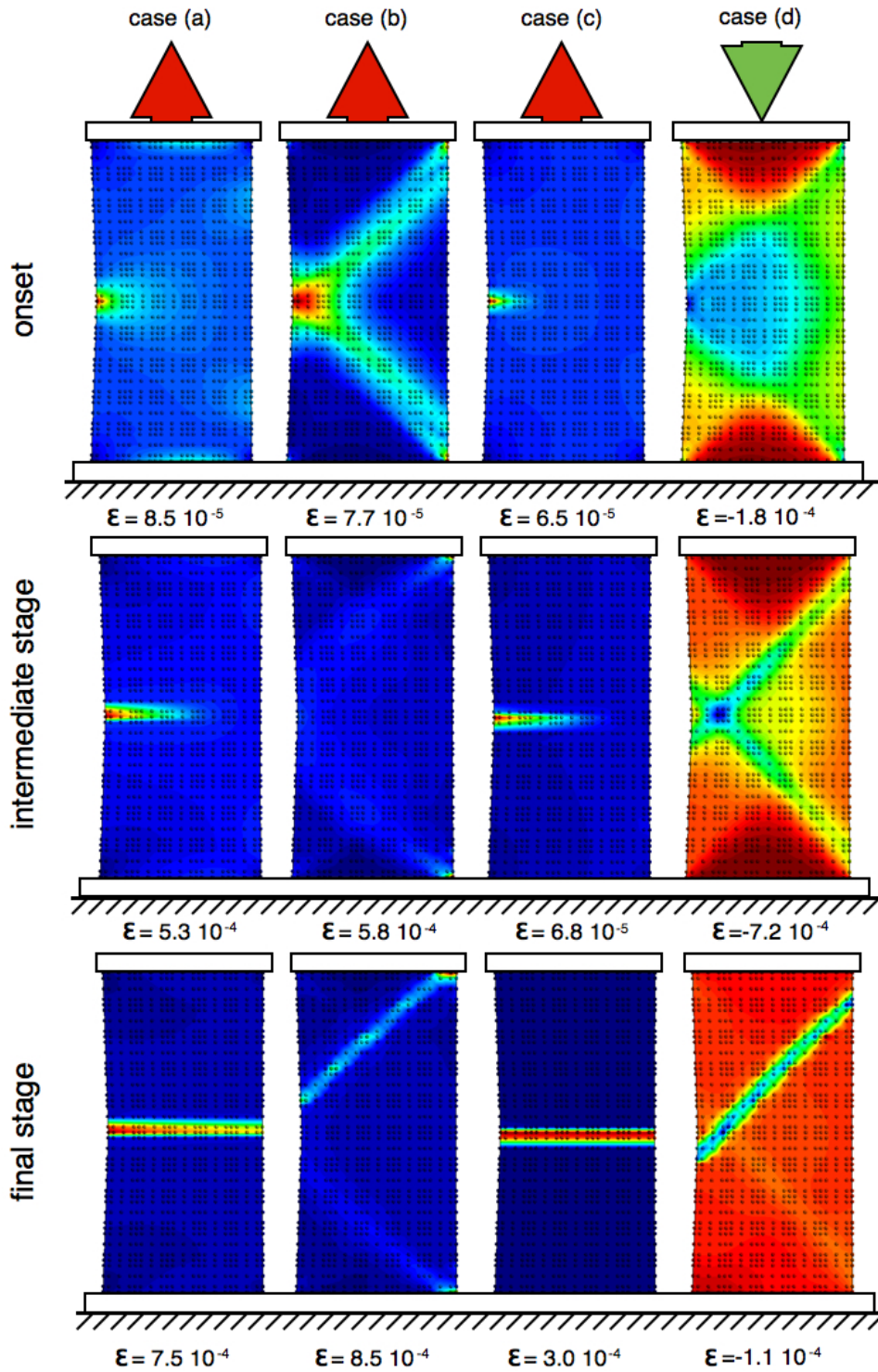


Figure 8.4: Shaded iso-contours of vertical nominal strain for the first four cases (columns) at three stages (rows): the onset of localization, an intermediate stage and the final step of the calculation. Note that the shading for each figure has its own maximum and minimum values, so that all the gradients could be made visible.

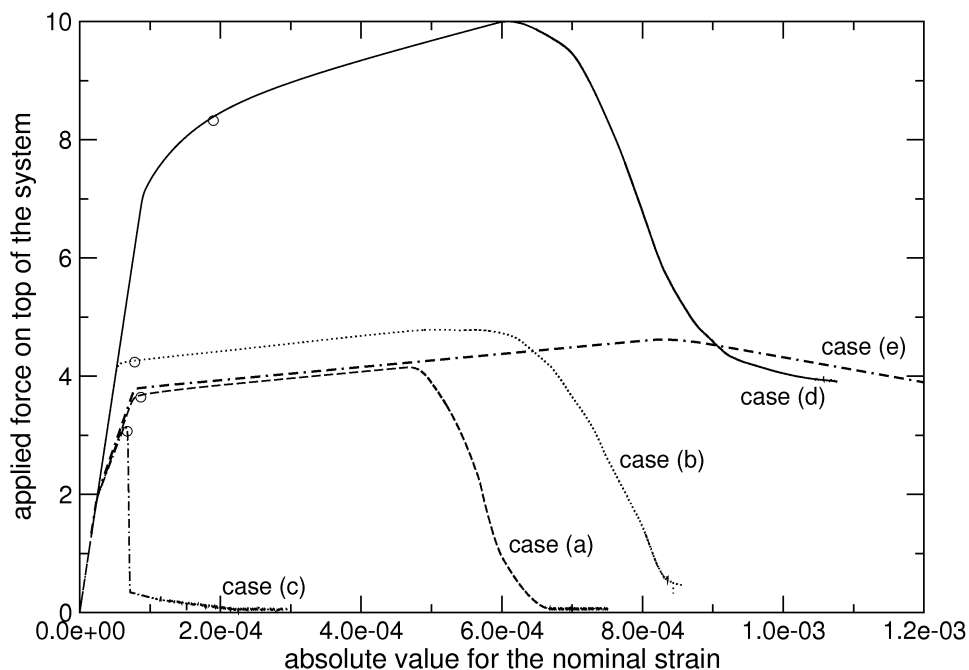


Figure 8.5: The force conjugate in the sense of work to the displacement applied at the top of the specimen in the four investigated cases. The points at which the strain plots for the onset of strain localization (Figure 8.4) were taken are indicated by the circles.

All the geometries which include a geometrical imperfection lead to strain localization. This process is accompanied by a drop in the applied force which reaches a residual state (Figure 8.5). This drop appears because of the overall weakening of the structure as a consequence of the strain localization but its magnitude is also influenced by the softening of the cohesion and tensile strength in the plastic regions. Case e consists of a single element without tapering, having the same material properties as in case a. The deformation remains homogeneous and the force - displacement curve (dotted-dashed-dashed curve in Figure 8.5) is the direct expression of the constitutive relations. Comparing the curves for case e and case a (dashed line), one sees that the localization process is initiated in the hardening range, prior to the maximum load.

The hydrostatic stress (equation 8.1) is presented with coloured iso-contours for case a before and after the strain has localized in Figure 8.6. The complete structure is under extension (dark red) before the failure plane initiates from the geometrical imperfection on the left side. While the localization region cuts through the whole block from the left to the right, strain softening sets the cohesion and the tensile strength to (almost) zero. The orange line in Figure 8.6b represents hydrostatic stresses between 0.0073 and zero. This line is within the fracture where no further stress can be transferred. The release of stress within the structure leads to a release of elastic deformation. In addition, there is still the diffuse plastic deformation which developed before

the localization occurred. The combination of both factors are responsible for the compressional residual stress in the two apparently *separated* parts in Figure 8.6b.

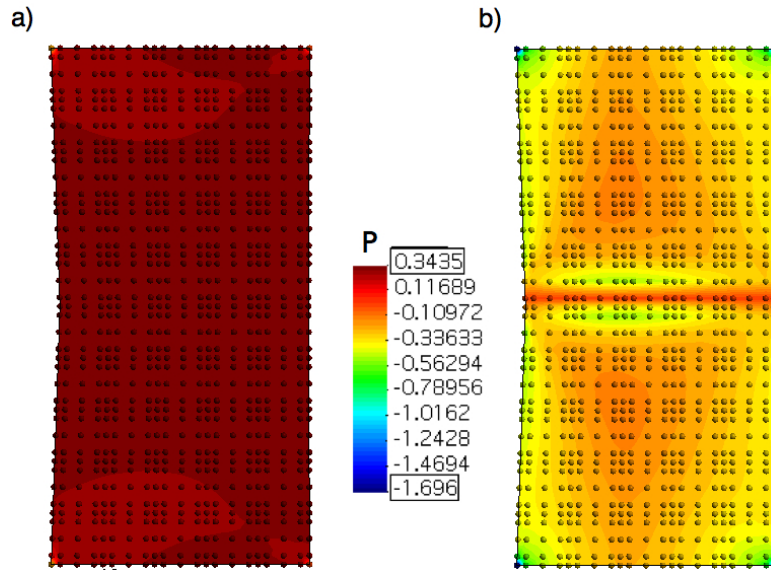


Figure 8.6: Shaded iso-contour plots of the hydrostatic stress for case a before the strain localizes (a) and afterwards (b).

These results confirmed that the implemented constitutive relations lead to strain localization in zones which can be interpreted as opening mode fractures. The applicability of the numerical tools being established, the next subsection addresses the question of how a brittle layer attached to a membrane reacts when the latter is stretched.

8.3.2 The prototype for the experiment with gypsum

We now consider a layer of brittle material with length L and thickness h resting on an elastic membrane (Figure 8.7). The interface between the solid and the membrane is elastic in this section. These conditions were already studied by Bai & Pollard (2001) based on elastic fracture mechanics. In contrast to them, the following calculations are assuming plasticity theory.

The membrane is represented numerically by a series of spectral interface elements, one being shown in its computational domain (spanned by the ξ axis over the segment $[-1; +1]$) in Figure 8.8. Each element consists of n pairs of nodes. The two nodes of the same pair share the same position in the physical space (the thickness of the element in Figure 8.8 is zero). The integer n is the same as the order of the $n \times n$ spectral elements used in the bulk such that there is continuity of the displacement interpolation from the bulk to the interface. The interface sustains a jump in the displacement which is computed by taking the difference between the displacement of the

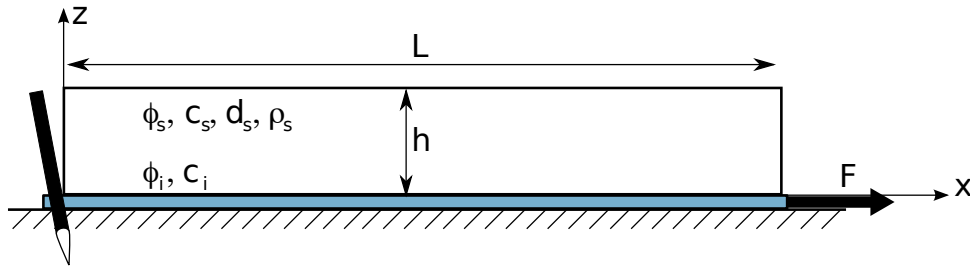


Figure 8.7: The layer of length L and height h is resting on an elastic membrane, corresponding to the elastic foam of the experiments. The membrane is fixed on the left side.

upper and lower layers of nodes in Figure 8.8. This jump is given specific properties described by an elastic response and a non-linear response which is constructed with a plasticity theory with a Coulomb criterion truncated in tension with hardening and softening on the cohesion and the tensile strength. The boundary conditions are defined as follows: the bottom layer nodes cannot be displaced vertically and their horizontal displacement is set to increase linearly with their position along the interface to reach a maximum value at $x = L$, which is the loading parameter in time (Figure 8.7). This linearly increasing displacement corresponds to the displacement applied by the elastic foam which has been considered in the experiments. The nodes of the upper layer are free to evolve in response to the specific properties of the membrane and the interaction with the gypsum layer.

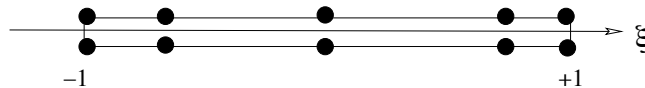


Figure 8.8: A spectral interface element for the connection of 5x5-noded spectral elements of the bulk to the elastic foam. This interface has specific material properties and can accommodate plastic strain in opening and shear.

Development of fractures

The first calculation (g-3 in Table 8.2) relies on a mesh composed of four by four 64-noded elements. The material properties for the bulk and the interface are presented in Table 8.3 and Table 8.4. Figure 8.9 shows shaded iso-contour plots of accommodated horizontal strain at four steps of the calculations corresponding to the time of the onset of a new fracture. The localization of the horizontal strain within the specimen initiates at the top of the layer. Blue colours represent small and red colours large strain. The gradient in the color code reveals the direction of propagation. The mesh and the loading is symmetric so it is not surprising

8.3. FE calculation

calculation	elements in the direction		dimensions		nodes per element
	x	z	length	thickness	
g-1	8	1	6.750	1	25
g-2	8	1	6.750	1	64
g-3	4	4	6.750	1	64
g-4	4	4	3.375	1	64
g-5	4	4	1.688	1	64
g-6	4	4	0.844	1	64
g-7	4	4	0.422	1	64
g-8	8	4	6.750	1	64

Table 8.2: Number of elements which were considered and the dimension of the discretized domain.

calculation	E	ν	ϕ_s	$\gamma_m = 0$		$\gamma_{max} = 10^{-4}$		$\gamma_{res} = 5 \cdot 10^{-4}$	
				c_s	d_s	c_s	d_s	c_s	d_s
g1 - g8	$2.55 \cdot 10^4$	0.2	30°	2.80	$0.51 \cdot 10^{-1}$	$2.80 \cdot 10^{-1}$	$0.51 \cdot 10^{-1}$	$2.80 \cdot 10^{-2}$	$0.51 \cdot 10^{-3}$

Table 8.3: The elastic and plastic parameters of the brittle layer.

calculation	K	G	ϕ_i	$\gamma = 0$		$\gamma_{res} = 1.0$	
				c_i	d_i	c_i	d_i
g1 - g7	$2.50 \cdot 10^7$	$1.00 \cdot 10^7$	30°	$3.00 \cdot 10^8$	$4.50 \cdot 10^8$	$3.10 \cdot 10^8$	$4.60 \cdot 10^8$
g8	$2.50 \cdot 10^7$	$1.00 \cdot 10^7$	30°	$1.00 \cdot 10^{-4}$	$2.00 \cdot 10^{-4}$	$1.70 \cdot 10^{-4}$	$3.40 \cdot 10^{-4}$

Table 8.4: The elastic and plastic parameters for the interface. Note that K and G have the dimension of Pa/m.

that the first fracture is created in the middle of the layer. It occurs for a nominal strain of $\sim 4.9 \cdot 10^{-5}$, identified by the force drop recorded in Figure 8.10 and marked by the letter *I*. It could be expected, that the next two fractures occur simultaneously in the middle of the still intact regions on the left and the right side of the first fracture. The second fracture does indeed appear at almost the same amount of nominal strain in the middle of the right block and cuts through the layer at $\sim 5.0 \cdot 10^{-5}$ nominal strain. This second fracture is marked by the drop in the load-displacement curve in Figure 8.10 indicated by a dashed line and the letter *II*. The drops *I* and *II* are difficult to distinguish because the difference in nominal strain between them

is very small. The second fracture initiates, like the first fracture, from the top. However, in the left region the strain localizes at $\sim 6.7 \cdot 10^{-5}$ nominal strain (dashed line at *III* pointing to the curve g-3 in Figure 8.9c). This delay in strain is rather large and is likely due to the viscosity effect introduced in the constitutive relations although this interpretation has not been checked by numerical means by varying either the viscosity or the rate of loading. The distribution of horizontal strain at $\sim 7.4 \cdot 10^{-5}$ nominal strain is presented in Figure 8.9d. It is seen that all the fractures accommodate different amounts of tensile strain (opening), the first showing the largest and the third fracture the lowest amount of straining.

Our initial intention was to continue these calculations to discover further strain localization in fractures which partition the initial layer in blocks of even smaller size hoping to get a direct approach to the saturation effect. It was nevertheless decided to stop the simulations after a nominal strain of $\sim 9.8 \cdot 10^{-5}$ for numerical reasons only. The stress within the zone of localized deformation are close to zero and the localized strain keeps on increasing. The accuracy of the numerical scheme for the update of the stress and internal variables (the accumulated plastic deformation) is sensitive to the time step adopted for each increment of deformation. By experience, it is found rather appropriate to relate this time step to the maximum equivalent plastic strain increment found in the discretized domain and normalized by the norm of the elastic strain increment. However, the proximity of the stress state from the zero stress renders the time increment too small to continue the straining to trigger subsequent strain localization. Another strategy was proposed. The geometry and the position of the set of say N fractures are known from the first FE calculation and consequently the length of the independent block is $L/(N + 1)$. It is thus proposed to study again the same prototype as the one presented in Figure 8.7 except for the length of the block which is now reduced to $L/(N + 1)$. The history of the straining will be of course different. Nevertheless, since the newly studied regions correspond to regions where the deformation was essentially elastic in the previous run, these differences in history should be minor. Before presenting these new results, the mesh sensitivity of our calculation is further analysed.

The influence of the mesh

The mesh sensitivity of these calculations has already been mentioned at least twice. We have found that the localized strain occupies a region of width set by the mesh since it evolves at least three neighbouring nodes. The objective now is to test the influence of the mesh on first, the onset of the localization process in fractures and second, the final number of fractures for the same nominal strain. To investigate the mesh sensitivity, calculations were done for three different element numbers keeping the dimensions of the structure constant. Further information

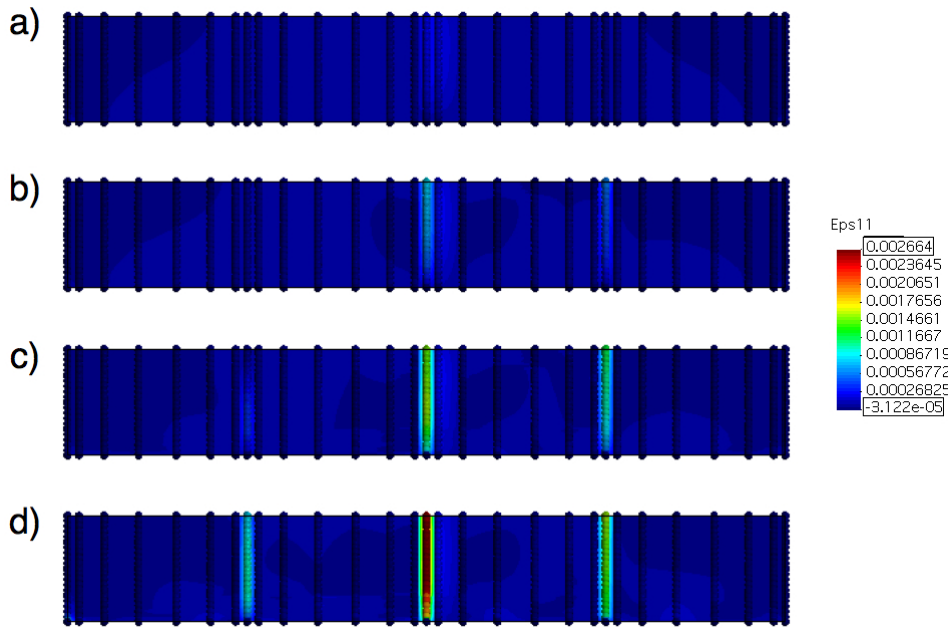


Figure 8.9: Shaded iso-contours of the horizontal strain at four steps of the calculation g-3. In (a) the first fracture has initiated at the top, indicated by the light blue shading. In (b) the first fracture has propagated downwards and a second fracture has initiated in the right half of the layer. The initiation of the third fracture is observed on the left half of the structure and (d) shows the end of the calculation, when all three fractures have cut through the whole layer.

on the dimensions of the specimens and the considered meshes are found in Table 8.2 and the material properties are presented in Table 8.3 (g-1, g-2 and g-3) and Table 8.4. The applied force as a function of the nominal strain for the three structures is presented in Figure 8.10. The deformation localizes at almost the same nominal strain and the same force is applied before a significant drop occurs in all cases. However, differences in the residual strengths after the first fracture is fully propagated, are observed. The two coarser meshes (g-1, g-2) show only a central fracture, where three fractures were created in the finer mesh (g-3). Hence, finer meshes favour the strain localization and the coarser meshes favour the decrease of the residual strength. This second conclusion is certainly counter intuitive.

The mesh sensitivity beyond the onset of the first fracture localization is due to a second failure mechanism not observed for the coarse mesh of the first calculation g-3. It is indeed found with finer meshes that there is a trend for the strain to localize along the interface with the membrane. This second failure mechanism is a delamination process (shear and opening) which initiates from the left and right lateral sides and propagates towards the central section. Every time a node yields, there is a small drop registered by the load-displacement curve. The

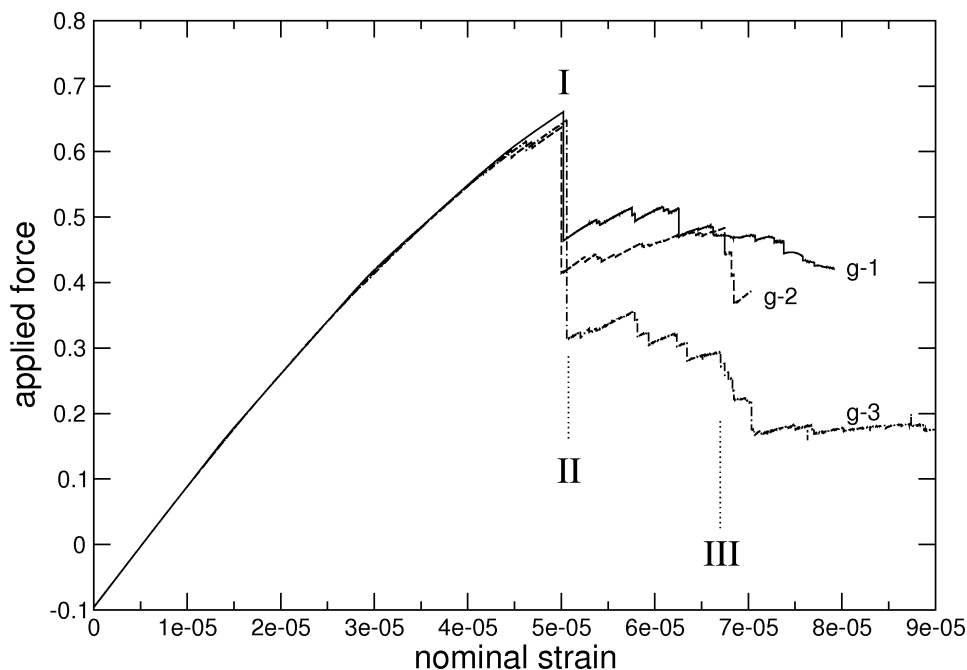


Figure 8.10: The load-displacement curve for the same geometry but three different meshes obtained with 8 25-noded, 8 64-noded and 16 64-noded elements in g-1, g-2, and g-3, respectively. The maximum force which the structure can sustain before the first fracture is created is approximately the same for the three meshes. However, the number of fractures captured by each mesh is different. The coarser meshes in g-1 and g-2 show only one fracture. The fine mesh of g-3 was able to create three fractures which are labelled by I, II and III. The smaller drops in the graphs are caused by yielding of points on the interface, next to the interface.

membrane interface is strong and the material is failing next to it following its boundary. This delamination was partly expected since we have a discontinuity in shear stress at the right and left bottom corner. Indeed, the left and right lateral wall are stress free whereas the interface with the membrane is sheared. A discontinuity in the stress field is thus necessary to satisfy mechanical equilibrium. Such discontinuities are well known in linear elasticity (Timoshenko & Goodier, 1951). It was expected that the numerical discretization would be unable to capture this discontinuity. However, the engineering reasoning was that the wealth of the displacement discretization due to the spectral element was going to be sufficient to approximate this discontinuity by a large gradient. It is certainly the case with, however, the surprising result that the stress concentration and the hardening/softening properties of the bulk material leads to the onset and the propagation of the delamination towards the central region (Figure 8.13). This delamination isolates the main part of the gypsum layer from the stretching membrane. It thus limits the loading in extension of this main part, influencing the number of the tensile fractures

which could be initiated. The delamination and its implications are further discussed after the next subsection which questions the initiation of fracturing.

Fracture initiation

The first example g-3 showed that the fractures can initiate from the top or from the bottom of the brittle layer. It is quite impressive, at least to the author, that the observations from the analogue experiments have shown the same trend. There, the first fractures initiated at the top and the later fractures initiated from the bottom area. The calculations for the mesh-sensitivity showed that the fractures were always separating the layer in two pieces of the same length. Hence, in view of the numerical problems reported earlier, we adopt the new strategy which consists of considering prototypes having a fraction of the length of the initial structure. Results are reported for structures with the full, half and quarter of the length of the first prototype (g-3), while keeping the same layer thickness. Details of the geometry and the mesh are provided in Table 8.2. Shaded iso-contours presenting the horizontal strain after the initiation of the first fracture are presented in Figure 8.11a to (c). Plots in (b) and (c) are constructed by symmetry as to reconstruct the full length of the specimen. It is observed that the fracture for the full-length specimen starts from the top of the layer. The initiation is from the membrane for the two blocks of half and a quarter of this full length.

The reason for this difference in the initiation point is found by the inspection of the hydrostatic stress field just before the onset, by comparing Figure 8.12a to (c) obtained for the full, the half and the quarter length specimen, respectively. In the initial stage of the calculation, the top of each layer is under horizontal tension. The extensional strain, which is applied at the bottom, increases the stress magnitude in the structure. As soon as the stress reaches the elastic limit of the material, plastic deformation occurs. Diffuse plasticity occurs in the extensional zone at the top in a broad region of deformation having the shape of a wide trough (Figure 8.12a). The dark-red iso-contour is marking the limit of the extent of the plastic region. The material below is essentially elastic, except at the two lower corners of the domain. During the widening of this diffuse plastic zone, there is initiation of strain softening in the central region of the specimen. This softening explains the lighter red colour within the trough, close to the top surface. The softening within the trough, which migrates towards the bottom of the layer, is conducive to the lowering of the stresses. The fracture is thus initiated at the top, within the weakened zone as soon as the trough reaches the bottom of the structure. The hydrostatic stress in (b) and (c), where the fracture initiates at the bottom, show a thin (yellow-green) zone above the interface which indicates low stresses. These weak zones correspond to delamination. However, between the two delaminated regions at the bottom, a tensile stress builds up, which triggers the frac-

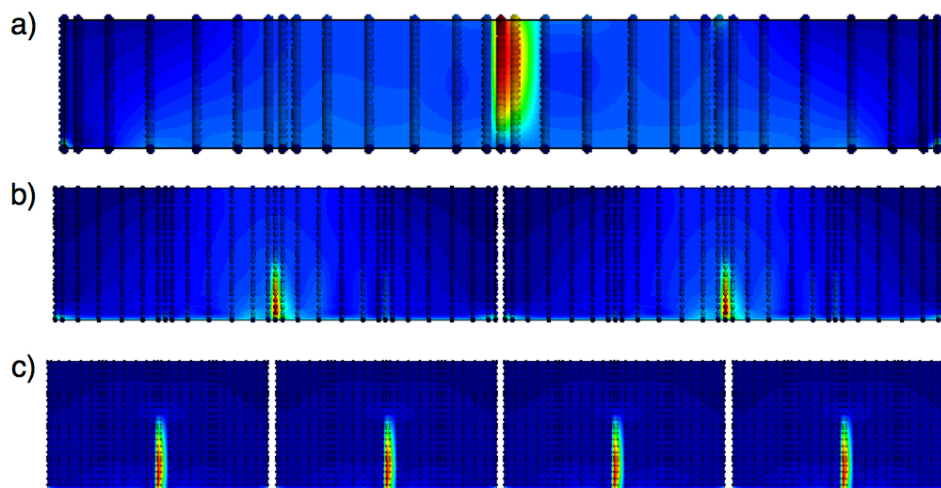


Figure 8.11: Shaded iso-contours of the horizontal strain after the onset of strain localization for calculations g-3, g-4 and g-5, at nominal strains of $5.1 \cdot 10^{-5}$, $5.9 \cdot 10^{-5}$ and $3.4 \cdot 10^{-4}$, respectively. (a): the fracture initiates in the full length structure (g-3) from the top, indicated by the larger strains (red colour, $\max. \epsilon_{xx} = 2.7 \cdot 10^{-4}$). Each of the structures has been divided by a fracture in two pieces of the same length. (b) shows the initiation of a fracture from the bottom region of a structure with the half length of the previous structure ($\max. \epsilon_{xx} = 2.3 \cdot 10^{-4}$). (c): a structure with a quarter of the initial length fractures with the initiation at the bottom ($\max. \epsilon_{xx} = 5.7 \cdot 10^{-4}$).

turing from the bottom towards the top, before the diffuse plastic zone could propagate to the bottom. The example with the half structure length (b) shows relicts of the trough, discussed before, that did not propagate fast enough towards the bottom of the layer. It is recognized by the dark-red zones on the left and right along the top surface. The fracture initiated at the bottom even before the plastic zone at the top could develop in (c), the quarter length specimen.

A more detailed view of the fracture initiation is now presented with the example of g-5 consisting of a quarter of the structure length. Shaded iso-contours in Figures 8.13a to (d) are presenting the plastic strain in opening, the hydrostatic stress, the equivalent plastic strain in shear and the von Mises stress after the initiation of the fracture from the bottom and its propagation to the middle of the layer. The direction of propagation is recognized in (a) from the colours in the middle region. The largest amounts of extensional strain are found in the lower part of the zone representing the crack. The right and left lower corners of the structure have already opened up, as indicated by the small yellow regions in (a) and also failure in shear has occurred over the part of the structure next to the interface (c). The iso-contours of the hydrostatic stresses present a stress concentration (dark-red) in the central region where the crack tip is. The hydrostatic and the von Mises stress show a thin zone of very low stresses on the bottom of the layer. These zones are markers of the strain localization associated to the

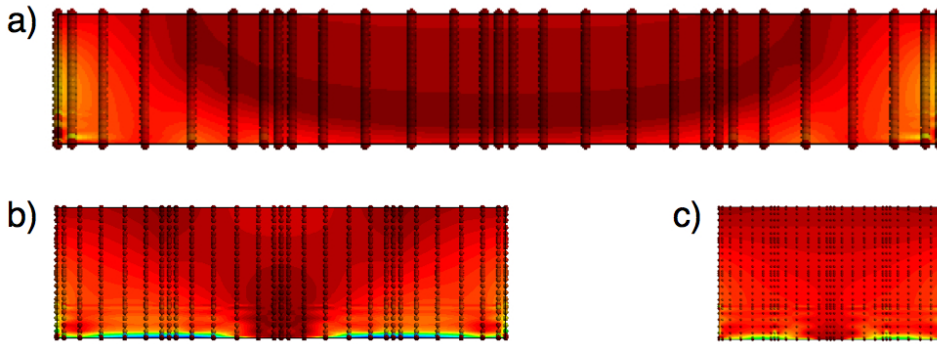


Figure 8.12: Shaded iso-contours of the hydrostatic stress fields for three structures of different length, approximately at the fracture initiation. In (a) a zone of large stresses and diffuse plastic deformation propagates from the top downwards. The strain begins to localize in a thin vertical zone as soon as the plastic zone reached the bottom ($P_{max} = 0.059$, $P_{min} = -0.834$). In (b), the diffuse plastic zone did not have the time to propagate to the bottom. Between the delaminated zones at the bottom of the structure another stress concentration builds up and the fracture initiates at the bottom ($P_{max} = 0.050$, $P_{min} = -1.326$). In (c) the fracture initiated at the bottom before the plastic zone at the top could initiate ($P_{max} = 0.048$, $P_{min} = -1.803$).

delamination process which occurs within the material parallel to the strong and intact interface with the membrane. That observation leads to the conclusion that a layer does not need a weak interface to delaminate. Interface parallel cracks initiate from the stress-free lateral walls next to the interface and propagate within the solid towards each other. This process is responsible for the fracture initiation from the bottom which is documented in the previous calculations.

Fracture saturation

The first fracture is created through the middle length of the layer because of the symmetry of the structure and the assumption of homogeneous material properties. We continue the application of the new strategy consisting in studying specimen having length with are a fraction only of the initial length. The objective is now to analyse the interaction between delamination and fracture saturation. The following calculations were done on structures with one fourth, one eights and one sixteenth, corresponding to the cases g-5 to g-7, respectively. Each structure is discretized with 4x4 64-noded elements.

The shaded iso-contour plots of horizontal strain in Figure 8.14 present the fracture development within the samples at the stage when no further increase in the force applied to the membrane, shown in Figure 8.15, is observed. This levelling-off of the applied force indicates that the resistance of the structure has achieved its maximum and thus that delamination is com-

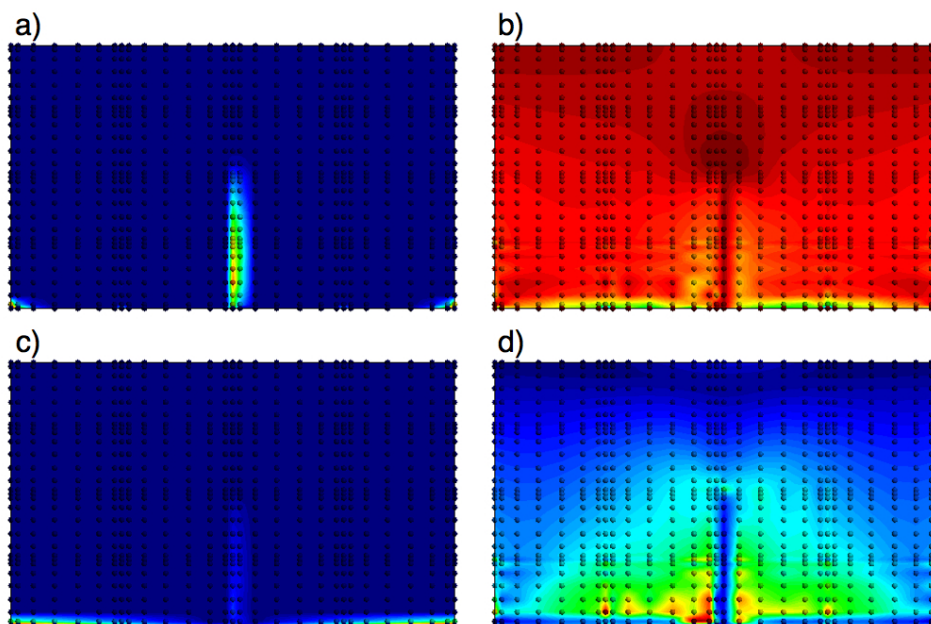


Figure 8.13: Shaded iso-contours presenting plastic strain in opening (max. $\gamma^o = 5.8 \cdot 10^{-4}$) in (a), the hydrostatic stress ($P_{max} = 0.051$, $P_{min} = -2.352$) in (b), the plastic strain in shear (max. $\gamma^s = 3.0 \cdot 10^{-3}$) in (c) and the deviatoric, von Mises, stress ($Q_{max}^{vm} = 2.263$) shortly after the fracture has initiated at the bottom of of the setting g-5. The length of the structure is a quarter of the full length which implies that this block is bounded by two fractures. Hence, this calculation is a continuation of g-3 but also g-4. A thin zone of plastic deformation next to the interface within the layer indicates delamination.

plete in a band parallel and next to the membrane. At that stage the stresses within the structure do not increase and therefore, fractures which have not cut through till then, will not propagate further. The levelling-off of the load is thus a marker of the fracture saturation. A cross cutting fracture is seen in Figure 8.14a and, to its left, another fracture has initiated, which was not able to cut through the whole layer. The calculations g-6 (b) and g-7 (c) conclude that no fracture divides the whole layer. However, in g-6, two fractures were created at the same strain and have almost succeeded in reaching the upper surface of the structure. The fracture in g-7 stopped in the middle of the layer. This comparison between delamination and fracturing leads to the conclusion that fracture saturation is reached at fracture spacing which is less than the length of the specimen in g-5 and larger than in g-6. The mean fracture spacing in a 40 mm thick layer was presented in the previous chapter and is 12 mm. Assuming, that g-6 has the potential to create a single cross cutting fracture, the minimum fracture spacing would be 16 mm which is rather close to the experimental result, despite the uncertainties in the value of the material properties.

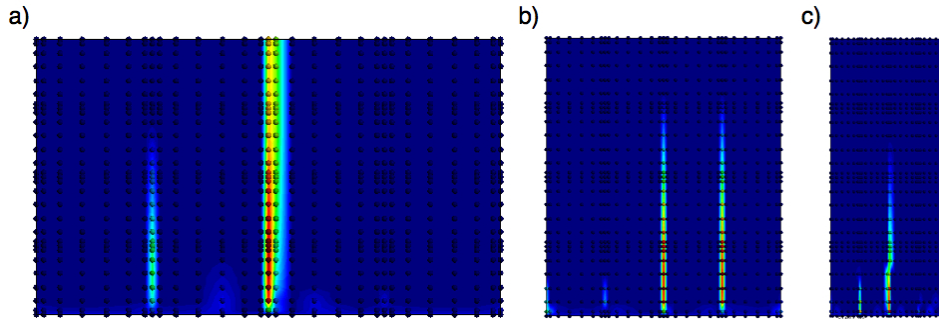


Figure 8.14: The shaded iso-contours of horizontal strain for structures of a quarter (g-5), one eights (g-6) and one sixteenth (g-7) of the full length at the end of the calculation, when no further increase in applied force is observed. In structure g-5 (max. $\epsilon_{xx} = 5.7 \cdot 10^{-3}$), in (a), a fracture is cross cutting the whole layer, whereas the fractures in g-6 (max. $\epsilon_{xx} = 4.0 \cdot 10^{-3}$) in (b) and g-7 (max. $\epsilon_{xx} = 1.0 \cdot 10^{-2}$) in (c) stop within the structure. Fracture saturation seems to be reached for a structure length between (a) and (b).

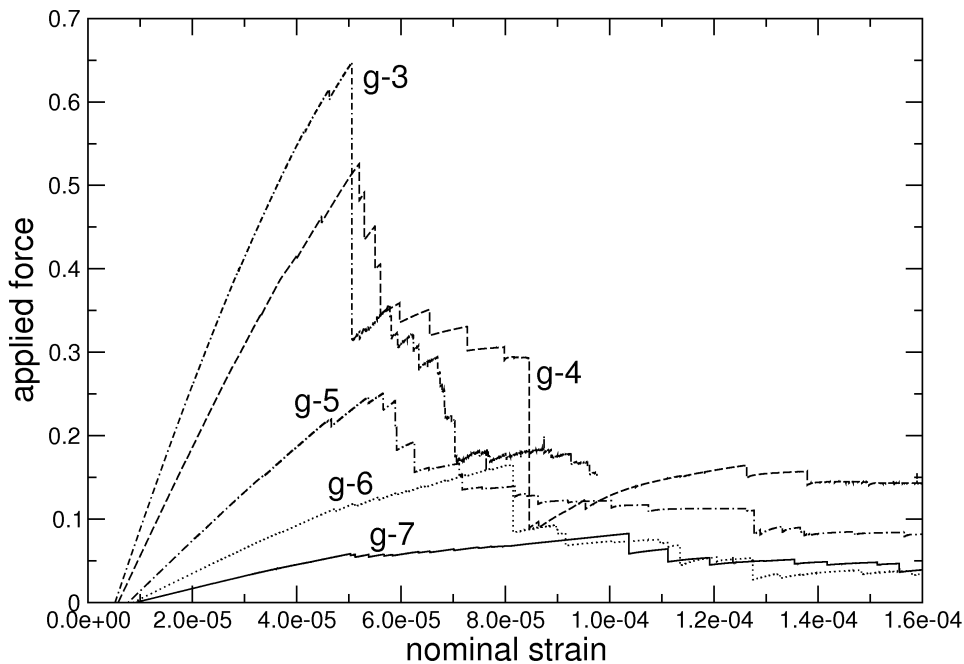


Figure 8.15: The applied force conjugate to the nominal strain of the results for different block lengths but same thicknesses. g-3 represents the structure of full length, g-4 with the half, g-5 a quarter, g-6 an eights and g-7 one sixteenths of the full length.

8.3.3 Frictional interface between a brittle layer and an elastic membrane

This subsection presents the results of the calculation based on the material properties for case g-8 defined in Table 8.2. In contrast to the previous calculations the interface is now assumed to

have negligible cohesion and negligible tensile strength (Table 8.4). The material properties of the bulk have not changed (Table 8.3) compared to the previous subsections. The domain of the solid has been discretized with 8×4 64-noded spectral elements.

Shaded iso-contours of opening strain (γ^o), hydrostatic stress (P), shear strain (γ^s) and von Mises stress (Q^{vm}) just before the initiation of the second fracture set are presented in Figure 8.16a to (d). For comparison of these new results and the one presented previously for the strong interface, the same type of plots are presented in Figure 8.17a to (d). Although the number of nodes is not the same in the two calculations, the plots for the plastic opening strain and the horizontal strains provide almost the same information. The difference comes from the stress in the region next to the interface. The weak interface has been activated in shear and opening. To the contrary, the layer delaminates in a thin region within the bulk material when the interface is strong. The delaminated zone which propagates from the sides of the structure towards the center is recognized in the plot for the equivalent von Mises stress in Figure 8.17d. Since the first fracture became almost a stress free surface, delamination at its boundary with the interface has also occurred. Hence, there exist two different types of stress free surfaces. One on the left and right side of the structure and an additional one which separates the layer in two pieces, created by the fracturing. This observation is underpinned by the symmetric von Mises stress field in (d) which shows that the left and right part of the layer behave indeed as individual blocks. The softened zones due to the delamination are seen in the hydrostatic stress field (c) as blue and green regions.

The applied force on the membrane is presented as a function of the nominal strain in Figure 8.18 for three cases. g-1, and g-3 (layers with an elastic interface but different mesh densities) and g-8 (the interface is frictional). Although the meshes are different, the following discussion tentatively tries to compare the results since the geometry is the same. At low strains the force increases identically up to a nominal strain of $1.5 \cdot 10^{-5}$, at which the weak interface is activated. Note the small striations in the applied load at this specific value of the strain. From that nominal strain on, the force develops differently with a stiffer response for the strong interface. The difference between the curves is the difference in work done by delamination of the interface and delamination within the solid next to the interface in g-8 and g-3 & g-1, respectively. Consequently, there is a lower peak load in calculation g-8 compared to the welded layers (g-3 and g-1). However, in all calculations, the first main force drop is connected to the localization of the first fracture, which appears at the same nominal strain ($\sim 4.9 \cdot 10^{-5}$). This result proves the mesh independency at the onset of strain localization when the first fracture is created. The two calculations with the 64-noded elements (g-3 and g-8) show almost the same residual force, smaller than the residual force for g-1. There is thus a mesh dependency for the residual force

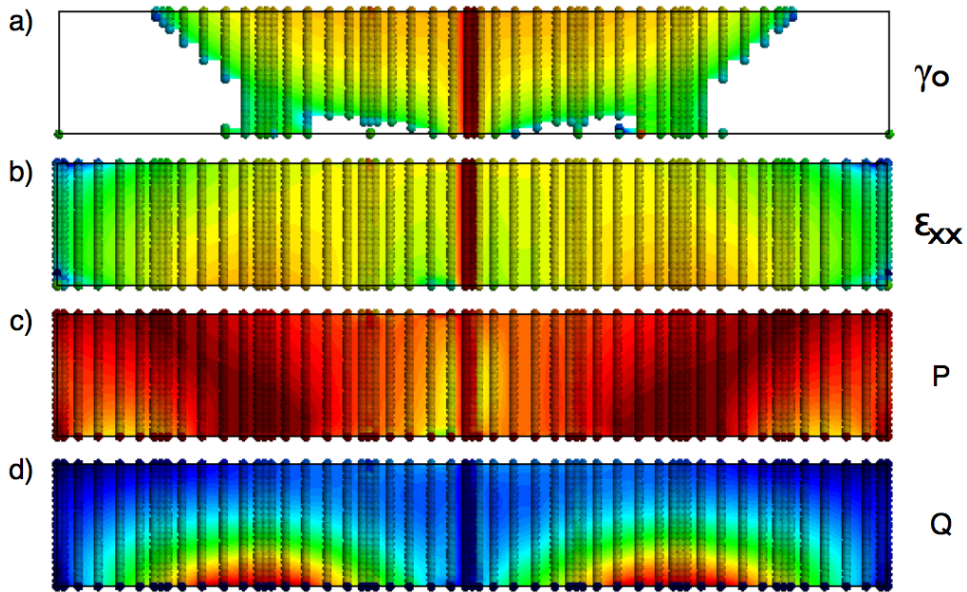


Figure 8.16: Weak interface: Shaded iso-contours of the plastic strain in opening (max. $\gamma^o = 1.7 \cdot 10^{-3}$, min. $\gamma^o = 2.0 \cdot 10^{-8}$) in (a) and the horizontal strain (max. $\epsilon_{xx} = 1.6 \cdot 10^{-3}$, min. $\epsilon_{xx} = 2.3 \cdot 10^{-8}$) in (b), both with a logarithmic scale after $8.0 \cdot 10^{-5}$ nominal strain. The hydrostatic stress field ($P_{max} = 0.050$, $P_{min} = -1.147$) in (c) and the von Mises stress ($Q_{max}^{vm} = 2.623$, $Q_{min}^{vm} = 0$) in (d) show the new stress free central surfaces, created by the first fracture.

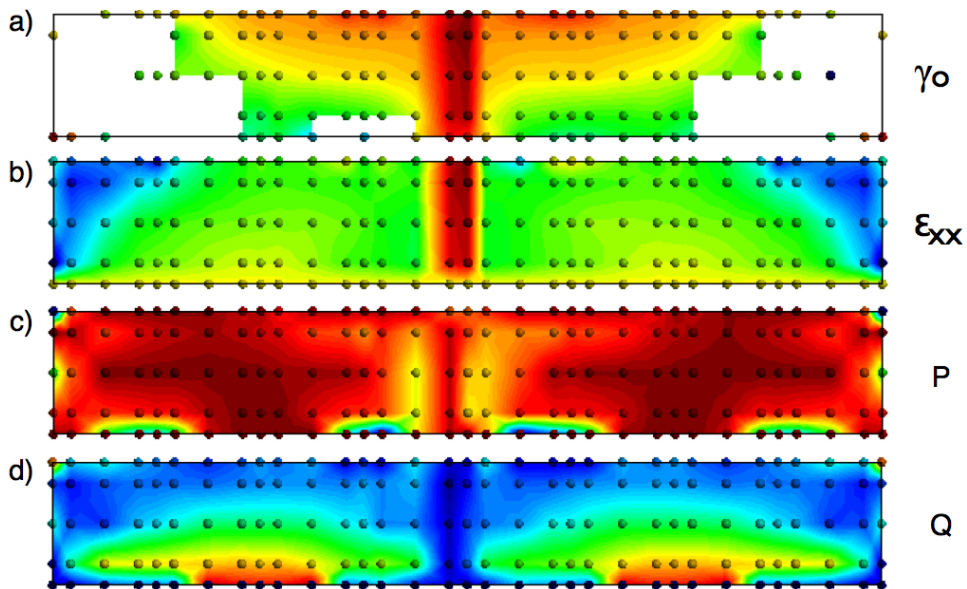


Figure 8.17: Strong interface: Shaded iso-contours of the plastic strain in opening (max. $\gamma^o = 5.6 \cdot 10^{-4}$, min. $\gamma^o = 8.1 \cdot 10^{-8}$) in (a) and the horizontal strain (max. $\epsilon_{xx} = 5.8 \cdot 10^{-3}$, min. $\epsilon_{xx} = 1.5 \cdot 10^{-8}$) in (b), both with a logarithmic scale after $8.0 \cdot 10^{-5}$ nominal strain. The hydrostatic stress field ($P_{max} = 0.051$, $P_{min} = -1.035$) in (c) and the von Mises stress ($Q_{max}^{vm} = 2.849$, $Q_{min}^{vm} = 0$) in (d) show the new stress free central surfaces, created by the first fracture.

which has already been noted.

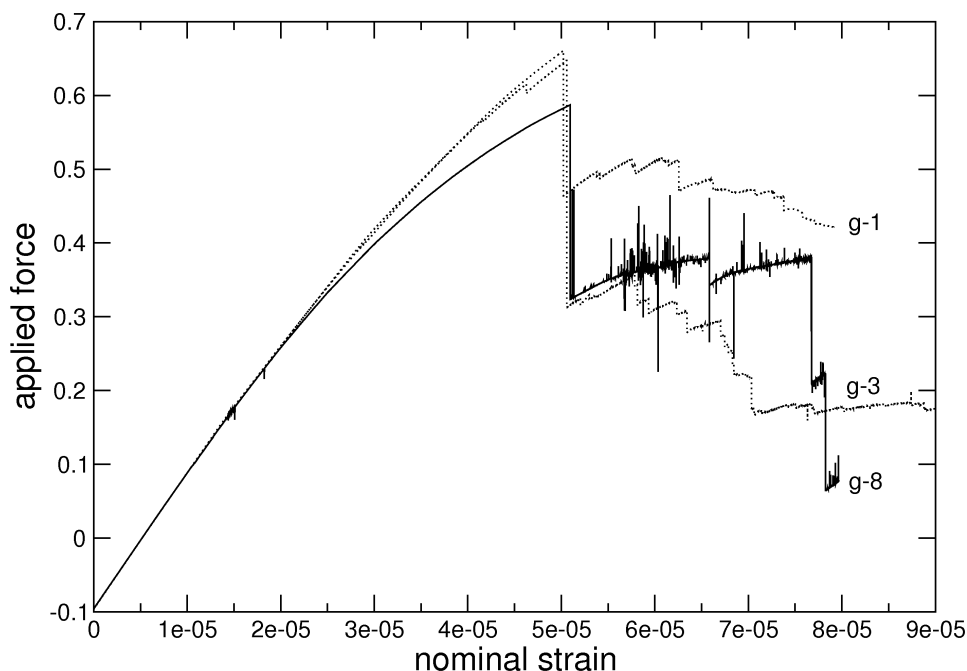


Figure 8.18: The applied force conjugate to the nominal strain of the membrane for the case of an elastic interface (g-1, g-3) and for a frictional interface (g-8). The structure in g-1 is built with a 8x1 25 noded element mesh, g-3 consists of a 4x4 and g-8 of a 8x4 64 noded element mesh

8.4 Conclusion

The first main conclusion of the finite-element calculations is that the strain localization process which is introduced to reproduce mode-I fracturing is also responsible for the initiation of a delamination process in a region parallel to the membrane. This delamination region is not at the interface with the membrane, if this interface is assumed strong compared to the bulk material. In that instance delamination occurs within a boundary layer next to the interface in the bulk material. It has to be pointed out that this is an extreme case which has not been investigated in the experiments since a sand layer was decoupling the gypsum from the foam plate. The interface between beds of carbonate or sandstone, often composed of shales, are weaker than the main rock and thus bulk delamination will not occur.

The second main conclusion is that delamination is responsible for the decoupling of the main part of the gypsum layer from the stretched membrane and thus for the fracture saturation. That result from the FE-study underpins the observation in the analogue experiments, where the saturation of fracturing was related to slip between the gypsum and the foam plate within

the decoupling sandlayer. Hence, theories which assume welded layers without the possibility to delaminate like Bai & Pollard (2000) will always predict tension fracture spacings which are less than they are physically possible. Instead of using welded layer theories to explain small fracture spacings, other causes for dense fracturing should be evoked. Axial splitting has been shortly introduced in the introduction chapter of Part II and can explain denser fracture spacings than the ones which were observed in the present study. Large pore-fluid pressures could initiate hydraulic fracturing and provide another mechanism which is capable to create fractures with smaller spacing than tension fractures.

Another feature which has been observed in the experiments with gypsum powder was the initiation of the first fractures from the top. We could show with the application of plasticity theory that the initial stresses are tensile at the top. During extension, the extensional stress at the top increases and a plastic zone builds up, which triggers the initiation of the fracture from the top. The initiation of fractures from the bottom has been shown to be related to the delamination at the bottom of the layer. Hence, there is a critical length of the specimen which is found to be between the half and a quarter of the full length of the specimen, at which the basement delaminates fast enough in terms of applied strain, so that the fracture initiates from the bottom.

The investigation of the mesh sensitivity has shown that there is no mesh-dependency on the nominal strain at which the first fracture initiates. However, it is observed that the discretization makes a difference in the residual strength of the structure, after the first significant force drop due to the first fracture. Finer meshes favour further strain localization after the first and the coarser meshes favour the decrease of the residual strength. Also, the extensional strain tends to localize at the boundary between two spectral elements, where the distances between the nodes are the denser.

The next step in the numerical study of fracturing using plasticity theory is to consider multilayered structures. A three layer prototype should be considered, consisting of two layers of material *A* with in between a layer with different strength properties *B*. Extensional deformation will be applied to the bottom of the prototype. Fractures will form, which will not only propagate straight through but show different patterns. The aim of this study will be to capture straight, wavy and staircase like fracture patterns which were observed in the analogue experiments with cohesive powders in the previous chapter. Thus, the contrast in the mechanical properties will define the fracture pattern. Cooke et al. (2001) have investigated the importance of weak interfaces on the fracture pattern with the boundary element method to analyse frictional slip and associated opening-mode fracture propagation in two dimensions. They have shown that a weak interface in front of a propagating crack can off-set the propagation of the fracture to create stair-

case like patterns. However, differences in the rock properties in multilayered sequence have not been investigated with the finite-element method and plasticity theory.

The calculations in this chapter have quantified the importance of delamination. However, the calculations are very computer time intensive especially when the mesh is fine or higher-order spectral elements are used. To circumvent these problems, the next chapter tries to develop an analytical solution based on limit analysis to capture mode-I fractures and delamination.

Chapter 9

Application of the maximum strength theorem to the experiments with gypsum

9.1 Introduction

The maximum strength theorem is now applied to capture the different modes of failure observed experimentally and further explained by numerical means in the two previous chapters. The material properties of the bulk material and of the interface between the elastic membrane and the layer of gypsum are controlling the selection of one of the two modes of failure, first delamination of the interface and second, a vertical opening fracture through the central region of the gypsum layer. It is found that the size of the structure does influence that selection, when the interface is assumed to be fully activated. Otherwise, the extent of the activation of the interface, if it is the dominant failure mode, is function of the material properties, the gypsum density and the height of the layer.

9.2 The support function for the truncated Coulomb criterion

The strength domain of the gypsum powder and of the interface between the layer and the membrane is bounded by the Coulomb criterion, truncated in tension to account for mode I type of fractures, Figure 9.1. Let us denote the stress vector acting on the interface or the fault or fracture through the layer by the vector \underline{T} which is decomposed in a normal component σ_n and a tangential component τ in the direct basis $\{\underline{n}, \underline{t}\}$. The boundary of the strength domain consists of the classical Coulomb lines defined by the angle of friction ϕ and the cohesion c in the $\{\sigma_n, \tau\}$ space. These two lines are truncated in tension by a segment parallel to the τ axis defining the tensile strength d . The bulk material is characterized by the three parameters ϕ , c and d and the

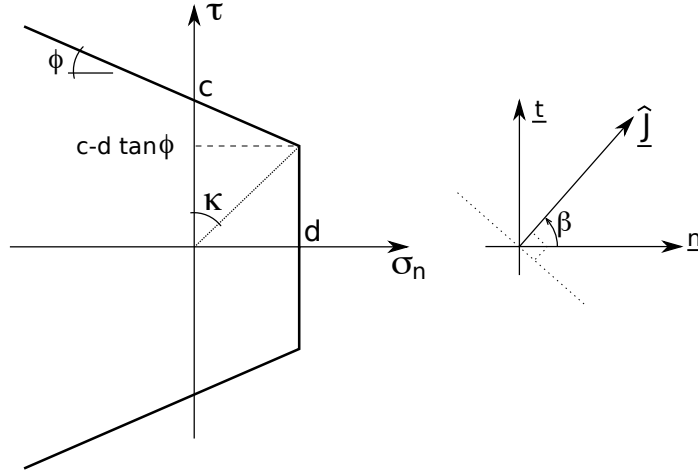


Figure 9.1: The strength domain is bounded by the Coulomb criterion truncated in tension. The jump over any interface is oriented in the same stress space by the angle β measured positively anti-clockwise with respect to the normal.

subscript d for the same set of letters will be used to characterize the basal interface properties, seen as a "décollement".

The virtual power over any discontinuity in the velocity field is defined by the product of the stress vector and the virtual velocity jump $\underline{T} \cdot \hat{\underline{J}}$. This jump is the difference in velocity between the positive and the negative sides of the discontinuity, the positive side being oriented by the normal \underline{n} . The velocity jump is oriented with respect to this normal by the angle β , Figure 9.1. The stress vector is unknown and the upper bound to the tectonic force requires simply to define the maximum virtual power or resisting power, a quantity which is constructed graphically (see Maillot & Leroy (2006) and chapter two of this thesis). This maximum power is a function of the orientation of the velocity jump and is often referred to as the support function. Its expression for the truncated Coulomb criterion of Figure 9.1 is

$$\begin{aligned}
 \text{case (0): } \beta = 0, & \quad \pi(\hat{\underline{J}}) = d\hat{J}, & (9.1) \\
 \text{case (1): } |\beta| < \pi/2 - \phi, & \quad \pi(\hat{\underline{J}}) = \hat{J}[d \cos \beta \pm (c - d \tan \phi) \sin \beta], \\
 \text{case (2): } |\beta| = \pi/2 - \phi, & \quad \pi(\hat{\underline{J}}) = \hat{J}c \cos \phi, \\
 \text{case (3): } \pi/2 - \phi < |\beta| \leq \pi, & \quad \pi(\hat{\underline{J}}) = +\infty.
 \end{aligned}$$

If the velocity jump is oriented along the normal ($\beta = 0$), then the support function is equal to the tensile strength times the norm of the velocity jump (case 0). The illustration in Figure 9.1 is for an orientation of the jump vector corresponding to case 1 in chart 9.1 (the \pm sign) is for positive and negative angles β , respectively). Case 2 corresponds to a velocity jump normal to

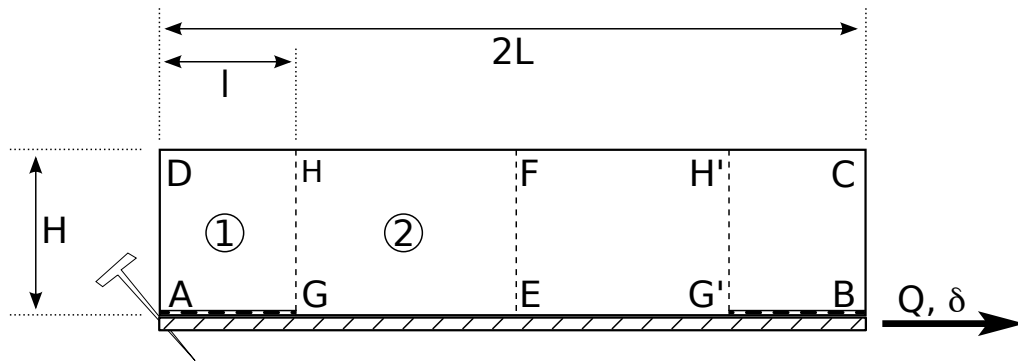


Figure 9.2: The prototype consists of a rectangular region composed of an homogeneous material resting on a membrane which is stretched. The dissipation occurs over the interface between the membrane and the gypsum layer (segments AG and $G'B$), the opening fracture (segment EF) and the slip along the vertical segments GH and $G'H'$ which are necessary to ensure the compatibility of displacement of the various rigid blocks.

the Coulomb line and the support function is then dependent on the cohesion and the friction angle. Case3 corresponds to an angle β larger in absolute value than $\pi/2 - \phi$ and the support function is infinite. Velocities in that case are of no interest since the support function is infinite. Velocity fields and jumps which are oriented according to cases 0 to 2 are said to be pertinent.

9.3 The prototype and the virtual velocity field

The prototype of the experiment is composed of a layer of gypsum with the cross section corresponding to the domain $ABCD$ in Figure 9.2 of thickness H and length $2L$. The layer of gypsum rests on a membrane of foam which corresponds to the hatched thin layer below the segment AB on the same figure. The left termination of the membrane, below point A , is fixed to the rigid base. The right end, below point B , is displaced by δ thanks to the application of the force Q for which an upper bound is sought. The prototype assumes homogeneous material properties defined by the strength domain presented in the previous section for the interface AB and the bulk material in $ABCD$.

The failure mode is composed of two parts. The first part consists of the line EF in Figure 9.2 which corresponds to the first tensile fracture observed experimentally. The second part corresponds to the slip and opening of the interface between the membrane and the gypsum along the segments AG and $G'B$ of length l which is an unknown of the problem. The two blocks $GEFH$ and $EG'H'F$ are displaced towards the right as rigid bodies. The delamination along AG and $G'B$ requires a jump in the velocity field with a vertical component to be pertinent

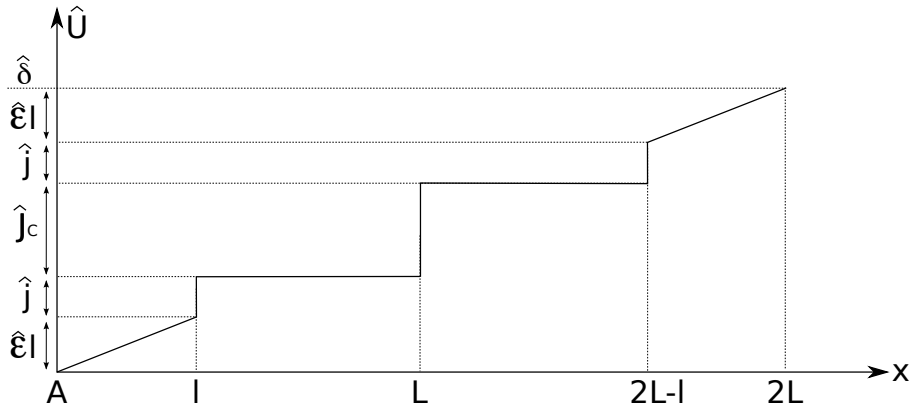


Figure 9.3: The virtual velocity of the membrane is linear where there is delamination and constant where the gypsum layer is displaced rigidly with no slip. The central jump corresponds to the opening fracture and the two external are necessary for pertinence of the whole velocity field.

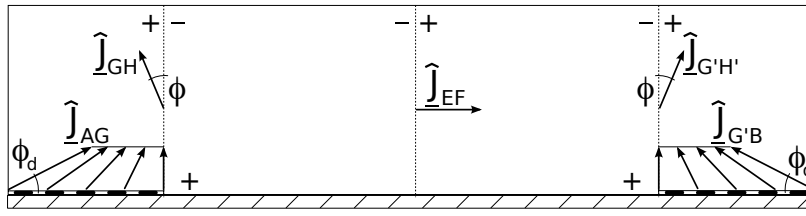


Figure 9.4: The jump vectors over the discontinuities of the prototype in Figure 9.2.

and, consequently, the block $AGHD$ and $G'BCH'$ have not only an horizontal virtual velocity component but also a vertical component to be pertinent. These two regions of width l are thus moving vertically with respect to the central region which is only translated horizontally. The lines GH and $G'H'$ are then discontinuities where dissipative powers have to be accounted for. This strong assumption that every subdomain of the gypsum layer is displaced by a rigid body motion is certainly appealing for the construction of an analytical solution but has the drawback to introduce a dissipation along two segments crossing the whole specimen height. It is most likely that this dissipation is more localized to a small region around the tip of the delamination zones, points G and G' .

The velocity field is now constructed in details starting with the membrane. The stretching of the membrane is assumed constant below the delaminated regions and given by the virtual strain rate $\hat{\epsilon}$. The virtual velocity of the membrane is thus linear in these two regions (AG and $G'B$), as shown in Figure 9.3. The x -axis is parallel to the membrane and has its origin at point A shown in Figure 9.1. The two central blocks are fixed with respect to the membrane and there is no slip along the interface. The membrane velocity below these two central blocks is thus

piecewise constant. The central jump of intensity \hat{J}_c introduced in Figure 9.3 corresponds to the opening of the central mode I fracture. There are also two jumps at $x = l$ and $x = 2L - l$ of equal intensity \hat{j} corresponding to the opening component of the velocity jump across the two segments GH and $G'H'$. This horizontal component is necessary for the jumps to be pertinent, as it will be demonstrated. The virtual velocity of point B where the force is applied takes for value

$$\hat{\delta} = 2\hat{\epsilon}l + 2\hat{j} + \hat{J}_c . \quad (9.2)$$

The velocity of the gypsum layer is piecewise constant. Only the two blocks to the left of the central fracture are discussed benefiting from the symmetry of the failure mechanism. They are referred to as block 1 (region $AGHD$) and block 2 (region $GEFH$), as indicated in Figure 9.2. The velocity of the block 1 in the horizontal direction is constant and chosen to be equal to the velocity $\hat{\epsilon}l$ of the membrane before the jump at point G . The vertical component is assumed proportional with the unknown scalar α to this velocity so that the whole vector reads

$$\hat{\underline{U}}_1 = \hat{\epsilon}l(\underline{e}_x + \alpha\underline{e}_y) , \quad (9.3)$$

in which $\{\underline{e}_x, \underline{e}_y\}$ is an orthonormal basis. The velocity jump along AG is then

$$\hat{\underline{J}}_{AG} = \hat{\epsilon}l\left[\left(1 - \frac{x}{l}\right)\underline{e}_x + \alpha\underline{e}_y\right] , \quad (9.4)$$

the normal to this interface $\underline{n} = \underline{e}_y$ pointing towards the plus side. The horizontal component of this jump is a decreasing function of x tending to zero as x reaches the value of l . The jump is thus in case 0 defined in (9.1) at point G . It is proposed to choose the scalar $\alpha = \tan \phi_d$, so that the jump corresponds to case 2 at point A . The jump vector is then sweeping through the cone corresponding to case 1 as one moves from point A to G . To summarize, the velocity of the first block and the velocity jump over AG are

$$\begin{aligned} \hat{\underline{U}}_1 &= \hat{\epsilon}l(\underline{e}_x + \tan \phi_d \underline{e}_y) , \\ \hat{\underline{J}}_{AG} &= \hat{\epsilon}l\left[\left(1 - \frac{x}{l}\right)\underline{e}_x + \tan \phi_d \underline{e}_y\right] . \end{aligned} \quad (9.5)$$

The block 1 is moving virtually vertically with respect to block 2 and the velocity jump between this two blocks needs to have a horizontal component \hat{j} to be pertinent. The smallest value which can be considered ensures that the velocity jump is in case 2. The velocity jump is then

$$\hat{\underline{J}}_{GH} = \hat{\epsilon}l \tan \phi_d [-\tan \phi \underline{e}_x + \underline{e}_y] , \quad (9.6)$$

orienting the discontinuity GH by the normal $\underline{n} = -\underline{e}_x$. The membrane does sustain the same horizontal velocity jump denoted earlier by \hat{j} which reads:

$$\hat{j} = \hat{\epsilon}l \tan \phi_d \tan \phi . \quad (9.7)$$

9.4. The least upper bound to the force

The velocity of the central block denoted block 2 is now deduced from the velocity of block 1

$$\underline{\hat{U}}_2 = \hat{\epsilon}l(1 + \tan \phi \tan \phi_d)\underline{e}_x = \frac{\hat{\epsilon}l \cos(\phi - \phi_d)}{\cos \phi \cos \phi_d} . \quad (9.8)$$

The central fracture corresponds to a jump in velocity which is horizontal to be in case 0 and corresponds to the vector

$$\underline{\hat{J}}_{EF} = \hat{J}_C \underline{e}_x , \quad (9.9)$$

choosing the normal $\underline{n} = \underline{e}_x$.

9.4 The least upper bound to the force

The objective is now to apply the maximum strength theorem to obtain the least upper bound to the force Q .

The external power has two contributions, the first due to the force Q on the velocity $\hat{\delta}$ and the second due to the power of the virtual velocity and the gravity forces. It reads

$$\mathcal{P}_{\text{ext}} = Q\hat{\delta} - 2\hat{\epsilon}l^2 \tan \phi_d \rho g H , \quad (9.10)$$

where ρ is the material density and g the gravity acceleration.

The maximum resisting power is the sum of the contributions from each of the discontinuities which are AG , $G'B$, GH , $G'H'$ and EF . The vertical discontinuities GH and $G'H'$ are in case 2, the central discontinuity in case 0 and the two horizontal discontinuities are covering the cone defined in case 1 as one moves from point A to G or from point B to G' . The total resisting power is the sum of the distribution of the support function over the length of these discontinuities and this quadrature in our problem is

$$\mathcal{P}_{\text{mr}} = \hat{\epsilon}l^2(d_d \tan \phi_d + c_d) + 2\hat{\epsilon}lH \tan \phi_d c + \hat{J}_C dH . \quad (9.11)$$

The maximum strength theorem ensures that the external power is always less than the maximum resisting power so that the force Q is bounded by the upper bound

$$\begin{aligned} Q_u &= \hat{\epsilon}l^2(d_d \tan \phi_d + c_d) + 2\hat{\epsilon}lH \tan \phi_d c \\ &\quad + \hat{J}_C dH + 2\hat{\epsilon}l^2 \tan \phi_d \rho g H , \end{aligned} \quad (9.12)$$

having set the velocity of the membrane at the end point B, defined in equation (9.2) and based on (9.7), to one, for sake of normalization:

$$\hat{\delta} = \frac{2\hat{\epsilon}l \cos(\phi - \phi_d)}{\cos \phi \cos \phi_d} + \hat{J}_C = 1 . \quad (9.13)$$

The upper bound in (9.12) is function of the three scalars $\hat{\varepsilon}$, l and \hat{J}_C which are related by (9.13) so that only two of these three scalars are independent. The jump on the central discontinuity is substituted in terms of l and $\hat{\varepsilon}$ so that the upper bound reduces to

$$Q_u = dH + \hat{\varepsilon}l\mathcal{A} + \hat{\varepsilon}l^2\mathcal{B}, \quad (9.14)$$

with $\mathcal{A} = \frac{2Hd \sin(\phi - \kappa)}{\cos \phi \sin \phi}$,

$$\mathcal{B} = 2\rho gH \tan \phi_d + c_d + d_d \tan \phi_d.$$

The objective is to minimize the upper bound in (9.14) to obtain the least force by choosing the appropriate values of the two free scalars which are constrained by the geometry and the statement that the velocity jump of the central discontinuity is positive or zero

$$0 \leq l \leq L, \quad 0 \leq \hat{\varepsilon} \leq \frac{\cos \phi \cos \phi_d}{2l \cos(\phi - \phi_d)}. \quad (9.15)$$

The central point of this minimization is the sign of the scalar \mathcal{A} defined in (9.14). This scalar is negative, if

$$\mathcal{A} \leq 0 \iff \phi_d \leq \kappa, \quad (9.16)$$

the angle κ being defined in Figure 9.1. This condition is independent of the size of the prototype and only function of the material properties of the interface and of the bulk material.

The second scalar \mathcal{B} in (9.14) is always positive. If the scalar \mathcal{A} is positive ($\phi_d > \kappa$) then the upper bound is an increasing function of both, $\hat{\varepsilon}$ and l . The least upper bound is thus obtained for $\hat{\varepsilon} = 0$ and $l = 0$. Delamination is not taking place. Consequently, the failure mode is by the central fracture ($\hat{J}_C = 1$) and the least upper bound is $Q_{lu} = dH$. Consider now \mathcal{A} to be negative ($\phi_d < \kappa$) and the least upper bound in (9.14), independent of $\hat{\varepsilon}$, is reached for

$$l_{lu} = -\frac{\mathcal{A}}{2\mathcal{B}}, \quad (9.17)$$

if that value is less than L . It is set to L otherwise, corresponding to a complete delamination of the interface between the membrane and the gypsum layer. The least upper bound is then

$$Q_{lu} = dH - \hat{\varepsilon}_{lu} \frac{\mathcal{A}^2}{4\mathcal{B}}, \quad (9.18)$$

where the scalar $\hat{\varepsilon}_{lu}$ is the maximum in the range defined in (9.15) or the value for setting Q_{lu} to zero, to ensure that the tectonic force is not negative. Note that if $\hat{\varepsilon}_{lu}$ is set by the maximum value in (9.15), then the central discontinuity has a zero virtual velocity. The opening fracture is not activated and the failure mode consists only of the partial delamination. If the value of $\hat{\varepsilon}_{lu}$ is set to ensure that the least upper bound is not negative, then the central fracture is marked by a jump amplitude of finite size. This mixed failure mode, partial delamination and opening fracture, occurs for a zero applied load and is thus more difficult to interpret.

9.5 Size effects

A fully delaminated interface concomitant with a central fracture is equivalent of setting $l_{lu} = L$ and respecting the condition that $\hat{J}_C \neq 0$. In that case, the three vertical discontinuities in the velocity field GH , EF and $G'H'$ are reduced to a single one. The whole structure is thus virtually lifted and there is no need any more to consider a jump \hat{j} , which was needed to separate the virtually lifted part 1 from the horizontally moving part 2 (Figure 9.2). Hence, only the jump over the discontinuity EF and along the activated décollement are composing the power of internal forces which reads:

$$\mathcal{P}_{mr} = \hat{\epsilon}L^2 (c_d + d_d \tan \phi_d) + \hat{J}_C Hd . \quad (9.19)$$

The velocity of the membrane in point B ($\hat{\delta}$) simplifies from (9.13) to:

$$\hat{\delta} = 2\hat{\epsilon}L + \hat{J}_C . \quad (9.20)$$

The power of the external forces remains identical to the expression in (9.10). The least upper bound is thus:

$$Q_u = Hd + \hat{\epsilon}L (\mathcal{A}' + L\mathcal{B}) , \text{ with } \mathcal{A}' = -2Hd \quad (9.21)$$

There are various scenarios possible when minimizing Q_u in terms of forces with respect to $\hat{\epsilon}$, depending on the sign of the term $(\mathcal{A}' + L\mathcal{B})$ in (9.21). If this term is positive, $\hat{\epsilon}$ is chosen to be zero, $\hat{J}_C = 1$ and the least upper bound reads:

$$Q_{lu} = Hd . \quad (9.22)$$

For negative values of the term $(\mathcal{A}' + L\mathcal{B})$, $\hat{\epsilon}$ is chosen as large as possible within the range:

$$0 \leq \hat{\epsilon} \leq \frac{1}{2L} , \quad (9.23)$$

based on (9.20) and the constraint that \hat{J}_C has to be in the interval $[0;1]$. In that case, only delamination along the basal interface occurs, without the creation of a central fracture ($\hat{J}_C = 0$).

The least upper bound is given by:

$$Q_{lu} = \frac{\mathcal{B}}{2} . \quad (9.24)$$

Q_{lu} is restricted to positive values. This constraint leads to a maximum value of $\hat{\epsilon}$ which is

$$\hat{\epsilon} \leq \frac{-Hd}{L(\mathcal{A}' + L\mathcal{B})} . \quad (9.25)$$

Hence, there exists a solution, at which neither $\hat{\epsilon}$, nor \hat{J}_C are zero and hence, delamination and fracturing occurs. Note, that this result provides a least upper bound to the force which is zero.

The transition from fracturing without delamination to the full activation of the interface happens, when the term $(\mathcal{A}' + L\mathcal{B})$ is zero. There exists thus a critical length of the specimen

$$L_{crit} = \frac{2Hd}{2\rho gH \tan \phi_d + c_d + d_d \tan \phi_d}, \quad (9.26)$$

which is depending on the bed thickness H . Note, that this dependency is not existing, when the cohesion and the tensile strength of the interface are disregarded.

9.5.1 Application to the experimental work

The application of this approach to predict the saturated fracture spacing is now considered. We take the material properties for the compacted gypsum powder from the analogue experiments from the previous chapter. The tensile strength is 107 Pa and the cohesion is expected to be 646 Pa. The friction angles for the interface (ϕ_d) and the gypsum (ϕ) are both equal to 30° and $c_d = d_d = 0$. The angle κ is 10° which results in no delamination, since \mathcal{A} is positive ($\phi_d > \kappa$). Hence, fracturing is the only possible failure mode. Furthermore this result is independent of the length of the specimen. This is in contradiction with the laboratory experiments where fracture saturation was observed.

The possibility of a fully activated interface and a central fracture was studied in the previous section, choosing l_u equal to L . Assuming that the tensile strength and the cohesion are given with the values above and no cohesion of the interface in (9.26), provides a uniform fracture spacings of 18 mm, independent of the layer thickness. Varying the tensile strength d to 75 Pa and the cohesion on the interface to 40 Pa yields in a fracture spacing of 8, 11 and 12 mm for 5, 20 and 40 mm thick layers of gypsum powder, which is in good agreement with the mean values of the measurements.

However, the velocity field which has been introduced for the piecewise delamination along the interface has potential to be improved by avoiding the two vertical discontinuities GH and $G'H'$. One possibility would be to provide a support function which accounts for the fracture propagation in the interface, with zero dilation at points G and G' . The second possibility would be to consider a non-uniform velocity field in the regions $AGHD$ and $G'BCH'$ with the purpose to let the jump vector vanish to zero at the tip of the delaminated zone. The result would be, like in the first proposal, a decrease in the work against gravity and thus an optimization of the upper bound Q_{lu} .

Another idea is followed in the next section, where the traction vector in the activated part of the interface is assumed to be known which leads to a non-dilating virtual velocity field in the layer above the interface.

9.6 Modified velocity field

The prototype still consists of the rigid layer (region $ABCD$, Figure 9.4) of length $2L$, thickness H and the specific weight ρ . The strength of the interface is assumed to be weaker than the layer in a first step. Due to the stretching of the membrane with the strain rate $\dot{\epsilon}$ two different modes of failure are assumed which are the delamination between the layer and the membrane on the one hand and an opening mode fracture within the layer on the other hand. The delamination happens along lines AG and $G'B$. Let us assume, that instead of opening and shear failure, only shear failure will occur in the delaminated zone with length l . In section 2 it is stated that the support function for a velocity jump which is parallel to the failure plane will lead to an infinitely high value (case 3 in equation 9.1). However, the knowledge of the traction vector \underline{T} on the failure plane can limit this value. On the example of a block resting on a horizontal plane which is presented in Figure 9.6 it shown, how the unknown stress along the delaminated zone is determined. The block weights $G = \rho g ab$, a being the length of the base and b the thickness. Assuming Andersoninan stress field, the vertical stress in the interface is constant over a when a force pushes the block from the left. The Mohr circle on the left side of the figure shows the stress state in the interface, when the interface fails in shear. The traction vector \underline{T} is given by the point where the circle touches the failure envelope and is given by:

$$\underline{T} = \sigma \underline{n} + \tau \underline{t} = \frac{G}{l} \underline{n} + \left(c + \frac{G}{l} \tan \phi \right) \underline{t} \quad (9.27)$$

The orientation of the jump vector \underline{J} is chosen to be parallel to the tangent in order to minimize the work against gravity. It has to be noted at this point that \underline{T} is based on an assumption which means, that the result will not be a bound in the sense of limit analysis!

However, it is a try getting closer to the observed fracturing from the analogue experiments. As stated above, we assume from the Mohr-circle construction that the stresses on a failure plane is $\sigma = \rho g H$ and $\tau = c_d + \sigma \tan \phi_d$. Hence, the virtual power along the delaminated length l can be written as

$$\text{Sup} [\underline{T} \cdot \underline{J}] = \underline{T} \cdot \underline{J} = (c_d + (\rho g H) \tan \phi_d) \underline{J} .$$

The second type of discontinuities occurs along the line EF of the solid layer. It represents an opening mode fracture (case 0 in 9.1) and divides the layer in two rigid blocks of different velocity. The velocity jump will thus be in the normal direction of the discontinuity. The velocities of the solid layer (U_s) and of the membrane (U_m) are piecewise linear and read:

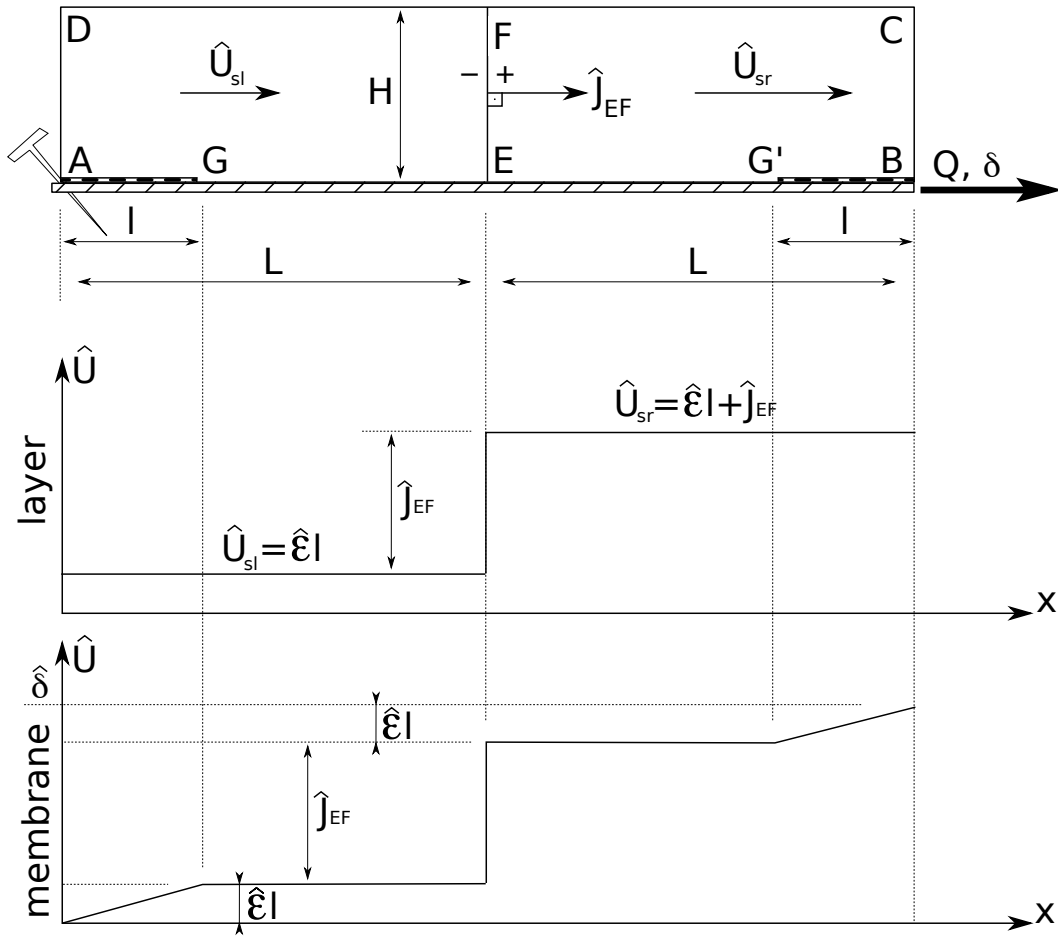


Figure 9.5: The prototype with its geometry and velocity fields for the gypsum layer and the elastic membrane.

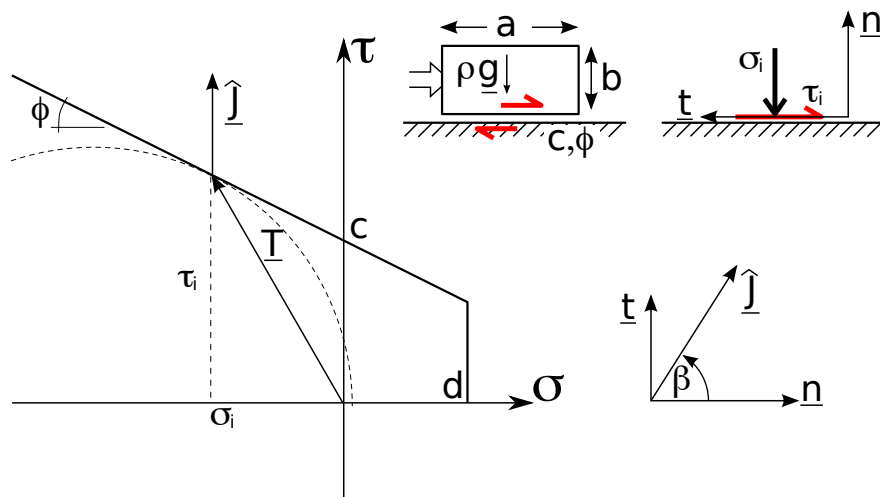


Figure 9.6: The stresses along the activated interface are provided by the construction of the Mohr-circle under the assumption of an Andersonian stress field.

$$\begin{aligned}
 0 \leq x \leq l &\Rightarrow U_s = \hat{\epsilon}l \\
 &U_m = \hat{\epsilon}x, \\
 l \leq x \leq L &\Rightarrow U_s = U_m = \hat{\epsilon}l, \\
 L \leq x \leq 2L - l &\Rightarrow U_s = U_m = \hat{\epsilon}l + \hat{J}_{EF}, \\
 2L - l \leq x \leq 2L &\Rightarrow U_s = \hat{\epsilon}l + \hat{J}_{EF}, \\
 &U_m = \hat{\epsilon}(2l + x - 2L) + \hat{J}_{EF}.
 \end{aligned}$$

The total extension of the elastic membrane is $\hat{\delta}$ and is set to 1. The jump over the discontinuity EF has the norm $\hat{J}_{EF} = \hat{\delta} - 2\hat{\epsilon}l = 1 - 2\hat{\epsilon}l$ and the term for the internal power reads:

$$P_{int} = \hat{\epsilon}l^2 (c_d + (\rho gH) \tan \phi_d) + (1 - 2\hat{\epsilon}l)Hd.$$

The power of the external forces is only the work of the external Force Q and gravity does not play a role:

$$P_{ext} = \hat{\delta} Q = Q.$$

Thus, the upper bound of the force is given by the theorem of virtual work $P_{ext} = P_{int}$:

$$Q_u = \hat{\epsilon}l^2 (c_d + \rho gH \tan \phi_d) - 2\hat{\epsilon}lHd + Hd. \quad (9.28)$$

The force will be as long positive as the strain rate is larger than zero and

$$\hat{\epsilon} \leq \frac{c_d + \rho gH \tan \phi}{d H}.$$

The minimum of Q_u as a function of the length l is found by setting to zero the derivative $\frac{\partial Q}{\partial l}$, providing:

$$l_{min} = \frac{Hd}{c_d + \rho gH \tan \phi_d},$$

which is found to be independent of the strain rate $\hat{\epsilon}$. It has to be noted, that the assumptions on the stresses along the activated interface are the same as proposed by Price (1966) when he introduced his frictional coupling theory for the minimum fracture spacing. It is of no surprise that the same assumptions lead to the same result. Hence, the maximum distance between to neighbouring fractures to create a further crack cannot be less than $2l_{min}$.

The analogue experiments with compacted gypsum powder 40 mm, 20 mm and 5 mm thick layers showed a saturated fracturing with mean-values for the fracture spacing of 12 mm, 10 mm and 9 mm. Using the material properties proposed before ($d = 75 \text{ Pa}$, $c_d = 40 \text{ Pa}$, $\phi_d = 30^\circ$), leads to a spacing of 11, 10 and 5 mm. It is interesting to observe that without having cohesion on the interface, the fracture spacing of a layer without additional burial pressure than its self weight, is independent on the thickness of the unit and results in a spacing of 13 mm, which is still in the corridor of the measured spacings of the experiments.

The second question is, what happens if the interface between the membrane and the layer has a higher strength than the layer? One could simply assume that delamination takes place right next to the interface in the solid above. This assumption is supported by the finite element calculations in the previous chapter. There was observed that delamination occurs next to the elastic interface in the brittle layer. The strength domain of the gypsum is also used for the interface in the following to account for no slip along the interface. The minimum length of delamination can therefore be not less than

$$l_{min}^{tot} = \frac{Hd}{c + \rho gH \tan \phi},$$

Applying the material properties for the compacted gypsum, with 648 Pa cohesion and 107 Pa tensile strength, provides 1, 3 and 5 mm minimum fracture spacing for 5, 20 and 40 mm thick layers.

Part III

Bending fractures

Chapter 10

A new experimental device to create bending fractures

Frictional coupling between layers, within a fold results in a complex partial distribution of the deformation in extension or compression generated by the overall flexure. Part II of this thesis has addressed fracturing, where extensional strain is applied to brittle layers. In this Part III, a new experimental device is introduced to produce fractures during bending. The influence of frictional coupling and the position of a layer with respect to the neutral axis is varied so that extensional and compressional strain could be generated during bending.

10.1 Introduction

The knowledge of the fracture density, orientation and aperture within a folded multilayered rock is essential for the evaluation of dynamical properties of oil and gas reservoirs within folds. The experimental device introduced here is proposed as a tool to quantify the key parameters which controls the fracturing.

Rives et al. (1992) investigated fracture patterns and fracture spacings in experiments where they bended an elastic plate with a brittle coating. They described the evolution of the fracture spacing distribution in terms of applied strain as being exponential in the early stages of fracturing. This distribution becomes log-normal to normal, when fracture saturation is observed. Unfortunately, no variation of the thickness of the brittle layer is reported. A similar technique, bending a 0.45 cm thick elastic plate with a brittle coating of different thicknesses, varying between 0.016 mm and 0.373 mm were used by Wu & Pollard (1995). They studied saturated fracture spacing related to the layer thickness and concluded that fracture spacing indeed increases with layer thickness but could not confirm if the relationship is linear or exponential.

Spyroopoulos et al. (1999) stretched a rubber plate with layers of a clay-water mixture and confirmed the interpretation of the field measurements by Ladeira & Price (1981) and Narr & Suppe (1991). These authors all state that there is a linear relationship between saturated fracture spacing and layer thickness.

Flexing is not stretching, has been stated by Supak et al. 2006 in their experimental study on flexure induced faulting with partly liquefied plaster. They noted, that although stretching and flexing induce similar traits, stretching differs fundamentally from flexing. With precaution, they stated that the characteristic spacing does not scale with layer thickness for under flexure, whereas the fractures caused by stretching do scale with the layer thickness. Their investigation was aiming at flexure related fractures and faults in subduction zones within the brittle lithosphere. The length scale of interest differs from ours, since we are interested in fracturing at the bedding scale. However, the difference between stretching and bending is essential in the two studies.

In the early stages of the fold development, a first set of fractures is sometimes found. This set due to axial splitting is observed when the maximum and minimum principal stresses are horizontal. Further compression leads to a second type of fractures, which are parallel to the fold axis. They are created when the curvature of the fold reaches a critical value. Depending on the interfacial properties between the layers, the neutral axis of deformation, where no stretching nor compression takes place, is found in a single or within each layer of the multilayer sequence. Strong bonding between the individual layers will prohibit bed parallel slip. The structure in Figure 10.1a bends cylindrically continuously with a single neutral axis of deformation, shown in the middle of layer II. Note, that the neutral axis is not necessarily always in the middle of the structure and its position depends on the non-linear material properties. It is indeed in the middle of the structure, if the material is homogeneous and the deformation is elastic. The fractures will initiate in the outer arc of the fold, caused by tensile stresses due to the stretching of the layer I above the neutral axis. As soon, as fracturing at the outer arc is initiated, the neutral axis migrates into the initially compressional region.

When bed parallel slip is allowed, each layer composing the whole sequence has its own neutral axis. The extreme case is, when there is no coupling between the layers (Figure 10.1b) and each layer within the structure reacts with its own neutral axis. The more bed parallel slip is allowed during flexure, the less stretching from the neighbouring layers in addition to the applied curvature is composing the total deformation of the individual layers. Concentric, cylindrical bending of a multilayered sequence will develop a specific fracture pattern. The prestresses due to burial depth is disregarded in the following reasoning. The thickness of each individual bed stays constant while the deflection increases, the interface between the layers is

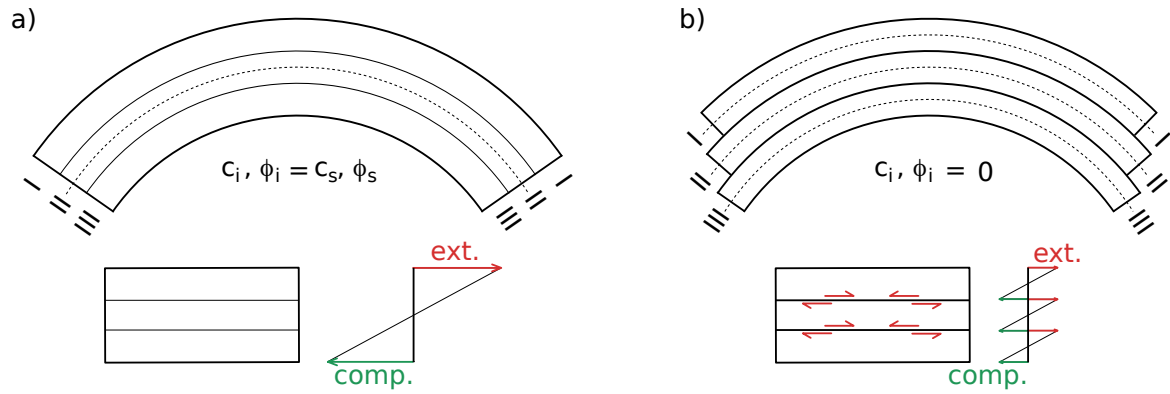


Figure 10.1: The interfacial properties control the type of deformation of each individual layer during an overall bending. Not only bending but also stretching or compression will be applied to the individual concentric layers. In (a), no slip in the interface results in a single neutral axis (dashed line) in the middle of Layer II, because the frictional properties along the interface are equal to the properties of the solid. Hence, the fractures initiate on the top of layer I and then propagate into the compressional layer III. The friction angle and cohesion along the interface are zero and each layer has its own neutral axis (dashed lines) (b). The radius of curvature is the smallest in layer III and fractures initiate there, assuming cylindrical bending and concentric layers.

allowed to shear and opening is prohibited. Consequently, the radius is linearly increasing with bed thickness from the inner arc towards the outer arc of the bended structure. The curvature is thus larger in the inner layers than in the outer layers of the fold. Hence, the fractures in layer III will initiate earlier than in the outer regions (layer I).

In the light of this argument, the influence of the layer thickness on the fracture spacing in the bending experiments of Wu & Pollard (1995) has to be treated with precaution, since the brittle coatings are attached to the elastic substratum having a much larger thickness than the brittle layer. It is believed that the layers are not showing fractures, dominantly due to flexure but due to stretching of the thick elastic layer on the extensional side of the neutral axis of the fold, similar to layer I in Figure 10.1a.

10.2 Experimental device and creating the specimen

The initial stage of the experimental setup is shown in Figure 10.2a and (b) in a cross section and a top view, respectively. The device consists of two rows of three rigid vertical limbs L which are connected to the horizontal elastic polycarbonate plate P (Bayer Makrolon, 1500 mm long, 500 mm wide) of constant thickness (12 mm). The limbs were built from 40x40 mm aluminium bars (Kanya extrusion system) and each consists of two parts (L_u, L_l). Each part has the shape

10.2. Experimental device and creating the specimen

of a triangle, in cross section, and they are clamped together with the polycarbonate plate in between to ensure a stiff connection. Two wooden panels (S), 18 mm thick, are screwed in a vertical position to provide lateral boundaries for the analogue material (G). The maximum dimensions for the specimen are 1000 mm in length and 500 mm in width. The left limb is pinned at its bottom (B_l) on a table so that displacement in the vertical and horizontal directions are forbidden but the rotation around the axis A_l is allowed. Wheels mounted on the two outer right limbs (B_r) make it possible to move the two sides towards each other or to pull them apart as can be seen in Figure 10.2c and (d). The displacement δ at point B_r is forced by the engine (E) which pulls or pushes the wheels at a constant speed. This displacement forces the plate to bend to a symmetric anticline or a syncline.

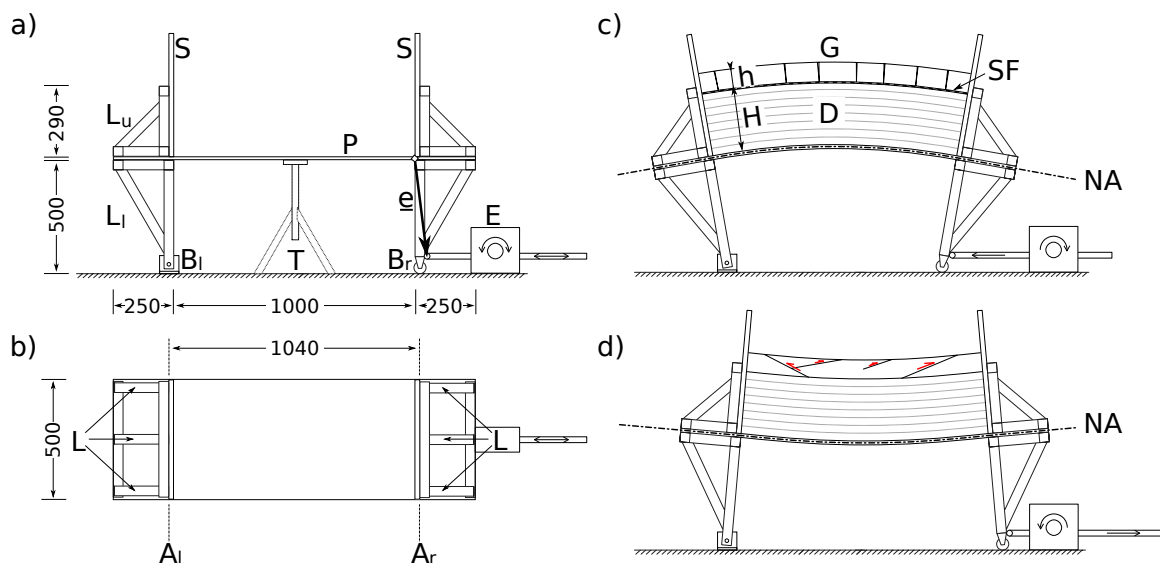


Figure 10.2: Longitudinal sections of the experimental device (a), a plan view (b) at the initial stage. The bending to an anticline (c) and to a syncline (d), *NA* indicating the neutral axis. The experimental device is composed of: Limb (*L*), upper part of the limb (L_u), lower part of the limb (L_l), polycarbonate plate (*P*), base of the left limb (B_l), base of the right limb (B_r), the engine (*E*) which moves a piston, applying the deformation to the right basement (B_r), left Axis of the device (A_l), right axis of the device (A_r), vertical screwed wooden panels 18 mm (*S*), the specimen (*G*) of thickness (*h*) and the foam plates (*D*) which create the offset (*H*) between the polycarbonate plate and the specimen. The stretch-fabric (*SF*) applies the extensional strain at the bottom of the specimen.

The mode of deformation of the specimen depends on its position with respect to the neutral axis of the structure. The experimental setup is designed such that the polycarbonate plate defines the neutral axis (*NA*) since its length remains constant during bending. Additional ex-

tension or compression to the pure bending strain is applied to the mechanical unit depending on the vertical distance between the plate and the analogue layer. This distance is created by a stack of thin Styrofoam plates which are incompressible in our experiments although this property could be modified in future experiments. It is for that reason that the experiment sketched in Figure 10.2d could not be realized and the experiments including bending to a syncline in the preliminary tests, consisted of a specimen without offset (D).

This experimental device makes it possible to investigate the behaviour of different layers from the inner arc, which is dominated by compression, towards the outer arc of a fold, which is dominated by extension. The additional extensional strain, away from the neutral axis, when forming an anticline (Figure 10.2c), is applied to the specimen at its bottom by a stretch-fabric (SF), being clamped to the lateral sidewalls (S). This fabric has the special property to have negligible Poisson's effect when being stretched. This special feature ensures that the fabric does not contract in the out of plane direction when it is stretched by bending.

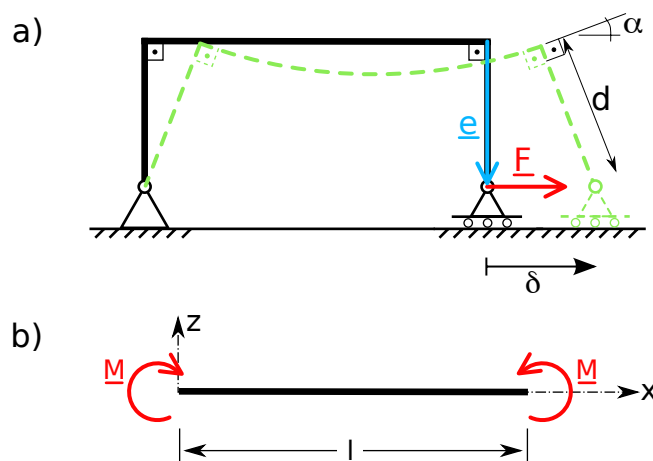


Figure 10.3: Static idealisation of the experimental device with the applied force F at the distance e in the initial stage. The dashed line represents the deformed setup after displacing the right base by δ (a). A simplified system with the bending moment M caused by the force acting on the right limb and the reaction forces on the left limb. Any loads by the specimen and the self weight of the plate have been disregarded in a first approximation.

The idealised deformed frame and an equivalent 2D static system is presented in Figure 10.3 (a) and (b). The plate is thus loaded on the left and the right side with a bending moment (M). The bending moment distribution in the plate is approximately constant, disregarding gravity forces. The bending moment is expressed as $\underline{M} = \underline{e} \wedge \underline{F}$, \underline{e} being the distance between the plate and the point of application of the force F which is needed to move the base of the right limb (B_r). The relationship between the radius of curvature (ρ) and the bending moment reads

$$\frac{1}{\rho} = -\frac{w_{,xx}}{(1 + w_{,x}^2)^{3/2}} \quad \text{with} \quad w_{,xx} = -\frac{M(x)}{EI},$$

where $w_{,xx}$ is the second partial derivative with respect to x of the deflection w , EI is the bending stiffness, product of the the Young modulus and the moment of inertia. The radius of curvature is approximately constant and the deformed plate follows a circular shape. The validity of this assumption is questioned in Appendix C.

10.2.1 Preparation of the setup

Gypsum powder is chosen as the analogue material following the idea of Van Gent et al. (2009) who investigated faulting. The polycarbonate plate is supported from below with a tripod (T) during the preparation of the specimen, Figure 10.2a, to avoid the bending of the plate by the additional loading caused by the compaction of the layer. The free longitudinal sides are closed temporarily with wooden panels. They define the thickness of the uncompacted layer and guarantee the stability of the specimen during compaction. The powder is poured on the polycarbonate plate to obtain a thickness which is around twenty percent larger than the final layer thickness, to account for compaction.

The knowledge of the material properties is needed for scaling the results to field conditions. Van Gent et al. (2009) provide values for cohesion and tensile strength for different void-ratios. The cohesion which is basically due to the van der Waal forces, is strongly dependent on the grade of compaction. Therefore the compaction of the gypsum layer is done in two steps to create reproducible results. In the first step, the powder is compressed with a small, 50x100 mm indenter and an almost flat surface is created. In a second step, a thick foam plate, having the dimensions of the specimen is put above the gypsum layer, with a stiff, heavy plate on its top for the final compaction. The result is an almost homogeneous layer of gypsum powder with a flat surface, essential for the documentation of the fracturing. Before the experiment starts, the temporary sidewalls are removed to provide a free view to the specimen from the sides.

10.3 Results and discussion

This section presents preliminary results to show the applicability of the new experimental device. It will be shown that there is indeed a difference in the relationship between fracture spacing and layer thickness whether a layer is bended or a combination of bending and stretching is applied.

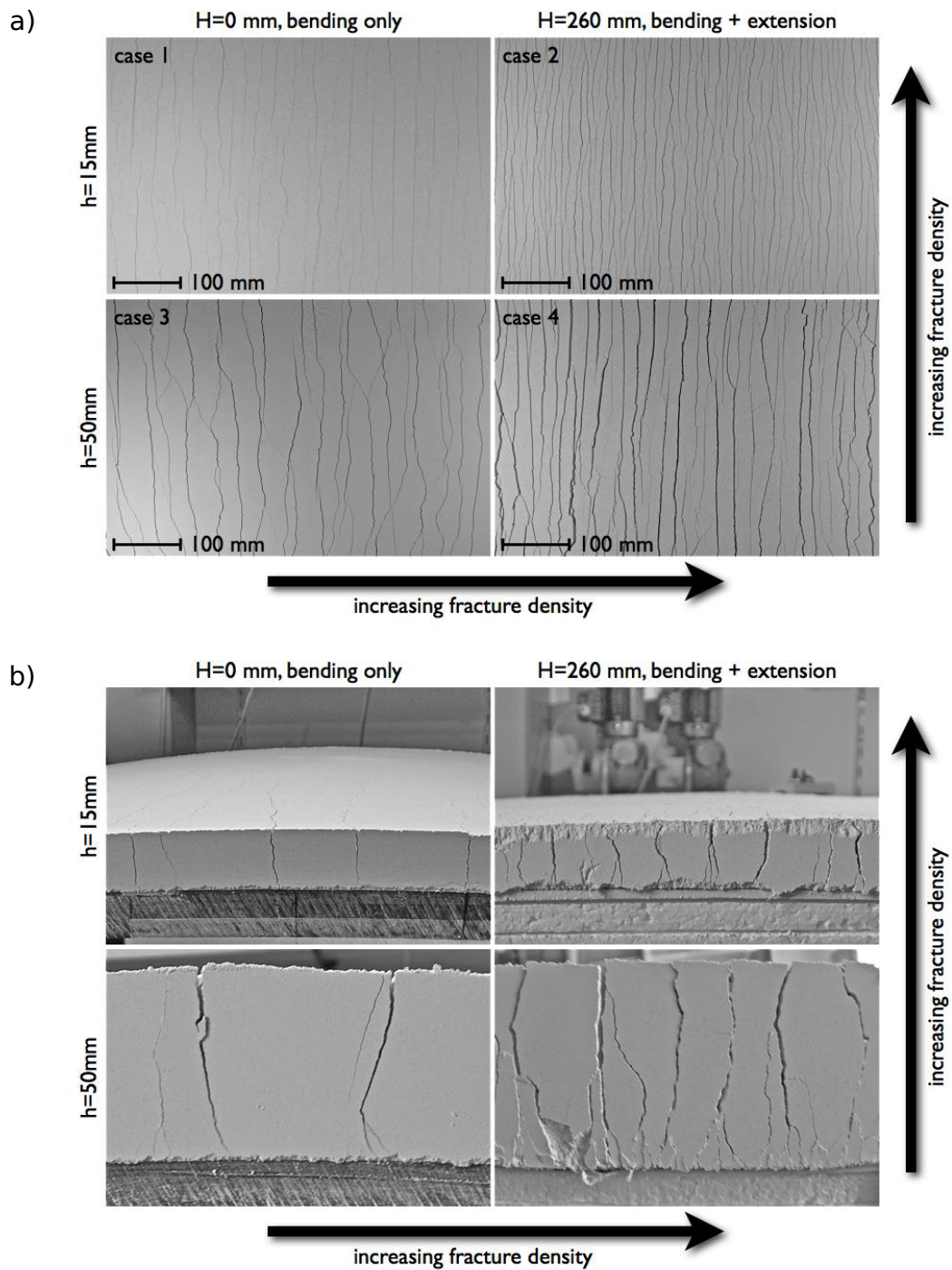


Figure 10.4: Top views, each 550x370 mm (a) and side views (b) of the bended (left column) and bended & extended (right column) for the 15 mm (upper row) and 50 mm (lower row) thick layers. Bending alone leads to coarse fracture spacing compared to the combined mode of bending and extension. The bed thickness appears to have an important influence on the fracture spacing if the bed is away from the neutral axis.

10.3.1 Bending to an anticline

Four different combinations of thicknesses h and offsets H , $[h,H]$, have been tested to show the applicability of the new experimental device:

case 1: $[h,H] = [15 \text{ mm}, 0 \text{ mm}]$,

case 2: $[15 \text{ mm}, 260 \text{ mm}]$,

case 3: $[50 \text{ mm}, 0 \text{ mm}]$,

case 4: $[50 \text{ mm}, 260 \text{ mm}]$.

The results are presented in Figures 10.4a and (b) for bending to an anticline with the curvature for which fracture saturation appears to be reached. The number of fractures is defined as the average number of fractures intersecting the lower and upper boundary of each picture in Figure 10.4a. The spacing is obtained by dividing this average number by the length of the picture. In cases 1 and 3 where the layers are only bended ($H = 0$) the spacing is ~ 28 mm. The bed thickness (h) has thus no influence on the spacing. The fracture spacings created by a combined mode of extension and bending are presented in the right column of Figures 10.4a and (b), case 2 and 4 respectively. The patterns show a denser spacing than the ones created by bending only and is in the range of 10 mm and 17 mm for case 2 and case 4, respectively. The bed thickness plays a role in the fracture spacing.

The influence of the bed thickness on the fracture density, absent for pure bending, is remarkable when comparing the fracturing in the layers with an offset to the neutral axis of the polycarbonate plate. The difference in fracture spacing between cases 2 and 4 is +70 %. However, the fracture aperture is larger for thick layers (case 3) than for thinner ones (case 1) under bending conditions.

10.3.2 Reverse bending from an anticline to a syncline

After the first stage of the experiment, where the fracturing of the specimen by bending to an anticline is created, the plate is bended in the opposite direction to a syncline. That second stage was done for the cases 1 and 3, with the gypsum layers directly on the polycarbonate plate. The reason for that choice is found in the incompressibility of the Styrofoam plates which provide the offset to the polycarbonate plate, see Figure 10.2d. The resulting compression is zero at the base of the specimen and increasing with layer thickness.

The deformation is characterized by two features. In the early stage of reverse bending a second, orthogonal set of fractures (B) is created, presented in Figure 10.5. The cross cutting fractures (A) created by the first bending are boundaries for the new appearing set.

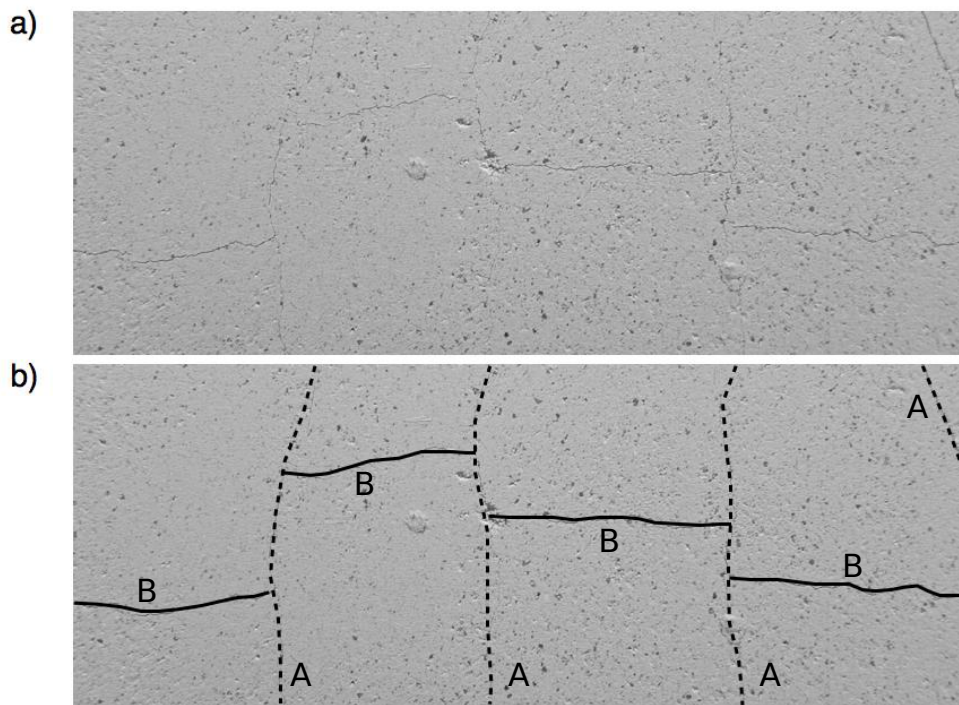


Figure 10.5: Top views of a layer which has been bended to a syncline, after being bended to an anticline. The two sets of fractures presented in (a) are highlighted in (b). The first set of fractures (A) are limiting the second set (B, solid lines) which were created during bending inversion.

The second feature is shown in Figure 10.6 and appears at a later stage of bending. It consists of thrusts (C), striking parallel to the first fracture set which is now closed because of the reverse bending. From the side, it seems that the thrusts are running subparallel to the surface providing a spalling mode of failure. These faults accommodate the shortening and built up a relief. The thrusts are in general striking parallel the first set of fractures along the surface and show occasionally a change in dip to follow their conjugate direction at the secondly created set of fractures.

10.4 Conclusion

A new experimental device and a first set of results on bending fractures has been presented. The new idea is that the layer of thickness (h) is bended at a selected distance from the neutral axis (H). The deformation consists of bending and stretching at the base of the specimen. These

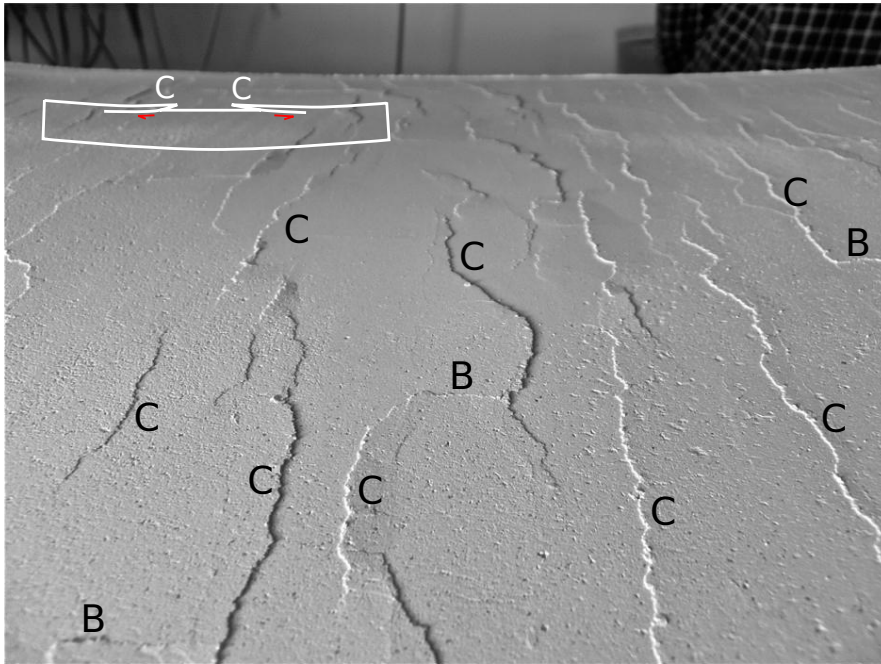


Figure 10.6: Oblique side view of the layer which is bended to a syncline after it was deformed to an anticline. A relief has formed which consists of small shallow thrusts (C), initiated as surface parallel fractures, which accommodate the shortening. The inset in the upper left corner shows a sketch of the thrusting.

two modes are varied during a series of experiments to create different fracture patterns. The influence of the bed thickness (h) and the distance between the layer and the neutral axis (H) are essential when investigating fracturing due to folding. The thinner the layers and the further away they are from the neutral axis, the larger is the fracture density. Free slip along the bedding planes of a multilayered sequence results in a bending only of each layer. This setting is represented by the experiments where a single layer is bent without an offset from the plate. Bending without additional extension leads to a fracture density which is not affected by the individual layer thickness. The fracture aperture is larger in order to accommodate the larger strains which are found in thicker layers. The additional lateral extension creates a fracture spacing, strongly dependent on the individual layer thickness. It is also shown that bending inversion creates a set of fractures which is perpendicular to the first created set of fractures. The first set perturbs the fracturing during the second deformation step to create a ladder pattern, which has also been described by Rives et al. (1994).

10.5 Acknowledgements

The work has been done in collaboration with F. K. Lehner from the University of Salzburg during my vacation in Austria. Prof. F. Neubauer, head of the Geology Department, financed the experimental device and provided the facilities. His help is very much appreciated. Thanks also to H. P. Steyrer for his help while documenting the experiments and for some delightful discussions.

Chapter 11

Conclusion and Perspective

This thesis is hoped to contribute to the development of quantitative tools which are intended first, to validate structural interpretations and second, to estimate the fracture density of layered rock.

11.1 Kink-folds

Kink-folding in layered sequences requires to activate interface slip and compaction of the bulk material in the two hinges. The initial tilt of the layers, referred to as a geometrical imperfection, and the burial depth are two essential parameters which control the development of the kink-fold.

This last statement has been validated by the experimental study on multiple layers of paraffin wax. The geometrical imperfection triggers the localization of the deformation in a kink-fold which evolves until a thrust is created. The imperfection is three-dimensional and the fold develops accordingly starting from one lateral side (right) of the experimental device. Consequently, the fracture pattern is marked by this 3D effect. The fractures are radial towards the left wall as it is found in the field around periclinal fold terminations. Once the fold has developed laterally, the structure is essentially 2D and a second fracture family develops in the fold extrado. The combination of the two families defines a rhomboidal pattern. Another important observation is that kink hinges are not rotating continuously but in a step-wise manner.

The analytical work on the kink-fold confirms some of these findings. The weaker the interfaces are, the more the folding event is favoured, compared to two other failure modes which are the thrusts and the compaction bands. The dominance of each mode is defined in a new failure map proposed in the space spanned by the burial depth and the initial dip angle of the layering. Shallow burial depths and small geometrical imperfections favour thrusting while large imperfection angles promote kink-folds. The onset of the kink-fold is described by two scenarios. First,

at deep burial depths, slip-enhanced compaction bands, with small width, dominate the onset. Further shortening results in an increase in the band width until the kink is formed. Second, at shallow burial depths and large geometrical imperfections, the kink initiates with a band having a thickness comparable to the multiple layer thickness. Slip and not compaction dominates.

Several amendments to the prototype adopted for the theoretical work could be proposed to come closer to the experimental setup for kink-folds. The symmetry of the structure could be broken by accounting for frictional properties at the interface with the rigid frame and the piston, Figure 11.1. The folded structure consists of five rigid blocks, separated by hinges, where the strain is localized. The left, middle and right blocks are moving rigidly. The two remaining blocks are the left and the right limb of the kink-fold. They are kink bands where interfacial slip dominates. The new kinematics is richer and should promote the dominance of the kink-fold with respect to the two other failure mechanisms which are the thrust and the compaction band.

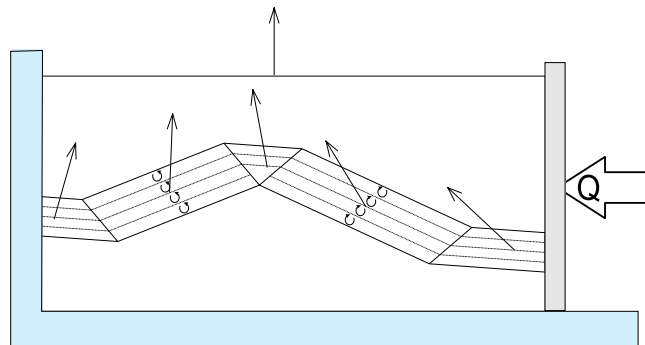


Figure 11.1: A potential extension of the theoretical study on kink-fold is to account for asymmetry and lateral friction with the side walls.

Another amendment to the prototype for the theoretical work on kink-folds concerns the hinges. They are predicted to rotate in a continuous manner whereas they are observed to rotate incrementally during the experiments, Figure 11.2. One reason for that difference could be the rheology of kink hinges. No weakening is introduced in the theory whereas evidence for intense fracturing is observed in the laboratory. The weakening could be accounted for by decreasing either the friction angle or the cohesion of the hinges. This weakening was essential in the thrusting sequences constructed by Cubas et al. (2008) and could have a similar effect in our context. The weakened hinges could give a longer lifespan to a kink (with kink band rotation but no widening upon further shortening). The kink would cease to dominate when the rotation becomes inevitable and a new kink in the pristine material is favoured. This evolution is illustrated in Figure 11.2 where four sets of hinges are presented. The first kink is bounded by the first set of hinges and it becomes deactivated when, within its band, a second kink is initiated

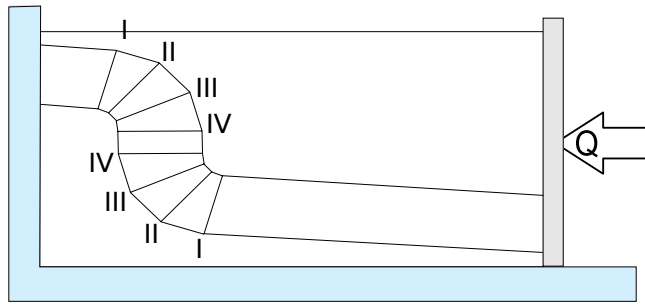


Figure 11.2: The modified prototype for a kink fold evolution showing four steps of incremental hinge rotation.

and bounded by the second set of hinges. The Russian nesting dolls scenario continues in four steps. This scenario would fit perfectly to the field observations and interpretations of Bazalgette (2005). The calculations should still be feasible analytically since the abandoned sections of the old kinks are passively convected with the transformation.

11.2 Fault-propagation folds

The Fault-propagation folds according to the construction of Suppe & Medwedeff (1984) combine the propagation of a fault below a kink-fold which band widens but does not rotate. Hinges are considered as velocity discontinuities and are assigned frictional and cohesive properties. A general construction of the exact velocity field is proposed based on Hadamard's jump condition. It is found that the geometrical construction of Suppe & Medwedeff (1984) could be invalid because mechanical equilibrium is not satisfied for certain values of the hinge friction angle. Analytical solutions for the force (upper bound) necessary to develop this structure has been proposed. This force is compared with the force necessary to produce a thrust cross-cutting instantaneously the kink-fold. The least of the two forces defines the dominant mechanism, folding or thrusting. It is shown that weak hinges (small friction angles) are essential to ensure a finite life-span to the fold.

This theoretical work could be pursued with two ideas. First, the construction of Suppe & Medwedeff (1984) is not optimum in the sense of limit analysis. It is known that hinges are not oriented to conserve bed thickness so some of the geometrical rules are too restrictive. The second idea is that the hinges are not simply frictional but can also compact. Also, bed-parallel slip could occur within the kink band and has been disregarded so far. The kink-fold which is composing the region where the ramp has not yet propagated should be seen more as the kink-fold discussed in the previous section. There is certainly a strong link between Chapter 4 and 5

of this thesis which has not been exploited.

This connection should certainly be extended to the analogue modelling of kink-folds. Experiments with brittle paraffin layers should indeed be designed to shed light on the evolution of fault-propagation folds. A setup is proposed in Figure 11.3. The mechanical unit consists of multiple paraffin layers and rests partly on a layer of plasticine. The second half of the mechanical unit rests on a rigid block which is clamped to the bottom of the loading cell and presents a predefined ramp at its right top corner. The thickness of the unit above the plasticine is larger than above the block. This difference should be responsible for triggering the failure of the multilayer at the predefined ramp.

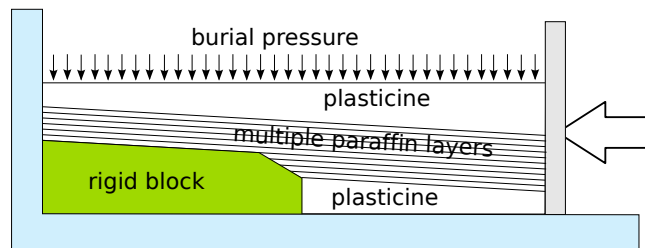


Figure 11.3: A proposed experimental setup for creating fault-propagation folds with brittle paraffin layers under compression. The ramp is part of the rigid block on the left which is clamped to the bottom of the device. The burial pressure, the initial layer dip and the friction on the ramp should control whether thrusting and/or folding will occur.

11.3 Fractures in a layered sequence

11.3.1 Fracture spacing and delamination

The analogue experiments consist of layers of compacted cohesive powders resting on a pre-compressed foam plate. Extension of the compacted powders is achieved by relaxing the foam. Fracture spacing and layer thickness are linearly related confirming the findings of Garrett & Bailey (1977), Ladeira & Price (1981) and Narr & Suppe (1993) in the laboratory and in the field. The fracture spacings at the end of the experiments, when saturation seems to be reached, has a log-normal distribution in terms of frequency. This result has also already been reported by Rives et al. (1992), who studied fracturing in outcrops and from experiments with brittle coatings. These agreements between our observations and those found in the literature have at least the merits to validate the idea to use gypsum powder as an analogue material.

The evolution of the number of fractures within a layer is described with an exponential function in terms of the nominal strain, as it is common practice to do when saturation occurs.

This saturation corresponds to the observation that no further fractures are initiated and the additional straining is captured by fracture opening only. In addition, gaps are opening between the piston and the specimen and between the backstop and the specimen. This latter observation is only possible if at least a part of the interface is slipping. There is thus delamination between the foam plate and the layer, which plays an important role in the fracturing and its saturation.

The development of the delamination and its competition with the fracture process is further quantified with the finite-element analysis based on plasticity theory and strain localization. The delamination is found to occur even if the layer is assumed welded to the foam plate. The delamination then occurs within the bulk material in a thin zone parallel to the welded interface. The delamination propagates parallel to the interface from the stress-free sides and also from the newly created mode I fractures. No further fractures are created once delamination is completed, since no increase in the stress within the layer is possible. Hence, a saturated fracture spacing is reached as soon as the interface, or a thin zone next to the interface within the solid, is activated in shear and opening. This result is surprising, since several studies on fracture spacings have used the argument of welded layers, beginning with Hobbs (1967) and more recently by Bai & Pollard (2000). Our result, once confirmed by others, would mean that a prototype which does not account for the activation of the interface underestimates the minimum possible fracture spacing.

Another result of the finite-element calculation is that the first fractures initiate at the top of the extended layer whereas the subsequent ones are propagating from the bottom upwards. The experiments show the same trend.

The main conclusion of the finite-element analysis on the delamination is further studied with the external approach of limit analysis. A new criterion is proposed to determine whether delamination or a central fracture occurs. This criterion relies on a comparison of the frictional properties of the interface and the tensile strength of the bulk material. A new relation is proposed for the minimum fracture spacing. These results were obtained with a virtual velocity field which has the disadvantage to introduce discontinuities across the specimen starting at the tip of the delamination zones. A velocity field with bulk dissipation restrained to the neighbourhood of the tip of the delamination zone would be more realistic.

11.3.2 Perturbation of fracture propagation in multilayers

The fracture development in a multilayered sequence with alternating material properties was investigated experimentally. Gypsum, quartz sand and other cohesive powders were used for composing the various layers. The contact surface between these layers is an interface which properties depend on the two adjacent materials. It is shown that depending on the contrast of

the material properties, straight, wavy or stair-case like crack paths are created. The reason for that behaviour is found in the failure mode (shear and/or opening) within the weaker layer and also in the possible slip of the interfaces. The fracture propagation across weak interfaces is offset if slip occurs. The stronger the interface, the less offset there is.

Weaker layers fail in shear with a failure plane dipping at an oblique angle. The less the contrast in the mechanical properties of two units is, the straighter is the fracture path through the whole sequence.

The goal of further experimental studies should definitely be to get a better understanding of the fracture propagation from, for example an alternating sequence of three layers, the central one being weaker than the two others. Changing the contrast of the strength properties of the neighbouring units and also varying the strength of the interface, by selecting various materials on its two sides, will result in various fracture paths. Further calculations with the finite-elements method should also be done to follow closely the propagation path which cannot be observed so easily during the experiments. The experience gained with the numerics should lead to new prototypes for the analytical approach, which should definitely be extended to multilayered sequences.

11.3.3 Bending fractures

A new experimental device has been constructed to produce bending fractures. The preliminary experiments have shown that the layer thickness has no influence on the fracture spacing if the specimen is loaded in pure bending. Additional basal extension, as it is observed in the outer arc of a fold, shows however a strong dependency of the layer thickness on the spacing. These findings could be refined with a series of experiments using the existing facilities. The account of a confining pressure to reproduce burial pressure would require however an extension of this setup.

A cycle of bending (to an anticline and then to a syncline) resulted in two sets of fractures which are perpendicular to each other. The first set created is interpreted as tension fractures and the second set to appear is due to axial splitting. The propagation of the second set is perturbed by the presence of the first set leading to a ladder like pattern on the top surface.

The scaling of these experimental results to field conditions remains an open question. One should of course start by quantifying more thoroughly the material properties of the analogue materials. Ideally, a powder testing machine, as it is used in the pharmaceutical industry, should be placed next to the experimental device to ensure the same conditions in terms of humidity and grade of compaction.

References

- ASHBY, M.F., 1972. A first report on deformation-mechanism maps. *Acta Metallurgica* 20, 887-97.
- BAI, T. and POLLARD, D.D., 2000a. Fracture spacing in layer rocks: a new explanation. *Journal of Structural Geology* 22, 43-57.
- BAI, T. and POLLARD, D.D., 2000b. Closely spaced fractures in layered rocks: initiation mechanism and propagation kinematics. *Journal of Structural Geology* 22, 1409-1425.
- BAI, T. and POLLARD, D.D. and Gao, H., 2000. Spacing of edge fractures in layered materials. *International Journal of Fracture* 103, 373-395.
- BART-SMITH, H., HUTCHINSON, J.W., FLECK, N.A., EVANS, A.G., 2002. Influence of imperfections on the performance of metal foam core sandwich panels. *International Journal of Solids and Structures* 39, 4999-5012.
- BAZALGETTE, L., 2005. Relations plissement-fracturation multi-échelle dans les multicouches sédimentaires du domaine élastique-fragile. Thèse de doctorat, Université de Montpellier II, Mémoire géosciences Montpellier, v.36.
- BIOT, M.A., 1957. Folding instability of a layered viscoelastic medium under compression. *Proceedings of the Royal Society London*, A242, 444-445.
- BIOT, M.A., 1961. Theory of folding of stratified, viscoelastic media and its application in tectonics and orogenesis. *Geological Society of America Bulletin* 72, 1595-1632.
- BIOT, M.A., 1963. Theory of stability of multilayered continua in finite, anisotropic elasticity. *Journal of The Franklin Institute* 276, 2, 128-153.
- BIOT, M.A., 1963. Stability of multilayer continua including the effect of gravity and visco elasticity. *Journal of The Franklin Institute* 276, 3, 231-252.
- BIOT, M.A., 1964. Theory of internal buckling of a confined multilayered structure. *Geological Society of America Bulletin* 75, 563-608
- BIOT, M.A., 1965. Theory of similar folding of the first and second kind. *Geological Society of America Bulletin* 76, 251-258.
- BIOT, M.A., 1965. Further development of the theory of internal buckling of multilayers. *Geological Society of America Bulletin* 76, 833-840.

- BOBILLO-ARES, N.C., BASTIDA, F. and ALLER, J., 2000. On tangential longitudinal strain folding. *Tectonophysics* 319, 53-68.
- BRAUN, J. and SAMBRIDGE, M., 1994. Dynamical Lagrangian Remeshing (DLR): A new algorithm for solving large strain deformation problems and its application to fault-propagation folding. *Earth and Planetary Science Letters* 124, 211-220.
- BUCHER, W., 1933. *The deformation of the Earth's crust*. Princeton University Press.
- BUDIANSKY, B., FLECK, N.A., 1994. Compressive kinking of fiber composites: a topical review. *Applied Mechanics Review* 47, part 2, S246-S250.
- BUITER, S.J.H., BABEYKO, A.Y., ELLIS, S., GERYA, T.V., KAUS, B.J.P., KELLNER, A., SCHREURS, G. and YAMADA, Y., 2006. The numerical sandbox: comparison of model results for a shortening and an extension experiment, in *Analogue and numerical modelling of crustal-scale processes*, edited by Buitter, S.J.H. and Schreurs, G. pp. 29-64, London Geological Society Special Publication.
- CHAMBERLAIN, R.T., 1910. The Appalachian folds of central Pennsylvania. *Journal of Geology* 18, 337-382.
- CHAPPLE, W.M., 1968. A mathematical theory of finite amplitude rock folding. *Geological Society of America Bulletin* 79, 456-466.
- CHAPPLE, W.M., 1969. Fold Shape and Rheology: The folding of an isolated viscous-plastic layer. *Tectonophysics* 7, 97-116
- CHESTER, J.S. and CHESTER, F.M., 1990. Fault-propagation folds above thrusts with constant dip. *Journal of Structural Geology* 12, 903-910.
- COBBOLD, P.R., COSGROVE, J.W. and SUMMERS, J.M., 1971. Development of internal structures in deformed anisotropic rocks. *Tectonophysics* 12, 225-253.
- COLLIER, M., 1978. Ultimate locking angles for conjugate and monoclinial kink bands. *Tectonophysics* 48, T1-T6.
- COOKE, M., 1996. Frictional slip and fractures associated with faults and folds. Unpublished Ph.D. thesis, Stanford University.
- COOKE, M.L. and Underwood, C.A., 2001. Fracture termination and step-over at bedding interfaces due to frictional slip and interface opening. *Journal of Structural Geology* 23, 223-238.
- CUBAS, N., LEROY, Y.M. and MAILLOT, B., 2008. Prediction of thrusting sequences in accretionary wedges. *Journal of Geophysical Research* 113, B12412, doi:10.1029/2008JB005717.
- DAHLSTROM, C.D.A., 1969. Balanced cross-sections. *Canadian Journal of Earth Sciences* 6, 743-747

- DAHLSTROM, C.D.A., 1970. Structural geology in the eastern margin of the Canadian Rocky Mountains. *Bulletin of Canadian petroleum geology* 18, 332-406.
- DE BRAEMAECKER, J.C. and BECKER, E.B., 1978. Finite element models of folding. *Tectonophysics* 50, 349-367
- ENDIGNOUX, L. and MUGNIER, J. L., 1990. The use of a forward kinematical model in the construction of balanced cross-sections. *Tectonics* 9, 1249-1262.
- ELLIOTT, D., 1965. The quantitative mapping of directional minor structures. *Journal of Geology* 73, 865-880.
- ELLIOTT, D., 1976. The energy balance and deformation mechanisms of thrust sheets. *Philosophical Transactions of the Royal Society A283*, 289-312.
- ENGELDER, T. and PEACOCK, D.C.P., 2001. Joint development normal to regional compression during flexural-flow folding: the Lilstock buttress anticline, Somerset, England. *Journal of Structural Geology* 23, 259-277.
- ERSLEV, E., 1991. Trishear fault-propagation folding. *Geology* 19, 617-620.
- FORTIN, J., STANCHITS, S., DRESEN, G., GUÉGUEN, Y., 2006. Acoustic emission and velocities associated with the formation of compaction bands in sandstone. *Journal of Geophysical Research* 111, B10203.
- GARRETT, K.W. and BAILEY, J.E., 1977. Multiple transverse fracture in 90° cross-ply laminates of a glass fibre- reinforced polyester. *Journal of Materials Science* 12, 157-168.
- GARRETT, K.W. and BAILEY, J.E., 1977. The effect of resin failure strain on the tensile properties of glass fibre- reinforced polyester cross-ply laminates. *Journal of Materials Science* 12, 2189-2194.
- GOGUEL, J., 1952. *Traite de Tectonique*. Masson & Cie, Paris.
- GROSS, M.R., 1993. The origin and spacing of cross joints: examples from Monterey Formation, Santa Barbara Coastline, California. *Journal of Structural Geology* 15, 737-751.
- GUITON, M.L.E., LEROY, Y.M. and SASSI, W., 2003. Activation of diffuse discontinuities and folding of sedimentary layers, *Journal of Geophysical Research* 108, B4, 2183.
- HALLBAUER, D.K., WAGNER, H. and COOK, N.G.W., 1973. Some observations concerning the microscopic and mechanical behaviour of quartzite specimens in stiff, triaxial compression tests. *International journal of rock mechanics and mining sciences* 10, 713-726.
- HANDIN, J.W., FRIEDMAN, M., LOGAN, J.M., PATTISON, L.J. and SWOLFS, H.S., 1972. Experimental folding of rocks under confining pressure: buckling of single layer rock beams. *American Geophysical Union Monograph* 16, 1-28.
- HARDY, S., 1997. A velocity description of constant-thickness fault-propagation folding. *Journal of Structural Geology* 19, 893-896.

- HARDY, S. and FINCH, E., 2007. Mechanical stratigraphy and the transition from trishear to kink-band fault-propagation fold forms above blind basement thrust faults: A discrete-element study. *Marine and Petroleum Geology* 24, 75-90.
- HAYES, C.W., 1891. The overthrust faults of the southern Appalachians. *Geological Society of America Bulletin* 2, 141-154.
- HELGESON, D.E., AYDIN, A., 1991. Characteristics of joint propagation across layer interfaces in sedimentary rocks. *Journal of Structural Geology* 13, 897-991.
- HOBBS, D.W., 1967. The formation of tension joints in sedimentary rocks: an explanation. *Geological Magazine* 104, 550-556.
- HUBBERT, M.K., 1937. Theory of scale models as applied to the study of geological structures. *Geological Society of America Bulletin* 48, 1459-1520.
- ISSEN, K.A., RUDNICKI, J.W., 2001. Conditions for compaction band in porous rock, *Journal of Geophysical Research* 105, B6, 21529-21536.
- JAIN, A., GUZINA, B.B. and VOLLER, V.R., 2007. Effects of overburden on joint spacing in layered rocks. *Journal of Structural Geology* 29, 288-297.
- JAMISON, W., 1987. Geometric analysis of fold development in overthrust terranes, *Journal of Structural Geology* 9, 207-219.
- JOHNSON, A.M. and ELLEN, S.D., 1974. A theory of concentric, kink, and sinusoidal folding and of monoclinial flexuring of compressible, elastic multilayers. I. Introduction. *Tectonophysics* 21, 301-339.
- JOHNSON, K.M. and JOHNSON, A. M., 2002. Mechanical models of trishear-like folds. *Journal of Structural Geology* 24, 277-287.
- KAMPFER, G. and LEROY, Y.M., 2009. Imperfection and burial-depth sensitivity of the initiation and development of kink-folds in laminated rocks. *Journal of the Mechanics and Physics of Solids* 57, 1314-1339.
- KARNIADOKIS, G. and SHERWIN, S.J., 1999. *Spectral/hp Element Methods for CFD*. Oxford University Press.
- KOYI, H.A. and MAILLOT, B., 2007. Tectonic thickening of hanging wall units over a ramp, *Journal of Structural Geology* 29, 924-932.
- LADEIRA, F. L. and PRICE, N. J., 1981. Relationship between fracture spacing and bed thickness. *Journal of Structural Geology* 3, 179-183.
- LANKFORD, J., 1995. Compressive failure of fibre-reinforced composites: buckling, kinking, and the role of the interphase. *Journal of Materials Science* 30, 4343-4348.
- LATHAM, J-P, 1983. The influence of mechanical anisotropy on the development of geological structures. Unpublished Ph.D. Thesis, University of London.

- LAUBSCHER, H.P., 1962. Die Zweiphasenhypothese der Jurafaltung. *Eclogae Geologicae Helveticae* 55, 1-22.
- LEROY, Y., ORTIZ, M., 1989. Finite element analysis of strain localization in frictional materials. *International Journal for Numerical and Analytical Methods in Geomechanics* 13, 53-74.
- LEROY, Y. M., GUITON, M. L. E. and TRIANTAFYLLIDIS, N., 2002. Post-buckling of an elastic plate over an inviscid and buoyant fluid. *International Journal of Solids and Structures* 39, 3873-3891.
- MAILLOT, B. and LEROY, Y.M., 2003. Optimal dip based on dissipation of back thrusts and hinges in fold-and-thrust belts. *Journal of Geophysical Research* 108, B6, 2320-2336.
- MAILLOT, B. and LEROY, Y.M., 2006. Kink-fold onset and development based on the maximum strength theorem. *Journal of the Mechanics and Physics of Solids* 54, 2030-2059.
- MAILLOT, B. and KOYI, H., 2006. Thrust dip and thrust refraction in fault-bend folds : analogue models and theoretical predictions, *Journal of Structural Geology* 28, 36-49.
- MANDAL, N., Deb, S.K. and Khan, D., 1994. Evidence for a non-linear relationship between fracture spacing and layer thickness. *Journal of Structural Geology* 16, 1275-1281.
- MANDL, G., 2000. *Faulting in Brittle Rocks*. Springer-Verlag, Berlin and Heidelberg New York.
- MANDL, G., 2005. *Rock joints, the mechanical genesis*. Springer-Verlag, Berlin and Heidelberg.
- MASSIN, P., TRIANTAFYLLIDIS, N. and LEROY, Y.M., 1996. Stability of a density-stratified two-layer system. *Comptes Rendus de l'Académie des sciences Paris*, t. 322, serie II a, 407-413.
- MERCIER, E., OUTTANI, F. and FRIZON DE LAMOTTE, D., 1997. Late-stage evolution of fault-propagation folds: principles and example. *Journal of Structural Geology* 19, 185-193.
- MITRA, S., 1990. Fault-propagation folds: geometry, kinematic evolution and hydrocarbon traps. *Bulletin of the American Association of Petroleum Geologists* 74, 921-945.
- MOSAR, J. and SUPPE, J., 1992. Role of shear in fault-propagation folding. in *Thrust Tectonics*, edited by K. R. McClay, 123-137, Chapman and Hall, London.
- NARR, W. and SUPPE, J., 1991. Joint spacing in sedimentary rocks. *Journal of Structural Geology* 13, 1037-1048.
- NESTOROVIĆ, M.D., TRIANTAFYLLIDIS, N., 2004. Onset of failure in finitely strained layered composites subjected to combined normal and shear loading. *Journal of the Mechanics and Physics of Solids* 52, 941-974.
- OUTTANI, F., ADDOUM, B., MERCIER, E., FRIZON DE LAMOTTE, D. and ANDRIEUX, J., 1995. Geometry and kinematics of the South Atlas Front, Algeria and Tunisia. *Tectonophysics* 249, 233-248.
- PATERSON, M.S. and WEISS, L.E., 1966. Experimental deformation and folding in phyllite. *Geological Society of America Bulletin* 77, 343-374.

- PATERSON, M.S. and WEISS, L.E., 1968. Folding and boudinage of quartz-rich layers in experimentally deformed phyllite. *Geological Society of America Bulletin* 79, 795-812.
- POLLARD, D.D. and AYDIN, A., 1988. Progress in understanding jointing over the past century. *Geological Society of America Bulletin* 100, 1181-1204.
- PRICE, N.J., 1966. *Fault and joint development in brittle and semi-brittle rocks*. Pergamon Press, Oxford.
- PRICE, N.J., COSGROVE, J.W., 1990. *Analysis of Geological Structures*. Cambridge University Press.
- RAMBERG, H., 1961. Contact strain and folding instability of a multilayered body under compression. *Geologische Rundschau* 51, 405-439.
- RAMBERG, H., 1963. Fluid dynamics of viscous buckling applicable to folding of layered rocks. *Bulletin of the American Association of Petroleum Geologists* 47, 485-505.
- RAMBERG, H., 1964. Selective buckling of composite layers with contrasted rheological properties, a theory for simultaneous formation of several order of folds. *Tectonophysics* 1, 307-341.
- RAMSAY, J.G., 1967. *Folding and fracturing of rocks*. McGraw-Hill, New York.
- RAWNSLEY, K.D., PEACOCK, D.C.P., RIVES, T. and PETIT, J.-P., 1998. Joints in the Mesozoic sediments around the Bristol Channel Basin. *Journal of Structural Geology* 20, 1641-1661.
- RECHES, Z. and JOHNSON, A.M., 1976. A theory of concentric, kink and sinusoidal folding and monoclinical flexuring of compressible, elastic multilayers. VI. Asymmetric folding and monoclinical kinking. *Tectonophysics* 35, 295-334.
- RIVES, T. and PETIT, J.-P., 1990. Experimental Study of Jointing Cylindrical and Non-Cylindrical folding In: *Mechanics of Jointed and Faulted Rock* (edited by Rossmanith), Balkema, Rotterdam.
- RIVES, T., RAZACK, M., PETIT, J.-P. and RAWNSLEY, K.D., 1992. Joint spacing: analogue and numerical simulations. *Journal of Structural Geology* 14, 925-937.
- RIVES, T., RAWNSLEY, K.D. and PETIT, J.-P., 1994. Analogue simulation of natural orthogonal joint set formation in brittle varnish. *Journal of Structural Geology* 16, 419-429.
- ROSEN, B.W., 1965. Mechanics of composite strengthening. In: *Composite Materials* pp. 37-75. American Society of Metals, Metals Park, OH.
- RUDNICKI, J.W. and RICE, J.R., 1975. Condition for the localization of deformation in pressure-sensitive dilatant materials. *Journal of the Mechanics and Physics of Solids* 23, 371-394.
- SALENÇON, J., 1974. *Théorie de la plasticité pour les applications à la mécanique des sols*. edited by Eyrolles, Paris, (English translation : *Applications of the theory of plasticity in soil mechanics*, John Wiley & Sons Ltd, Chichester, 1977).

- SALENÇON, J., 2002. De l'élasto-plasticité au calcul à la rupture. Editions École Polytechnique, Palaiseau and Ellipses, Paris.
- SALVINI, F. and STORTI, F., 2001. The distribution of deformation in parallel fault-related folds with migrating axial surfaces: comparison between fault-propagation and fault-bend folding. *Journal of Structural Geology* 23, 25-32.
- SCIAMANNA, S., SASSI, W., GAMBINI, R., RUDKIEWICZ, J.L., MOSCA, F. and NICOLAI, C., 2004. Predicting hydrocarbon generation and expulsion in the Southern Apennines Thrust Belt by 2D Integrated Structural and Geochemical Modeling: Part I - Structural and thermal evolution. In: *Deformation, fluid flow, and reservoir appraisal in foreland fold and thrust belts*, edited by Swennen, R., Roure, F., Granath, J.W., pp.51-67, A.A.PG. Heldberg series 1.
- SOULOUMIAC, P., LEROY, Y. M., MAILLOT, B. and KRABBENHOFT, K., 2009. Predicting stress distributions in fold-and-thrust belts and accretionary wedges by optimization, *Journal of Geophysical Research* 114, doi : B09404 10.1029/2008jb005986.
- SPYRROPOULOS, C., GRIFFITH, W.J., SCHOLZ, C.H. and SHAW, B.E., 1999. Experimental Evidence for Different Strain Regimes of Crack populations in a Clay Model. *Geophysical Research Letters* 26, 1081-1084.
- STEARNS, D.W., 1978. Faulting and forced folding in the Rocky Mountains foreland. *Geological Society of America Bulletin* 151, 1-37.
- SUPAK, S., BOHNENSTIEHL, D.R. and BUCK, W.R., 2006. Flexing is not stretching: An analogue study of flexure-induced fault populations. *Earth and Planetary Science Letters* 246, 125-137.
- SUPPE, J., 1983. Geometry and kinematics of fault-bend folding. *American Journal of Sciences* 283 (7), 684-721.
- SUPPE, J. and MEDWEDEFÉ, D. A., 1984. Fault-propagation folding. *Geological Society of America Bulletin, Abstracts with programs* 16, 670.
- SUPPE, J. and MEDWEDEFÉ, D. A., 1990. Geometry and kinematics of fault-propagation folding. *Eclogae Geologicae Helveticae* 83, 409-454.
- SUTCLIFFE, M.P.F., FLECK, N.A., 1993. Effect of geometry on compressive failure of notched composites. *International Journal of Fracture* 59, 115-132.
- TIMOSHENKO, S.P and GOODIER, J.N., 1951. *Theory of Elasticity*. Engineering Societies Monographs, 2nd Edition, McGraw-Hill.
- TRIANAFYLLIDIS, N. and LEROY, Y.M., 1997. Stability of a frictional, cohesive layer on a viscous substratum: Validity of asymptotic solution and influence of material properties. *Journal of Geophysical Research* 102 (B9), 20, 551-20,570, doi:10.1029/97JB01442.
- VAN GENT, H.W., HOLLAND, M., URAJ, J.L. and LOOSVELD, R., 2009. Evolution of fault zones

- in carbonates with mechanical stratigraphy - Insights from scale models using layered cohesive powder. *Journal of Structural Geology*, doi:10.1016/j.jsg.2009.05.006.
- VOGLER, T.J., HSU, S.-Y., KYRIAKIDES, S., 2001. On the initiation of kink bands in fiber composites: Part II. analysis. *International Journal of Solids and Structures* 38, 2653-2682.
- WADEE, M.A., EDMUNDS, R., 2005. Kink band propagation in layered structures. *Journal of the Mechanics and Physics of Solids* 53, 2017-2035.
- WEISS, L.E., 1968. Flexural-Slip folding of foliated model materials. In: Baer, A.J., Norris, D.K., (Eds.), *Geological Survey of Canada, GSC paper 68-52*, pp. 294-333.
- WHITTAKER, A., GREEN, G.W., 1983. *Geology of the Country around Westonsuper-Mare. Memoir of the Geological Survey of Great Britain, Sheet 279 and parts of 263 and 295.*
- WILKERSON, S. M. and MEDWEDEFF, D. A., 1991. Geometrical modeling of fault-related folds: a pseudo-three-dimensional approach. *Journal of Structural Geology* 13, 801-812.
- WU, H. and POLLARD, D.D., 1992. Propagation of a set of opening-mode fractures in layered brittle materials under uniaxial strain cycling. *Journal of Geophysical Research, B, Solid Earth and Planets* 97, 3381-3396.
- WU, H. and POLLARD, D.D., 1995. An experimental study of the relationship between joint spacing and layer thickness. *Journal of Structural Geology* 17, 887-905.
- ZEHNDER, A. T. and ALLMENDINGER, R. W., 2000. Velocity field for the trishear model. *Journal of Structural Geology* 22, 1009-1014.
- ZOETEMEIJER, R. and SASSI, W., 1992. 2D reconstruction of thrust evolution using the fault-bend fold method. In: *Thrust tectonics*, edited by K. McClay, pp. 133-140, London Geological Society Special Publication.

CURRICULUM VITAE

Name: Günther KAMPFER
Nationality: Austria
Date and place of birth: 14.01.1977, Villach/Austria
Profession: Civil Engineer
Marital status: married
e-Mail: g.kampfer@gmx.at



Key Qualification:

Experience in tunnel design and construction according to the principles of the New Austrian Tunnelling Method (NATM), experience with numerical analysis for underground structures, analysis of land-slides, slope support and retaining structures, hydraulic & river engineering, reinforced concrete design, geomechanical analysis of geological structures using numerical and analytical methods, analogue modelling of geological structures.

Education:

2007 – 2010: Ecole Normale Supérieure, Paris
Doctoral Thesis : Folds and tension fractures in stratified rocks
at the Laboratoire de Géologie.

1997 - 2003: Technical University of Graz, Austria
Dept. Civil Engineering - Geomechanical Engineering
Degree: October 2003, Diploma Engineer (equivalent M.Sc.)

Professional Experience:

04 2009 - 07 2009 **Shell**, Carbonate Team in Rijswijk/ The Netherlands (Internship)
04 2008 - 08 2008 **Shell**, Carbonate Team in Rijswijk/ The Netherlands (Internship)
09 2005 - 10 2007 **Geoconsult ZT-GmbH**, Salzburg/ Austria (Project Engineer)
04 2005 - 10 2005 **Technical University of Vienna**/ Austria (Research Assistant)
11 2004 - 04 2005 **3G Software und Measurement**, Graz/ Austria (Project Engineer)
06 2004 - 10 2004 **Bernard+Partner ZT-GmbH**, Hall in Tirol/ Austria (Project Engineer)



Directeur de Thèse:

LEROY, Yves M

Responsable de l'Ecole doctorale:

QUIDELLEUR, Xavier

la Directrice de l'Ecole normale supérieure:

CANTO-SPERBER, Monique

Président du jury:

FRIZON de LAMOTTE, Dominique